HARVARD UNIVERSITY
Graduate School of Arts and Sciences

DISSERTATION ACCEPTANCE CERTIFICATE

The undersigned, appointed by the

Harvard John A. Paulson School of Engineering and Applied Sciences

have examined a dissertation entitled:

"Motion Compensation of Cardiac Catheters: Steering and Control"

presented by: Paul Loschak

candidate for the degree of Doctor of Philosophy and here by certify that it is worthy of acceptance.

Signature _____

Typed name: Professor R. Howe

Signature _____

Typed name: Professor R. Wood

Signature _____

Typed name: Professor C. Walsh

Date: July 19, 2016

Motion Compensation of Cardiac Catheters: Steering and Control

A dissertation presented

by

Paul M. Loschak

to

Harvard Paulson School of Engineering and Applied Sciences

in partial fulfillment of the requirements

for the degree of

Doctor of Philosophy

in the subject of

Engineering Sciences

Harvard University

Cambridge, Massachusetts

July 2016

Dissertation Advisor:
Professor Robert D. Howe

Author:
Paul M. Loschak

Motion Compensation of Cardiac Catheters: Steering and Control

Abstract

Advanced navigation of steerable flexible manipulators can enable a wider range of surgical procedures and interventions to be done less invasively. The techniques described here were designed for applications in cardiac catheterization, but can also be applied to other body systems. I present an investigation into orientation and positioning navigation of ultrasound imaging catheters, friction analysis for active stiffness changing, and catheter bracing solutions for left atrial interventions.

Contents

List of Tables

List of Figures

Acknowledgments

I would like to begin by thanking Professor Rob Howe for his stellar advising. His guidance was absolutely instrumental in helping me grow as a researcher. I would like to thank Professor Rob Wood and Professor Conor Walsh for their support in my course work, research projects, and more. And thank you Dr. Laura Brattain and Alperen Degirmenci for being my partners in crime through most of this work.

I would like to thank many engineers, researchers, and colleagues for supporting my development as an engineer and a researcher. From the BioRobotics lab I'd like to thank Dr. Neil Tenenholtz, Qian Wan, Yashraj Narang, Dr. Douglas Perrin, Dr. Leif Jentoft, Dr. Peter Hammer, Dr. Yaroslav Tenzer, Prof. Frank L. Hammond III, Dr. Lael Odner, Dr. Ignacio Galiana Bujanda, Dr. Samuel B. Kesner, and Dr. Robert Schneider. I would also like to thank many members of the MicroRobotics Lab, the BioDesign Lab, the Wyss Institute, Dr. Kevin Galloway, Dr. Daniela Faas, Dr. Amy Kerdok, Dr. Simon DiMaio, and Dr. Lawton Verner.

I would like to thank a wide range of medical doctors, surgeons, researchers, and support staff for helping me learn about the worlds beyond the engineering lab: Cory Tschabrunn, Dr. Elad Anter, Dr. Diego Porras, Dr. Nik Vasilyev, Dr. Ryan Callahan, Dr. Ajith Thomas, Dr. Stephen Chang, Dr. Adam Kibel, Dr. Smita De, and Dr. Michael Curley.

I would like to thank the undergraduate students I supervised: Leah Gaffney, Demetrio Anaya, Vincent Chow, Ali Forelli, Steve Burke, Emi Zumbro, Ryan Neff, Jimmy Huang, Jack Zhou, and Aaron Graham-Horowitz. I hope I taught them a little bit about how to do research and how to be an engineer. Although they might not know it, they taught me so much more.

I would like to thank the U.S. National Institutes of Health and the American Heart Association for funding this research. I would like to thank the Harvard Paulson School of Engineering an Applied Sciences, the Harvard Paulson SEAS Teaching Labs, and the Harvard Derek Bok Center for Teaching and Learning.

I would like to thank my parents and sister, my extended family, and my amazing communities of friends across the Northeast, the continent, and the world that have been

supporting me over the last six years. And the Harvard Law School cafeteria for keeping me nourished.

Dedicated to my friends and family for helping me keep my balance on this journey

Chapter 1

Introduction

1.1 Motivation

Heart disease is the leading cause of death in the United States and most other industrialized nations (Kung et al. (2008)). While many cardiac illnesses, diseases, and disorders can be treated medically, there are also many cases necessitating surgical intervention. Depending on the procedure, surgical intervention requires access to some internal or external regions of the cardiac anatomy. Although certain interventions require open access to the heart, it can be advantageous in many cases to use a minimally invasive approach such as cardiac catheterization. This thesis focuses on technologies to improve the utility of cardiac catheterization in surgical interventions.

In order to understand the motivations for further developing catheterization techniques, first we begin with an abridged look at existing methods for cardiac access. Traditionally, cardiac access in surgery has been achieved by open chest/open heart procedures in which part of the rib cage is temporarily removed to gain manual access to the heart. In recent decades, engineers and clinical researchers have developed techniques and technologies for reducing the invasiveness of those procedures. Mini-thoracotomies reduce trauma to the patient while providing a small open access to the heart. Laparoscopic instruments (long, rigid rods which are manipulated externally to the patient) enable tissue monitoring or

interaction inside the thoracic cavity through small ports in the patient's chest wall. Robotic assistance has a similar level of invasiveness, but provides the added benefits of improved surgeon dexterity, comfort, and accuracy.

In contrast to directly accessing the heart with rigid tools, cardiac catheteriation is a minimally invasive method for gaining access to the heart. Catheters are long, thin, flexible plastic instruments that enter the peripheral vasculature (typically through the brachial or femoral blood vessels) and are actuated from outside the patient. They are typically equipped with sensors for recording measurements or end effectors for interacting with tissue. This is useful for diagnosis and treatment of a variety of conditions including atrial fibrillation, balloon angioplasty, stent placement, and valve replacement (Moscucci (2013)).

Besides reducing invasiveness, cardiac catheterization is also beneficial because it enables procedures to be done while the heart is still beating. This is advantageous when compared with existing procedures (such as valve repair) which require stopping the heart in order to gain access to the interior. This requires rerouting blood oxygenation through a cardiopulmonary bypass machine (abbreviated as CPB and also known colloquially as heart lung bypass). While the cardiopulmonary bypass machine is an important technology that enables life-saving techniques, it is also known to be associated with additional risks of stroke and long-term cognitive deficiencies (Murkin et al. (1999); Roach et al. (1996)). Therefore we are interested in developing techniques and technologies that can accomplish the same procedures while reducing the risks of surgical trauma.

The downsides of cardiac catheterization motivate our work to improve the state of the art. Simple procedures requiring minimal localization, minimal imaging, and simple tools are currently being done in catheter labs across the world. More complex procedures are difficult to perform with catheters due to many reasons. Achieving accurate intracardiac imaging and localization is challenging due to the inherent drawbacks of available imaging modalities. Closed-chest intracardiac imaging techniques are either expensive (magnetic resonance imaging), exposing patients and staff to radiation (x-ray fluoroscopy, computed tomography), or difficult to obtain and comprehend (ultrasound). Accurate manipulation

and navigation are also challenges which require years of training to master. This is due to the cognitive burden from kinematic differences between manual adjustments and the resulting catheter tip motions. Additionally, navigational disturbances result from cyclical cardiac and respiratory motion. Chapters 2-5 of this thesis address the issues of intracardiac imaging, manual navigation difficulty, and cyclical motion disturbances.

Catheter stiffness and bracing stability also contribute to the difficulty in using catheters for complex procedures. In some instances it is important for catheters to have very low stiffness (to avoid damaging tissue), and in other instances stiffness and stability are important for applying high forces (such as in biopsy sampling). Switching catheters requires time and effort, and it reduces the positioning accuracy which was achieved during navigation with the flexible catheter. Chapters 6-7 of my thesis address these issues by presenting potential solutions for catheter stiffness and bracing against cardiac structures.

It is the goal of this thesis to improve the techniques and technologies associated with minimally invasive surgery. Combined with existing clinical technology and expertise, the systems and solutions presented in this thesis aim to enable more complex procedures to be done through cardiac catheterization.

1.2 Background and Prior Art

My thesis investigates navigating off-the-shelf flexible instruments and stabilizing custom built instruments. I focus on flexible instruments that are actuated by a mechanical element inside. This includes pull wire and shape memory alloy type actuation, but excludes actuation by magnetic field. While I do not focus on catheter construction in this thesis, a review of existing methods for catheter construction by Ali et al. (2016) is available. The following subsections provide context for the existing flexible manipulator products and research prototypes.

1.2.1 Commercially Available

Commercially available flexible manipulator systems for medicine are useful for teleoperating catheters in a range of interventional and electrophysiological procedures. Systems such as the Amigo (Catheter Robotics (2016)), CorPath (Corindus (2016)), and V-Drive (Stereotaxis (2016a)) are designed for clinician comfort. Clinician consoles provide control knobs for remotely steering the catheter from a comfortably seated position. Radiation shielding allows clinicians to image using x-ray fluoroscopy without wearing lead. While these systems are useful for improving clinician safety and comfort, they are limited in their improvements to function and navigation. Interfaces in control knob joint space do not mitigate the difficulties of navigating catheters through direct manual control. Other systems such as EPOCH (Stereotaxis (2016b)) and Sensei (Hansen Medical (2016)) enable Cartesian teleoperation control (similar to the robotic assistance provided by the rigid tool minimally invasive da Vinci Surgical System (Intuitive Surgical (2016))) in addition to the safety and comfort benefits mentioned above. These systems do not offer automated navigation. Automated navigation has been proposed in the patent literature (Creighton IV et al. (2008)), but a commercial system has not yet been demonstrated.

1.2.2 Research Prototypes

Teleoperated (Non-Automated) Catheter Navigation

Multiple research prototypes for teleoperative (non-automated) catheter manipulation have been tested in bench top experiments (Thakur et al. (2009); Park et al. (2010); Arai et al. (2002)). These systems tend to use friction rollers to interact with off-the-shelf catheters. These systems provide many of the same benefits as commercially available teleoperation prototypes. Additional benefits include limited automation such as moving the catheter to earlier recorded positions which the catheter was teleoperated to (Cercenelli et al. (2007)). Some systems have been tested in animal models *in vivo* (Cercenelli et al. (2007); Wang et al. (2010)).

Automated Catheter Navigation

Automated navigation of flexible manipulators has been explored through research prototypes in a variety of medical and non-medical applications. A helpful review of the recent state of the art in kinematics of flexible manipulators is available (Webster and Jones (2010)). While all of these systems involve some form of kinematic calculations for navigating continuum robots, systems can be differentiated from each other by actuation types and target working environments. The existing research prototypes which are most relevant to the work presented in this thesis examine pull-wire or shape memory alloy actuated manipulators on the same size scale as cardiac catheters. These systems were designed to navigate inside tube structures (such as vasculature) and then validated in bench top experiments (Camarillo et al. (2009a); Ganji and Janabi-Sharifi (2009); Penning et al. (2011); Jagadeesan et al. (2009)). A limited effort has thus far been devoted to catheter inaccuracies and nonlinearities (Jagadeesan et al. (2008); Jung et al. (2012)) or contact with the environment (Khoshnam et al. (2015); Yip and Camarillo (2016)). Only one study has demonstrated automated catheter tip navigation *in vivo* with limited accuracy results (Ganji et al. (2009)).

Needle-Sized Manipulators

Other robot systems on a smaller size scale may be actuated by manipulating pre-curved concentric tubes (Webster III et al. (2006); Sears and Dupont (2006)) or steerable needles with beveled tips (Webster et al. (2006); DiMaio and Salcudean (2005)). These systems are steered with different actuators and kinematic calculations due to their constructions. A concentric tube robot has been successfully teleoperated in a set of*in vivo* studies on swine (Vasilyev et al. (2013)). Other concentric tube robots are exploring urological, neurological, and pulmonary applications through phantom model and cadaveric studies (Hendrick et al. (2015)).

Endoscope-Sized Manipulators

Robot systems on a larger size scale can be actuated by pull-wires, pneumatic chambers, or embedded actuators. While these systems require larger holes for introduction and are less maneuverable than thinner manipulators, these systems can be navigated more accurately and can exert higher forces on tissue. Flexible manipulator systems for the following procedures have been examined through bench top testing in phantom environments or *ex vivo* animal tissues: transapical valve implantation (Vrooijink et al. (2014)), brain tumor removal (Seung et al. (2015)), transurethral intervention (Goldman et al. (2013)), colonoscopy (Chen et al. (2010a)), and an endoscope with multiple sections (Bardou et al. (2010)). A limited number of flexible manipulator researchers have demonstrated *in vivo* animal testing including closed-chest percutaneous tele-operated epicardial surgery (Ota et al. (2009)) and abdominal single-port access respiratory motion compensation (Ott et al. (2011)).

Non-medical Manipulators

A discussion on flexible manipulators in medicine is incomplete without highlighting key contributions from non-medical systems. Denavit-Hartenberg parameters can be applied to elephant-trunk sized manipulators as in Jones and Walker (2006). A study on hyper redundant flexible manipulators solves forward and inverse kinematics and examines continuum versus jointed approaches Chirikjian and Burdick (1995). Other studies examined dynamics models, mechanics, and cosserat models applied to parallel manipulators (Mochiyama and Suzuki (2002); Rucker and Webster III (2014); Gravagne et al. (2003)). Further specifics on the contributions of medical or non-medical systems will be described in the following chapters.

1.3 Thesis Contributions

The work presented in this thesis contributes to the literature on flexible manipulators. Chapters 2-5 contribute the first instances of flexible manipulator automated orientation control, automated steering of cardiac imaging catheters, rejection of disturbance inputs

to the manipulator body, and multiple degree of freedom (DOF) navigation by predictive filtering for cyclical physiological motions. Chapter 6 contributes the first use of a friction model for actively controlling the stiffness of a flexible manipulator consisting of spherically jointed vertebral segments. Chapter 7 contributes the first prototype cardiac catheter brace that deploys within the heart and stabilizes catheters during a procedure.

1.4 Thesis Outline

This thesis presents the development of three engineering solutions aiming to improve the state of cardiac catheterization care. A robotic system for automatically pointing cardiac ultrasound imaging catheters was developed from initial concept to pre-clinical *in vivo* animal experiments. A robotic system for actively changing the stiffness of custom-built cardiac catheters was developed from initial concept to bench top prototype. A device for bracing catheters inside the heart was developed from initial concept to bench top prototype.

Chapter 2 describes the initial concept and prototyping of a robotic system for automatically pointing cardiac ultrasound imaging catheters. The system consists of a kinematics-based control strategy and the physical implementation of a 4-DOF robot for manipulating cardiac ultrasound imaging catheters. The distal bending section of the ultrasound catheter was kinematically isolated from the body of the catheter, thus simplifying the kinematics to cases in which catheter bending only occurs at the tip. Bench top position and orientation control experiments demonstrated that the system navigated through space with position errors ranging from $1.0 - 1.9$ *mm* RMS and orientation errors 0.17° - 0.3° RMS.

Chapter 3 presents the redesigns of the physical implementation of the robot in order to prepare for *in vivo* animal studies. After initial testing was completed in Chapter 2, it became necessary to improve the actuator layout and the catheter handle-to-motor interface. The updated designs facilitate quick connection and disconnection between the catheter and the robot, enabling the clinician to easily switch between manual and robotic navigation. The motions in each joint were tested to ensure accurate joint-level control of the catheter handle. Results showed that the system adjusted joints with errors ranging from 0.30° -

0.71°, which is well within the required error tolerance for accurate catheter tip navigation.

Chapter 4 describes an updated kinematics-based control strategy for accurately steering the ultrasound catheter *in vivo*. During *in vivo* studies, the catheter body experiences bending throughout the patient vasculature. This unwanted motion causes disturbances to the catheter tip during navigation. The kinematic isolation strategy described in Chapter 2 is not robust to this unwanted motion. Therefore, a more robust strategy for catheter body disturbance rejection was developed and tested on the bench top (mean errors 0.5 *mm* and 0.18°) and *in vivo* (mean errors $1.1 - 2.0$ *mm* and 0.44° - 0.65°).

Chapter 5 derives and implements a respiratory motion compensation strategy as an extension to the catheter body disturbance rejection method described in Chapter 4. A method for estimating cyclical respiratory motion disturbances is described. Estimated motion values are used to create a set of moving coordinate frames which are then applied to the disturbance rejection algorithm. An Extended Kalman Filter is used to predict target motion. These strategies were first tested with a respiratory motion simulator on the bench top (mean errors 0.7 *mm* and 1°) and then tested through *in vivo* animal studies (mean errors $1 - 2$ *mm* and $1°-3°$).

Chapter 6 presents a model for adjusting the stiffness of a custom-built flexible manipulator. The design of the manipulator is from an existing multi-segmented flexible structure in which all segments are connected by cables. Tension on the cables increases the stiffness of the manipulator. While the basic design of this type of manipulator is known, I present a novel model for calculating the friction in each joint and therefore calculating the stiffness of each joint or the over all manipulator. The model was validated through bench top experiments.

Chapter 7 presents a design for a brace that can stabilize cardiac catheters as they cross through the interatrial septum from the right to left sides. The brace is a small structure which is flexible enough to snake through patient vasculature, easily deployable, and structurally supportive. A model for sizing braces to the patient anatomy is also presented. The prototype cardiac bracing structure was tested through bench top experiments.

Chapter 8 summarizes the contributions from the work presented in this thesis. Designing and building these systems and devices led to valuable insights on cardiac catheterization systems while providing important ground work for future research.

Chapter 2

Steering Ultrasound Imaging Catheters in Initial Bench Top Experiments

2.1 Introduction

Chapters 2-5 of this thesis focus on technological development for improving ultrasound (US) imaging and localization in catheter procedures. We examine a specific type of imaging catheter: intracardiac echocardiography (ICE). ICE catheters, which will also be referred to as US catheters, use an US array transducer in the tip of a catheter to transmit side-facing images of soft tissue structures in real time. These steerable devices acquire US images of adjacent tissues from the distal tip. They can be guided through the vasculature to various organ systems such as the inside of the heart, where they can provide views of fast moving heart structures with resolution that may not be possible with external probes. US catheters can also be used for continuous monitoring of RF energy delivery during cardiac ablations (Calkins et al. (2008); Ren and Marchlinski (2007); Epstein et al. (1998); Marrouche et al. (2003)).

US catheters can increase the safety and effectiveness of procedures while being

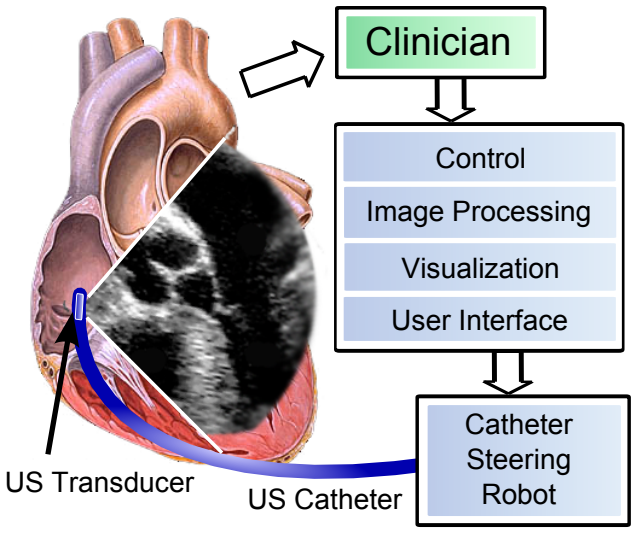

Figure 2.1: *Diagram of the system steering an US imager in the heart.*

minimally-invasive, portable, and cost effective (Cooper and Epstein (2001); Dravid et al. (2008)). However, its use is limited because steering the imaging plane is highly challenging and requires significant training to master. The difficulty in navigating US catheters has limited its use to critical phases of procedures such as performing transseptal punctures, in which the safety benefits of using US catheters have been proven to offset the cost and difficulty required to use them (Moscucci (2013); Jongbloed et al. (2003)). Therefore, we aim to develop a system for automatically navigating US imaging catheters (Fig. 2.1).

While some of the commercially available robotic catheter systems (Hansen) may be used with US catheters, no existing commercial or research prototype robots provide solutions for controlling the orientation of the tip of a catheter. Orientation control is essential for steering an imager towards a target. Therefore a significant learning curve in manual US catheter manipulation remains.

This chapter presents the first known work on controlling catheter position and orientation (pose). Preliminary results on positioning and imager steering were published (Loschak et al. (2013a)). Here we present an expanded analysis on the US catheter steering system to enable new diagnostic and treatment capabilities. A model was developed to relate catheter control actions with catheter tip locations and US imaging plane orientations. Next,

algorithms for visualization strategies for specific tasks were created in conjunction with the bending model. Finally, we validated the model with a 4-DOF robot by automatically navigating the US catheter to a desired pose and pointing the imager at desired targets. This work aims to help clinicians quickly achieve the needed views during procedures while reducing patient and staff exposure to radiation and reducing procedure times.

2.1.1 Ultrasound Catheters

The catheter consists of a plastic handle that can be rotated about or translated along its axis (Fig. 2.2). At the proximal end two pull wires connect to the pitch bending knob and two other pull wires connect to the yaw bending kob. The four pull wires (spaced 90° apart in cross section) extend along the length of the catheter body through the bending section to their attachment points at the distal tip.

The catheter body is $90 - 110$ *cm* long. The most distal 2 *cm* tip of the catheter is rigid and contains the US transducer. Just proximal to the US transducer is the 5 *cm* long bending section, which is designed to be less rigid than the body such that pull wire deflection causes most bending to occur in the bending section. Steering is done by rotating two knobs (pitch and yaw), rotating the handle of the catheter (roll), and translating the handle.

The US catheter used for system validation in this chapter was a 10 *Fr* (3.30 *mm* diameter) 110 *cm* long catheter with a 64-element 2D ultrasound transducer at its distal tip (AcuNav, Biosense Webster, USA). AcuNav is the most common side-facing US catheter in clinical use at present. The catheter handle with joint inputs is labeled in Fig. 2.2. The resulting tip motions are diagrammed in Fig. 2.3.

2.2 Kinematics

The robot uses kinematic calculations to determine the necessary joint adjustments for positioning and orienting the US catheter. Section 2.2.1 describes the US catheter's available DOFs and the assumptions that are made in the steering kinematics. Section 2.2.2 describes forward calculations to solve for the tip pose given the joint knobs. Section 2.2.3 describes the

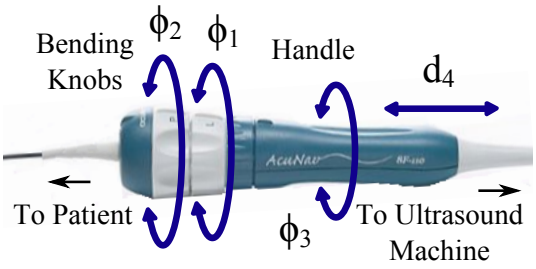

Figure 2.2: *AcuNav ultrasound imaging catheter handle showing four control DOFs.*

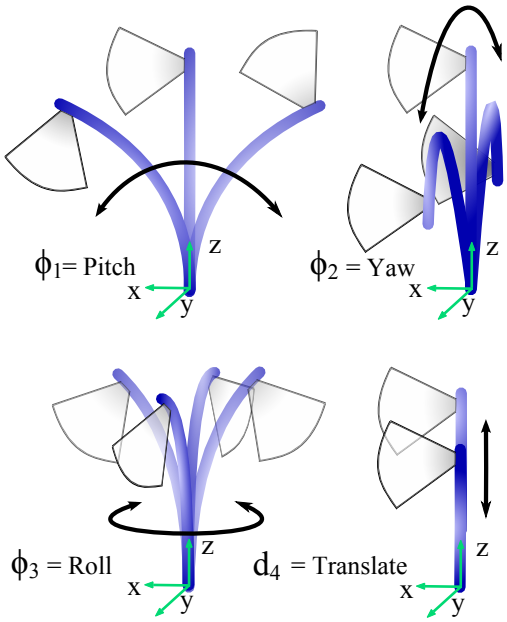

Figure 2.3: *Corresponding tip motion directions.*

inverse calculations to solve for the joint knobs given the tip pose. Section 2.2.4 describes the strategy for spinning the US imager, which requires precise and simultaneous adjustment of many DOFs. Section 2.2.5 applies this strategy to a method for instrument tracking in which the US catheter can constantly monitor a working instrument. Lastly, Section 2.2.6 describes a method for positioning the imager at a kinematically feasible set of points around a target in 3D space.

2.2.1 Kinematics Strategy

Kinematic calculations for the robotic positioning of long, thin flexible manipulators have been examined through many strategies. Material mechanics models (Camarillo et al. (2009b)), geometrically-derived analytical models (Penning et al. (2011)), Denavit-Hartenberg parameter-based models (Ganji et al. (2009)), and remotely actuated continuum models (Gravagne et al. (2003); Rucker and Webster (2011)) have been developed. However, control of catheter tip orientation has not yet become a focus of investigation. We will use geometrically-derived analytical models as the basis of our approach to control the 3-DOF position and 1-DOF of orientation for the US catheter.

Typical steerable cardiac catheters for tissue interaction reach desired positions with three DOF: one plane of bending, handle roll, and handle translation. Alternatively, the three DOF could be: bending in pitch, bending in yaw, and handle translation. Either strategy is sufficient for steering tools in which the rotation of the tool about its tip does not need to be controlled. In contrast with typical cardiac catheters, the side-facing US catheter requires an additional DOF. It is not sufficient to only locate the tip of the catheter in the desired location. The imager must also be pointed in the desired direction. Therefore, US catheters are designed to have four DOF: bending in pitch, bending in yaw, handle roll, and handle translation. Different sets of kinematic calculations utilize the four DOF in different ways depending on which visualization mode the clinician activates.

Our kinematics model the relationship between the joint space control knobs and the task space US imager pose. The kinematic model was based on geometric principles and

classic robot kinematics. Closed-form kinematic solutions have been derived for both the forward and inverse cases. This model is unique in that it is the first model known to the authors capable of calculating both the position and orientation of the catheter tip for catheters with two bending directions. With orientation information, it is then possible to determine the location and direction of the US image.

A number of simplifying assumptions are made to enable the initial steering accomplishments demonstrated in this chapter. The model assumes that catheter bending occurs in the bending plane (neglecting the effects of plastic torsion), the catheter bends with a constant radius of curvature (which has been examined previously by Gravagne et al. (2003)), and that dynamic effects of catheter motion are negligible due to low-speed actuation. The model ignores the nonlinear effects of pull wire slack. This is examined further in Chapters 4-5.

We also ignore the output lost in the transmission due to catheter construction. Actuating the bending knobs increases tension to the pull wires, which then shortens the length of the catheter and causes unmodeled bending to happen in the body of the catheter. In this chapter the robot is designed to constrain motion by maintaining a fixed distance between the handle and the bending section. The fixed base enables the kinematic model to assume that joint-level inputs are conveyed directly to the distal bending section of the catheter without nonlinear losses throughout the catheter body. This is re-examined in Chapter 4.

The last assumption for deriving the kinematic solution to the system involves positional joint coupling in bi-directional bending. Solving for the tip orientation of a traditional serial manipulator would normally require multiplying the origin orientation by transformation matrices corresponding to each joint's orientation change in the proper order (depending on the manipulator). However, the bi-directional bending catheter is a manipulator in which pitch and yaw can occur simultaneously. We begin by making the assumption that the effects of positional coupling between bending directions are negligible. It is assumed that applying pitch then yaw will yield the same kinematic results as applying yaw then pitch (Fig. 2.4). The orientation of the bent catheter can be calculated by rotating about an axis

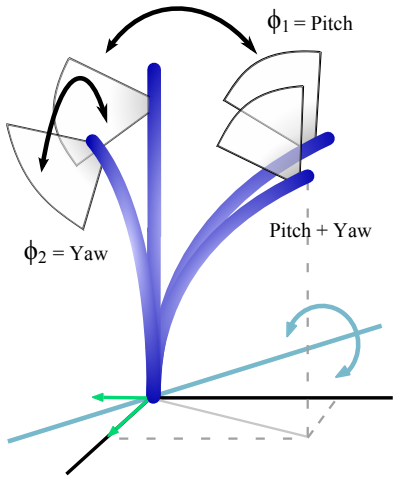

Figure 2.4: *Pitch and yaw of this parallel continuum manipulator are de-coupled in position control.*

(Fig. 2.4 blue line) which represents the ratio of yaw to pitch input to the system. This claim was validated in Loschak et al. (2013a).

2.2.2 Forward Kinematics

The forward kinematics model uses the catheter handle inputs to calculate the position and orientation at the catheter tip. The catheter handle inputs correspond to the four controllable actuated DOFs as in Fig. 2.3. The first input bending knob, ϕ_1, controls yaw in the right-left plane. The second input bending knob, ϕ_2, controls pitch in the posterior-anterior plane. The third input, ϕ_3, controls roll by catheter handle rotation. The fourth input, d_4, controls translation by advancing and retracting the catheter handle. The constants for catheter radius, R_c, length of bending section, L, and effective knob diameter, D_K, must be known as well.

Intermediate variables (Fig. 2.5(a)) are useful to describe the bending of the distal section (Penning et al. (2011)). The ratio of yaw to pitch,

$$\theta = \tan^{-1}\left(\frac{\phi_1}{\phi_2}\right), \tag{2.1}$$

is the angle between the bending plane and the $X-Z$ plane. The amount of pitch and yaw

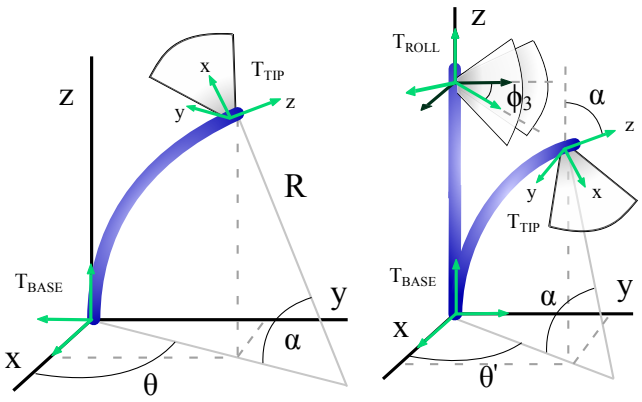

Figure 2.5: *(a) Catheter bending geometry, (b) inverse kinematics.*

pull wire deflections due to the bending knobs are ΔL_1 and ΔL_2, where

$$\Delta L_1 = \phi_1 \frac{D_K}{2}, \Delta L_2 = \phi_2 \frac{D_K}{2}. \tag{2.2}$$

Curvature can be described by the angle

$$\alpha = \sqrt{\left(\frac{\Delta L_1}{R_c}\right)^2 + \left(\frac{\Delta L_2}{R_c}\right)^2} \tag{2.3}$$

and the radius of curvature is

$$R = \frac{L}{\alpha}. \tag{2.4}$$

The catheter tip position from bending can be calculated in terms of R, α, and θ as

$$X = R\left(1 - \cos\alpha\right)\cos\theta \tag{2.5}$$

$$Y = R\left(1 - \cos\alpha\right)\sin\theta \tag{2.6}$$

$$Z = R\sin\alpha. \tag{2.7}$$

It should be noted that θ and Z in this stage of the calculations are only dependent on adjustments in the bending knobs (and not handle rotation or translation). Handle rotation and translation will be applied in a later step.

The tip orientation due to bending can be calculated by the equivalent axis theorem

$$R_{TILT}(\alpha, \mathbf{u}) = \begin{bmatrix} u_1^2 V_\alpha + C_\alpha & u_1 u_2 V_\alpha - u_3 S_\alpha & u_1 u_3 V_\alpha + u_2 S_\alpha \\ u_1 u_2 V_\alpha + u_3 S_\alpha & u_2^2 V_\alpha + C_\alpha & u_2 u_3 V_\alpha - u_1 S_\alpha \\ u_1 u_3 V_\alpha - u_2 S_\alpha & u_2 u_3 V_\alpha + u_1 S_\alpha & u_3^2 V_\alpha + C_\alpha \end{bmatrix}. \tag{2.8}$$

This rotates the orientation by angle α about a new axis $\mathbf{u}$ that is orthogonal to the bending plane (Schilling (1992)). Here $C_\alpha = \cos\alpha$, $S_\alpha = \sin\alpha$, and $V = (1 - \cos\alpha)$. The unit vector $\mathbf{u}$ is calculated by cross products of vectors relating the catheter tip to the base of the bending section and the center of the bending arc. A 4x4 transformation matrix, $T_{TILT}(\phi_1, \phi_2, u)$, is then assembled to tilt the bending tip with respect to the bending base. This contains (7.4) as the rotation and values from (7.1)-(7.3) as tip position. Next the handle rotation and translation matrices, $T_{ROLL}(\phi_3)$ and $T_{TRANS}(d_4)$, are pre-multiplied to calculate the final position and orientation,

$$T_{TIP} = T_{TRANS}(d_4) T_{ROLL}(\phi_3) T_{TILT}(\phi_1, \phi_2, \mathbf{u}). \tag{2.9}$$

2.2.3 Inverse Kinematics

The inverse kinematic model uses (7.9) as input and solves for the single possible catheter configuration. The z-axis of the orientation at the catheter tip is assumed to be tangent to the catheter arc. Therefore, it is possible to solve for intermediate variables α and R which describe the bending in Fig. 2.5(b). Calculating the dot product of the world z-axis and the catheter tip z-axis defines the tilt

$$\alpha = \cos^{-1}\left(\mathbf{z}^0 \cdot \mathbf{z}^{TIP}\right). \tag{2.10}$$

Now we must analyze rotation, but it is currently not possible to identify whether the bending plane's rotation occurred due to the bending direction θ, handle roll ϕ_3, or a combination of both. Therefore in the meantime we can use the x and y values of the

catheter tip to solve for a nominal angle value

$$\theta' = \tan^{-1}\left(\frac{y}{x}\right) \tag{2.11}$$

which will be used to calculate the true θ. Equation (7.4) may be applied once again to rotate the tip orientation by α about an axis orthogonal to the bending plane. The orthogonal axis $\mathbf{u}'$ is used to find the true value. Applying (7.4) results in transforming the tip orientation to an intermediate orientation in which the new z-axis is collinear with the world frame z-axis. The resulting angle between the nominal x-axis and the world frame x-axis is the handle rotation angle, ϕ_3. In this way, we have systematically "undone" the bending to reveal the inputs that will allow the catheter to achieve the desired configuration. With ϕ_3 we may calculate the true θ and the pull wire displacements:

$$\Delta L_1 = R_c \alpha \sqrt{1 + \tan^2 \theta}, \tag{2.12}$$

$$\Delta L_2 = -R_c \alpha \tan\theta \sqrt{1 + \tan^2 \theta}, \tag{2.13}$$

$$d_4 = Z_{TIP} - R \sin\alpha. \tag{2.14}$$

With all four catheter inputs known, converting the values to actuator space becomes trivial. The inverse kinematic function allows the system to use the catheter's desired position and orientation and calculate the required motor commands. Position control (without orientation information) can be achieved with minimal calculation by using (2.1)-(7.3) to solve for ϕ_1, ϕ_2, and d_4.

2.2.4 Imager Spinning

The bi-directional bending catheter is a 4-DOF system which can be position controlled to any point in the workspace by using three DOF. The extra DOF can then be used to orient the imaging plane in any direction that is orthogonal to the tip of the catheter. This provides safe imaging because the US plane can be rotated about the axis of the catheter tip while the ICE catheter is fixed to the same location. Fig. 2.6 demonstrates the process of navigating the catheter to the same position in space using two different steering methods: yaw combined

with roll, or only pitch. The US imager points in a different direction depending on which steering strategy is used.

In Fig. 2.6(A) the catheter begins with the imager pointed to the left. It is first bent in yaw to reach a new position while the imager remains pointed to the left. The catheter is then rolled by 90° about the base to point the imager out of the plane towards the reader.

In Fig. 2.6(B) an identical catheter in the original position is bent in pitch causing the imager to point upwards.

In Fig. 2.6(C) the two navigation strategies are overlaid. For each position there exists a solution set of specific combinations of pitch, yaw, and roll adjustments that reach the same position in space with a different orientation to aim the imager in a different direction. In practice, this means that the imager may be rotated in 1-DOF about the tip of the catheter without displacing the catheter tip by carefully manipulating the three joints simultaneously (Fig. 2.7). This technique enables the robot system to spin the US imager across regions of tissue while collecting images.

Coordinating motion between the three joints is extremely difficult to accomplish manually. Robotically, this task becomes as straightforward as specifying the amount of US imager rotation desired. The desired relative US imager spin angle, ψ, is applied to the tip's mobile z-axis coordinate frame. The new catheter pose is calculated by

$$T_{SPIN} = \begin{bmatrix} \cos\psi & -\sin\psi & 0 & 0 \\ \sin\psi & \cos\psi & 0 & 0 \\ 0 & 0 & 1 & 0 \\ 0 & 0 & 0 & 1 \end{bmatrix}, \tag{2.15}$$

$$T_{NEW} = T_{TIP} T_{SPIN}. \tag{2.16}$$

The controller (described in Section 2.3.3) then rotates the imager while maintaining the fixed position of the catheter tip.

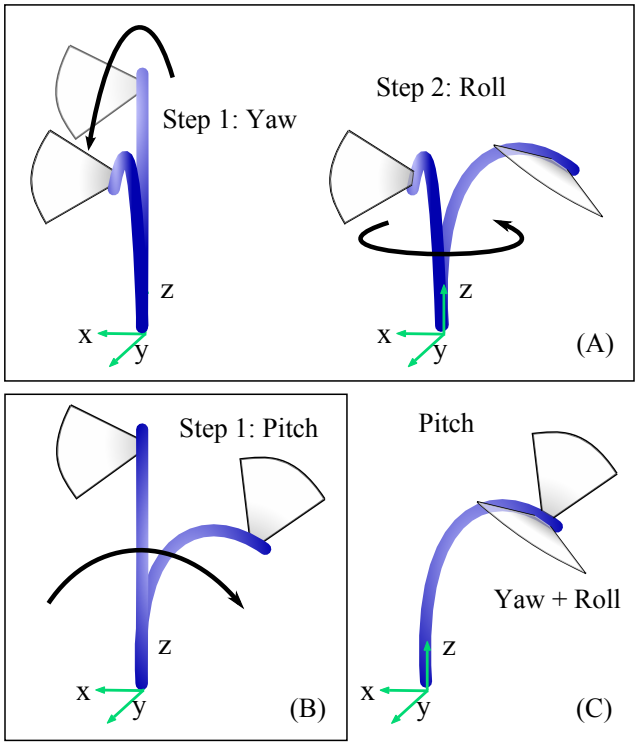

Figure 2.6: *(A) Yaw and roll are applied to the catheter. (B) Pitch is applied to the catheter. (C) The two cases are overlaid demonstrating that the catheter may be position controlled to the same location with varying orientations.*

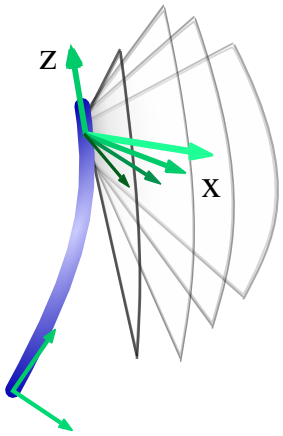

Figure 2.7: *Imager spinning from fixed catheter location.*

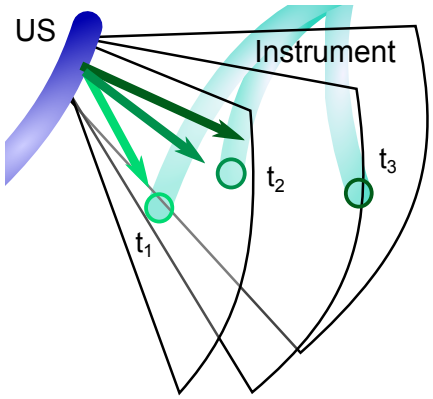

Figure 2.8: *US imager tracks catheter instrument tooltip. Tooltip is navigated to three sequential locations* (t_1, t_2, t_3) *within the US catheter imaging workspace.*

2.2.5 Instrument Tracking

The imager spinning calculation described above in Section 2.2.4 can be applied to track an instrument tooltip (e.g. ablation catheter) while keeping the US catheter fixed in a safe location. The system tracks by measuring the location of the tooltip and spinning the US imager to keep the tooltip consistently within the US imaging plane. The tooltip location is measured by electromagnetic (EM) tracking. Fig. 2.8 demonstrates an ablation catheter being manually moved by the clinician to three different locations around a pulmonary vein opening (PVO) in the left atrium. The green arrows represent vectors within the imaging plane, where the imaging plane is continuously adjusted to point directly at the tooltip target while keeping its tip at a fixed and safe location. We achieve this by computing the angle between the target and the US imaging plane and then using 7.10. The controller (described in Section 2.3.3) maintains the position of the catheter tip. It is assumed that the tooltip is within the imaging depth of the US transducer (up to 15 *cm*) and within the 90° wide image angle. If the tooltip is moved outside this range then the US catheter must be navigated to a new position in order to continue visualizing the tooltip.

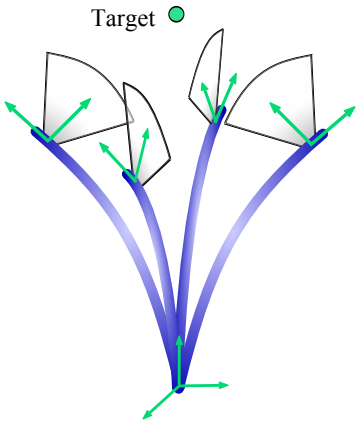

Figure 2.9: *Example of positions moving the catheter around a target while aiming the imager at the target.*

2.2.6 Imager 3D Positioning

In the previous sections a method for imager rotation was described in which a desired angular change is specified while the position must remain constant. In this section, a different imaging technique with an opposite goal is developed. The tip of the US catheter can be rotated around a stationary target while maintaining US imager alignment focused on that target. The US catheter is made to rotate in a circle around a point in space at a constant focal distance, F_D, away from the point. Fig. 2.9 shows a simulation of this motion. For each F_D and object location (within the workspace) there is a solution set of potential catheter positions that will enable the imager to continue pointing directly at the object. The solution set exists at the intersection of the sphere created by the focal distance and a chordal plane through that sphere. The direction of the chordal plane depends on required catheter curvatures for pointing the imager directly at the target. The radius of the chordal plane is related to F_D and L.

The solution set is calculated by first examining the location of the target and identifying the plane of bending. The plane of bending includes the object and the catheter. Within this plane there are two solutions enabling the imager to be F_D away from the target and pointed directly at the target. These two solutions are analogous to the classic robot arm "elbow up,

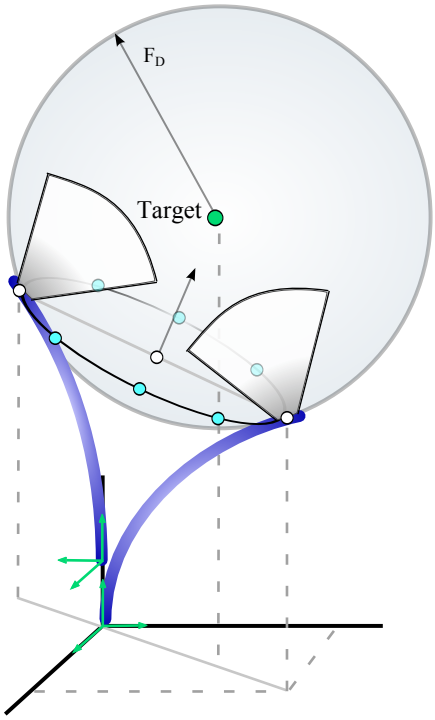

Figure 2.10: *Solution set geometry.*

elbow down" case for conventional robot arms. These solutions are calculated by solving

$$T_{xyz}(\alpha,\theta)T_{roll}(\theta)T_{pitch}(\alpha)T_{US}T_{FD} - T_{object} = 0 \tag{2.17}$$

for α, where T_{xyz} is the transformation due to the catheter bending calculated by (7.1)-(7.3), T_{roll} is a function of θ (which is a function of the target location), T_{pitch} is obtained by rotating about the y-axis by α, T_{US} is the constant transform from the tip of the bending region to the center of the US imager (d_{US}), T_{FD} is the constant transform from the US imager to the target along the x-axis, and T_{object} contains the position of the target. Only the target position is used; not orientation. This calculation differs from (7.9) because yaw is not needed to point the imager directly at the target while the target is in the same plane as catheter bending.

The x, y, and z coordinates from the 4th column of (7.11) are

$$\begin{bmatrix} \frac{L}{\alpha}\left(1-c_\alpha\right)c_\theta + d_{US}c_\theta s_\alpha - F_D\left(s_\theta s_{US} - c_\theta c_\alpha c_{US}\right) - O_x \\ \frac{L}{\alpha}\left(1-c_\alpha\right)s_\theta + d_{US}s_\theta s_\alpha - F_D\left(c_\theta s_{US} + s_\theta c_\alpha c_{US}\right) - O_y \\ \frac{L}{\alpha}s_\alpha + d_{US}c_\alpha - F_D s_\alpha c_{US} - O_z \end{bmatrix} = 0 \tag{2.18}$$

where (O_x, O_y, O_z) refers to the position of the target object. A single-variable nonlinear zero-finding algorithm is used to solve for α in the first and second rows of (7.12). Positive F_D calculates the elbow up α and negative F_D calculates the elbow down α. Both α values returned are the closest to zero (minimum bending effort) and they will satisfy both the O_x and O_y equations. The third row is then used to solve for the required handle translation. Both α values are input to the forward kinematics to calculate the elbow up/down catheter tip positions, shown in Fig. 2.10 as white dots. Next, a vector is formed from the midpoint between positions and the target. This is the normal vector of the chordal plane. The solution set of possible locations for positioning the catheter to image the target exists on the circle where this chordal plane intersects the F_D sphere. Equally spaced positions around the circle (denoted by blue dots) were chosen for experimental validation of the calculations.

Each position on the circle represents a point at which the catheter is capable of achieving the proper curvature to point the imager directly at the target and be F_D away from the target. But by simply navigating the catheter to each of these positions, the imager may not necessarily point at the target. A significant amount of imager spinning (up to $\pm 180°$) may be necessary. The roll adjustment can be pre-calculated through the kinematics and executed in conjunction with positional navigation. This will roll the catheter first and then position the catheter tip accurately at each desired point around the chordal circle such that minimal imager spinning adjustments at each location are needed.

2.3 Validation Methods

A robot was designed to interface with the off-the-shelf US catheter handle. The accuracy requirements of the sensing and control strategy were calculated. Two iterative kinematics-based control strategies were developed in order to converge the catheter pose to a desired position or a desired pose.

2.3.1 Robot

The robot was designed to actuate the four catheter manipulation DOF used in the model (Fig. 2.11). Each DOF was actuated by 6.5 W brushed DC motors driven by digital positioning controllers (EPOS2, Maxon Motor, Switzerland). The actuation strategy was designed for two motors (pitch and yaw bending knobs: Figs. 2.12-2.13) to be grounded to the catheter handle, one motor (roll: Fig. 2.14) to be grounded to the linear stage, and one motor (translation) to be grounded to the table. Two bending knob actuators mounted directly to the catheter handle were connected to the knobs by timing belts. The proximal and distal ends of the catheter handle were connected to ball bearings allowing rotation about the handle center axis. The roll actuator was connected to the catheter handle by a timing belt. The entire system was mounted to a lead screw driven translation stage. The constructed robot is pictured in Fig. 2.15. The green dashed outline shows the US catheter handle inside the knob drivers.

For initial testing the catheter handle and the distal bending section of the catheter were constrained to be held away from each other at the maximum possible distance. A fixture supported the distal bending section while still allowing free rotation about the handle axis (Fig. 2.16).

The US catheter was outfitted with an EM tracker mounted just distal to the bending section and just proximal to the US imager (Fig. 2.17). The sensor is aligned with the long axis of the catheter, fastened into place with parafilm, and calibrated. Calibration relates the key locations of the catheter to the EM tracking system (Fig. 2.18). The coordinate frames on the catheter correspond to the transducer pose, CT, the tip of the bending section, BT, the

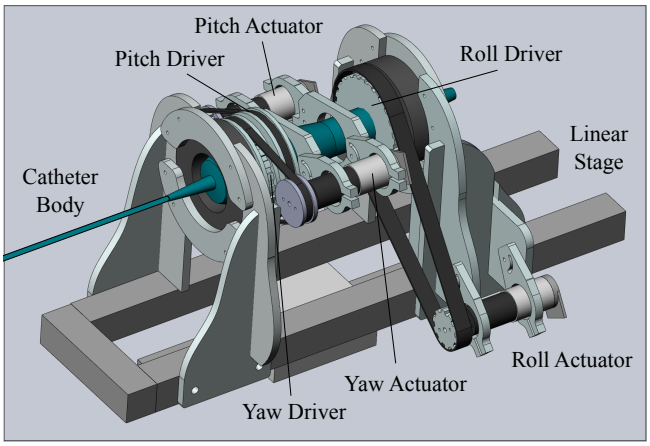

Figure 2.11: *CAD model of US catheter steering robot with 4-DOF.*

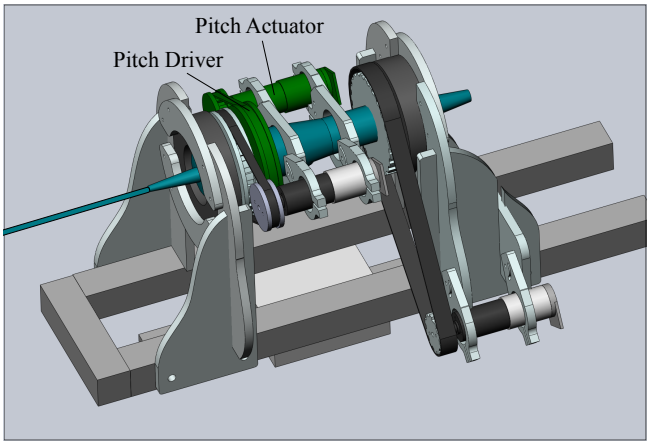

Figure 2.12: *CAD model of US catheter steering robot with 4-DOF. Pitch-related components are highlighted green.*

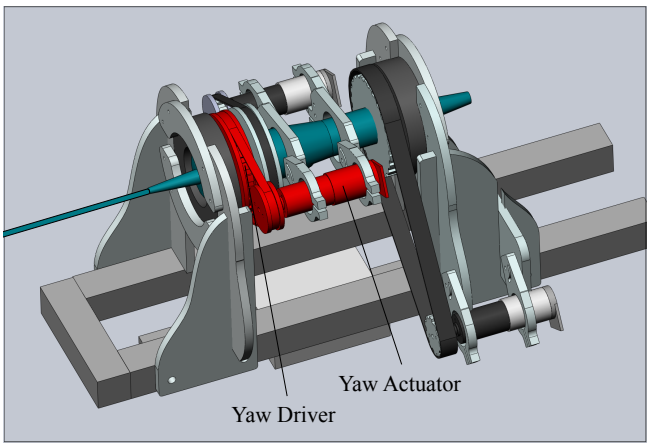

Figure 2.13: *CAD model of US catheter steering robot with 4-DOF. Yaw-related components are highlighted red.*

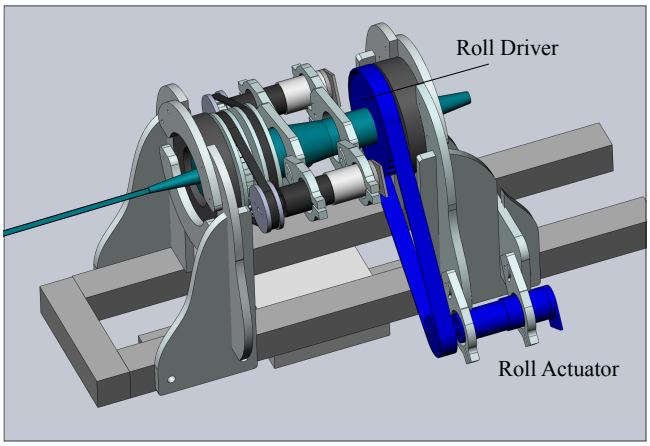

Figure 2.14: *CAD model of US catheter steering robot with 4-DOF. Roll-related components are highlighted blue.*

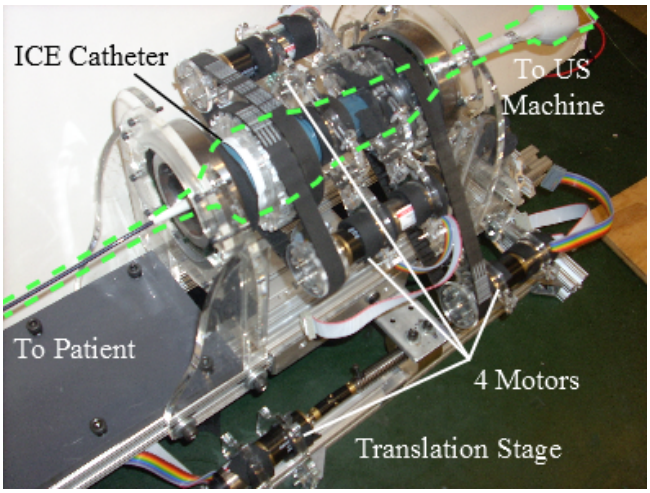

Figure 2.15: *US catheter steering robot with 4-DOF (dashed outline shows catheter handle location within control actuators).*

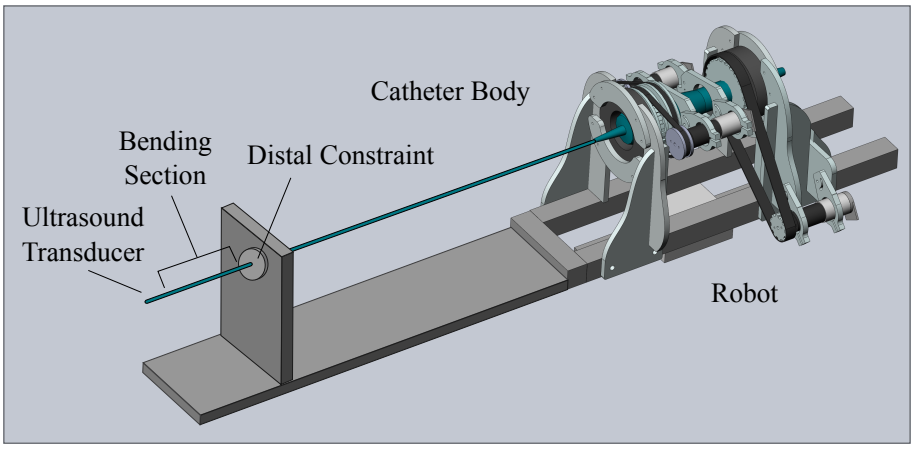

Figure 2.16: *US catheter steering robot with 4-DOF (dashed outline shows catheter handle location within control actuators).*

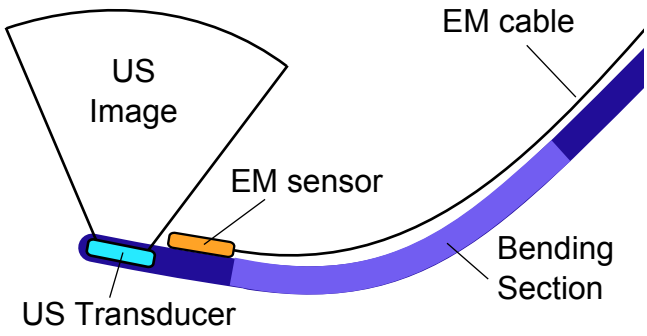

Figure 2.17: *US catheter with one EM sensor mounted near the distal tip.*

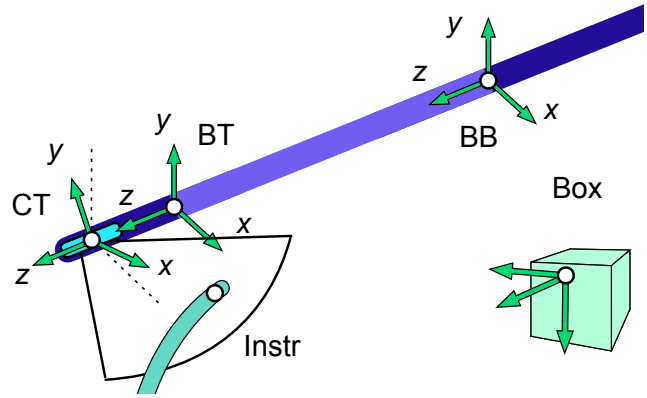

Figure 2.18: *US catheter with one EM sensor mounted near the distal tip.*

base of the bending section, BB, and the working instrument target, $Instr$, with respect to the EM emitter, Box. In these initial experiments the catheter body is fixed and the BB pose acts as a reference zero point fixed in space.

2.3.2 Accuracy Requirements

Controlling the US imager pose involves both the catheter tip sensor accuracy and the US imager properties. The specifications of the sensing system, the US imager, and catheter dimensions are used to predict the allowable error that can exist in the system while the US catheter is still successfully imaging its target. The catheter tip pose is measured by 6-DOF electromagnetic (EM) trackers with accuracy rated at 1.4 mm and 0.5° across a 60 cm cube workspace. The clinical settings (electrophysiology suites) and bench top settings are

designed to minimize EM interference, and relative pose measurements between nearby sensors are more accurate than the manufacturer's specification. The thickness of the US plane is important for determining how well-aligned the imager must be. The US plane thickness varies by depth from the transducer and a conservative approximation is 4 mm. EM tracker errors may result in misalignment of the US plane with the target. Fig. 2.19 shows the example case of a 3 mm ablation catheter target located 70 mm away from the transducer. In each diagram the solid lines refer to the ideally located US imager and the dotted lines referred to the maximum error US imager. The red dots mark the center of the ablation catheter and the center of the US imaging plane. The maximum EM angle error, 0.5°, would result in 0.6 mm error between the center of the ablation catheter and the centerline of the US imager. The maximum EM position error, 1.4 mm, would result in 1.4 mm error. In the worst case scenario of both the angle and position errors the distance between the ablation and US imager centerlines would be 2.0 mm. Due to the 4 mm thickness of the US imaging plane this maximum error would still result in the US imager intersecting with the edge of the target. An additional error of 1.5 mm would be allowable before the narrowest section of the US imaging beam is no longer able to visualize the ablation catheter. Therefore we can be confident that the EM tracking system is accurate enough to be used in US catheter navigation. Better accuracy will improve the imaging quality, but this comes at the cost of navigation time. The accuracy of the catheter navigation is inversely related to the time required to converge at the desired pose. To balance the trade off between accuracy and time, allowable positioning and orientation errors (typically 2 mm and 0.45°) are programmed into the controller.

2.3.3 Position Controller (3-DOF)

The system features a 3-DOF control strategy specifically for converging the US catheter tip to a desired position. The 3-DOF position controller contains two parts: (1) a single command for navigating across large distance, and (2) an iterative loop for navigating small distances.

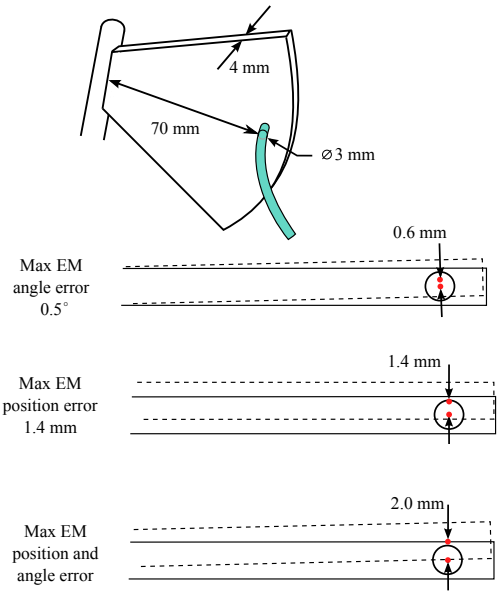

Figure 2.19: *Diagram of EM accuracy with the US imager and the angle error.*

For large distance movements above a specified distance threshold the inverse kinematics calculations use the desired task space position, X_D, to calculate the joint space solution, Q_D (Fig. 2.20 (*top*)). A low-level servo control loop drives each actuator to reach the commanded joint angles, Q. The catheter is bent and then an EM sensor on the tip of the catheter measures its position, X_{EM}. Due to uncertainties with polymer effects in continuum robots and inaccuracies in the system, the joint inputs calculated directly from inverse kinematics typically do not position the catheter tip precisely at the desired position. Therefore this initial position step is followed by an iterative cycle of small position adjustments to reach the target precisely.

Small distance movements below the specified threshold are done through an iterative control loop of measurement, calculation, and joint knob adjustment. The tip sensor is used to measure the error between the current measured and target positions. This is the desired change in task space coordinates, ΔX, which is used in an inverse Jacobian calculation,

$$\Delta Q = J^{-1}\Delta X, \tag{2.19}$$

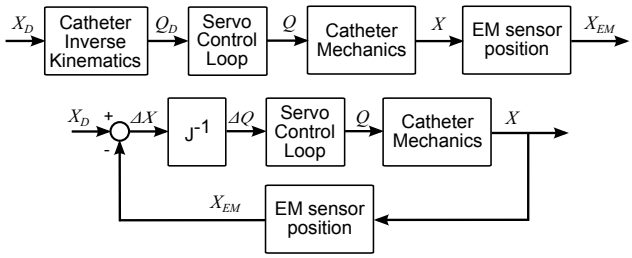

Figure 2.20: *Position controller (top) inverse kinematics loop for large motions, (bottom) Jacobian-based feedback loop for small corrections.*

to obtain the change in commanded joint angles, ΔQ. The Jacobian matrix,

$$J = \begin{bmatrix} \frac{\delta x}{\delta P} & \frac{\delta x}{\delta Y} & \frac{\delta x}{\delta T} \\ \frac{\delta y}{\delta P} & \frac{\delta y}{\delta Y} & \frac{\delta y}{\delta T} \\ \frac{\delta z}{\delta P} & \frac{\delta z}{\delta Y} & \frac{\delta z}{\delta T} \end{bmatrix}, \tag{2.20}$$

is a differentiation of (7.1)-(7.3). This calculation is a linearization of the workspace about the current location of the catheter tip. The values P, Y, and T represent the pitch, yaw, and translation DOFs. Equation (2.20) uses knowledge of the joint knobs to infer the current tip position. This inference is sufficiently accurate only in the constrained bench top setting. Once ΔQ is obtained the servo control loop adjusts the joint knobs, then the catheter moves, and the tip pose is sensed again. The cycle of measurement and adjustment continues as in Fig. 2.20 (*bottom*) until the catheter has reached the desired position within a specified threshold.

2.3.4 Serial Position and Imager Controller (4-DOF)

The 4-DOF control strategy for positioning the catheter tip and adjusting the imager direction is an expansion upon the 3-DOF positioning controller described above. Two calculations are done in series: a proportional controller adjusts handle roll, and the 3-DOF small position adjustment converges the tip to the correct location. Although both the imager angle and the catheter position are dependent on roll and pitch/yaw/translation, it will be shown that controlling roll and position in series leads to accurate results. Fig. 2.21 is a diagram

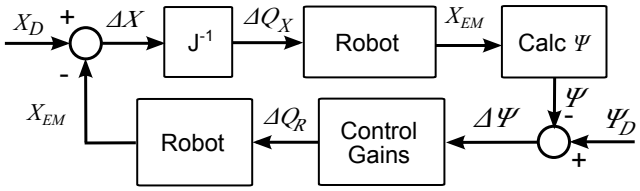

Figure 2.21: *Control diagram for position and imaging angle adjusted in series.*

of this strategy. First, the catheter is navigated by position control (Fig. 2.20) towards the desired position, X_D. The joint-level servo control, catheter mechanics, and EM sensing steps are summarized as "Robot." Next, the orientation of the catheter tip (contained in X_{EM}) is used to calculate the angle between the image plane and the target, ψ. This angular difference is multiplied by a proportional gain $(K_P < 1)$ and the roll actuator rotates the catheter handle by ΔQ_R. Then the position controller is activated again to ensure that the catheter tip remains at the correct position. Position changes affect ψ (unless the robot performs translation only), which is recalculated and the roll axis is adjusted again. This loop of position adjustment, angle measurement, roll adjustment, and position measurement continues navigating the catheter tip towards the desired pose. US images are recorded when both the imager angle and the catheter tip position have reached their desired targets within a specified threshold.

2.4 Experimental Results

The robot platform was used to validate the US catheter steering algorithms on the bench top. Position steering and US imager orientation tests were conducted with the catheter in air without recording US images. During instrument tracking tests the US catheter was introduced through the side of a water tank and navigated to record US images.

2.4.1 Position Steering

The kinematic and control methods described above were used to move the catheter tip to a sequence of specific locations along a path across the workspace. These experiments focused

solely on position control, without regard to the imaging plane directionality. Therefore only three DOFs required for positioning (chosen to be pitch, yaw, and translation) were used. Square paths were chosen because this shape requires the robot to adjust all three DOFs to navigate to each point. The controller moved the catheter tip towards the desired point until it reached the location (within a tolerance of 2 *mm*). Then the robot was commanded to move to the second point, and so on. Shapes in various planes were tested and typical results are shown in Fig. 2.22. The catheter tip successfully navigated to each position within the specified accuracy threshold distance, resulting in positioning error 1.9 *mm* RMS. The joint space adjustments required for creating this trajectory are shown in Fig. 2.23, illustrating the difficulty in manually achieving tip control through simultaneous adjustment of three control inputs.

2.4.2 Imager Spinning

The imager spinning algorithm was used to adjust the angle of the imaging plane 11 times in increments of 5° per adjustment. The 4-DOF controller rolled the catheter handle to rotate the US imager while adjusting the tip to remain stationary in its original position. The results of one example trial are shown in Fig. 2.24. The green lines represent the same vector in the imaging plane as the imager is rotated. The color intensity represents the order in which rotations occurred. The lightest green arrow represents the starting angle of the imager and the darkest green represents the final angle. The control inputs which led to accurate positioning and angular adjustments are shown in Fig. 2.25, once again demonstrating the difficulty in manually achieving this type of motion. This sweeping test was repeated ten times in varying regions of the workspace. The angular adjustment 5° per step resulted in 0.25° RMS error and unwanted catheter tip displacement 1.0 *mm* RMS error.

2.4.3 Instrument Tracking

The instrument tracking algorithm was tested on a phantom in a water tank environment. The US catheter was introduced through the side of the water bucket. The phantom left

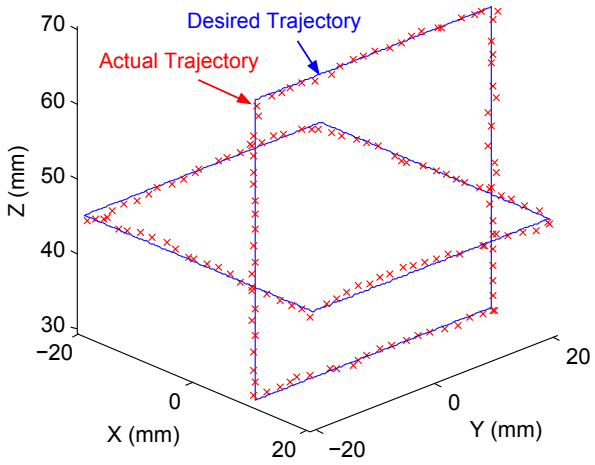

Figure 2.22: *Catheter position control experimental results. Lines are commanded positions, symbols are measured positions.*

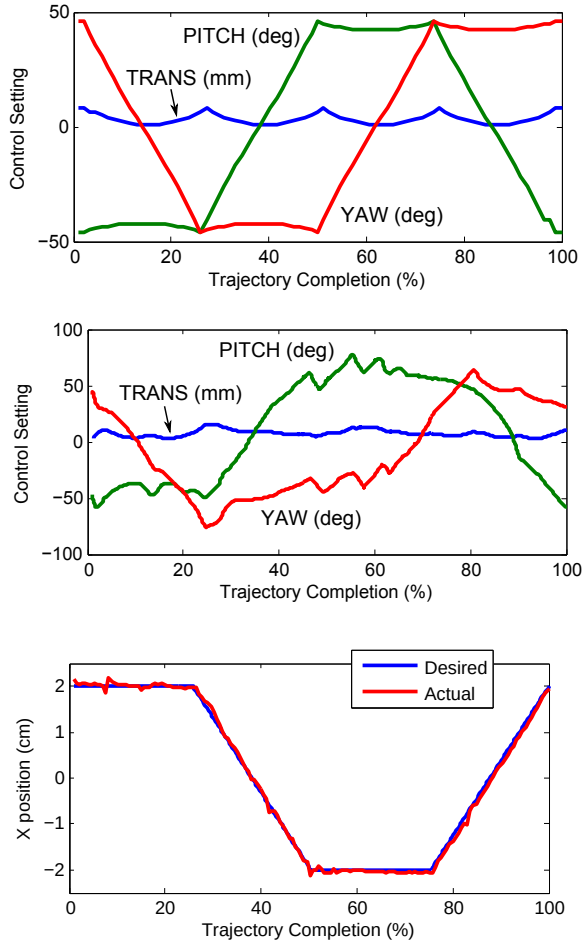

Figure 2.23: *(top) Calculated joint adjustments required to navigate the catheter tip in a square trajectory. (middle) Actual joint adjustments required to navigate the catheter tip in a square trajectory. (bottom) Accurate x-axis catheter tip trajectory resulting from actual joint adjustments.*

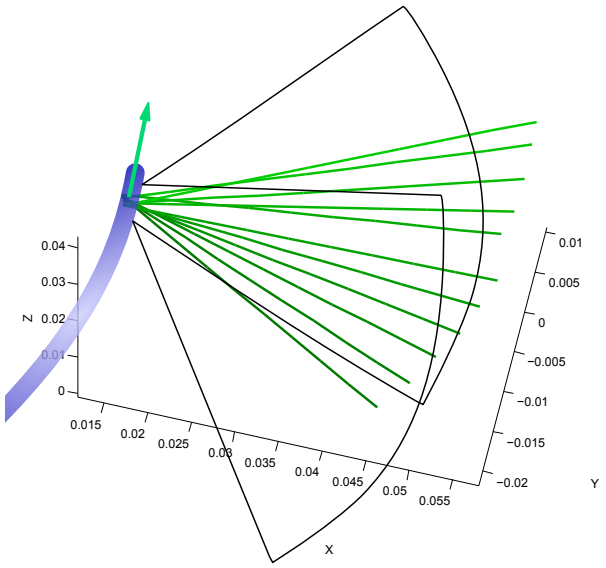

Figure 2.24: *Example results of imager spinning tests. Green lines represent the same vector within each imaging plane as the imager is rotated.*

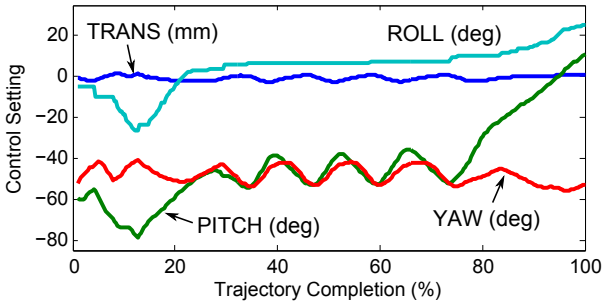

Figure 2.25: *Example of actual joint adjustments required to rotate the US imager while remaining at a fixed location.*

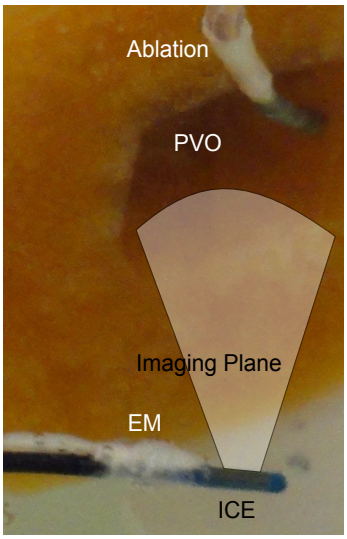

Figure 2.26: *Tracking the instrument tip near PVO*

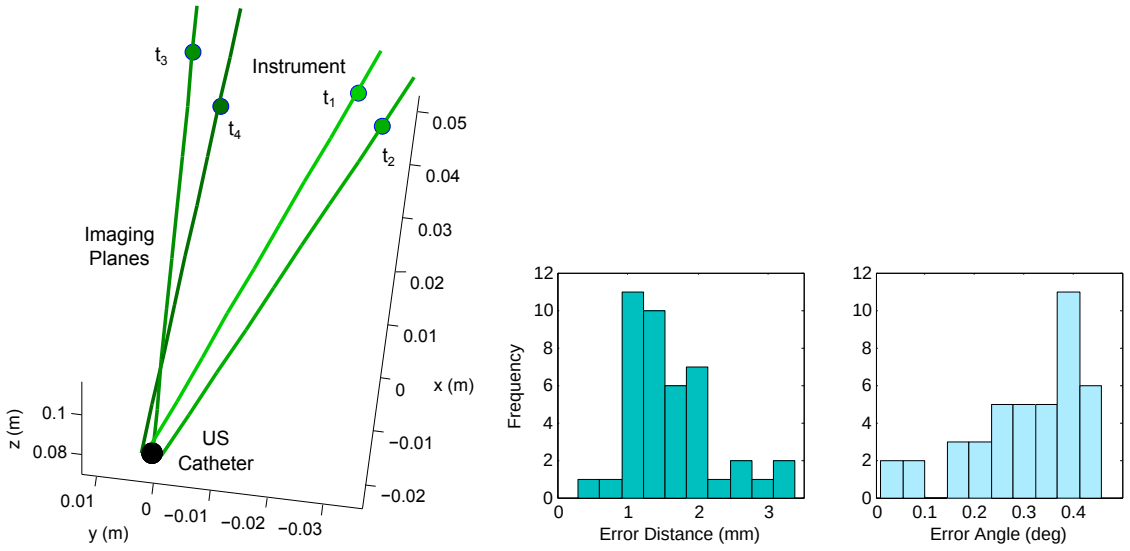

Figure 2.27: *(top) Example results from three instrument tracking trials. Lines show imaging plane vectors intersecting ablation tooltip positions represented by circles. Targets are within ±1 mm of the imaging plane centerline, thus appearing in the images. (bottom) Additional instrument tracking results based on EM-reported angle errors.*

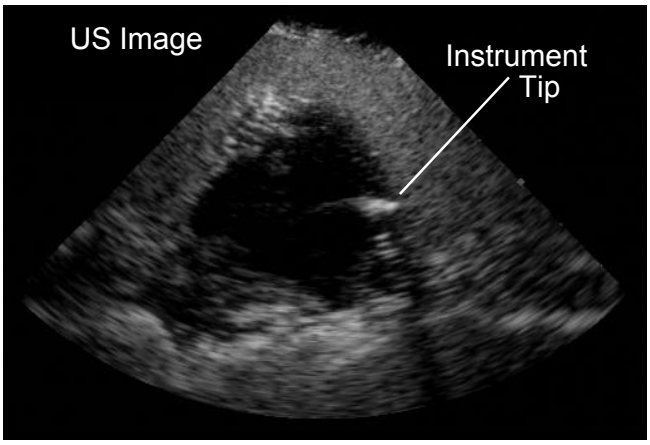

Figure 2.28: *US image of instrument tip during instrument tracking.*

atrium was made from a gelatin mixture containing powdered fiber supplement to mimic the echogenic properties of live tissue in US imaging (Bude and Adler (1995)). The mixture was molded into the shape of a left atrium with an opening roughly 40 mm by 40 mm. The atrium contained four tunnels to represent PVOs. The instrument was designed from a 3 mm diameter section of catheter tubing with an EM sensor mounted inside the tip. It closely resembled the dimensions and echogenic properties of an ablation catheter tooltip. The tooltip was manually moved to various positions around the PVOs while the US catheter system tracked it. Fig. 2.26 shows the experiment setup and Fig. 2.27 (*top*) plots the imaging plane as it followed the tooltip in four example data points. The green circles represent tooltip positions (t_1, t_2, t_3, t_4) that were randomly chosen. The lines show a top-down view of imaging planes as they intersect with the tooltip. The black circle represents a cross-section of the tip of the US catheter. It can be seen that the targets are within ± 1 mm of the imaging plane centerline. A larger set of instrument tracking test results is shown in Fig. 2.27 (*bottom*). The angular tracking accuracy was RMS 0.3°. The US imaging plane has a non-zero thickness which enables the instrument tip to remain visible even though the instrument tip is ± 1 mm away from the US imager centerline, as seen in Fig. 2.28.

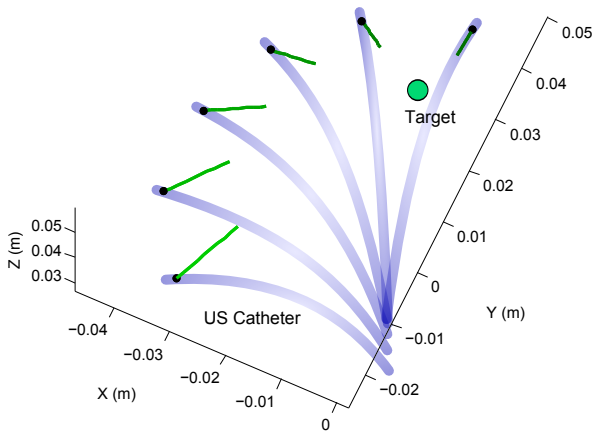

Figure 2.29: *Results of 3D pointing tests (green vectors represent the imaging plane pointing at the target).*

2.4.4 Imager 3D Positioning

The imager 3D positioning and pointing algorithm was used to traverse a half-circle around a virtual target while imaging it from a fixed distance. Experimental results are shown in Fig. 2.29. Blue dots represent the location of the US imager at each position around the half-circle. The green lines represent a vector in the imaging plane which was adjusted by the robot system to point at the target. The robot reached its commanded positions with 1.6 *mm* RMS error and pointed the imager at the object with 0.17° RMS error. Since cardiac anatomy poses many constraints on catheter motion, in practice it is expected that small sections of curvature (rather than large regions of the solution set) may be useful for imaging cardiac structures from multiple angles.

2.4.5 Image Processing

The US catheter was connected to a Siemens Acuson X300 US imaging system to record images during various navigation tasks. The water tank contained gelatin phantom objects. Closely-spaced 2D images of the gelatin objects were acquired across a user-specified region. Since US images are inherently noisy, the images were altered first to reduce the speckle noise. Images were then spatially registered into a common Cartesian coordinate frame using the tip EM tracker locations and interpolated and compounded into a gridded 3D

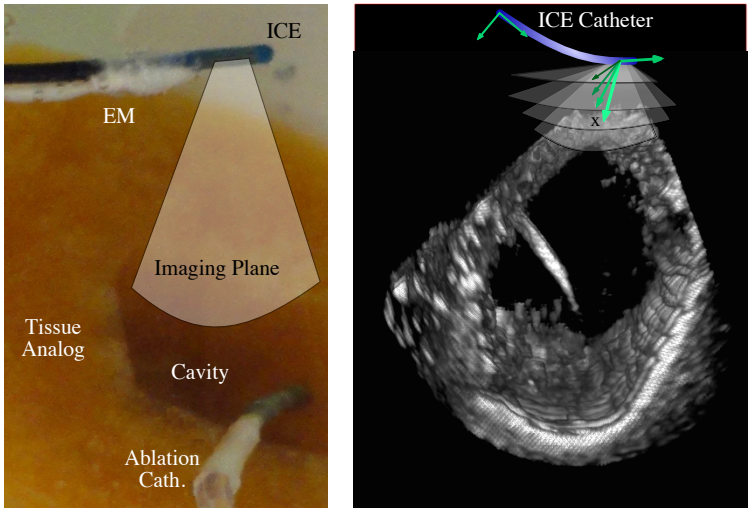

Figure 2.30: *(left) Gelatin tissue phantom with US catheter and ablation catheter, (right) constructed 3D volume*

volume. Example volumes generated are shown in Fig. 2.30. This process is discussed in greater detail in (Brattain et al. (2014); Brattain (2014)).

2.5 Discussion

The results of the validation studies demonstrated accurate positioning and imager spinning capabilities of the system. This enables clinicians to move the US catheter to a safe location and image structures that are difficult to focus on by manual manipulation. Imager spinning is useful for reconstructing volumes, performing diagnoses, or lesion assessment during ablation. Imager spinning in conjunction with instrument tracking enables monitoring instrument-tissue interactions during procedures. The system also demonstrated imaging a virtual target from multiple sides. This approach can enable other visualization strategies, such as allowing a user to choose from a set of possible viewing angles. Throughout trials, the tip of the catheter was navigated to the desired position within the 2 *mm* allowable error threshold and the US imager was rotated to point at targets with sub-degree error.

The system is able to interface directly with US catheters which are already approved by regulatory organizations and have been clinically implemented for over a decade. This

improves clinical feasibility and integration with existing clinical practices at the cost of requiring a greater control effort to overcome nonlinearities and unmodeled disturbances in catheter steering. Off-the-shelf catheter steering accuracy suffers from pull wire friction, backlash in handle knobs, and polymer effects. Many of these effects were ignored during this initial study by constraining the body of the catheter and limiting navigational motion to slow speeds. By constraining the distal bending section, the isolated bending motion could be studied thoroughly.

We choose to examine these effects in the following chapters as we further develop the system for use in *in vivo* animal studies. Future work in algorithm design aims to improve the robustness of the controller for navigating the catheter when the distal section is less constrained. This will be necessary for *in vivo* studies in which the body of the catheter is loosely constrained throughout the vasculature. Additionally, a new design for the robot with quick catheter installation and release is needed in order to conduct *in vivo* studies.

The algorithms developed for this system are useful for any long, thin, flexible tools that rely on achieving a specific orientation with respect to the target in order to complete a task. While this system was developed for use with cardiac catheters, the steering algorithms are applicable to other long, flexible manipulators in other organ systems or industrial uses as well.

2.6 Conclusion

US catheters are currently limited in their clinical usage due to the difficulty of manually steering the US imager in joint space. Therefore, controlling the position and orientation of the catheter tip and the imaging plane is essential for improving current catheter-based procedures and enabling additional procedures to be performed using minimally invasive techniques. The tests described in this study represent the first examples known to the authors of applying US catheter position and orientation kinematics together to robotically enhance visualization.

With the incorporation of real time US visualization and image processing, the robot will

be able to process images of cardiac structures and use inverse kinematics to navigate the catheter tip and imaging plane while maintaining specific relationships with other objects in the heart. Robotic control of US catheters has the potential to shorten procedure times, improve patient outcomes, and reduce the training time required to master use.

Chapter 3

Robot Design for Steering Ultrasound Imaging Catheters In Vivo

3.1 Introduction

Following initial bench top experiments, it was necessary to adjust the robot design for clinical testing in animal models. This chapter details the updated system specifications and two iterative designs for manipulating the catheter handle. Experimental methods and results demonstrate the accuracy of the redesign. The new robot was then used for US catheter steering in an *in vivo* animal study.

3.2 Background

Existing commercial systems (described in Section 1.2.1) are designed to interface with either existing catheter handles (Amigo, V-sono) or require custom-designed catheters (Sensei). Our system is designed to interface with existing catheter handles. We control the 3-DOF position of the catheter and 1-DOF of its orientation by fully articulating the four DOF of US catheters.

3.3 Design Requirements

3.3.1 Degrees of Freedom

Similar to the first robot developed during initial studies (Section 2.3.1), the clinician-friendly robot was designed to position 4-DOF US imaging catheters in an animal operating room setting. It was designed to mate with the handle of any size AcuNav intracardiac echocardiography catheter (Biosense Webster, USA) (Fig. 2.2), and the mating profile could easily be adjusted to fit other types of catheter handles. The translational DOF (ϕ_4) translates the catheter along its axial direction (Fig. 2.3). This motion is necessary for advancing or retracting the catheter further into or out of the patient. A bending DOF twists the "L/R" (pitch, ϕ_1) knob to create a catheter bending motion and pitch the US imager. The other bending DOF twists the "P/A" (yaw, ϕ_2) knob to create a catheter bending motion which causes the imager to yaw. The last DOF (roll, ϕ_3) rotates the handle of the catheter to produce a roll motion about the long axis of the catheter handle. Hard stops inside the catheter limit pitch and yaw axis rotations to $\pm 90°$ relative to the catheter handle. The translation stage was designed to allow 15 *cm* of travel. These limits are enforced in software with a factor of safety to prevent collisions with hard stops. The roll axis was designed to enable continuous rotation.

3.3.2 Accuracy Specifications

The accuracy requirements of the four control knobs were determined by the sensors used for steering the catheter tip. The navigation controller relies on two types of measurements in order to accurately position the catheter tip and point at desired targets. First, readings from the encoders on the actuators serve as measurements for the controller to assume precisely where the joints are positioned. Second, measurements from the EM tracker at the tip of the catheter enable the controller to know the full pose of US imager. The accuracy of the US imager pose is limited by the accuracy of the EM tracking system (trakSTAR, Northern Digital Inc., Canada; 1.4 *mm* position and 0.5° orientation accuracy).

The relationship between the joint inputs and the catheter tip bending output is sensitive such that 1.5° of the pitch or yaw joint knobs produces average 1.4 *mm* motion at the tip. Therefore, it is important that the robot is able to adjust the rotational joint knob inputs to the desired angle within 1.5° and to adjust the translational joint within 1.4 *mm*. This level of accuracy is sufficient for navigating the US imager to the desired location and pointing in the desired direction.

3.3.3 Catheter Handle Insertion

The robot must be designed for simple, quick insertion and removal of catheters. In a typical procedure the clinician connects the US catheter to the transducer adapter for the US machine, manually introduces the US catheter to the vasculature, and then manually navigates the tip of the catheter to the general region of interest. In the robotic procedure the clinician must be able to then disconnect the US machine cable, insert the catheter handle into the robot, secure the catheter in place, and reattach the US machine cable. This process must be easily reversed to remove the catheter and resume manual control. A clinician with minimal experience in robotics should be able to connect the catheter to the robot (or remove the catheter from the robot) within 10 seconds.

3.3.4 Catheter Introducer Friction

Catheters are guided into the vasculature through an introducer, which is a plastic tube containing a rubber seal that prevents blood leakage. The introducer hinders rotational and translational movements of the catheter shaft due to friction against the seal. Clinicians compensate for this by using one hand to manipulate the catheter handle and another hand to grasp the catheter shaft (Fig. 3.1). The two-handed technique increases the amount of torque transmitted to the catheter tip during rotation. It also prevents the catheter from buckling outside the patient during insertion. The robot must be designed with features to assist in catheter shaft rotation and to prevent shaft buckling.

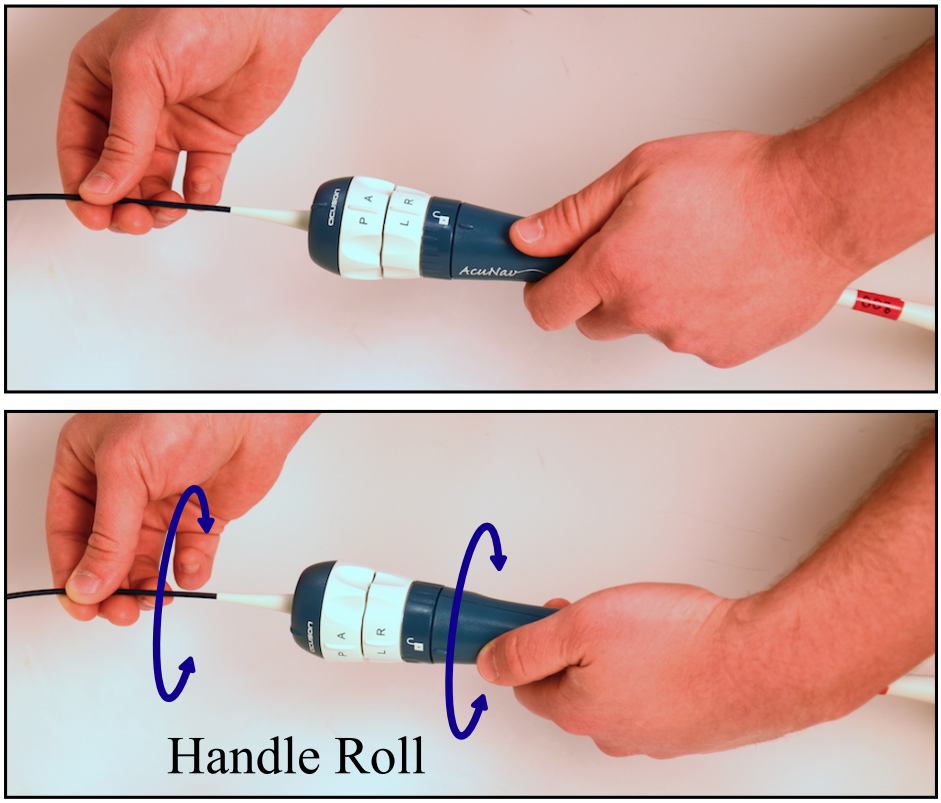

Figure 3.1: *Manual manipulation of handle roll requires coordinated two-handed movements*

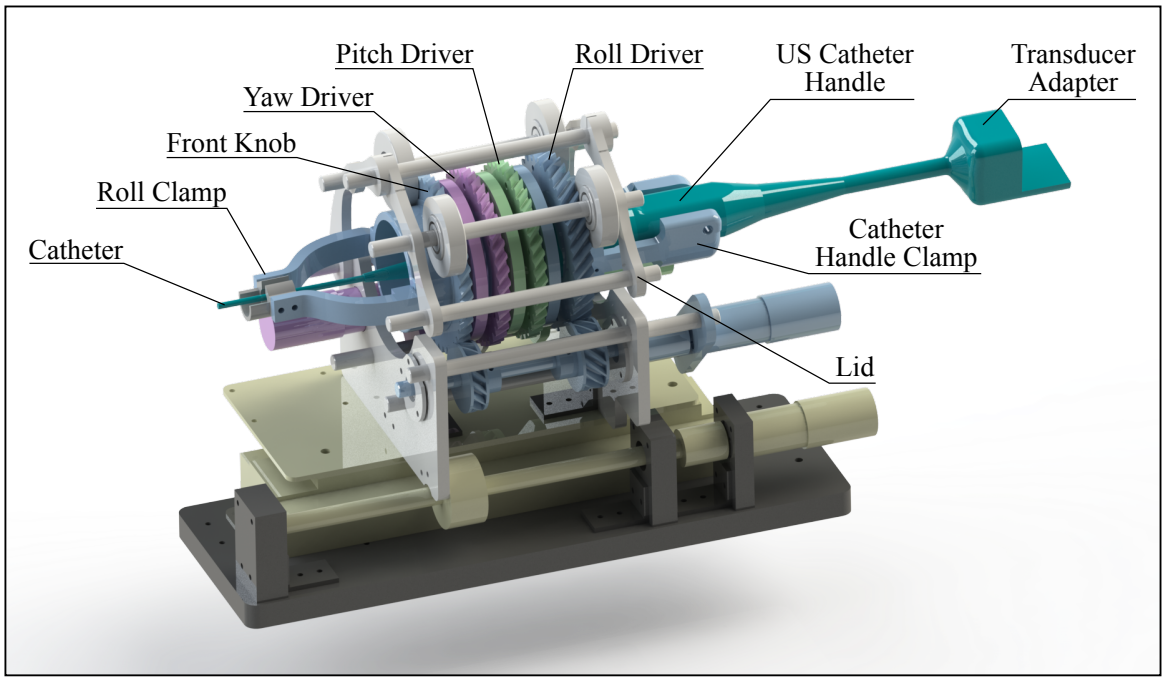

Figure 3.2: *CAD model of the complete robotic system*

3.4 Design Strategy

The complete robot is shown in Fig. 3.2. The key components are the rotational transmission (actuating pitch, yaw, and roll), the catheter cage (which holds the assembly together), and the linear stage (which enables translational motion). This arrangement enables actuation of all four DOF and facilitates easy insertion and removal of the catheter handle. Each key component is described in detail below.

3.4.1 Actuator Layout

The transmission for the three rotational DOFs was designed such that pitch, yaw, and roll actuators were mechanically attached to the translation stage. This resulted in a smaller footprint and quicker catheter handle insertion time, which were advantageous in the clinical setting.

The alternative actuator layout method was for the pitch and yaw actuators to be mechanically grounded to the catheter handle. This decouples all four DOFs and simplifies

the control since pitch and yaw can be actuated independently of other joint motions, but increases the inertial loads on the roll axis. Implementing this alternative layout would require either a longer catheter connection time or a higher part count. Therefore, we have chosen to implement the robot with rotation actuators mechanically grounded to the translation stage.

The downside to the chosen actuator arrangement is that roll, pitch, and yaw motion are coupled. Roll motion causes the entire catheter to rotate, which causes the relative positions of the pitch and yaw knobs on the catheter to change, thereby bending the catheter in unwanted motion. All roll motion must therefore be accompanied by complementary pitch and yaw rotations in order to maintain the desired knob positions on the catheter handle. This necessary compensation of pitch and yaw for roll motion is calculated in the robot software. The effectiveness of pitch and yaw compensation, as well as the accuracy of motion for each joint, is examined in Section 3.5.

3.4.2 Rotational Transmission

The rotational transmission grasps the catheter handle and manipulates the roll, pitch, and yaw DOFs of the catheter. The rotational transmission consists of four transmission knobs that are attached to coaxially rotating parts and constrained by ball bearings. The catheter is inserted by sliding the proximal end of the handle through the central bore of the transmission. The inner surfaces of the rings mate directly to the knobs of the catheter handle. The inner diameters are large enough for the transducer adapter to pass through, but small enough to cause a light press fit between the transmission drivers and the catheter knobs. Protrusions on the inside of the transmission drivers mate with matching depressions on the catheter knob (intended for finger pads during manual use). The outer surfaces of the rings are helical gears mated to the actuators.

The catheter handle clamp couples the roll driver to the US catheter handle. During handle insertion (Fig. 3.3), the catheter handle clamp is rotated downwards on its hinge to avoid obstructing the path of the large transducer adapter. The clamp is then rotated

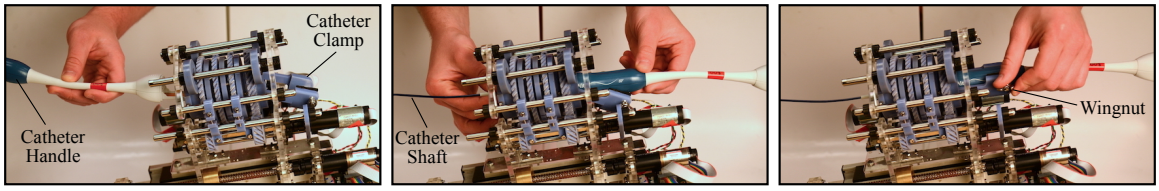

Figure 3.3: *A demonstration of catheter attachment to the robotic system. Attachment and detachment takes less than 10 seconds.*

upwards to mate with the catheter handle. The clamp is squeezed into place with a light press fit and the connection is tightened by a wingnut.

The transmission for the pitch and yaw DOFs consists of multiple components (Figs. 3.4, 3.5). Components related to yaw motion are colored purple, components related to pitch motion are colored green, and components related to roll motion are colored blue. The catheter handle is shown in teal. Part (D) is a helical gear that is fitted to the P/A knob. Part (E) is a bearing ring which positions eight ball bearings equidistantly around the grooved circumference of the gear (D). Part (F) is a cover to constrain the ball bearings in the axial direction. Each of these three parts can rotate independently of each other. Part (G) of the pitch DOF is another helical gear that is fitted to the L/R knob, and it is fully coupled to Part (F) of the pitch DOF via screws and press-fit pins. Part (H) is a second bearing ring which positions eight balls in place. Part (I) is a second cover which constrains the ball bearings on the pitch driver (G). The roll DOF consists of Part (J), a helical gear mated directly to the catheter handle by a set screw clamp, and is fully coupled to Part (I). Part (A) is the front knob, which mates to the roll clamp to transmit roll torques to the catheter shaft. Part (B) is a third bearing ring, which couples Parts (A) and (C). Part (C) is fully coupled to Part (D). The accuracy of the 3D printed bearing races is examined in the experiments section.

3.4.3 Catheter Cage

The rotational transmission is supported in a stable configuration from the top and bottom (Fig. 3.6). The bottom of the transmission is mated to the four driver gears. Three of the driver gears are connected to the roll, pitch, and yaw actuators. The fourth driver gear is

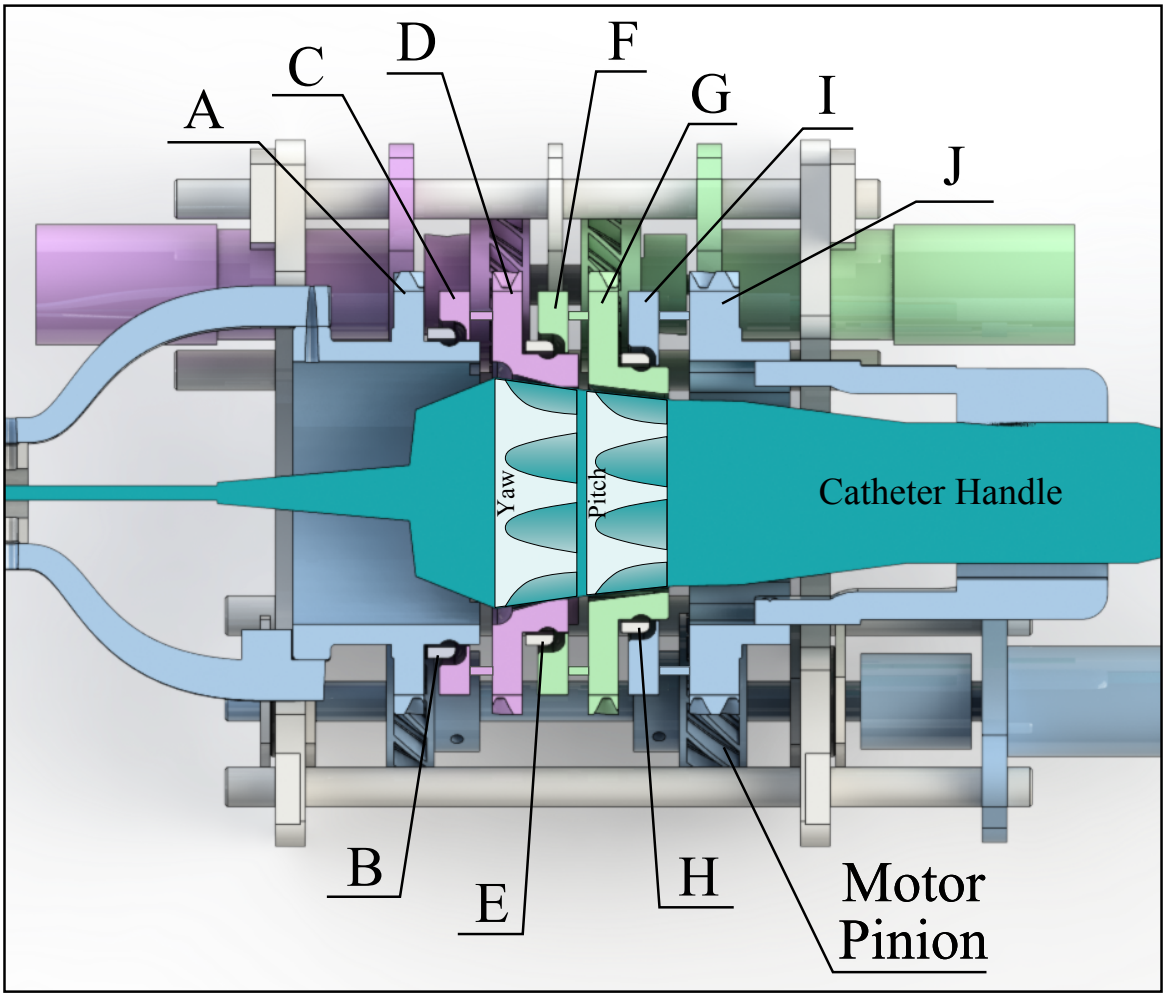

Figure 3.4: *Cross-sectional view showing knob interactions with the catheter. Parts B, E, H are bearings. Parts B, C, D, E enable yaw; parts E, F, G, H enable pitch; and parts A, B, H, I, J enable roll.*

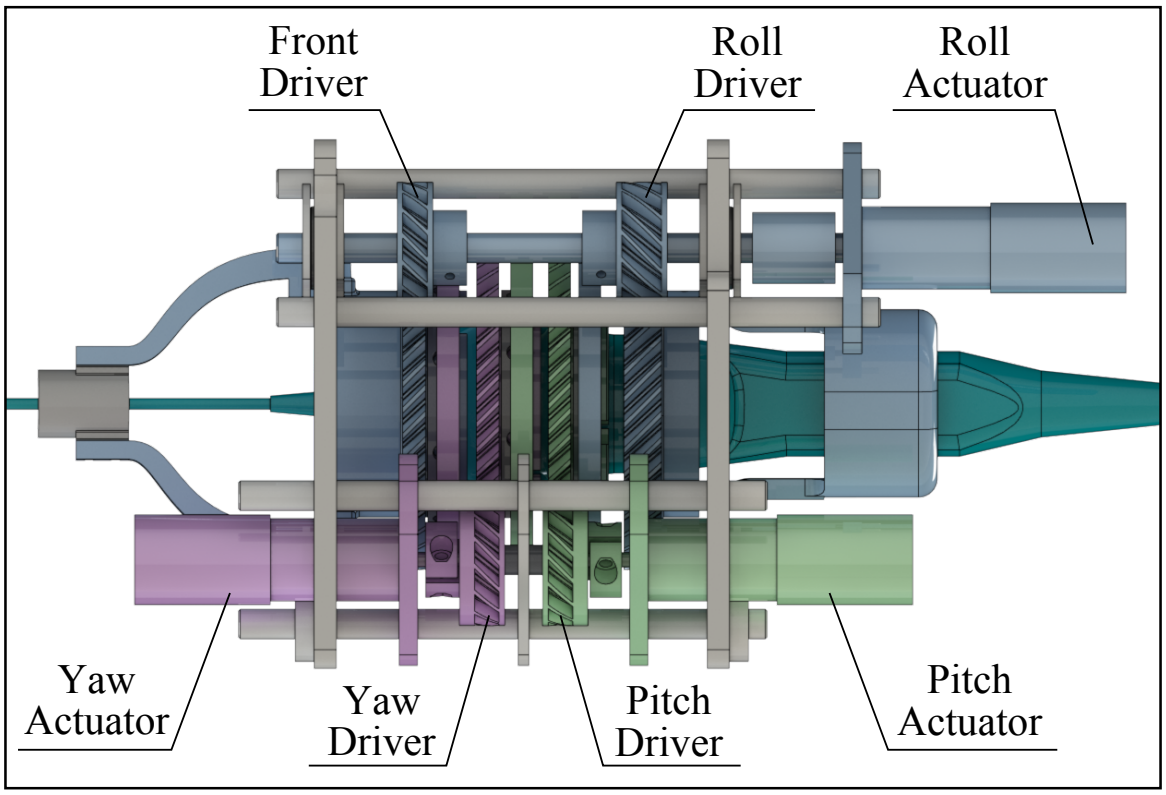

Figure 3.5: *CAD model showing a detailed bottom view of the rotational transmission*

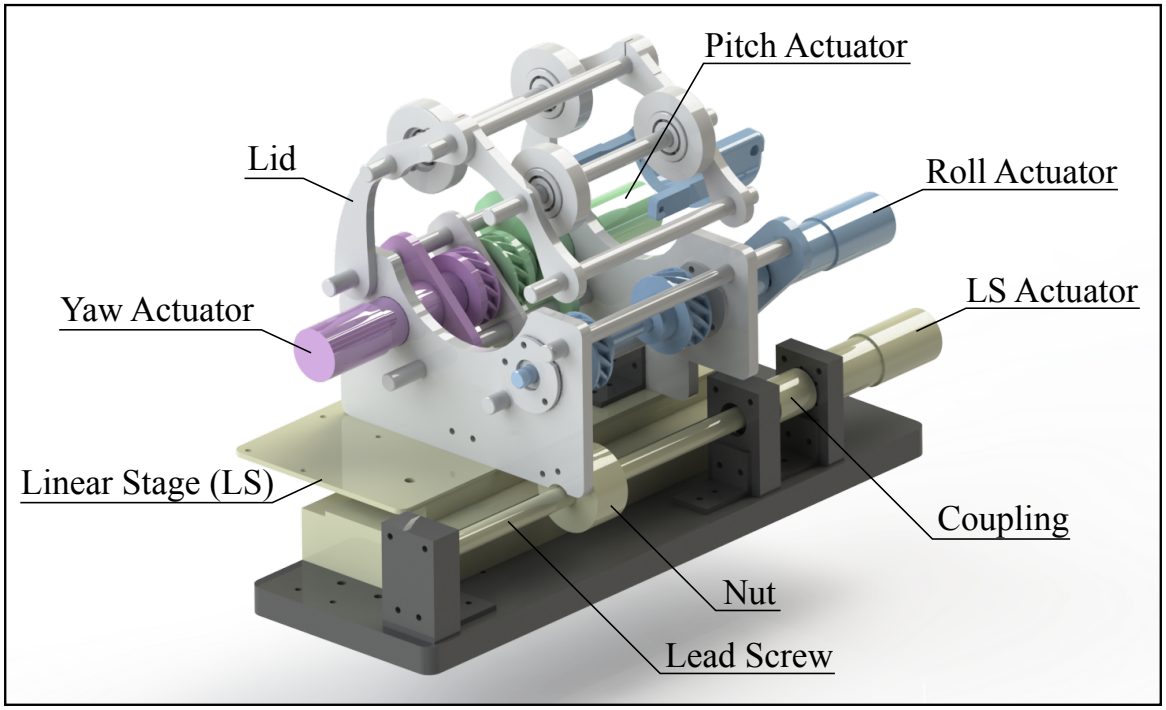

Figure 3.6: *CAD model showing actuator arrangement*

coupled to the roll gear and causes rotation of the front knob and the roll clamp. The top is constrained by a lid containing four rollers on ball bearings. Rollers allow free rotation of the catheter transmission without axial or radial deviation. The force between the rollers and the transmission can be adjusted by tightening or loosening the lid. Tightening the lid can improve performance by reducing gear backlash at the expense of causing increased friction and gear forces in the system.

3.4.4 Linear Stage

The translation stage travels along a linear slide and is actuated by a fast lead screw. This joint motion can be actuated independently of the other joints. Ball bearings are attached at both ends of the lead screw to ensure smoother operation.

3.4.5 Catheter Shaft Manipulation

In order to address two-handed manipulation of the catheter shaft, it was necessary to design a clamping mechanism which would anchor to the proximal end of the catheter. The roll clamp (Fig. 3.7) tightens around the catheter shaft on the proximal end close to the catheter handle. Two connectors join the clamp to the front helical gear (A) in order to provide torsional stiffness to the catheter shaft. The front gear (A) is then coupled to the roll actuator such that all roll motion transmits torque through the front gear to the roll clamp. Transmitting torque directly to the catheter shaft (instead of relying solely on the rotation of the catheter handle) achieves a greater rotational output, thereby increasing the efficiency of roll actuation and decreasing the amount of backlash in the catheter tip due to torsional windup along the shaft.

A set of telescoping plastic tubes encases the catheter shaft between the robot and the introducer in order to prevent buckling outside the patient. The tubes were designed to have an opening along the length, allowing the telescoping assembly to be placed on or removed from the catheter shaft after the catheter has been introduced to the patient. The catheter shaft bends and presses against the inner walls of the tube assembly during

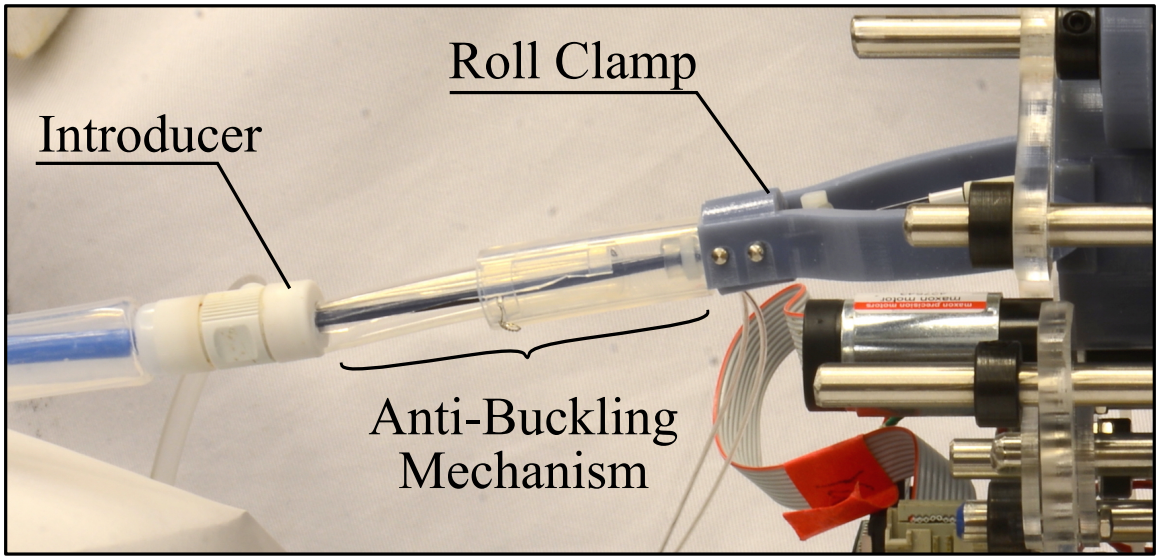

Figure 3.7: *Roll clamp and buckling prevention mechanisms*

insertion. The stiffness of the tubes prevents the catheter from buckling and becoming damaged. Preventing buckling outside the patient also increases the efficiency of insertion actuation. The tubes are functional even if the axes are bent at a slight angle. This gives the system robustness to variations in the alignment between the introducer and the axis of the robot during the procedure.

3.4.6 Robot Construction

The transmission knobs, including the internal features that mate with the catheter handle and the external helical gears that connect the motors to the knobs, were 3D printed (Objet Connex 500 printer, VeroBlue material, Stratasys, USA). The catheter cage, which grounds the catheter and the knobs to the translation stage, was constructed from 6.5 *mm* thick acrylic. The fully constructed robot is pictured in Fig. 3.8. The translation stage travels along a linear slide and is actuated by a fast-motion lead screw with pitch 1.27 *cm*. This joint motion can be actuated independently of the other joints. Ball bearings are attached at both ends of the lead screw to ensure smooth operation.

Each DOF is actuated by a servo-controlled brushless DC motor (EC-max, Maxon Motor,

Switzerland). Motor signals (generated by the steering controller) are sent to four motor controllers (EPOS2, Maxon Motor, Switzerland), which perform fast low-level control on the motor positions of each individual actuator. The translation motor has an 84:1 gear reduction and is coupled to the lead screw by a shaft coupling. Each of the three rotational joint motors has a 53:1 gear reduction. Helical gears in rotational joints have gear ratio 2.54. Lubricant was applied to the bearing surfaces in rotational joints to reduce friction. The robot was mounted on two scissor lifts to adjust the robot inclination for better alignment with the introducer, which helps reduce buckling.

3.5 Experimental Validation

The robotic US catheter steering system depends on accurate positioning and orientation steering in order to visualize the desired anatomical features and track the clinician's working instruments. In this section we identify potential error sources resulting from mechanical design and implementation, and then we test the motion of the robot to experimentally determine its accuracy. A high-resolution optical tracking system (Claron Technology Inc., Canada) with root mean square (RMS) accuracy 0.25 mm was used to collect position measurements at roughly 20 Hz.

3.5.1 Translation Stage Accuracy

The linear motion of the translation axis was first examined in order to verify that the axial deviation of the nut traveling on the lead screw is as small as possible. An optical tracking marker was placed on the lead screw nut and its displacement was measured by the tracker while the translation axis was made to traverse its full15 cm range of motion 10 times. The position measurements of the linear stage were compared with the desired straight path. The distance from each measured point to the desired straight line was calculated for each of the 4460 data points (Fig. 3.9). The average deviation from the centerline was calculated to be 0.07 mm, which is less than the specified accuracy of the optical tracking sensor.

Next, the backlash in the translation stage was examined. The rated backlash in the

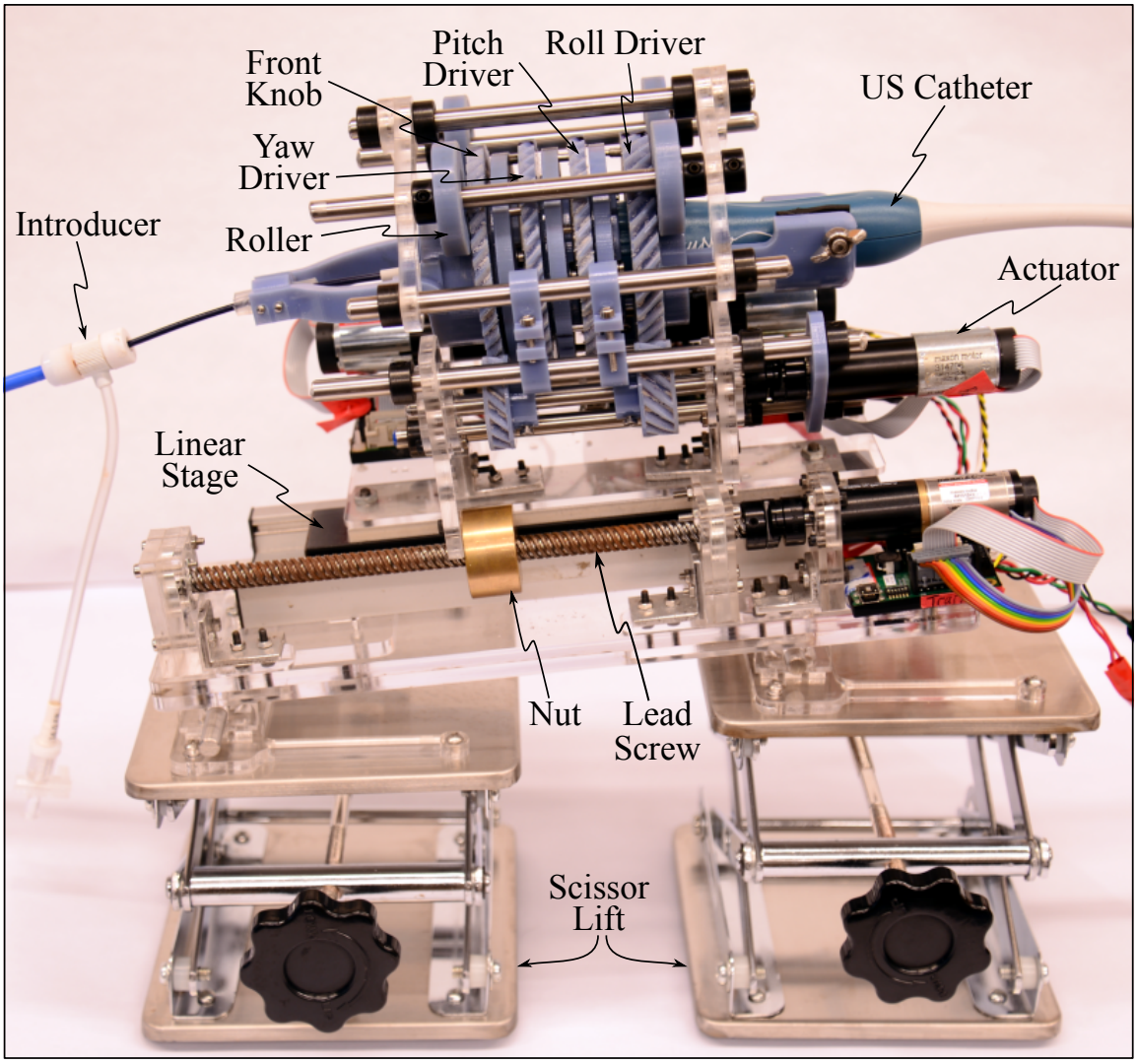

Figure 3.8: *Fully assembled robotic system*

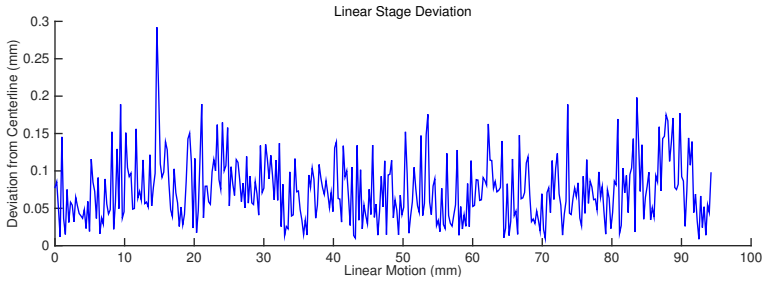

Figure 3.9: *Deviation in translation axis*

actuator gearhead is 1.6°. This amount of gearhead backlash is expected to cause up to 0.23 *mm* backlash (less than the specified sensor accuracy) when switching the direction of linear motion. Additionally, errors and misalignment in the mounting of the lead screw and motor shaft coupling may also contribute to the translation motion error.

The linear stage actuator was actuated to drive forwards and cause the lead screw to engage with the lead screw nut in the positive direction. Then the position of the linear stage was measured while the stage was driven forwards and backwards by a constant distance of 2.4 *mm*. During direction changes, a small amount of distance was lost as the lead screw rotated to engage with the threads in the opposite direction. This test was conducted 10 times with different constant distances (2.4 *mm*, 5.9 *mm*, and 11.8 *mm*). The average positioning error due to backlash was 0.06 *mm* ($\sigma = 0.03$ *mm*), which is less than the specified accuracy of the optical tracking sensor, and is assumed to be negligible in positioning the catheter.

3.5.2 Rotational Transmission Accuracy

The rotational transmission consists of three separate actuators to rotate pitch, yaw, and roll. Friction causes each joint to exert a small torque on neighboring joints when actuated. The resulting small joint motions are allowed by the backlash between helical gears. This effect was studied by attaching optical tracking markers to each of the four knobs and measuring their rotations during actuation of each of the three rotational DOFs.

The results of these experiments are summarized in Table 3.1. First, the pitch joint was repeatedly actuated from 0° to 12.51° in increments of 1.56°. Fig. 3.10 (*left*) shows pitch knob motion and the resulting effect on the yaw, roll, and front joints. The desired pitch adjustments were achieved with mean error 0.06° ($\sigma = 0.08°$). The yaw, roll, and front knobs experienced average unwanted rotation in each increment as noted in the first column of Table 3.1. The overall total unwanted deviation of each knob is listed as well. Second, the yaw joint was repeatedly actuated from 0° to 12.51° in increments of 1.5°. Fig. 3.10 (*middle*) shows yaw knob motion and the resulting effect on the pitch, roll, and front knobs. The

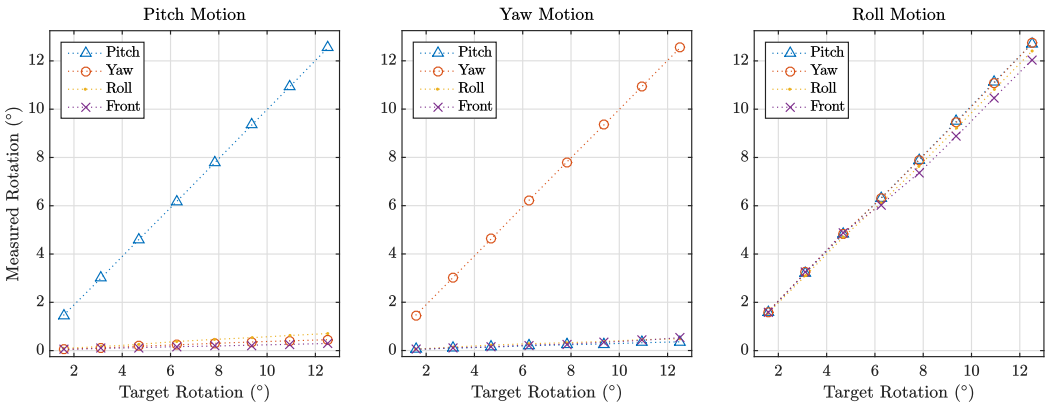

Figure 3.10: *Joint motion during (left) pitch, (middle) yaw, and (right) roll*

Table 3.1: *Joint motion study results*

		Actuated Gear		
		Pitch	**Yaw**	**Roll**
Error	**Pitch**	$0.06° \pm 0.08°$	$0.05° \pm 0.03°$ *total: 0.36°*	$0.11° \pm 0.06°$
	Yaw	$0.06° \pm 0.03°$ *total: 0.45°*	$0.04° \pm 0.05°$	$0.11° \pm 0.06°$
	Roll	$0.09° \pm 0.04°$ *total: 0.71°*	$0.06° \pm 0.03°$ *total: 0.49°*	$0.09° \pm 0.07°$
	Front	$0.04° \pm 0.02°$ *total: 0.30°*	$0.07° \pm 0.04°$ *total: 0.53°*	$0.22° \pm 0.30°$

Table 3.2: *Measured backlash in each helical gear. The numbers reported below are the amount of error in joint rotations due to directional changes.*

	Pitch	Yaw	Roll	Front
Mean	0.63°	0.45°	0.86°	0.18°
St. Dev.	0.01°	0.02°	0.01°	0.02°

desired yaw adjustments were achieved with mean error 0.04° ($\sigma = 0.05°$). The resulting errors in the pitch, roll, and front knobs are in the second column of Table 3.1. Third, the roll joint was repeatedly actuated from 0° to 12.51° in increments of 1.56°. The pitch and yaw joints were given equal motion commands to ensure that the relative rotations of the knobs with respect to the catheter handle remained constant during roll actuation. The front knob is mechanically coupled to the roll knob through gearing and therefore should exhibit the same amount of motion as well. Fig. 3.10 (*right*) shows the resulting rotations of all four joints. The desired adjustments were achieved with mean errors listed in the third column of Table 3.1.

The total backlash in each rotational joint of the robot is defined as the amount of rotation lost in directional changes. This is due to a combination of the backlash in the gearhead (rated at 1.6°) and the helical gears, with fasteners and material strain contributing a negligible amount of backlash. The total backlash was measured by rotating each joint by 14.08° in different directions 10 times. Backlash results are shown in Table 3.2. The yaw, pitch, roll, and front knobs experienced low mean backlash.

3.5.3 Catheter Shaft Motion

The effectiveness of the roll clamp and buckling prevention mechanisms were evaluated by repeatedly rotating and inserting the catheter in two experimental settings. The first setting (labeled “Introducer") was on the bench top with the catheter inserted through a 14 *F* introducer with a silicone rubber seal. The introducer was inside a smooth-walled tube (Teflon FEP, 1.3 *cm* inner diameter, 62 *cm* length). The second setting was in an *in vivo* porcine animal model during an interventional procedure with the robot. The catheter was

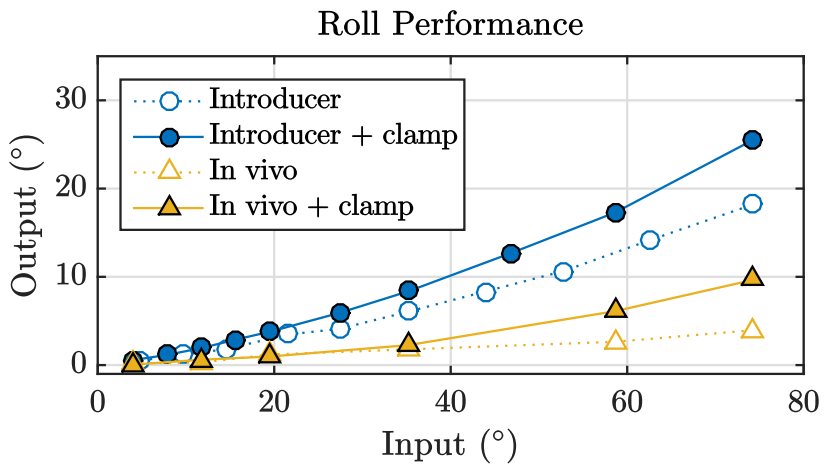

Figure 3.11: *Relationship between handle roll input and catheter tip roll output*

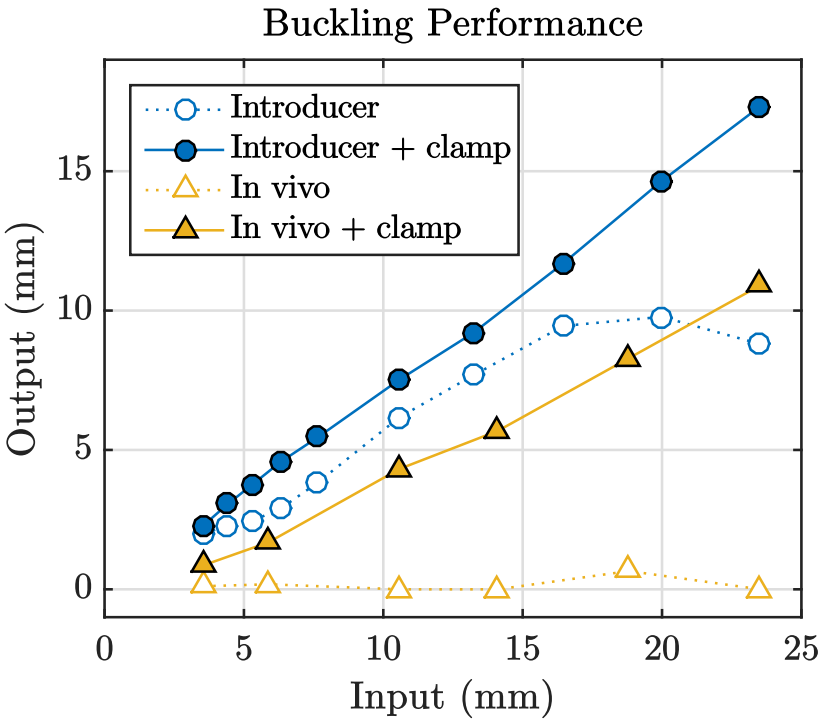

Figure 3.12: *Relationship between handle insertion input and catheter tip translation output*

introduced to the vasculature through a 14 *F* introducer and the distal tip was manually guided to the junction of the inferior vena cava and the right atrium under fluoroscopic-imaging guidance. Then the catheter handle was clamped into the robot. The *in vivo* protocol was approved by the Institutional Animal Care and Use Committee (IACUC). The animal received humane care in accordance with the *1996 Guide for the Care and Use of Laboratory Animals*, recommended by the US National Institutes of Health.

For each of these two settings, tests were conducted with and without the roll clamp and the buckling mechanism. Within each setting a repeated input was given to the robot and the resulting motion of the catheter tip was measured as output. The ratio of catheter tip output motion to catheter handle input motion is less than one in all cases, even with mechanical assistance from the roll clamp and the buckling prevention tubes. During roll tests this is due to friction on the catheter shaft causing torsional windup along the length of the shaft. During insertion tests this is due to two factors: (A) friction on the catheter shaft from the rubber seal of the introducer, which increases the amount of shaft buckling before the shaft stiffness overcomes the friction in the rubber seal, and (B) deformation of the catheter shaft as it conforms to the contour of the tubing before it begins to slide in through the rubber seal. Fig. 3.11 shows the performance of the roll clamp, and Fig. 3.12 shows the performance of the buckling mechanism in each setting.

3.6 Discussion

The error in the rotational transmission due to backlash was 43-89% less than the allowable joint position error, 1.5°. The linear tranmission backlash contributed negligible positioning error. Such small errors in the robot motion cause negligible errors in the catheter positioning and orientation control. The current construction is sufficient because the accuracy requirements of the system are determined by the accuracy of the EM sensor used for closed-loop tip control. If the EM sensor was replaced with a higher-accuracy sensor then some minor improvements to the system would need to be made in order to remain within the specifications. Existing errors are the results of friction in custom designed ball bearing

joints, small inaccuracies in the fabrication and assembly stages of the robot, limited sensor accuracy, and noise in the experimental setting. Mechanical errors could be mitigated with better manufacturing and assembly techniques.

The results of the handle insertion and rotation tests demonstrated that the roll clamp and buckling prevention tubes improved the effectiveness of the robot motion. During *in vivo* trials robot alignment with the introducer was subject to small shifts over time. Without the buckling prevention tubes, this misalignment combined with introducer friction caused the catheter shaft to buckle, thereby transmitting near zero translation to the distal tip of the catheter. The use of buckling prevention tubes was necessary in order to steer the catheter *in vivo*.

In addition to meeting the technical specifications, this design also served as an interesting exploration to the possibilities of 3D printing. By taking advantage of additive manufacturing we were able to design and fabricate ball bearing races which would be difficult to manufacture with conventional machining. The accurate dimensions of the bearing races enabled smooth ball bearing rotation for hundreds of hours of use. Additionally, the softness of the printed material enabled an important design parameter in robot construction and operation. By tightening the lid and squeezing the knob gears against the driver gears we can decrease backlash in the system (at the cost of increasing friction).

3.7 Conclusion

An accurate and user friendly actuation module is necessary for providing a clinically relevant robotic system for steering US catheters. In our study, we have demonstrated that our new robotic system satisfies the desired specifications. The design of the robotic system presented here offers a smaller footprint than our previous system, which is crucial for a clinical robot. The attachment and detachment procedure for the US catheter handle enables quick connect and disconnect from the robotic system. Measurements of the robot motion with the high-resolution optical tracker demonstrated that the robot is capable of positioning its joints and the catheter tip pose with sub-millimeter and sub-degree level

accuracy. The roll clamp and buckling prevention mechanisms improve the efficiency of catheter tip motions to handle inputs. Experimental validation of the actuation module has demonstrated that the US catheter can be manipulated with sufficient accuracy to achieve enhanced visualizations during catheter-based procedures.

Chapter 4

Disturbance Rejection and Navigation through Unconstrained Vasculature In Vivo

4.1 Background

This chapter develops and validates a model for steering the US catheter in unconstrained environments. Previously in Chapter 2 we developed a system for automatically pointing cardiac imaging catheters in a constrained bench top environment (Loschak et al. (2013a)). While this system has proven to be effective for bench-level steering, it was necessary to implement a more robust controller that can cope with the friction, backlash, and unconstrained catheter shaft motion that occurs during *in vivo* procedures. The following sections describe the motivation for redesigning the controller for improved robustness, the updated control strategy, the system characterization experiments, and the results from *in vivo* animal studies.

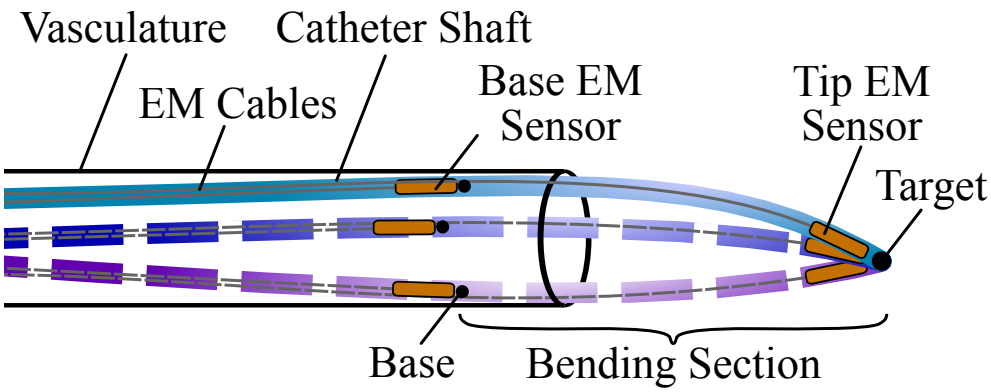

Figure 4.1: *Uncontrollable catheter shaft motion. Dashed lines show alternative locations of the catheter shaft due to uncontrolled motion within the vasculature. EM trackers measure the position and orientation of the catheter at two locations: at the base of the bending section, and at the tip.*

4.1.1 Constrained Catheter Motion

In the constrained motion studies of Chapter 2, the robotic system for steering cardiac imaging catheters relied on a set of physical constraints that isolated the bending to only the distal 5 *cm* bending section of the tip. The base of the bending section was constrained with respect to the catheter handle and robot. This catheter tip fixation succeeded in isolating the bending section of the catheter and simplified the control required for steering, which was necessary as the beginning stage in an investigation of catheter position and orientation steering.

4.1.2 Unconstrained Catheter Motion

Accurately maneuvering the 4-DOF catheter *in vivo* requires a controller that is robust to a number of inaccuracies and disturbances, which have been minimally addressed in the robotic flexible manipulator literature. Inside the plastic off-the-shelf catheter handle, slack pull wires connected to each bending knob exhibit large backlash regions that are non-linearly coupled to the rotations of both bending knobs (this relationship was examined in Loschak et al. (2013a)). Additionally, the long catheter shaft experiences compression, bending, and torsion in the vasculature. This reduces the effectiveness of the bending knobs, increases friction between the catheter and the vascular walls, and causes the location

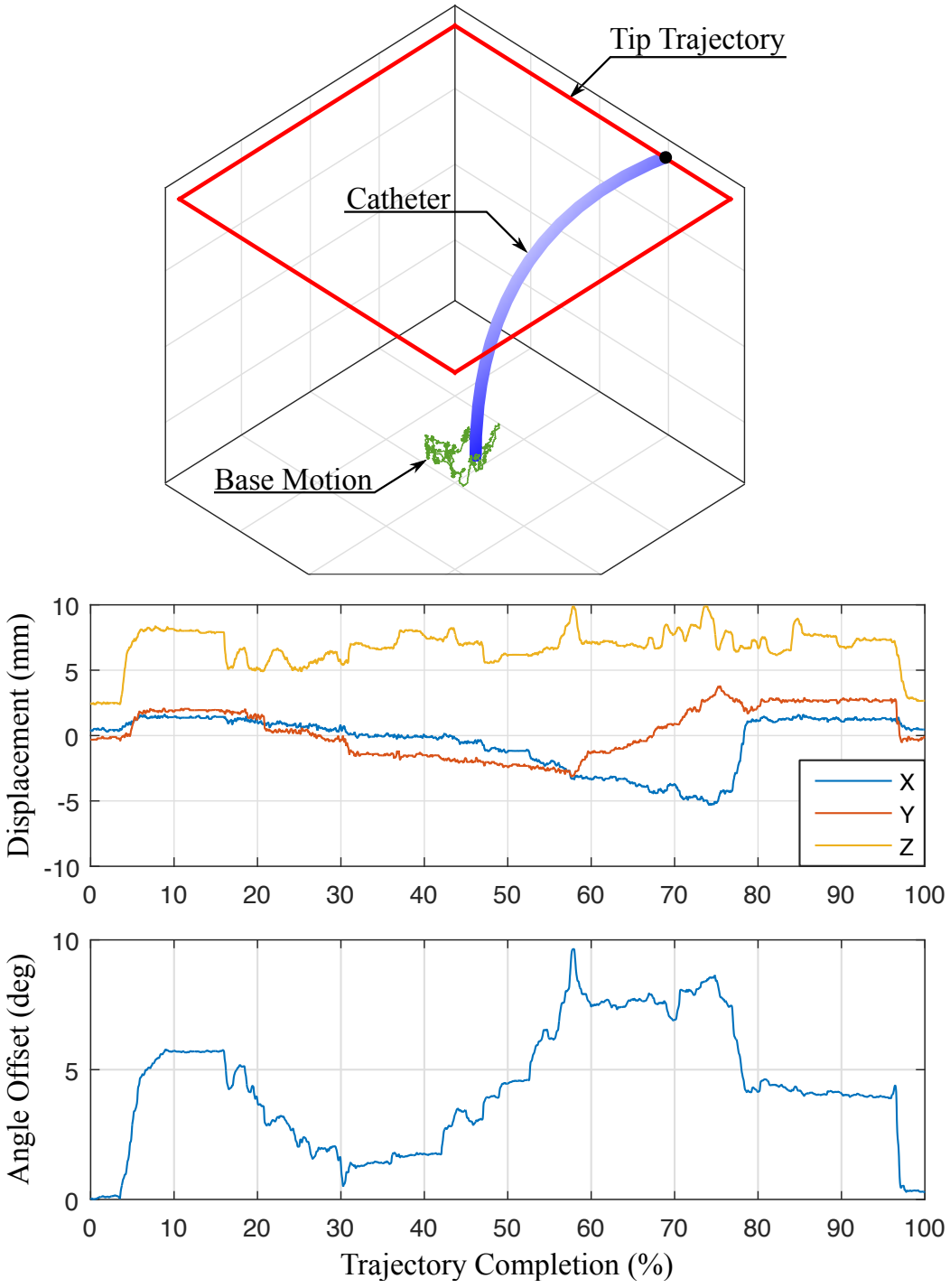

Figure 4.2: *Catheter navigation causes uncontrollable motion of the bending section base. (top) The base motion is measured (green) while the catheter tip is navigated along a square trajectory (red). (middle) The displacement of the base point in xyz coordinates and (bottom) the change in base point rotation about the catheter axis are measured.*

of the base of the bending section to vary, as portrayed in Fig. 4.1. Here the catheter is shown in three potential configurations. The proposed controller keeps the tip at the target location regardless of where the base is located. The uncontrollable motion of the base point during unconstrained bending significantly affects the ability of the catheter to converge to the desired pose. To illustrate typical base motion, Fig. 4.2 shows the uncontrollable motion of the bending base during catheter tip navigation of a square trajectory with the shaft unconstrained. The range of displacements of the bending base in the xyz-axes was measured as $[8.4\ mm, 6.4\ mm, 5.9\ mm]$ and the maximum angular deviation from the centerline was 9.65°.

The catheter passes into the patient vasculature through an introducer, which is a plastic tube containing a rubber seal to prevent blood outflow (Fig. 3.7). Friction in the introducer seal increases backlash in catheter rotation and increases the amount of catheter buckling during insertion. Respiratory and cardiac motions of the patient also contribute disturbance to the system, resulting in further inaccuracies. Patient vasculature is highly variable in diameter, stiffness, curvature, and length. Catheter translation is subject to backlash as the catheter body conforms to the near wall or the far wall of the vasculature (examined in Kesner and Howe (2010)).

While some of these effects may be avoided or reduced by altering the mechanical design of a catheter, it is less expensive and more readily clinically feasible for a robust controller to manipulate an existing off-the-shelf catheter. The following section describes a control strategy that will robustly converge the catheter tip to the desired position and point the US imager in the desired direction despite these effects and disturbances.

4.2 Kinematics

Previous research has mainly focused on 3-DOF continuum robot kinematics and did not consider the extra DOF required to control the heading of the US imaging plane (Penning et al. (2011); Webster and Jones (2010); Khoshnam et al. (2012); Ganji et al. (2009); Camarillo et al. (2009b); Seung et al. (2015)). Our kinematics derivation follows the methodology in

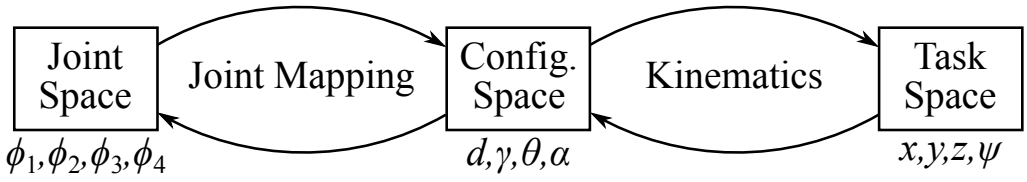

Figure 4.3: *Diagram showing the three spaces involved in describing the motion of the catheter, and the mappings between them.*

Table 4.1: *D-H parameters for the US catheter.*

Link	$\mathbf{a_i}$	$\mathbf{ff_i}$	$\mathbf{d_i}$	$\mathbf{`_i}$
$0 \rightarrow 1$	0	0	d	0
$1 \rightarrow 2$	0	0	0	γ
$2 \rightarrow 3$	0	0	0	θ
$3 \rightarrow 3'$	0	$-\pi/2$	0	0
$3' \rightarrow 4$	0	$\pi/2$	0	$\alpha/2$
$4 \rightarrow 5$	0	$-\pi/2$	$2\frac{L}{\alpha}\sin\frac{\alpha}{2}$	0
$5 \rightarrow 6$	0	$\pi/2$	0	$\alpha/2$
$6 \rightarrow 7$	0	0	0	$-\theta$

Webster and Jones (2010). With the use of two sensors (one at the tip and one at the base of the bending section (Fig. 4.1)) we extend this to enable 4-DOF control of US imaging catheters.

Three different parameter spaces are used to control the flexible manipulator: joint, configuration, and task space (Fig. 4.3). The joint space is the four actuator variables, pitch (ϕ_1), yaw (ϕ_2), roll (ϕ_3), and translation (ϕ_4) shown in Fig. 2.2 and 2.3. The configuration space variables ($d, \gamma, \theta, \alpha$) describe the shape of the catheter as shown in Fig. 4.4. Lastly, the task space describes the position of the catheter tip (x, y, z) and orientation of the imaging plane (ψ). The mapping from joint space to configuration space is based on the mechanical design of the robot and the manipulator, and is therefore system-specific; whereas the mapping from configuration space to task space is a kinematic mapping that is broadly applicable to flexible manipulators.

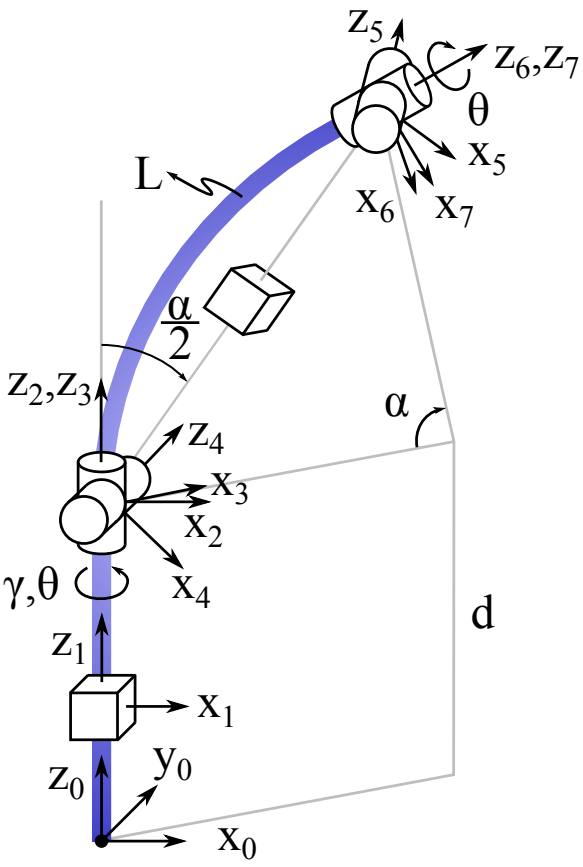

Figure 4.4: *Symbolic representation showing D-H parameters: translation, d, catheter handle roll, γ, bending plane angle, θ, bending angle around the global z-axis, α, length of the bending section, L.*

The accuracy of the mapping between configuration space and task space is based on the following idealized assumptions: the bending section of the catheter has a constant curvature along its length (circular arc); the bending catheter lies on a single plane; and the effects of torsion about the catheter tip are negligible. In reality, these assumptions lead to less accurate results. However, the idealized relationships between task space and configuration space can still provide valuable information regarding how the robot joints should be adjusted for the catheter tip to reach the desired pose.

4.2.1 Forward Kinematics

Forward kinematics map the configuration space to task space. Table 4.1 shows the D-H parameters used in the derivations. Frame 0 is defined as the base frame, and Frame 7 is

the catheter tip. Fig. 4.4 shows the configuration parameters, where d is the translation, γ is the catheter handle roll, θ is the angle between the x-axis of the catheter handle and the bending plane, and α is the bending from the global z-axis (i.e. the catheter body). L is the length of the bending section. The transformation matrix, $T(d, \gamma, \theta, \alpha, L)$, describes the pose of the catheter tip in base coordinates (Eq. 4.1).

$$T(d,\gamma,\theta,\alpha,L) = \begin{bmatrix} s_{\gamma+\theta}s_\theta + c_{\gamma+\theta}c_\theta c_\alpha & -s_{\gamma+\theta}c_\theta + c_{\gamma+\theta}s_\theta c_\alpha & c_{\gamma+\theta}s_\alpha & Lc_{\gamma+\theta}(1-c_\alpha)/\alpha \\ -c_{\gamma+\theta}s_\theta + s_{\gamma+\theta}c_\theta c_\alpha & c_{\gamma+\theta}c_\theta + s_{\gamma+\theta}s_\theta c_\alpha & s_{\gamma+\theta}s_\alpha & Ls_{\gamma+\theta}(1-c_\alpha)/\alpha \\ -c_\theta s_\alpha & -s_\theta s_\alpha & c_\alpha & d + Ls_\alpha/\alpha \\ 0 & 0 & 0 & 1 \end{bmatrix} \tag{4.1}$$

4.2.2 Inverse Kinematics

The idealized mapping from task space to configuration space begins with T and calculates α, d, θ, and γ. From the translational component of T we can calculate the distance from the catheter tip to the global z-axis as

$$\|x_{tip}, y_{tip}\|_2 = \|T_{14}, T_{24}\|_2 = L\frac{(1-c_\alpha)}{\alpha}, \tag{4.2}$$

where $\alpha \in \mathbb{R}^+$, c_α denotes $\cos\alpha$, and $\|\cdot\|_2$ is the l^2-norm. Then α can be calculated by computing the root of the nonlinear equation in Eq. 4.2. The idealized d is then calculated from T_{34}. The idealized angle θ is

$$\theta = \text{atan2}\left(-\frac{T_{32}}{s_\alpha}, -\frac{T_{31}}{s_\alpha}\right). \tag{4.3}$$

Lastly, the angle γ can be calculated from

$$\gamma + \theta = atan2(y_{tip}, x_{tip}) = atan2(T_{24}, T_{14}). \tag{4.4}$$

4.2.3 Joint Mapping

The desired configuration space motion can be mapped to the corresponding joint space inputs as

$$\phi_1 = 2R_c\alpha\cos\theta / D_{knob} \tag{4.5}$$

$$\phi_2 = -2R_c\alpha\sin\theta / D_{knob} \tag{4.6}$$

$$\phi_3 = \gamma \tag{4.7}$$

$$\phi_4 = d \tag{4.8}$$

where R_c is the radius of the catheter body and D_{knob} is the diameter of the pulley inside the catheter handle.

4.3 4-DOF Steering Control

The measured sensor information and idealized kinematic relationships are used together to calculate the joint space adjustments for tip convergence. The robot navigates the tip of the US catheter to reach the desired position while aiming the US imager in the desired direction by the controller in Fig. 4.8. It is not possible to control the full 6-DOF pose of the US imager, therefore the controller aims to adjust the 3-DOF position of the tip and the 1-DOF rotation of the US imager about the axis of the catheter tip.

4.3.1 Pre-Kinematics Calculations

Pre-kinematics calculations are used to prepare inputs for the kinematics calculations. Two EM sensors are used to resolve the configuration of the catheter tip (Fig. 4.5). One sensor is placed at the tip of the bending section, proximal to the US transducer such that the US beam is not distorted. The second sensor is placed at the base of the bending section to resolve physiological disturbances from the environment and the unmodeled behavior of the catheter body. Sensor readings are used in pre-kinematics calculations in order to

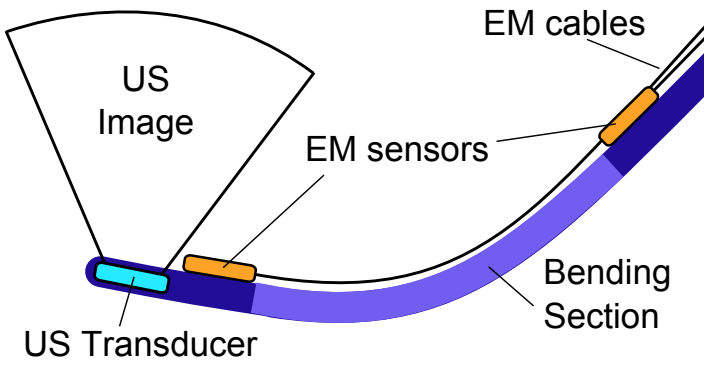

Figure 4.5: *EM sensors on US catheter.*

provide more information to the kinematics.

Fig. 4.6 shows each key location on the catheter. Sensor readings are related to the EM tracker emitter, which is referred to as "Box." The base of the bending section is referred to as "BB," the distal end of the bending section is referred to as "BT," and the catheter tip is referred to as "CT." The BB, BT, and CT positions are aligned when the catheter is in its straightened configuration. Due to catheter fabrication, the US imager is permanently rotated at an angle about the z-axis. The CT frame is defined to have its x-axis is aligned with the US imager, and as a result the CT frame is misaligned with BB and BT (represented by the dotted lines in Fig. 4.6) in the resting configuration. This angle must be calibrated for each US catheter before use. The target working instrument (i.e. ablation catheter), if applicable, is referred to as "$Instr$." Orientation information for "$Instr$" is not used in this work.

The coordinate transform convention used throughout this thesis is given by the example transform T_{Box-BB}, in which the BB pose is given with respect to Box. Four coordinate transforms are needed before beginning the kinematics calculations:

(1) The original catheter tip pose measured in the beginning of this motion, $T_{BB-CT_{orig}}$

(2) The catheter tip pose measured at the present moment in time, T_{BB-CT}

(3) The original base pose measured in the beginning of this motion, $T_{Box-BB_{orig}}$

(4) The base pose measured at the present moment in time, T_{Box-BB}

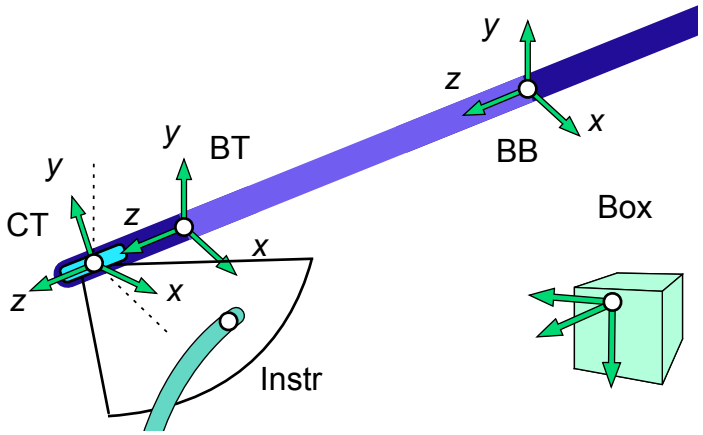

Figure 4.6: *Coordinate frames on US catheter.*

The original poses are measured once at the beginning of a motion in order to record the starting point and measure how much relative motion has occurred since the first command. For example, the user commands 5° of imager rotation relative to the current pose while maintaining the same position. First, the original CT pose is stored. Then, throughout navigation towards the target pose, the new CT pose measurement is used to calculate the total relative amount of imager rotation (rotation about the CT z-axis). Imager rotation continues until the target 5° relative rotation has been reached.

The original BB point is used to calculate the amount of catheter handle roll expressed at the bending section, γ_{curr}. It is not possible to use the current roll joint control knob value for measuring or estimating γ_{curr} because a significant amount of rotation is lost through torsion along the catheter shaft. Therefore, the rotation about the z-axis between the original and current BB poses enables the robot to calculate exactly how much roll rotation has actually occurred at the bending section.

The transform T_{BB-CT} represents the current CT pose with respect to the current BB. This is different from the previous kinematics (Section 2.2.1) which related the current CT measurement to a fixed BB pose because of its constraint to the long axis of the catheter. That strategy fails with the unconstrained catheter body because the BB point moves freely in the vasculature (Figs. 4.1, 4.2), and relating the current CT pose to a fixed BB position will cause the kinematics to assume an innacurate configuration. The transform T_{BB-CT} most

accurately represents the actual curvature at the tip of the bending section and is therefore used in the following configuration space calculations.

4.3.2 Configuration Space Parameters

Let T_{Sensor} be the transformation corresponding to the sensor reading at the current location of the catheter tip, where $T_{Sensor} = T_{BB-CT}$. The US imaging plane is the plane formed by the x- and z-axes of the tip pose. US imager rotation is measured in rotation of the x-axis about the z-axis of the tip pose. T_{Sensor} cannot be directly used in the inverse kinematics calculations since the rotational component of the sensor reading will have rotations that are induced by the unmodeled effects in the system; instead a kinematically feasible configuration $C_{curr} = [d_{curr}, \gamma_{curr}, \theta_{curr}, \alpha_{curr}]$ needs to be calculated based on the position $[x_{sensor}, y_{sensor}, z_{sensor}]$, and handle roll γ_{sensor} reported by the base sensor. Let $C_{curr} = [d_{curr}, \gamma_{curr}, \theta_{curr}, \alpha_{curr}]$ represent this kinematically feasible configuration, with pose T_{curr}.

The user indicates a desired position and change in heading, $X_{des} = [x, y, z, \Delta\psi]$. Calculating the desired catheter configuration, $C_{des} = [d_{des}, \gamma_{des}, \theta_{des}, \alpha_{des}]$, requires additional steps beyond using the inverse kinematics equations. Any change in catheter tip position induces a change in the imager heading that is dependent on the current and target positions. In order to arrive at the desired heading, this induced angular change $\psi_{induced}$ has to be calculated.

(1) Calculate inverse kinematics given $X_{des,xyz}$ and the current handle roll, γ_{curr}. A temporary target pose for representing the curvature of the configuration is calculated from these values. This pose is defined as T_{temp}, and the configuration parameters are labeled as $C_{temp} = [d_{temp}, \gamma_{temp}, \theta_{temp}, \alpha_{temp}]$.

(2) The position and curvature of the catheter at the temporary and desired configurations are equal. Therefore, the configuration parameters $d_{des} = d_{temp}$ and $\alpha_{des} = \alpha_{temp}$. However, the temporary pose only represents the target position and requires additional roll calculations to point the US imager (Fig. 4.7). We begin by calculating the angle between the

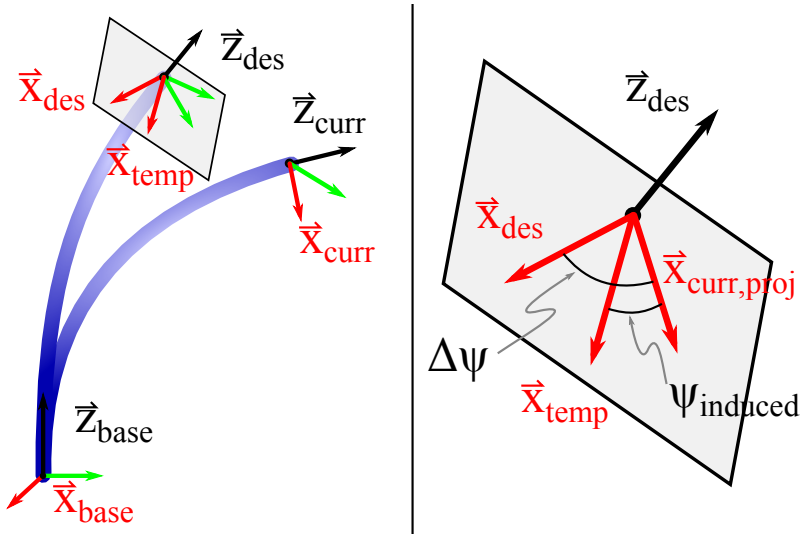

Figure 4.7: *The required configuration space roll adjustments is calculated by projecting the $\vec{x}_{curr}$ axis on to the $x-y$ plane of the desired coordinate frame.*

x-axis at the temporary pose and the x-axis at current pose. This is done by first projecting $\vec{x}_{curr}$ to the plane defined by the vectors $\vec{x}_{temp}$ and $\vec{y}_{temp}$,

$$\vec{x}_{curr_{proj}} = \vec{x}_{curr} - \left(\vec{x}_{curr} \cdot \vec{z}_{temp}\right) \vec{z}_{temp}, \tag{4.9}$$

and calculating the angle difference $\psi_{induced}$ between the x-axes,

$$\psi_{induced} = \cos^{-1}\left(\frac{\vec{x}_{curr_{proj}} \cdot \vec{x}_{temp}}{\|\vec{x}_{curr_{proj}}\|}\right). \tag{4.10}$$

To maintain directionality, we calculate the direction of the normal to the plane defined by $\vec{x}_{curr_{proj}}$ and $\vec{x}_{temp}$,

$$\xi = \vec{z}_{temp} \cdot \left(\vec{x}_{temp} \times \frac{\vec{x}_{curr_{proj}}}{\|\vec{x}_{curr_{proj}}\|}\right). \tag{4.11}$$

If $\xi < 0$ then the angle $\psi_{induced}$ is negated.

(3) At this point, we can point the US imager in the target direction by calculating the desired configuration parameters γ_{des} and θ_{des} as

$$\gamma_{des} = \gamma_{temp} + \psi_{induced} + \Delta\psi \tag{4.12}$$

$$\theta_{des} = \theta_{temp} - \psi_{induced}. \tag{4.13}$$

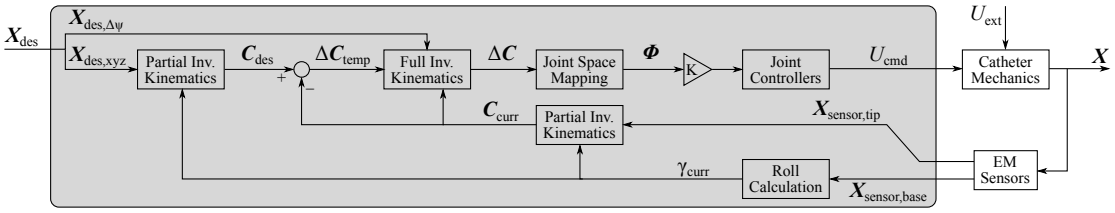

Figure 4.8: *The controller (gray box) receives the desired catheter tip pose and iteratively calculates joint angle adjustments to manipulate the catheter.*

The desired configuration is then related to the control inputs, ϕ_{1-4}. Convergence to the desired pose is an iterative process, in which the tip of the catheter is sensed, and the remaining relative change required to reach the desired pose is recalculated (Fig. 4.8). Image collection is triggered when the user-defined allowable translational and rotational error thresholds of the tip are satisfied.

4.3.3 External Disturbance Rejection

During *in vivo* procedures the catheter also experiences external disturbances due to respiratory motion, adjacent catheter motions in the same vessel, tissue motion due to displacement of adjacent organs, etc. We represent these external disturbances as U_{ext} in Fig. 4.8. U_{ext} can cause the catheter shaft to translate (Fig. 4.9 *left*) and/or rotate (Fig. 4.9 *right*). Our controller must be robust to this external input such that stability is guaranteed and the catheter tip does not diverge from the target location.

The workspace envelope of the catheter is a cylinder (Fig. 4.9). An external disturbance can move the base of the catheter so that the target point is no longer contained in the workspace. The condition for the target to remain within the workspace is to maintain $\|x_{des}, y_{des}\|_2 \leq R_w$, where R_w is the radius of the workspace cylinder. Calculating the workspace boundary from the base tracker pose enables real-time detection of out-of-workspace errors. In the clinical setting, such errors would stop catheter servoing and be reported to the clinician for repositioning the catheter. The following sections examine the response of the robotic system in the presence of external disturbances.

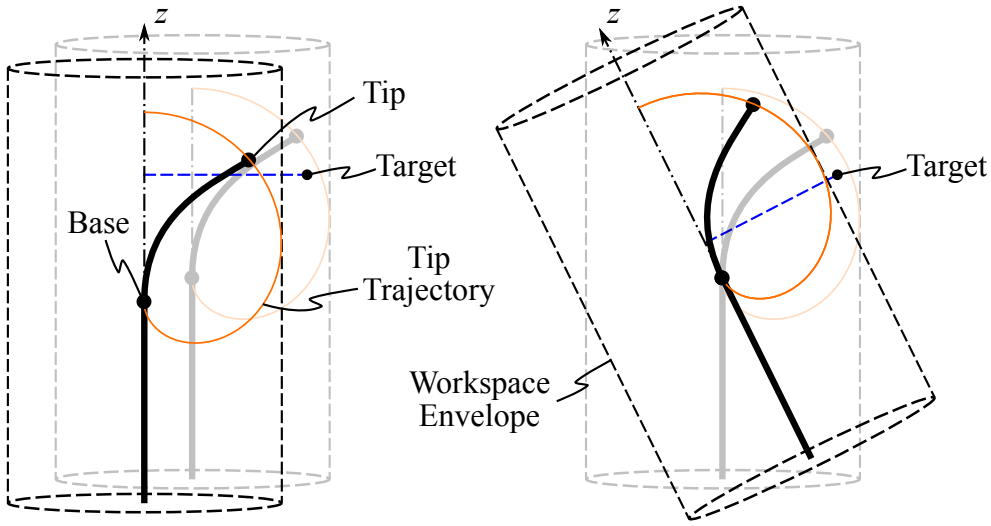

Figure 4.9: *Disturbance analysis. Disturbances in the base location of the bending section can cause (left) translations and/or (right) rotations, which can lead to the target exiting the workspace. The workspace of the US catheter is a cylinder, shown with dotted lines. The gray and black workspace cylinders correspond to the workspace before and after uncontrolled base motion. The tip of the catheter bends along the trajectory shown in orange. The blue dotted line represents the shortest distance between the target and the z-axis of the catheter base.*

4.4 Experiments and Results

The kinematic algorithms were implemented and tested on a robotic prototype for manipulating an US catheter. The robot (Fig. 3.8) was designed and tested in Chapter 3 (Loschak et al. (2015, 2016)).

The tip of the catheter is sensed by two 6-DOF electromagnetic (EM) trackers (trakSTAR, Ascension Technology/NDI, Canada). The tip tracker is mounted to the distal end of the bending section, just proximal to the US transducer. The base tracker is mounted to the proximal end of the bending section. The US imager plane is registered to the coordinate frame of the catheter bending section. The base of the bending section is 85 *cm* distal to the base of the catheter at the handle. The EM trackers have resolution of0.5 *mm* and 0.1°, and RMS accuracy of 1.4 *mm* and 0.5°.

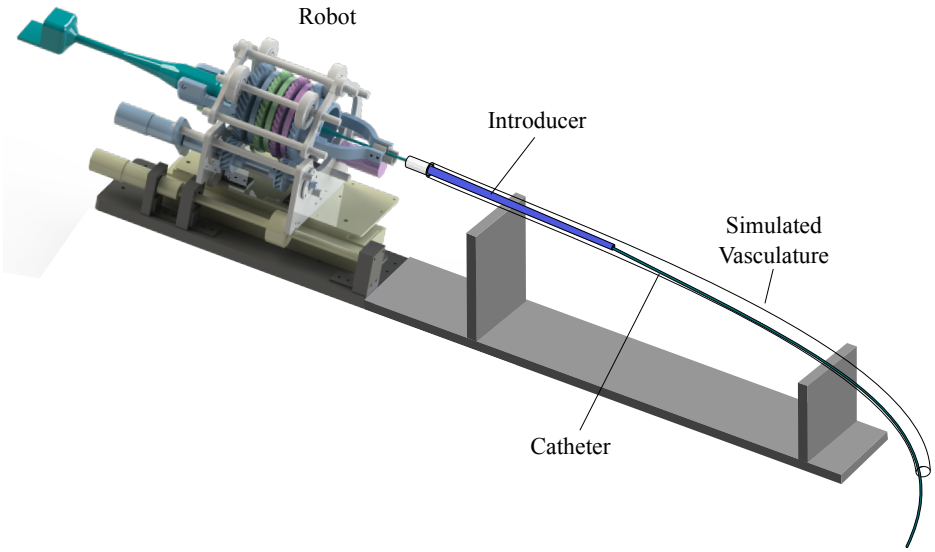

Figure 4.10: *Simulated vasculature for unconstrained bench top testing.*

4.4.1 Bench Top Motion

In preparation for *in vivo* studies, the performance of the controller was tested in a simulated vasculature environment on the bench top (Fig. 4.10). The catheter was introduced through a 14 *Fr* introducer into to a smooth-walled plastic tube (Teflon FEP, 1.3 *cm* inner diameter, 62 *cm* length). The distal bending section of the catheter was able to bend freely outside the distal end of the tube.

The first bench top motion study measured the ability of the robotic system to navigate the catheter tip through space along a 4 *cm* square trajectory of 80 setpoints. The catheter was navigated through multiple trajectory orientations and sizes. The US imager was adjusted to point in the same heading for all trials. An example trajectory is shown in Fig. 4.11, where the blue line is the target trajectory and the red line is the measured trajectory of the catheter tip. The catheter tip reached the desired set points with mean errors 0.92 *mm* ($\sigma = 0.12$ *mm*) and 1.01° ($\sigma = 1.05°$). The base tracker moved up to 8.4 *mm* away from the initial point. The average time to navigate to each set point (dependent on the allowable error threshold and the proportional controller gain) ranged from $1.5 - 3.7$ *sec*, which is well within a 5 *sec* specification for breathing motion.

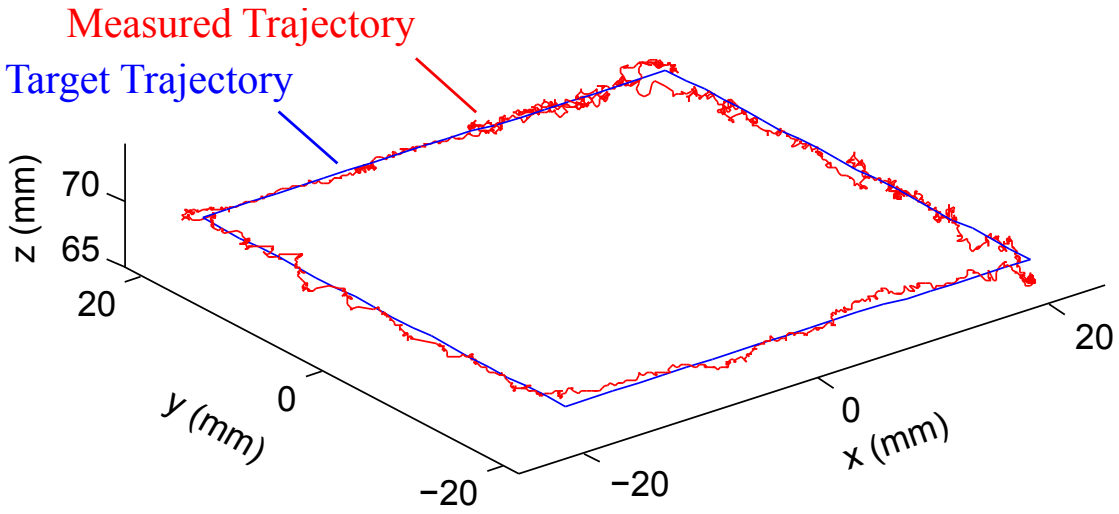

Figure 4.11: *The catheter navigates a* 4 *cm square trajectory of 80 set points while pointing the US imager in the same direction for all points.*

The next motion study isolated US imager rotation while maintaining a fixed position in space. The US imager was commanded to rotate 2° a total of 20 times with a specified allowable angular error threshold, while the position of the catheter tip was maintained within the 1 mm position error threshold (measured error mean 0.83 mm, $\sigma = 0.3$ mm). The average time to converge on the target imager heading ranged from 2.61 sec ($\sigma = 2.67$ sec) with error threshold 0.25° to 1.81 sec ($\sigma = 1.15$ sec) with error threshold 1°.

The last bench top study examined the performance of the system in response to a step disturbance. This is important because interaction with adjacent catheters can displace the shaft, and respiratory motion causes the heart and the supporting vasculature to shift. A step input disturbance was created by moving the vasculature phantom at the base of the catheter bending section, thereby displacing and slightly rotating the base of the catheter. The controller sensed the disturbance and made the necessary adjustments to converge back to the original tip pose. An example disturbance response test is shown in Fig. 4.12. The system was disturbed by moving the plastic tube before data collection. At $t = 0$ sec the controller was activated and the catheter converged to the target pose. Data collection began at $t = 5$ sec when the disturbance was removed (Fig. 4.12 (*top*)), causing a disturbance step input to the base of the bending section. This disturbance moved the catheter tip to the

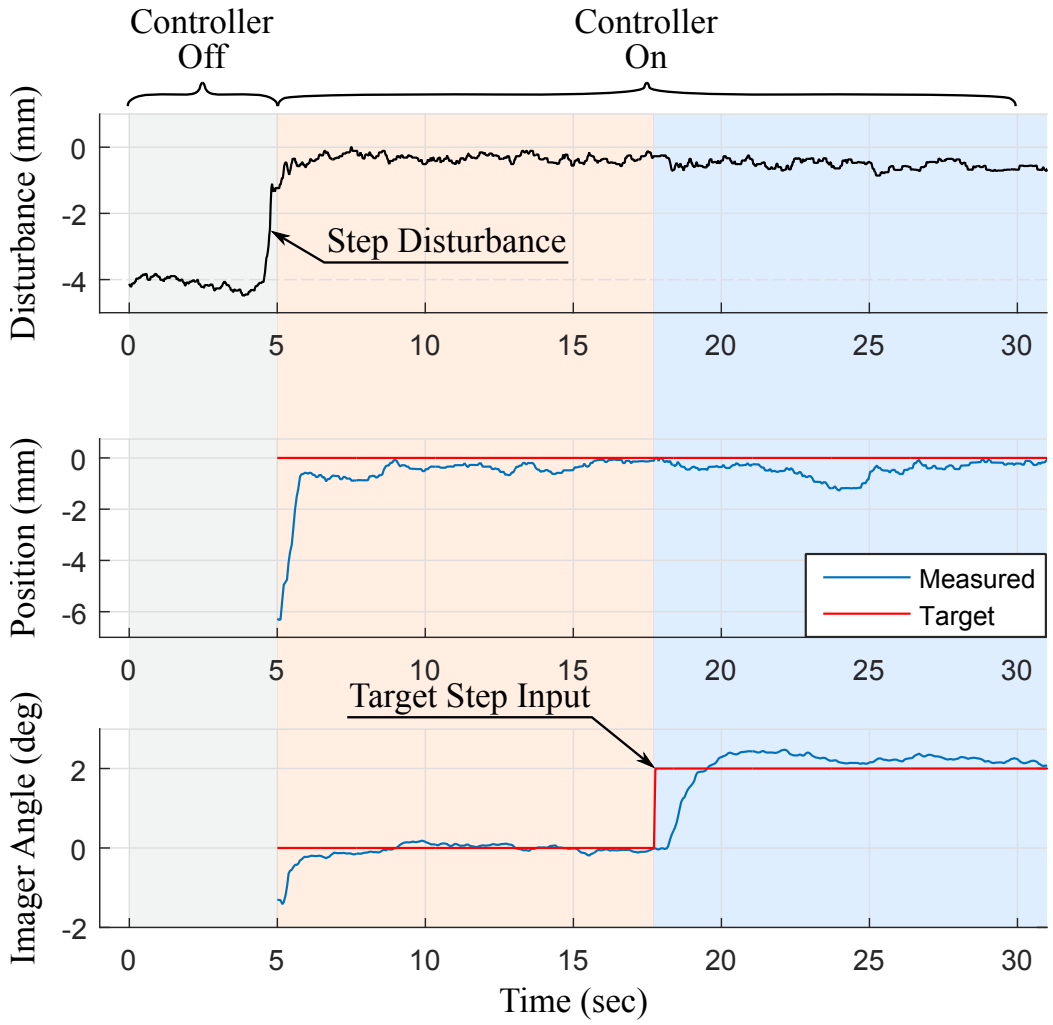

Figure 4.12: *Bench top tests demonstrating the ability of the robotic system to maintain the catheter tip at the target pose despite disturbance step and target step inputs.*

wrong pose (Fig. 4.12 (*middle, bottom*)). The controller then navigated the catheter tip back to the target pose. At $t = 17$ *sec* the user commanded a $\Delta\psi = 2°$ imager rotation (a target step input), changing the desired imager angle from $0°$ to $2°$ and maintaining the position at 0 *mm* from the target. The tip converged to the target pose with mean errors 0.5 *mm* ($\sigma = 0.3$ *mm*) and $0.18°$ ($\sigma = 0.12°$).

4.4.2 In vivo study

In vivo animal testing was performed on a 55 kg porcine model due to anatomical similarities between porcine and human cardiac anatomy. To create a repeatable step disturbance input, respiration was temporarily paused on inhalation. While the respirator is paused, the pressure inside the lungs gradually increases (due to oxygen input, diaphragm relaxation, and other physiological effects), causing the heart to displace slowly with constant velocity as a ramp input.

The disturbance to the base of the catheter bending section is shown in Fig. 4.13 (*top*) where low frequency changes are due to respiratory motion and high frequency changes are due to cardiac motion. Before data collection the controller was de-activated and the subject inhaled a breath, causing the catheter to displace 7 mm from the desired pose. Then the subject's breath was held for 30 seconds, causing the ramp input disturbance (shown in Fig. 4.13 (*top*) as the increasing line of constant slope). At $t = 5$ sec the controller was activated and overcame the step disturbance input from respiration to converge at the target pose. At $t = 20$ s the system was given a 2° step command of US imager adjustment. From $t = 5$ sec to $t = 30$ sec the ramp input continuously caused base displacement with an approximately constant velocity while the controller maintained the target tip pose. During the ramp input, the tip converged to the target pose and remained at the target pose with mean errors 1.1 mm ($\sigma = 0.7$ mm) and 0.44° ($\sigma = 0.31°$). The controller was also able to avoid divergence from the target pose while cardiac motion caused higher frequency (1.67 Hz) disturbance.

The goal of the robotic system *in vivo* was to quickly navigate the catheter tip and US imager to a target pose, collect images of target structures, and then navigate to the next target pose. The controller was designed to actively converge towards the target pose. US image acquisition was triggered once the catheter reached the target tip pose within a specified error threshold. During the *in vivo* study images for 4D reconstruction were collected at increments of 2° steps. US images were collected through multiple heart beats and then the catheter was moved to the next target pose with a step input to the target

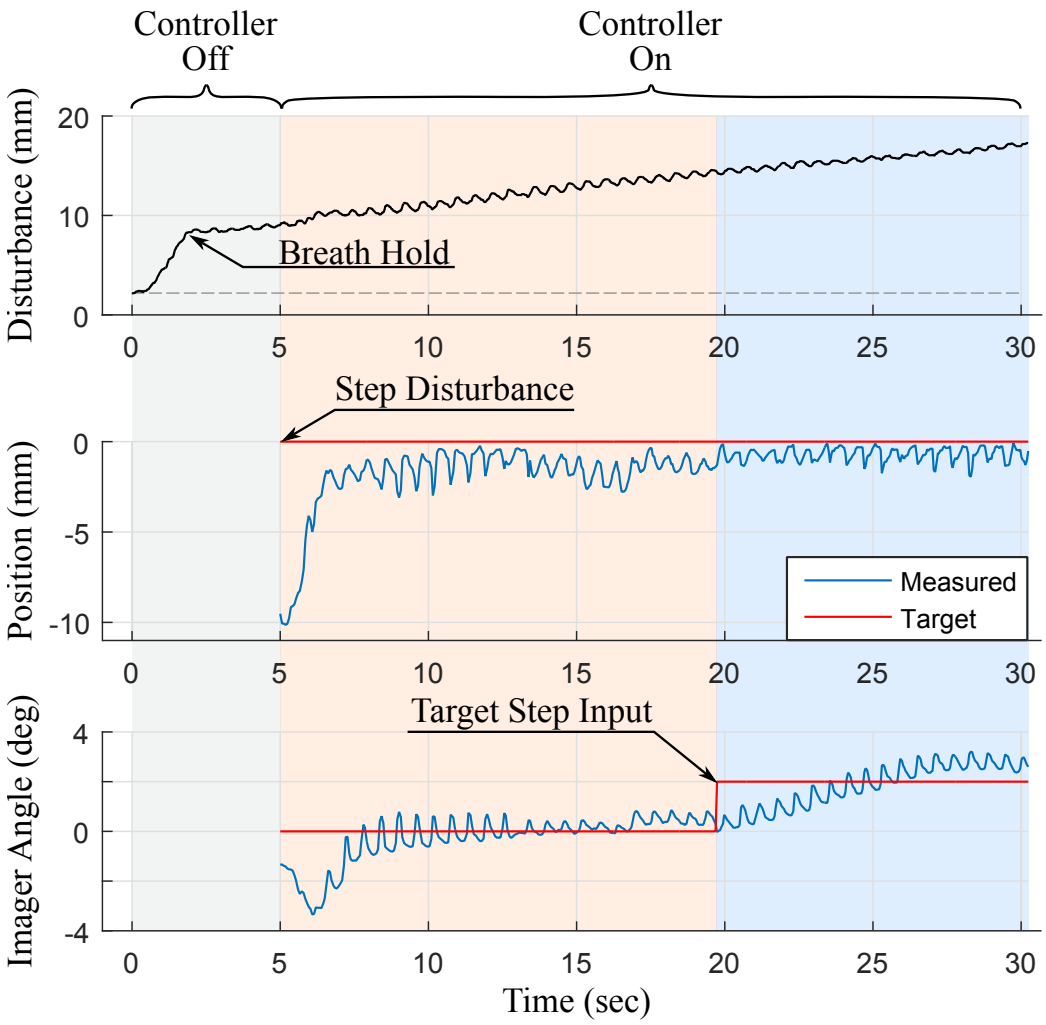

Figure 4.13: *In vivo tests demonstrating the ability of the robotic system to maintain the catheter tip at the target pose despite disturbance step, disturbance ramp, and target step inputs.*

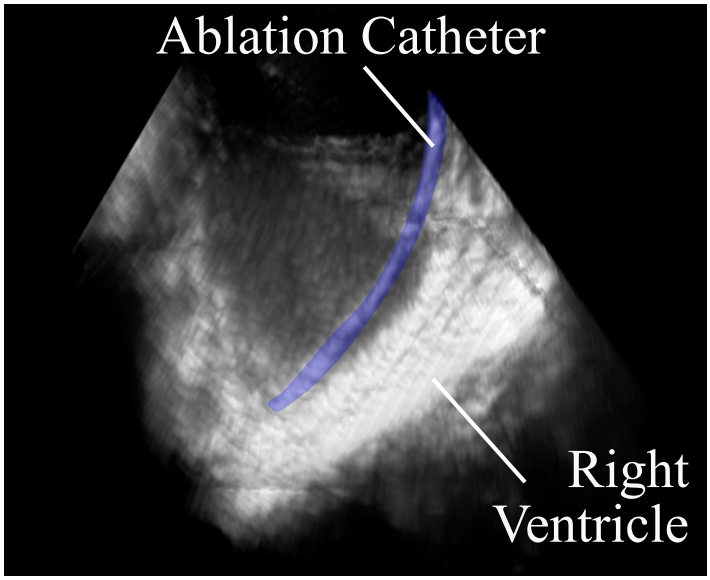

Figure 4.14: *In vivo 3D reconstruction of an ablation catheter inserted into the right ventricle.*

angle. After 80 sweeps the mean position error was 2.0 mm ($\sigma = 1.1$ mm), and the mean angular error was 0.65° ($\sigma = 0.51°$).

The acquired US images are reconstructed into 3D or 4D volumes to enhance visualization of anatomical structures and working instruments (Brattain (2014)). ECG data is used to gate frames and reconstruct a volume with images that were taken in the same phase of the heart cycle. An example of one reconstructed volume of an ablation catheter (highlighted in blue) in the right ventricle is shown in Fig. 4.14.

4.5 Discussion

The experimental results from bench top and *in vivo* studies demonstrated the robustness of the robotic system to converge the catheter tip at desired poses through both desired adjustments (target inputs) and undesired adjustments (disturbance step and ramp inputs due to respiration and other effects). An investigation of timing and accuracy demonstrated that the robot converged to the target pose faster and with more consistent timing when the allowable error threshold was greater. It is possible to navigate the position with sub-millimeter accuracy, but the longer convergence time is not necessarily practical depending

on the experimental setting.

4.6 Conclusion

This work presents a method for robustly and accurately navigating flexible manipulators through unconstrained environments with external disturbances. The control strategy was designed to calculate the configuration space parameters of the catheter based on the current tip pose and base rotation that were measured using two EM sensors. This enabled navigation to be robust to friction and backlash nonlinearities as well as external disturbances to the catheter body. Bench top results demonstrated accurate steering of the catheter tip while pointing the US imager in a specified direction, accurate US imager pointing while maintaining a fixed position in space, and maintaining a target pose despite step input disturbance to the catheter body. Results during an *in vivo* animal trial demonstrated accurate navigation and angular control of the US imager despite unmodeled step and ramp input disturbances due to respiratory motion and cyclical disturbances from cardiac motion. US images collected during the *in vivo* study were reconstructed into 3D and 4D volumes for enhanced visualization of cardiac structures.

Continued progress on the system includes automatically manipulating the US catheter to track cyclical respiratory motion. The speeds and accuracies demonstrated during unconstrained motion of the catheter tip indicate that it is possible for the catheter to track a cyclical 3D trajectory at the pace of respiratory motion. Additionally, a user interface will be designed for clinicians to directly interact with the system. Once complete, the robotic US catheter steering system will be able to provide enhanced visualizations of cardiac anatomy and working instruments during normal respiratory and cardiac motion. This work aims to improve the capabilities of flexible manipulators navigating in unconstrained environments.

Chapter 5

Respiratory Motion Compensation

5.1 Motivation

This chapter develops a method for robotically steering US catheters while compensating for cyclical respiratory motion disturbances to the system. As demonstrated in Chapter 4, the system can navigate the US catheter pose accurately despite disturbance inputs to the system. However, the system was not previously configured to compensate for respiratory motion. As a result, controlling the robot to steer towards the desired pose in the catheter coordinate frame frequently resulted in poor US imager alignment with the imaging target. We next seek to understand how respiratory motion affects the movement of cardiac catheters inside the heart so that we can compensate for it and image more accurately.

5.2 Background

5.2.1 Motion Tracking

Researchers have studied respiratory and cardiac motion with a variety of measurement and computational strategies. Electromagnetic (EM) data, typically referred to as Electro-Anatomical Mapping (EAM) in clinical practice, was collected during left atrial ablation procedures in order to study the effects of respiration on left atrial and pulmonary vein

motion (Noseworthy et al. (2005)). EAM mapping and ECG measurements were used to separate respiratory and cardiac components of cardiac motion with the goal of more accurate image fusion/registrations with pre-operative MRI (Roujol et al. (2013)). A Bayesian framework has been applied towards using intra-procedural 3DUS to adjust respiratory motion models from pre-operative MRI (Peressutti et al. (2013)).

Numerous algorithms for cardiac and/or respiratory motion tracking examine strategies for modeling physiological motions with the goal of applying prediction towards robotic intervention. A study on cardiac motion tracking used video to robustly track naturally occurring landmarks on the external surface of the heart in spite of visual occlusions (Ortmaier et al. (2005)). The researchers measured ECG and respirator pressure to serve as additional landmarks. In a study on respiratory motion compensation for radiation therapy (CyberKnife, Accuray, USA Accuray (2016)), researchers correlated X-ray imaging of internal structures with infrared measurements of external chest wall motion to create a deformation model in a human patient (Schweikard et al. (2000)). This model would then be applied to perform respiratory motion compensation during tumor radiation treatment by sensing external chest wall motion.

Many motion compensation techniques focus on frequency-based models. Richa et al. (2011) used a thin plate spline model and a dual Fourier series model with two sets of components to model respiratory and cardiac motions separately. A study for needle insertion used a Fourier series to model the dominant frequency components of respiratory motion (Riviere et al. (2001)). A Weighted Fourier Linear Combiner (WFLC) adaptively modeled the quasi-periodic signal and continuously updated the fundamental frequency and the Fourier components. A similar approach applied several frequency-based models towards cardiac motion tracking in order to accurately model respiratory motion, cardiac motion, and their coupled effects (Thakral et al. (2001)). Further studies on coupled heart lung effects used a combination of cardiac gating to isolate respiratory motion with a Linear Parameter Variant model (Cuvillon et al. (2005)). These results were then compared with the FLC technique (Cuvillon et al. (2006)) and with an amplitude modulation technique

(Bachta et al. (2009)) to demonstrate sub-millimeter tracking accuracy.

Gating is a different approach to managing physiological motions involving post processing rather than prediction. For example, the CARTO system for cardiac electrophysiology procedures uses gating to accurately gather data during motion (Biosense Webster (2016)). The system monitors cardiac and respiratory cycles in order to match anatomical information (such as electrical signals or chest wall motion) with the correct part of the cycle and the correct location with respect to a fixed coordinate frame. This allows the system to create accurate maps using data that was collected in the same phase of the cycle. The downside is that the gating system must wait a whole breath to collect the next set of data, so procedures take more time as a result.

5.2.2 Motion Compensation

Several robotic systems have employed motion tracking strategies to compensate for simulated or real anatomical motions. Most examples focus on rigid robots. A system for cardiac motion compensation during coronary artery bypass grafting (CABG) surgery used a high speed camera to perform high bandwidth visual feedback (Nakamura et al. (2001)). The slave tool and the image presented to the surgeon were both stabilized in real time. No modeling or prediction were used in this study. In later work towards CABG, ECG measurements and a model of cardiac motion were used in feed-forward control to synchronize a rigid robot with heart motion (Bebek and Çavusoglu (2007)). A third system compensated for cardiac and respiratory motion by using a Generalized Predictive Controller (GCP) modified to have repetitive properties (R-GPC) (Ginhoux et al. (2005)). Respiratory motions were canceled by applying the R-GPC to the respiratory disturbance. Cardiac motions, which are coupled to breathing motion and therefore cannot use the R-GPC technique, were canceled by using an adaptive disturbance predictor in combination with a GPC. In bench top studies, researchers used a GPC (Bowthorpe et al. (2014a)) and a Smith Predictor (Bowthorpe et al. (2014b)) to compensate for measurement delays and inaccuracies in slowly-acquired physiological motion data (such as US frames). A study on force control in laparoscopic-type instruments

used an iterative learning controller with wavelet packet decomposition to compensate for phantom cardiac movements (Cagneau et al. (2007)).

A rigid robot was designed for hand tremor cancellation in microsurgery (Riviere et al. (1998)). The system used a combination WFLC/FLC to adapt to changing frequencies and amplitudes while piezoelectrically actuating a beam to counteract tremor motion. The WFLC provided the time-varying frequency while the FLC provided zero-phase adaptations to amplitude and phase. Another study on a hand-held rigid robot focused on cardiac motion (Yuen et al. (2009)). A straight-rod tool driven by a linear voice coil actuator was used to compensate for rapid changes in mitral valve annulus motion. This system used an Extended Kalman Filter (EKF) (Parker and Anderson (1990)) and real time image processing on 3D US volumes (Novotny (2007)) to control the position of the tool tip in 1-DOF insertion/retraction.

The 1-DOF straight rod system was later adapted to 1-DOF catheter guidewire insertion/retraction with further study on friction, backlash, and force control (Kesner and Howe (2010, 2014)). A multi-DOF robotic system for steering flexible endoscopes was demonstrated to compensate for respiratory motion during *in vivo* porcine general surgery tests (Ott et al. (2011)). The endoscopic camera provided images that were used to visually servo the position of the endoscope to continuously point at liver tissue during breathing. A repetitive controller and feedforward terms were used to compensate for periodic breathing disturbances.

To date, the only prior *in vivo* motion compensation studies for flexible instruments known to the authors are Kesner and Howe (2014) (1-DOF catheter guidewire insertion/retraction for cardiac motion) and Ott et al. (2011) (multi-DOF flexible endoscope steering for respiratory motion). We aim to provide the third system demonstrating motion compensation for flexible instruments and the first system for steerable catheters.

5.3 Methods

Robotic compensation for respiratory motion must be achieved in order to continuously visualize a target. First, we examine potential motion compensation strategies and decide which to pursue. Second, we analyze physiological motion data to gain further insight on how breathing affects US catheter motion. Third, we define models that represent tip and base pose motion throughout the breathing cycle. Fourth, we derive predictive algorithms to eliminate time delays. Finally, we combine motion compensation with predictive filtering and determine how these strategies affect kinematics calculations. The following sections describe our methods for accurately steering US catheters *in vivo* while compensating for respiratory motion.

5.3.1 Motion Strategy

Breathing motion causes cyclical disturbance to the catheter pose. The magnitude of the disturbance depends on the location of the catheter within the heart, and this affects the tip of the bending section differently from the base of the bending section. In our initial *in vivo* studies (Section 4.4.2) the robot was able to reject breathing disturbances and navigate the pose of the US imager accurately with respect to the world coordinate frame. However, as breathing altered the location of the heart tissue with respect to the world coordinate frame, this resulted in poor US imager alignment while the robot was on. Fig. 5.1 shows the heart when the lungs are deflated (*left*) and inflated (*right*). The heart is displaced by breathing, but the robot steered the tip of the US catheter to remain in the same location in world coordinates (cardiac orientation changes and non-rigid deformation due to breathing are not shown). The system bends the catheter in order to maintain the world frame position, and this causes the US imager to point at different anatomy. As a result, the US imager points at the target only during a fraction of the respiratory cycle. The lack of sustained US imager alignment is a problem in two visualization modes.

(Mode 1) *Imaging tissue for volume reconstruction*. The US catheter pose is steered and localized during image acquisition, but it is not possible to localize a specific region of tissue

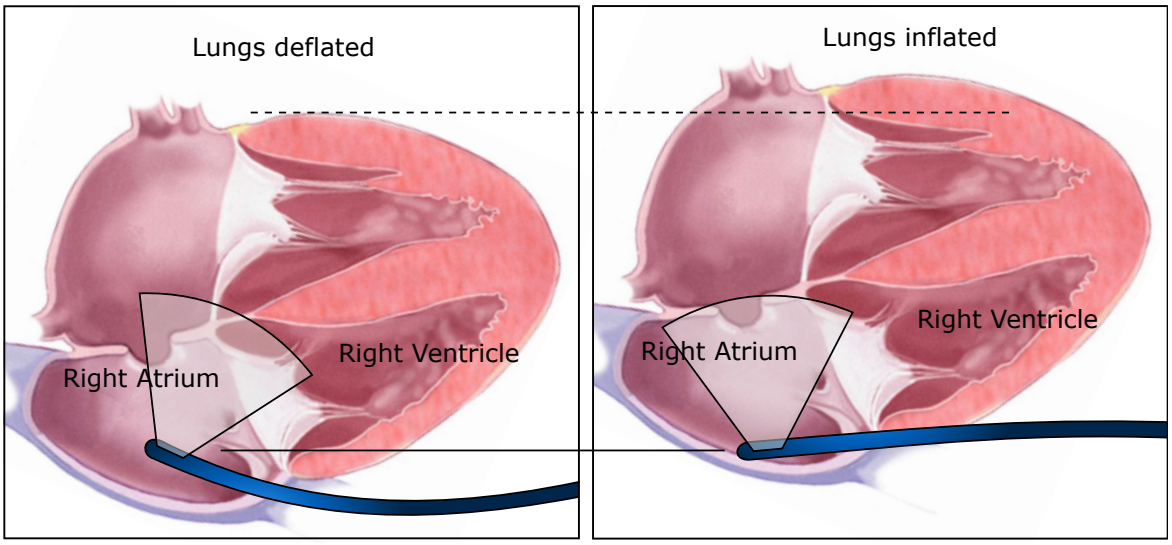

Figure 5.1: *Schematic of US imager misalignment due to breathing.*

given the current sensing strategy. Breathing motion causes coordinate frame drift, which results in the US imager pointing at different tissue. The imager must be made to continue pointing in the same direction relative to the disturbance by respiratory motion.

(Mode 2) *Instrument tracking*. The system is able to sense the location of the target instrument and the US catheter. However, the instrument in another region of the heart is disturbed differently by breathing motion, and the bandwidth limitations of the robot and the catheter cause US alignment delays, leading to discontinuities in visualization.

In both cases, knowledge of respiratory motion and how it compares to robot-actuated motion during catheter navigation is needed. The effect of respiratory motion on the catheter can be measured by the EM sensors on the US catheter, but this only measures respiratory effects while the robot is not actuating the catheter. If the robot is actuating any of the four catheter controls then the CT and BB pose measurements observe a combination of respiratory motion with robot-actuated motion, and it is not possible to observe either of those motions independently. This is because actuating the catheter handle control knobs causes bending along the length of the catheter body as well as in the bending section. This creates controllable motion of CT and uncontrollable motion of BB.

Three strategies to enable motion compensation by observing catheter pose separately

from anatomical motion are envisioned:

(Strategy A) A different catheter sensing strategy, such as grated fiber sensors, would be needed to measure the uncontrollable catheter body bending throughout the vasculature. A fiber sensor could be used to measure or estimate CT and BB motion specifically due to robot actuation. This would then require a redesign of commercially available US catheters.

(Strategy B) Real time image guidance and tissue tracking by MR or CT could provide respiratory motion information to the system. This information would enable the breathing effects on the catheter motion to be isolated from the robot-actuated motion. This would require significant advances in 3D tissue tracking from medical imaging.

(Strategy C) Continue using EM sensors to measure the effects of respiratory motion on the US catheter. Deactivate the motors and measure CT and BB pose motion due to breathing disturbance only. While actively steering, compare the current pose measurements to model-based breathing estimates. The difference reveals the motion due to robot actuation.

We aim to design a system that navigates existing off-the-shelf US imaging catheters. Widely available commercial US imaging catheters, localization software, and operating suites configured for certain types of cardiology are already designed for EM tracker sensing. For ease of clinical adoption, we choose to investigate Strategy C. We accomplish this by measuring the two available US catheter poses, CT and BB, and the working instrument pose, $Instr$, across multiple breathing cycles while the robot is not actuating the control knobs. A breathing model of each pose is calculated initially and then used throughout navigation to estimate the amount of motion from respiratory effects versus robot actuation. During Instrument Tracking it is possible to continuously sense the $Instr$ pose and update the $Instr$ model throughout time. This is because the working instrument is only affected by breathing motion (unless the clinician is manually navigating it). In contrast, once the CT and BB respiratory motion models are calculated it is not possible to update the models from CT and BB measurements as long as the robot is actuating the control knobs. Potential strategies for updating the CT and BB models using indirect measurements during robot motion are not examined here.

A downside to this strategy is the necessary assumption that the effects of respiratory motion are consistent throughout time. This is examined in the next section. If the US catheter moves to a new location in which respiratory motion affects the catheter differently, then the CT and BB models will not be updated to reflect this. Small changes in frequency can also eventually result in the model predicting poses which are out of phase with the breathing cycle. Therefore the system will continuously monitor the frequency with external sensing and update the frequency components of the CT and BB models accordingly. This will also be examined further below. An additional downside is that the system cannot directly measure tissue motion except through US image feedback. This means that the most accurate tissue imaging for volume reconstruction would require image processing on 2D US images in order to localize tissue features for control feedback. US image feedback for robot control is not examined in this work.

The system inherently has some delay for sensor measurements, calculations, and actuator commands to transmit pull wire forces to the catheter tip. This means that a target object may be in a different location by the time the robot is able to converge on the previously-desired pose. Therefore we examine a predictive filtering strategy to obtain the best target tracking results. With these strategies we demonstrate in the following sections that it is possible to maintain continuous US imager alignment with a target during respiratory motion.

5.3.2 Measuring Respiratory Motion

The effect of respiratory motion on cardiac catheters was studied during *in vivo* porcine tests from Chapter 4.4.2. The US catheter was outfitted with one EM tracker at the tip of the distal bending section and one EM tracker at the base of the distal bending section (Fig. 4.5). The US catheter was then introduced through the vasculature into the right heart (Fig. 5.2). The catheter pose was recorded throughout several breathing cycles as the animal's lungs caused the heart to rise and fall. These measurements were repeated in different locations in and around the right heart: right atrium, right ventricle, inferior vena cava, and superior

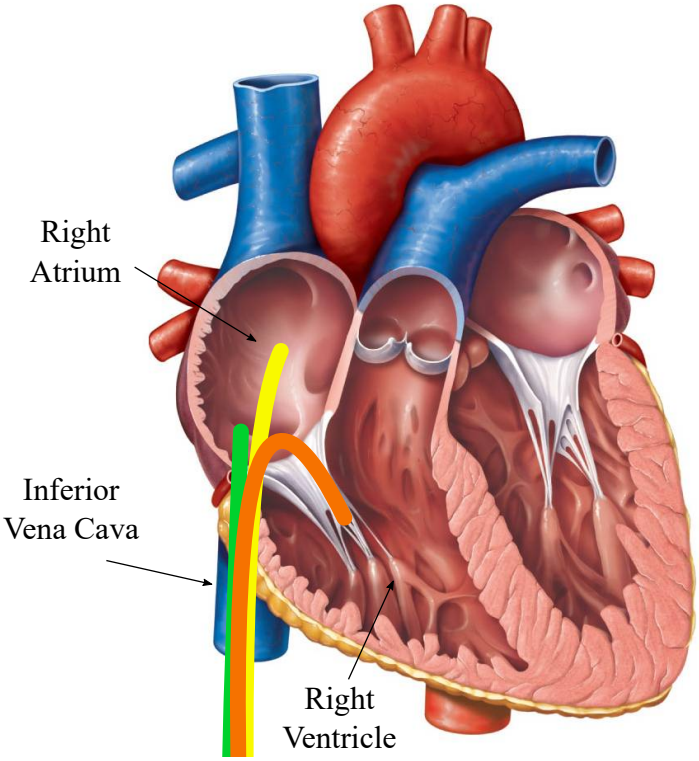

Figure 5.2: *US catheter in right atrium (yellow), right ventricle (orange), and inferior vena cava (green).*

vena cava. The US catheter handle was not actuated during measurements.

An example of the CT and BB pose data is shown in Figs. 5.3-5.4. The raw data demonstrated pose changes resulting from both cardiac (2 Hz) and respiratory (0.2 Hz) motions. The data was zero-phase low pass filtered to eliminate cardiac motion (low pass filter order 50, Hamming window, cut off frequency 2 Hz). The low pass filtered data was truncated by 35 samples on either side due to the edge effects. Low pass filtered CT and BB displacements of roughly $4-6$ mm are shown in Fig. 5.5. The motion study showed that in addition to displacing and rotating the whole catheter bending section, each breath also bent and rotated the tip, causing displacements of roughly 3 mm and rotations of $1-5°$ in each axis. This is evident in Fig. 5.6, which shows both the raw and the low pass filtered motion of CT with respect to BB.

After examining typical displacements and rotations due to breathing motion, the next step was to determine how consistent the disturbance was. The low pass filtered CT motion

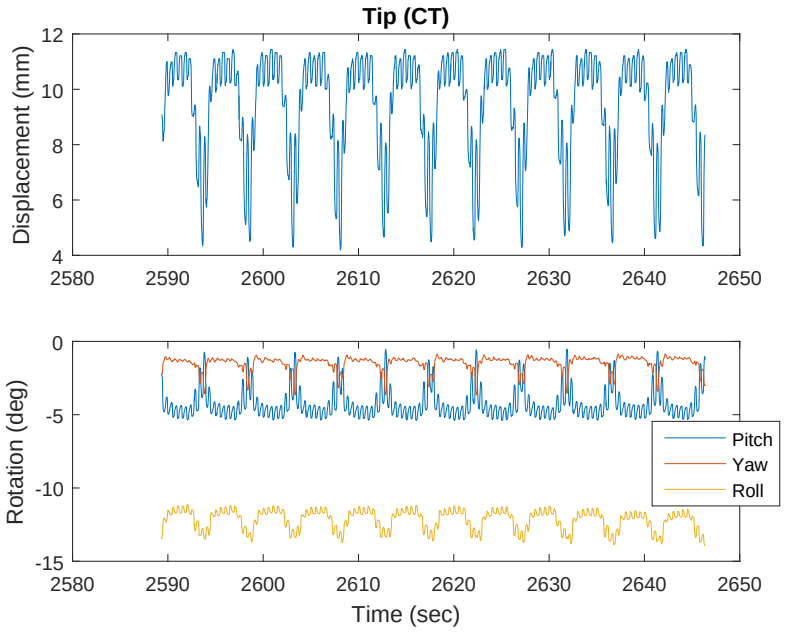

Figure 5.3: *Tip (CT) pose change due to cardiac and respiratory motion while in right atrium.*

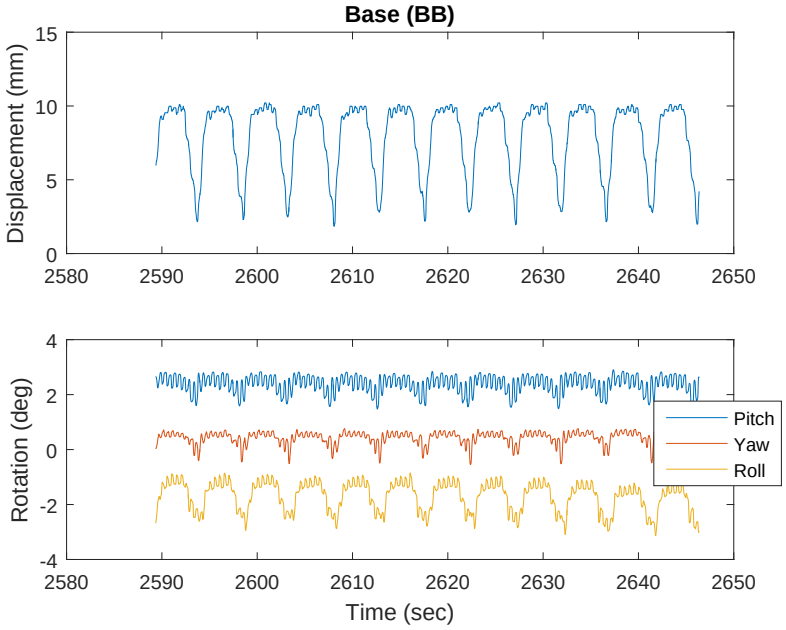

Figure 5.4: *Base (BB) pose change due to cardiac and respiratory motion while in right atrium.*

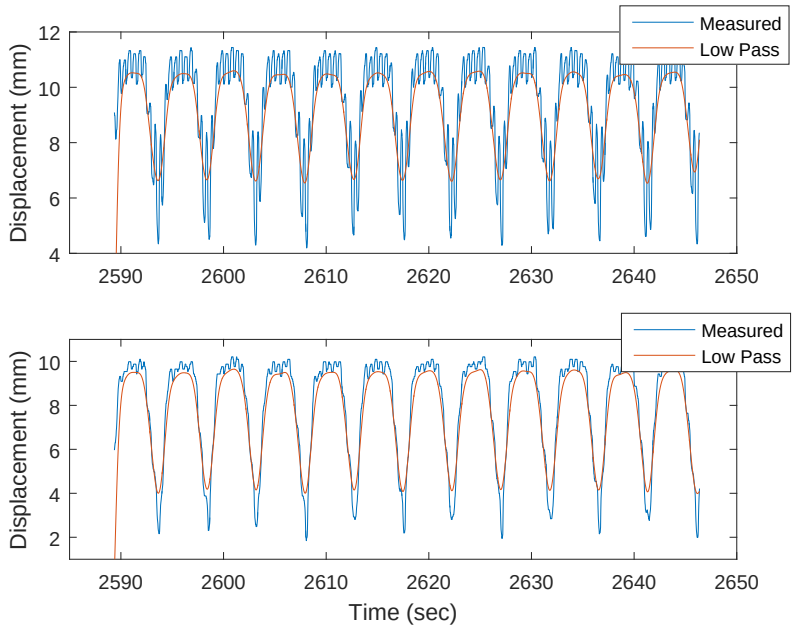

Figure 5.5: *Low pass filtered (top) tip and (bottom) base displacement to isolate breathing motion.*

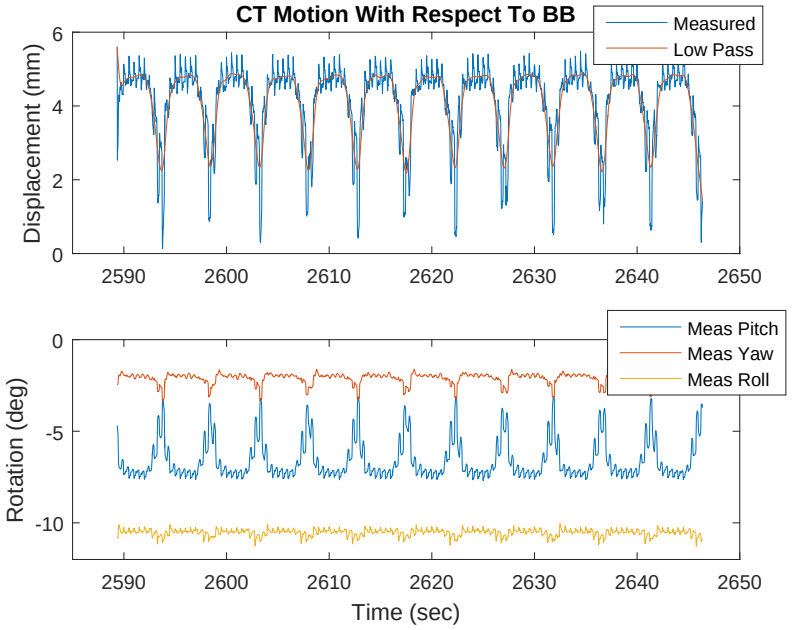

Figure 5.6: *Change in CT with respect to BB during cardiac and respiratory motion.*

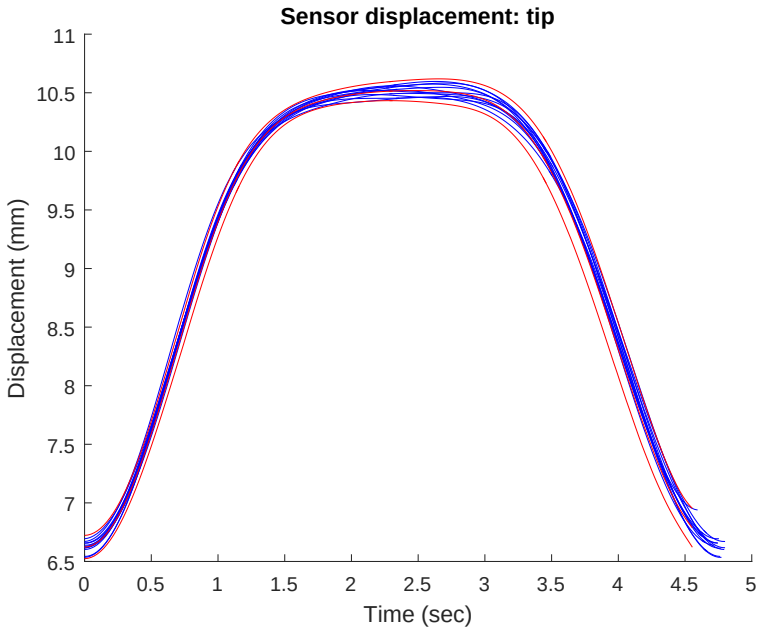

Figure 5.7: *Breath-to-breath variations in CT displacement.*

results from each individual breath in Fig. 5.5 were compared to one another in order to calculate breath-to-breath variations. Fig. 5.7 shows CT displacement for each individual breath. Each breath is marked in blue. The red lines indicate the mean breath displacement plus or minus one standard deviation. The maximum standard deviation of this data set was 0.11 mm. The resulting variations across all data sets are small enough to assume that amplitude variations are negligble.

5.3.3 Modeling Respiratory Disturbance

We define periodic models for the low pass filtered CT, BB, and $Instr$ disturbance motions due to respiration. Fig. 5.8 is a schematic with a green dotted line demonstrating typical CT, BB, and $Instr$ motion trajectories. Each coordinate frame breathing motion trajectory is cyclical but different from each other. The cycles will also change as the US catheter is moved to different regions of the heart. We model the disturbance motion for each point assuming that the US catheter remains in the same location of the heart. If the US catheter is relocated to a new region then a new model must be created.

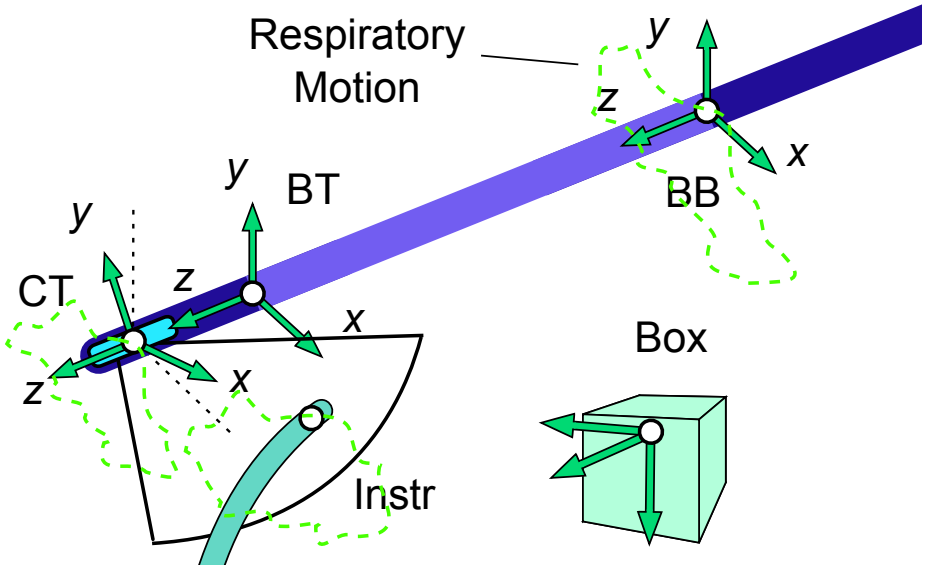

Figure 5.8: *Coordinate frame motion due to respiration.*

We begin with a 1D model of the *CT* y-coordinate. This will later be expanded to model the full 6-DOF pose. The 1D model of the *CT* y-coordinate is calculated using a process similar to Yuen et al. (2009), which was an expansion of Parker and Anderson (1990). In Eqn. 5.1 we approximate the 1D signal, $y(t)$, with a limited number of harmonics, m. This is represented as an m-order Fourier series with a constant offset,

$$y\left(t\right) = c + \sum_{i=1}^{m} r_i \sin\left(i\omega t + \phi_i\right) \tag{5.1}$$

where ω is the respiratory rate, c is the constant offset, r_i and ϕ_i are the harmonic amplitudes and phases, and $i \in (1, \ldots, m)$. This can be expressed as a time-varying Fourier series

$$y\left(t\right) = c\left(t\right) + \sum_{i=1}^{m} r_i\left(t\right) \sin\theta_i\left(t\right) \tag{5.2}$$

where $\theta_i(t) = i\int_0^t \omega(\tau)\,d\tau + \phi_i(t)$. The model for the Fourier series can be defined as

$$\boldsymbol{x}(t) \triangleq \begin{bmatrix} c(t) \\ r_i(t) \\ \omega(t) \\ \theta_i(t) \end{bmatrix}. \tag{5.3}$$

This model is initialized by measuring motion for at least two breaths. Breaths are typically under five seconds long, so 12 seconds of data are used to initialize the model. The harmonic amplitudes and coefficients are obtained by solving a linear estimation. Eqn. 5.1 is reparameterized in rectangular form as

$$y(t) = c_0 + \sum_{i=1}^{m} \left[a_i \sin(i\hat{\omega}_0 t) + b_i \cos(i\hat{\omega}_0 t)\right], \tag{5.4}$$

where a_i and b_i are the coefficients of the Fourier series in rectangular form and $\hat{\omega}_0$ is the initial estimate of the breathing rate. The 12 seconds of initialization data collected are $\tilde{\boldsymbol{z}} \triangleq [z(0), z(\Delta t), \ldots, z((N-1)\Delta t)]^T$, where N refers to the total number of initialization points and Δt is the time between measurement acquisitions. The mean time to acquire measurements is $\Delta t = 0.0234$ *sec* for the EM tracking system used. The rectangular form of the model is $\tilde{\boldsymbol{x}}_0 \triangleq [c_0, a_1, \ldots, a_m, b_1, \ldots, b_m]^T$.

We can relate $\tilde{\boldsymbol{z}}$ and $\tilde{\boldsymbol{x}}_0$ by the equation

$$\tilde{\boldsymbol{z}} = \boldsymbol{A}\tilde{\boldsymbol{x}}_0 + \boldsymbol{\nu}, \tag{5.5}$$

where $\boldsymbol{A}$ is given by

$$\boldsymbol{A}^T \triangleq \begin{bmatrix} 1 & 1 & \dots & 1 \\ \sin(\hat{\omega}_0 0) & \sin(\hat{\omega}_0 \Delta t) & \dots & \sin(\hat{\omega}_0 (N-1)\Delta t) \\ \vdots & \vdots & & \vdots \\ \sin(m\hat{\omega}_0 0) & \sin(m\hat{\omega}_0 \Delta t) & \dots & \sin(m\hat{\omega}_0 (N-1)\Delta t) \\ \cos(\hat{\omega}_0 0) & \cos(\hat{\omega}_0 \Delta t) & \dots & \cos(\hat{\omega}_0 (N-1)\Delta t) \\ \vdots & \vdots & & \vdots \\ \cos(m\hat{\omega}_0 0) & \cos(m\hat{\omega}_0 \Delta t) & \dots & \cos(m\hat{\omega}_0 (N-1)\Delta t) \end{bmatrix}$$

and $\boldsymbol{\nu}$ is a vector of measurement noise. The least squares estimate is then calculated by

$$\tilde{\boldsymbol{x}} = (\boldsymbol{A}^T \boldsymbol{A})^{-1} \boldsymbol{A}^T \tilde{\boldsymbol{z}}. \tag{5.6}$$

The estimate of the state at the moment of initialization, $\boldsymbol{x}(T|T)$, is initialized with the following values:

$c(T) = c_0$

$\omega(T) = \omega_0$

$r_i(T) = \left(a_i^2 + b_i^2\right)^{-\frac{1}{2}}$

$\theta_i(T) = \arctan(b_i, a_i)$.

This initialization process calculates a Fourier series model estimate of the CT pose y-coordinate cycle due to breathing motion. An example model is shown in Fig. 5.9. The blue line represents the raw EM measurements of the CT y-coordinate. The black line represents the low pass filtered CT y-coordinate with the edge effects removed. The red line represents the initialized Fourier series model estimate. The mean absolute error between the y-coordinate model values and the low pass filtered measurements is 0.057 mm ($\sigma = 0.041$ mm). The mean absolute model error for the x-axis is 0.037 mm ($\sigma = 0.027$ mm) and for the z-axis is 0.039 mm ($\sigma = 0.028$ mm).

The entire CT pose can be represented by seven parameters: x, y, z, and the rotation matrix converted to an equivalent axis representation (axis x-, y-, z-components, and angle of rotation). The 1D signal initialization process is done seven times for CT and seven times

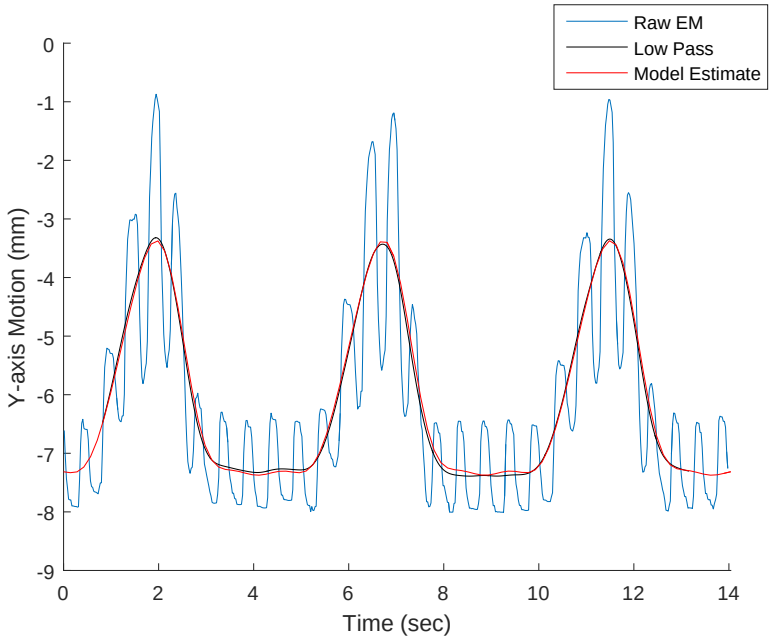

Figure 5.9: *Breathing model of low pass filtered CT y-coordinate motion.*

for BB.

Once calculated, the robot will begin actuating the pull wires and steering the catheter to compensate for this breathing model. During steering it is not possible to update most of the model parameters, yet the model must be accurate for as long as possible. The DC offset ($c(t)$), the amplitude components ($r_i(t)$), and the phase components ($\theta_i(t)$) cannot be re-measured or re-initialized while the robot is actively steering because CT and BB measurements are influenced by both breathing and robot steering. The frequency, however, can be measured from a different sensor and continuously updated. The frequency is first estimated based on the initialization measurements from Eqn. 5.5 but that estimate value typically becomes outdated within 30 seconds. As the original frequency estimate becomes less accurate, the predicted breathing pose goes out of phase with the actual breathing cycle. This leads to poor steering results.

Measuring the breathing frequency and recalculating the model greatly improves motion compensation accuracy. A fourth EM sensor is attached to the exterior chest wall of the animal for *in vivo* cases or to the plastic inferior vena cava (IVC) for bench top cases. A peak

detection algorithm calculates the breathing frequency from the fourth sensor and applies it to the original initialization data to recalculate the models.

The peak detection algorithm thresholds the breathing displacement data to isolate all values above the threshold. The time at increasing above the threshold is averaged with the time at decreasing below the threshold. This calculates the time at the center of each peak region. This may not necessarily align with the peak displacement value, but this approach is more reliable than simply identifying the time at the peak displacement value. The difference between the center times of the measured displacement and modeled displacement values then reveals the amount of drift in the breathing frequency. The frequency is then adjusted accordingly. The original initialization data with the new frequency value are used to recalculate the breathing model. This process repeats continuously.

As a result, a model can continue providing accurate CT and BB pose estimates for a much longer time if the catheter remains in the same region of the heart. The bench top mean absolute error between the model values and the raw EM measurements after 10 minutes was 0.24 mm ($\sigma = 0.16$ mm). The *in vivo* breathing model error after two minutes was typically 0.8 mm.

With accurate breathing models the system can begin actuating the US catheter control knobs. By using the models to estimate CT and BB motion at any point in time, it is possible to input target poses to the kinematics calculations and point the US imager at the proper target. Section 5.3.5 discusses the specifics of the pre-kinematics calculations and how these models are used.

5.3.4 Predicting Target Motion

Multiple time delays in the system cause problems when attempting to point the moving US imager at a target which is also moving but with a slightly different direction and amplitude. In software the sensor acquisition rate, motor communication, kinematic calculations, low pass filtering, and additional data processing are contributing factors. In hardware the motor torque limits and catheter construction cause delay as well. The system response

time is examined in Section 5.4. These delays cause the US catheter navigation to lag behind target motion, resulting in poor US imager alignment with the target. Therefore, we design a predictive filter to estimate the future target position and adjust the US catheter accordingly.

We use an EKF to estimate the position of the tracking target. A set of Kalman filter gains and prediction matrices is used for estimating the x-, y-, and z-coordinates of the target individually. For now we focus on using the EKF to predict the y-coordinate only. This process will then be repeated to predict the x- and z-coordinates as well.

Step-By-Step EKF Derivation

The model of the y-coordinate signal in Eqn. 5.3, $\boldsymbol{x}(t)$, is the state at a given point in time. We assume that the Fourier components evolve through a random walk. The state space model for the system is then

$$\hat{\boldsymbol{x}}\,(t+\Delta t) = \boldsymbol{F}(\Delta t)\hat{\boldsymbol{x}}(t) + \boldsymbol{\mu}(t), \tag{5.7}$$

where $\hat{\boldsymbol{x}}(t)$ is the best estimate of the state at the current time and $\hat{\boldsymbol{x}}(t+\Delta t)$ is the best estimate of the state at the next time point. The prediction matrix, $\boldsymbol{F}(\Delta t)$, is calculated as

$$\boldsymbol{F}(\Delta t) = \begin{bmatrix} \boldsymbol{I}_{m+1} & & \boldsymbol{0} & & \\ & 1 & & & \\ & \Delta t & 1 & & \\ \boldsymbol{0} & 2\Delta t & 0 & 1 & \\ & \vdots & & & \ddots \\ & m\Delta t & & & 1 \end{bmatrix}, \tag{5.8}$$

and $\boldsymbol{\mu}(t)$ is the random step of the states. The random step is assumed to be from a zero mean multivariate normal distribution represented by the environment uncertainty covariance matrix, $\boldsymbol{Q}$. The second part to the model is

$$z(t) = h(\hat{\boldsymbol{x}}(t)) + \nu(t). \tag{5.9}$$

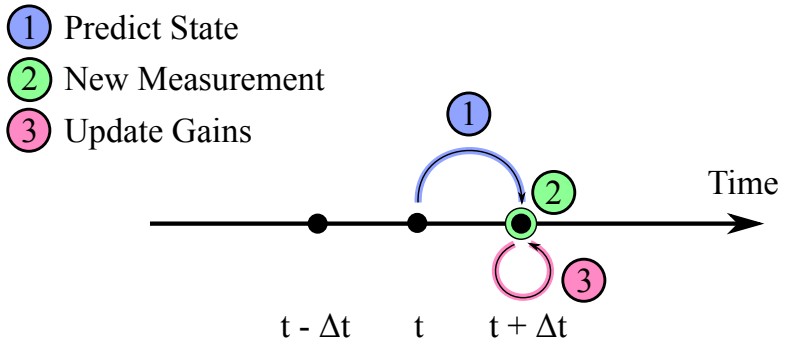

Figure 5.10: *Step-by-step EKF uses current information to predict the next time step. New measurements are used to update the Kalman gains.*

Here, $z(t)$ is the measurement of the signal. $h(\hat{\boldsymbol{x}}(t))$ is defined as $y(t)$. And $v(t)$ is zero mean Gaussian measurement noise with variance σ_R^2.

With this model we estimate the $2m+2$ model parameters of $\boldsymbol{x}$. The EKF estimates the nonlinear problem by linearizing about the current state estimate, $\hat{\boldsymbol{x}}(t|t)$. The EKF is computed by recursively predicting an estimate, collecting a new measurement, and then updating the parameters that can be used to predict the next estimate as in Fig. 5.10. The details are as follows: the present time is t. The prediction for the next state, $\hat{\boldsymbol{x}}\,(t+\Delta t)$, is calculated using Eqn. 5.7. Then Eqn. 5.2 is used to calculate the predicted value of the signal, $y(t+\Delta t)$. Next we use the current covariance matrix, $\boldsymbol{P}(t)$, to predict the covariance matrix, $\boldsymbol{P}(t+\Delta t)$, as in

$$\boldsymbol{P}(t+\Delta t|t) = \boldsymbol{F}\boldsymbol{P}(t|t)\boldsymbol{F}^T + \boldsymbol{Q}. \tag{5.10}$$

The Kalman gain, $\boldsymbol{K}$, is calculated by

$$\boldsymbol{K} = \boldsymbol{P}(t+\Delta t|t)\boldsymbol{H}^T S^{-1}, \tag{5.11}$$

where

$$S = \sigma_R^2 + \boldsymbol{H}\boldsymbol{P}(t+\Delta t|t)\boldsymbol{H}^T, \tag{5.12}$$

and the sensor matrix $\boldsymbol{H}$ is defined by

$$\boldsymbol{H}^T \triangleq \left(\frac{\partial h}{\partial x}\right)^T\Bigg|_{\hat{\boldsymbol{x}}(t+\Delta t|t)=\boldsymbol{F}\hat{\boldsymbol{x}}(t|t)} = \begin{bmatrix} 1 \\ \sin\theta_1(t+\Delta t|t) \\ \vdots \\ \sin\theta_m(t+\Delta t|t) \\ 0 \\ r_1(t+\Delta t|t)\cos\theta_1(t+\Delta t|t) \\ \vdots \\ r_m(t+\Delta t|t)\cos\theta_m(t+\Delta t|t) \end{bmatrix}. \tag{5.13}$$

After predictions for the state, the covariance matrix, and the Kalman gain are made, the system uses these values to calculate control commands and then moves the robot accordingly. Soon the next sensor measurement, $z(t+\Delta t)$, will be available. This new measurement is then compared with the predicted value in order to update the state estimate, $\hat{\boldsymbol{x}}(t+\Delta t|t+\Delta t)$, and the covariance matrix, $\boldsymbol{P}(t+\Delta t|t+\Delta t)$, as in

$$\hat{\boldsymbol{x}}(t+\Delta t|t+\Delta t) = \boldsymbol{F}\hat{\boldsymbol{x}}(t|t) + \boldsymbol{K}\left(z(t+\Delta t) - h(\boldsymbol{F}\hat{\boldsymbol{x}}(t|t))\right) \tag{5.14}$$

$$\boldsymbol{P}(t+\Delta t|t+\Delta t) = (\boldsymbol{I} - \boldsymbol{K}\boldsymbol{H})\boldsymbol{P}(t+\Delta t|t). \tag{5.15}$$

The covariance matrix, $\boldsymbol{P}$, is initialized as

$$\boldsymbol{P}(T|T) = \begin{bmatrix} \frac{\sigma_R^2}{N} & & & & & & & & \\ & \sigma_1^2 & & & & & & & \\ & & \frac{\sigma_1^2}{2^2} & & & & & & \\ & & & \ddots & & & & & \\ & & & & \frac{\sigma_1^2}{m^2} & & & & \\ & & & & & \sigma_\omega^2 & & & \\ & & & & & & \sigma_\theta^2 & & \\ & & & & & & & \ddots & \\ & & & & & & & & \sigma_\theta^2 \end{bmatrix}, \tag{5.16}$$

where σ_R^2 is the measurement noise variance, σ_1^2 is the uncertainty of the amplitude components, σ_ω^2 is the uncertainty of the fundamental frequency, and σ_θ^2 is the uncertainty of the phase components. Trial and error by Parker and Anderson (1990) determined that $\sigma_\theta^2 = 0.02\ rad^2$. The environment uncertainty covariance matrix, $\boldsymbol{Q}$, is a diagonal matrix with all values set to 10^{-4} except for q_ω, as in

$$\boldsymbol{Q} = \begin{bmatrix} 10^{-4} & & & & & & & & & & \\ & 10^{-4} & & & & & & & & & \\ & & 10^{-4} & & & & & & & & \\ & & & 10^{-4} & & & & & & & \\ & & & & 10^{-4} & & & & & & \\ & & & & & q_\omega^2 & & & & & \\ & & & & & & 10^{-4} & & & & \\ & & & & & & & 10^{-4} & & & \\ & & & & & & & & 10^{-4} & & \\ & & & & & & & & & 10^{-4} & \end{bmatrix}. \tag{5.17}$$

Step-By-Step EKF Simulation

The EKF was tested on pre-recorded data from early *in vivo* animal trials. The pre-recorded data came from the low pass filtered y-coordinate of the CT sensor motion due to breathing only (no robot actuation). The catheter tip was inside the right atrium of the live porcine subject. The zero phase low pass filtered data contained edge effects, but those edge effects have been cropped out of the data set for these initial step-by-step EKF simulations. The edge effects will be addressed in the next sections.

The first N data points were used for initializing the breathing model and calculating the first state, covariance matrix, and Kalman gain. Data points were given to the EKF sequentially to simulate the sensors measuring live. The EKF predicted the state for the next time point without knowing what the next measurement would be. Then the next pre-recorded measurement was given to the EKF, the matrices were updated, and the cycle

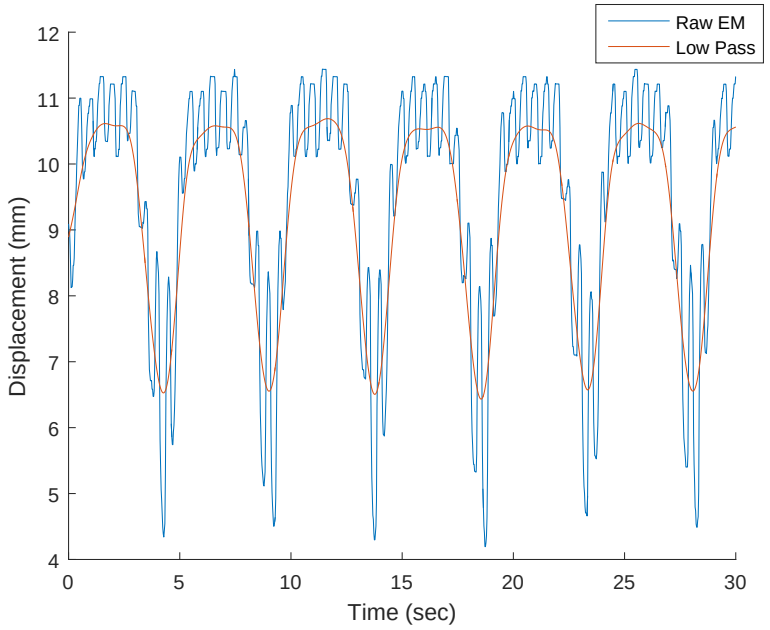

Figure 5.11: *CT displacement measurements and low pass filtered results (edge effects are manually removed).*

continued until the end of the data set. Fig. 5.11 first shows the raw EM measurements of the CT tip displacement and the low pass filtered results. The low pass filter edge effects have been cropped from the plot. Fig. 5.12 shows the low pass filtered CT motion with the results of the step-by-step EKF simulation. The red line represents the measured signal (which is the low pass filtered y-coordinate of the CT pose). The blue line, which begins at roughly $t = 12$ *sec* after initialization, represents each predicted signal point based on only pre-existing information. The mean absolute error between each predicted value and the measured value was 0.023 mm ($\sigma = 0.034$ mm). This error is significantly below the allowable error tolerances of the system, and therefore it is negligible.

Multiple-Step EKF Derivation

The above EKF results highlight the accuracy of the algorithm when predicting the value of the signal in the next time step, which is average $\Delta t = 0.0234$ *sec*. However, predicting the next time step is not sufficient for improving US imager alignment. The EKF must be adjusted to predict much farther beyond the next time step for two reasons:

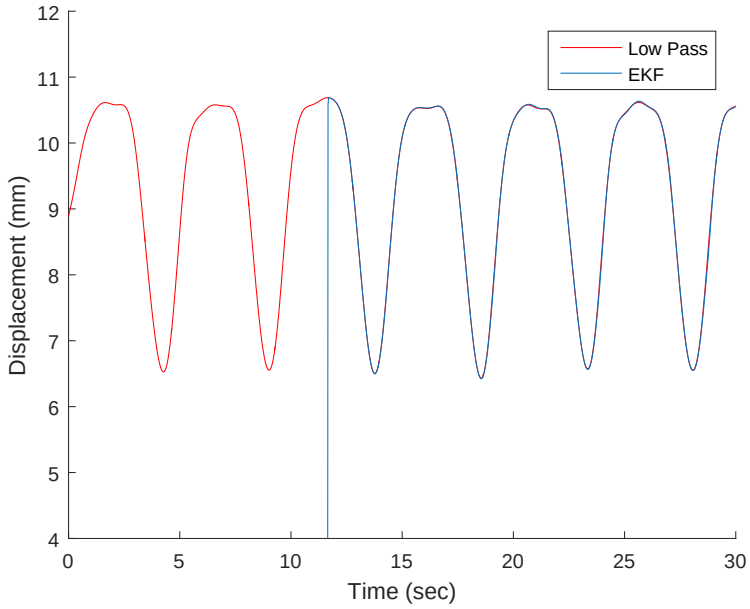

Figure 5.12: *Low pass filtered CT displacement (edge effects were manually removed) and step-by-step EKF prediction.*

(1) The hardware and software limitations of the system cause delays in US imager navigation. This means that the EKF must be able to calculate a prediction for some number of samples beyond the current moment in time. The appropriate number of time steps may change depending on which steering mode the robot is in.

(2) We must also account for the edge effects which result from low pass filtering. The window size of the currently implemented low pass filter causes the first and last 35 samples to become unusable. Incoming measurements are always low pass filtered in order to eliminate the cardiac disturbance, and therefore at any point in time the 35 most recent low pass filtered data points cannot be used. This means that the most recent reliable data point is perpetually outdated by $35 * 0.0234\ sec = 0.819\ sec$.

The number of samples to predict ahead due to hardware and software limitations is defined as M_1. The best value for M_1 will be determined experimentally with influence from the response time tests in Section 5.4. The number of unusable samples due to edge effects is defined as $M_2 = 35$ for the current low pass filter. The total number of samples to

predict, M, is defined as

$$M = M_1 + M_2. \tag{5.18}$$

Now we can adjust the EKF algorithm to predict many samples ahead, rather than one sample ahead (Fig. 5.13). The EKF initialization process is adjusted such that N points are collected and low pass filtered, but the first and last M_2 samples are not used in the least squares estimate for calculating the initial state. The initialized state is calculated for the time point $t = N - M_2$. Initial values for $\hat{\boldsymbol{x}}$, y, $\boldsymbol{P}$, $\boldsymbol{H}$, and $\boldsymbol{K}$ in the time points $t = N - M_2$ through $t = N + M_1$ are then predicted using prediction matrices of the appropriate time steps, as in

$$\boldsymbol{F}(M\Delta t) = \begin{bmatrix} \boldsymbol{I}_{m+1} & & \boldsymbol{0} & & \\ & 1 & & & \\ & M\Delta t & 1 & & \\ \boldsymbol{0} & 2M\Delta t & 0 & 1 & \\ & \vdots & & & \ddots \\ & mM\Delta t & & & 1 \end{bmatrix}. \tag{5.19}$$

The EKF predict/measure/update cycle then begins collecting one measurement per time step. At the current time, t, predictions at the time point $t + M_1$ are made ($\hat{\boldsymbol{x}}|_{t+M_1}$, $y|_{t+M_1}$, $\boldsymbol{P}|_{t+M_1}$, $\boldsymbol{H}|_{t+M_1}$, and $\boldsymbol{K}|_{t+M_1}$). When each new measurement is collected at time $t + \Delta t$ then the most recent N points are low pass filtered. The last M_2 points are unusable, but the $(t - M_2)$-th measurement value, $z(t - M_2)$, is updated accordingly. Then the estimated values for $\hat{\boldsymbol{x}}|_{t-M_2}$ and $\boldsymbol{P}|_{t-M_2}$ are updated based on the new information.

An example with numbers works as follows: $N = 500$, $M_1 = 20$, and $M_2 = 35$. The first 500 measurements are collected and 35 samples are clipped off either end. The reliable initialization measurements are between $t = 36$ and $t = 465$. The current time is $t = 500$. The EKF initialization estimates the values for $\hat{\boldsymbol{x}}$, y, $\boldsymbol{P}$, $\boldsymbol{H}$, and $\boldsymbol{K}$ between $t = 466$ and $t = 520$, but no measurement information is available yet for any of those time points. Now, at $t = 500$, we use the initialized Kalman matrices from $t = 465$ to predict the Kalman matrices at $t = 520$. Then we acquire a new measurement from $t = 501$, but the low pass

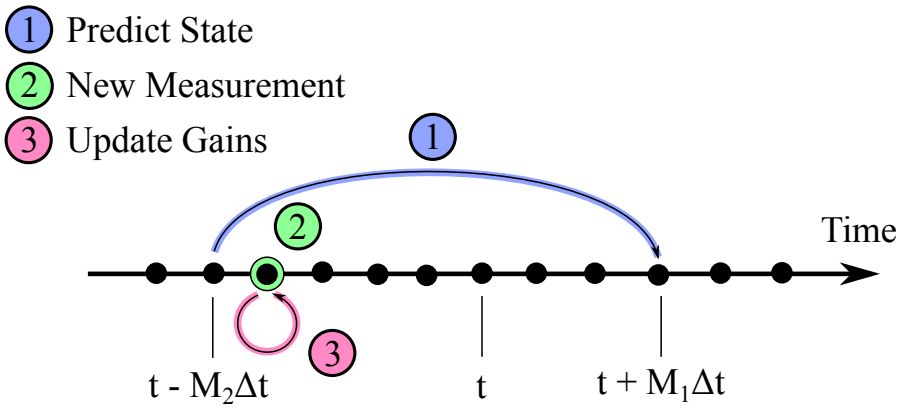

Figure 5.13: *Multi-step EKF uses past reliable information to predict a future time step. New measurements are used to update the Kalman gains for the past.*

filter renders the last 35 samples useless, so our newest reliable measurement is actually for the time $t = 466$. We then use the new measurement at $t = 466$ to update the Kalman matrices from $t = 466$. The cycle continues onward; at $t = 501$ we use $t = 466$ Kalman matrices to predict the state at $t = 521$. We acquire the $t = 502$ measurement, low pass filter the last 500 samples to obtain a reliable $t = 467$ measurement, and use this to update the $t = 467$ Kalman matrices. Then the $t = 467$ Kalman matrices are used to predict the state at $t = 522$, and so on. In this way the EKF can accurately predict information M_1 samples into the future, while also compensating for the M_2 samples lost from low pass filtering.

Multiple-Step EKF Simulation

The EKF was once again tested on pre-recorded data from early *in vivo* animal trials. The pre-recorded data came from the low pass filtered y-coordinate of the CT sensor motion due to breathing only. The catheter tip was inside the right atrium (RA) of the live porcine subject. The zero phase low pass filtered data contained edge effects. The multiple-step EKF estimation algorithm used the most recent reliable data that was not altered by the edge effects in order to estimate predictions for future time points.

The first N data points were used for initializing the breathing model and calculating multiple-step EKF matrices as discussed above. Subsequent data points were given to the

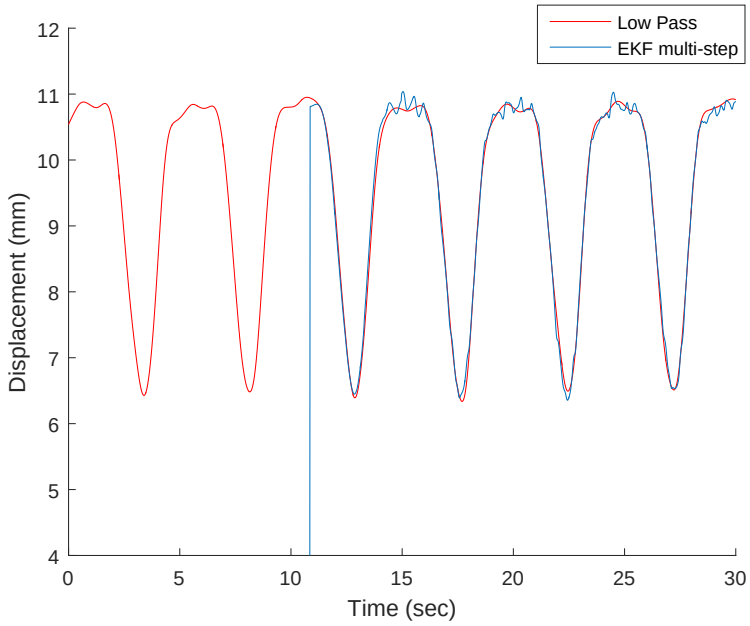

Figure 5.14: *Low pass filtered CT displacement and multi-step EKF prediction.*

EKF one at a time as though the sensors were measuring live. The EKF predicted the state for the future time point without knowing what the next measurement would be. Then the next measurement was given to the EKF and the multiple-step EKF cycle repeated until the end of the data set. Fig. 5.14 shows the results of the multiple-step EKF simulation. The red line represents the low pass filtered CT displacement. The blue line, which begins at roughly $t = 12$ *sec* after initialization, represents each predicted signal point based on only pre-existing information. The mean absolute error between each predicted value and the measured value was 0.088 mm ($\sigma = 0.114$ mm). This error was roughly four times higher than the step-by-step prediction. This discrepancy is expected because the step-by-step EKF uses much more recent information in order to make predictions. The multiple-step EKF uses predictions based on data that has been somewhat outdated by the time the new measurement is collected. Still, this error is significantly below the allowable error tolerances of the system, and therefore it is also negligible.

5.3.5 Pre-Kinematics Calculations

Pre-kinematics calculations are used to prepare inputs for the kinematics calculations. There are numerous ways to navigate the catheter tip depending on the clinician's goals, and pre-kinematics calculations must be done for each navigation method. In all cases the pre-kinematics calculations determine the current tip pose with respect to the current base ($T_{BB_{Mobile}-CT}$), the relative desired pose adjustments ($\Delta xyz\psi$), and the amount of BB roll in the bending section (γ_{curr}). The following poses are needed:

(1) The fixed base pose with respect to the EM tracker field generator coordinates, $T_{Box-BB_{Fixed}}$

(2) The current tip (CT) pose measured with respect to the fixed base, $T_{BB_{Fixed}-CT}$

(3) The estimated tip pose due to the breathing motion trajectory model, $T_{BB_{Fixed}-CT_{Traj}}$

(4) The current base (BB) pose measured with respect to the fixed base, $T_{BB_{Fixed}-BB_{Mobile}}$

(5) The estimated base pose due to the breathing motion trajectory model, $T_{BB_{Fixed}-BB_{Traj}}$

The fixed base pose, $T_{Box-BB_{Fixed}}$, is a constant coordinate transform that relates the catheter coordinate frame to tracking system coordinates. This constant transform can be defined at any point in the breathing cycle. It is defined once each time the US catheter is manually moved to a new location in the heart.

The current CT and BB poses are measured continously. The estimated tip and base poses, CT_{Traj} and BB_{Traj}, are recalculated continuously from the trajectory models at each time point. Multiplying the inverse of $T_{BB_{Fixed}-CT_{Traj}}$ by $T_{BB_{Fixed}-CT}$ calculates $T_{CT_{Traj}-CT}$, which is an estimate of the robot-actuated movement. A similar calculation is done to find $T_{BB_{Traj}-BB}$, which is an estimate of the uncontrollable BB motion due to robot actuation. These estimates can be used in order to find the relative amount of US imager angle adjustment, ψ, as well as the amount of catheter handle roll expressed at the bending section, γ_{curr}.

The inverse of $T_{BB_{Fixed}-BB_{Mobile}}$ and $T_{BB_{Fixed}-CT}$ are multiplied in order to find $T_{BB_{Mobile}-CT}$, which is the current CT with respect to the current BB. This transform represents the current bend of the catheter tip. Together the values $T_{BB_{Mobile}-CT}$, ψ, γ_{curr}, and $\Delta xyz\psi$ enable

the kinematics to calculate the current catheter configuration.

The relative desired pose adjustment, $\Delta xyz\psi$, is determined based on the type of motion desired:

(Mode 1) *Navigating to a Single Pose*. This is useful for imaging tissue for volume reconstruction. The desired pose adjustment is made equal to the difference between the current CT and the current CT_{Traj} poses plus an additional US imager rotation or displacement command. It is not possible with the given sensing strategy to directly measure the tissue location, but it is possible to maintain the catheter's pose in the heart chamber with respect to the breathing motion disturbance.

(Mode 2A) *Instrument Tracking - Position*. The position of the catheter tip is made equal to the working instrument. The US imager is not necessarily used. The CT and BB breathing models are not used.

(Mode 2B) *Instrument Tracking - Position w/EKF*. Fig. 5.15 diagrams the pre-kinematics calculations used in Mode 2B. The green dotted line represents cyclical CT and $Instr$ pose motion due to respiration only. The current CT pose measurement is $CT_{Current}$. The current expected CT due only to breathing is $CT_{Traj-Current}$. The difference transform between the measured and expected CT is given by $T_{CT_{Traj}-CT}$ (yellow arrow). The current measured $Instr$ pose is $Instr_{Current}$. The EKF-predicted future $Instr$ location is $Instr_{Future}$. The breathing models predict the expected breathing CT pose, $CT_{Traj-Future}$, at that time point. $T_{CT_{Traj}-CT}$ is then applied to $CT_{Traj-Future}$ in order to estimate CT_{Future}, which represents an expectation of where CT will be in the future based on its current relationship to the breathing model expectations. The desired pose adjustment is calculated as the difference between the $Instr_{Future}$ and CT_{Future}. Neither of these IT-Position modes are directly clinically relevant in navigating US catheters to collect US images, but they demonstrate the possibility of motion compensation with steerable cardiac catheters for other clinical applications.

(Mode 3A) *Instrument Tracking - Imager*. In these two modes the US imager is rotated to track a moving target while the position of the catheter tip is made to remain constant with respect to the heart chamber. In Mode 3A the target position is made equal to the

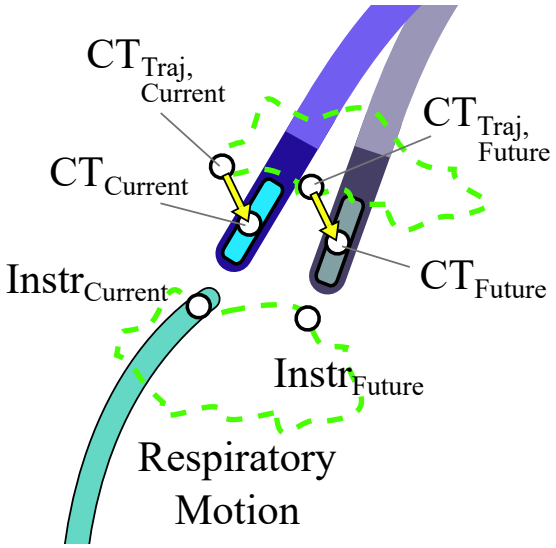

Figure 5.15: *Tracking the position of an instrument with predictive filtering (Mode 2B).*

CT_{Traj} position at that time point. The desired orientation change is calculated by the angle difference between the US imaging plane and the current location of the working instrument tip.

(Mode 3B) *Instrument Tracking - Imager w/EKF*. Fig. 5.16 diagrams the pre-kinematics calculations used in Mode 3B. The green dotted line represents cyclical CT and $Instr$ pose motion due to respiration only. The current expected CT pose due to breathing only is $CT_{Traj,Current}$, and the current measured CT pose is $CT_{Current}$. The yellow arrow represents the transform between the expected pose and the actual measured pose, $T_{CT_{Traj}-CT}$. The current target position is $Instr_{Current}$. The EKF is used to estimate the future target position, $Instr_{Future}$. The breathing model is used to calculate the future CT pose, $CT_{Traj-Future}$, for the same time point. $T_{CT_{Traj}-CT}$ is applied to $CT_{Traj-Future}$ to calculate the expected CT pose at that time point based on the current difference between the measured and expected poses: CT_{Future}. The orientation angle to adjust, $\Delta\psi$, is calculated between the future CT pose, CT_{Future}, and the future EKF-estimated target pose, $Instr_{Future}$. The position change is the difference between the currently expected CT pose, $CT_{Traj-Current}$ and the current measured CT pose, $CT_{Current}$.

In Section 5.4 all modes will be demonstrated through bench top testing. Modes 1, 3A,

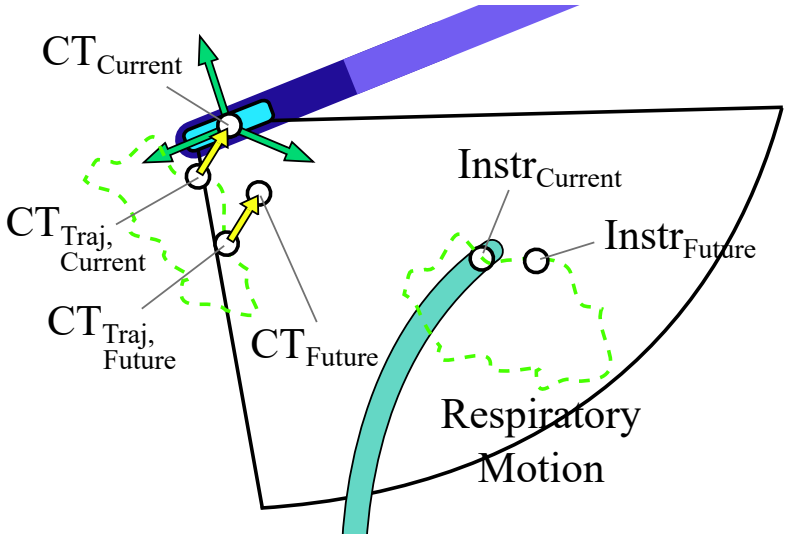

Figure 5.16: *Orienting the imager to tracking an instrument with predictive filtering (Mode 3B).*

and 3B will also be demonstrated *in vivo*.

5.3.6 Controller

The methods described above can be summarized in the instrument tracking (Mode 3B) controller diagram Fig. 5.17. The gray box includes system measurements and calculations. External disturbances from cardiac, breathing, and unconstrained catheter shaft motions affect the system. The blue box highlights the catheter breathing model. A set of CT and BB sensor measurements is used to calculate the breathing model. Once the robot begins actuation, the catheter breathing model can no longer be updated from CT and BB measurements. An EM sensor on the subject's chest continuously measures the breathing period which is used to update the breathing model frequency. The green box highlights target prediction. Physiological left ventricle (LV) motion shifts the target position. The target is sensed and its motion is predicted by the EKF. The Pre-Kinematics block uses the target prediction, catheter breathing model, and catheter sensor information to calculate $T_{BB_{Mobile}-CT}$, γ_{curr}, and $\Delta xyz\psi$. These values are grouped into the label $\Delta \boldsymbol{X}$. The Kinematics block then calculates the desired control knob adjustments $\Delta \boldsymbol{\Phi}$, the robot actuates the catheter handle, and the catheter moves. Unconstrained disturbances from the vasculature

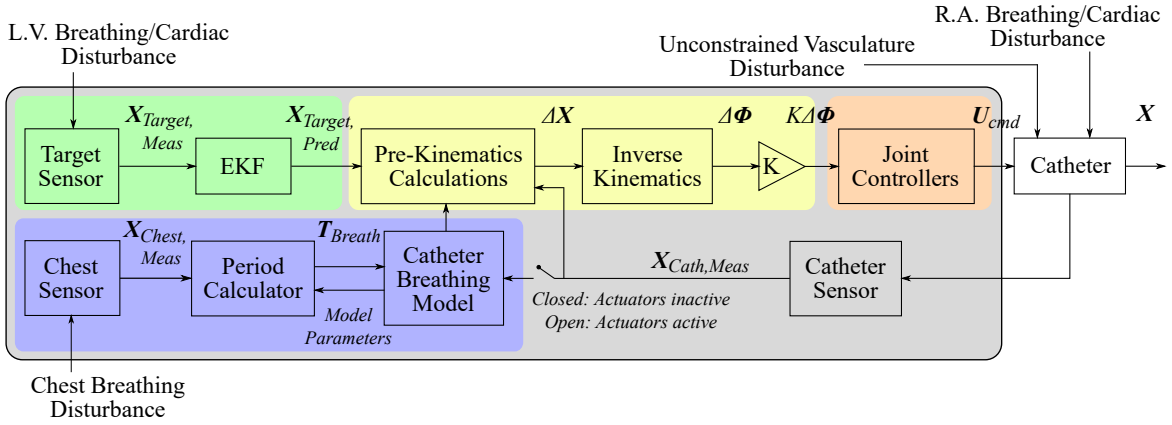

Figure 5.17: *Detailed motion compensation control diagram.*

affect the robot commands. Physiological motions in the RA disturb the catheter tip pose. The catheter tip sensor measurements are used to create a new set of pre-kinematics inputs and the controller iterates.

5.4 Experiments and Results

Experiments were designed to validate the motion compensation and predictive filtering methods described above. A motion simulator was designed to cyclically move the simulated vasculature and the imaging target at respiratory speeds. Bench top tests were conducted with the catheter in simulated vasculature (Fig. 4.10). A series of tests compared catheter navigation results while the target and/or simulated vasculature were either stationary or in cyclical motion. Then the system was validated in an *in vivo* animal model.

5.4.1 Bench Top Experimental Design

Respiratory Motion Simulator

A respiratory motion simulator (Fig. 5.18) was built for bench top motion compensation studies. The simulator was actuated by a DC motor rotating a sinusoidal cam to provide 1D cyclical motion. The sinusoidal trajectory was designed to have the same amplitude and frequency as typical porcine respiratory motion. The motor was located roughly 1 m

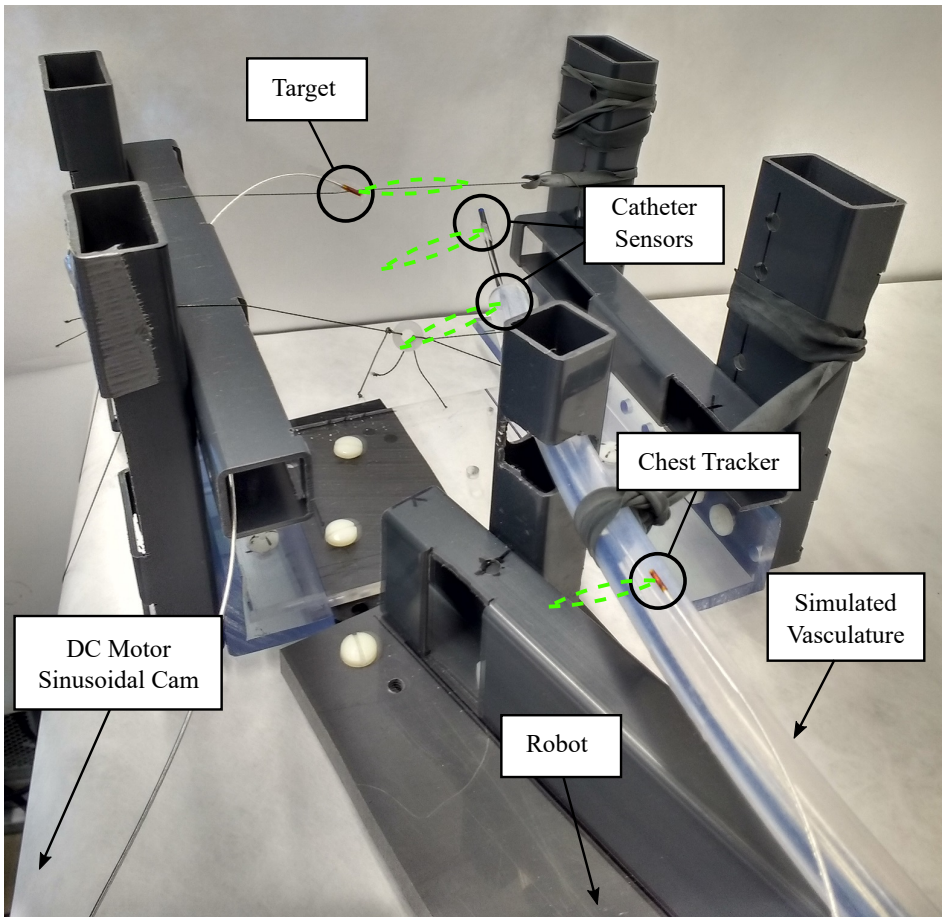

Figure 5.18: *Respiratory motion simulator.*

away from the EM emitter to ensure that it did not interfere with the EM field. Strings connected cam motion to a plastic frame which supported the target working instrument (*Instr*) and the plastic IVC tube. The frame was designed to enable adjustment of the motion amplitude such that the IVC and the *Instr* target could have different amplitudes, which is often the case *in vivo*. Although a simple sinusoid does not represent all of the detail of the cyclical respiratory motion, pre-recorded *in vivo* data was used to tune the robot motion compensation algorithms to ensure that the system would work *in vivo*. The sinusoidal simulator trajectory was sufficient for a proof of concept in bench top testing.

Introducer Seal

In previous studies the introducer seal caused numerous problems: (1) Friction between the introducer seal and the catheter body caused nonlinear effects on steering motion. Mechanical solutions were built into the robot to improve joint motion efficiency (Section 3.4.5). (2) During *in vivo* studies the EM tracker cables applied outward pressure opening the rubber seal, causing continuous blood leakage from the femoral vein. A saline drip was set up to apply gentle pressure against blood leakage. This replaced the blood leakage with a continuous saline leakage from the introducer seal.

Previous introduction methods were replaced with a new strategy. A brass tube (diameter 6 *mm*, length > 2 *cm*) was used to completely prop open the seal (Fig. 5.19), thereby eliminating the rubber-to-catheter friction from the introducer seal. Some friction from other sources still existed, but the negative effects of friction on steering motion were greatly reduced. The brass tube was fit into place by first sliding it over the catheter tip to rest at the proximal handle. After the US catheter was introduced to the RA, the tube was then forced into the seal. This process was borrowed from existing sheath and guidewire catheterization techniques. Silicone grease was packed into the tube around the US catheter body and EM sensor wires. This prevented blood from leaking through the introducer and eliminated the need for a saline drip. Silicone grease was also used in bench top experiments. This process was designed specifically for non-survival animal procedures in which an EM sensor must be attached to the exterior of the US catheter. This process can be changed or eliminated for an US catheter navigated by its internal EM sensors, which are currently not accessible to us for proprietary reasons.

5.4.2 Bench Top Experiments

The bench top testing setup is shown in Fig. 5.21. The robot was manually introduced through the rubber seal using the new introduction method and manually guided through the plastic IVC tube to reach the respiratory motion simulator. The *Instr* target in the form of an EM sensor was also connected to the motion simulator. The target was configured to

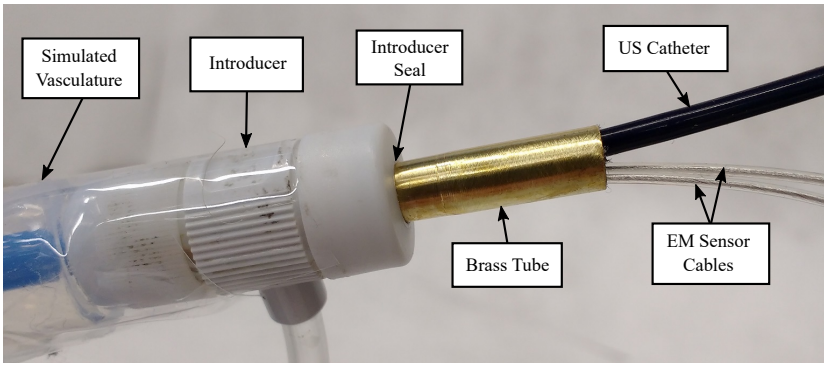

Figure 5.19: *Introducer seal stented open by a brass tube filled with silicone.)*

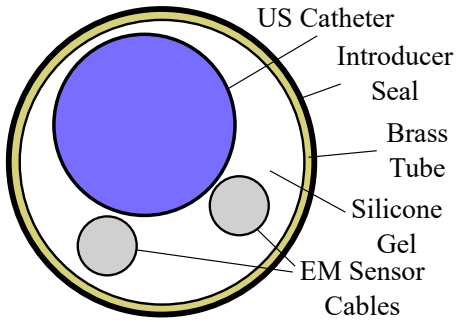

Figure 5.20: *Cross-sectional diagram of introducer seal.)*

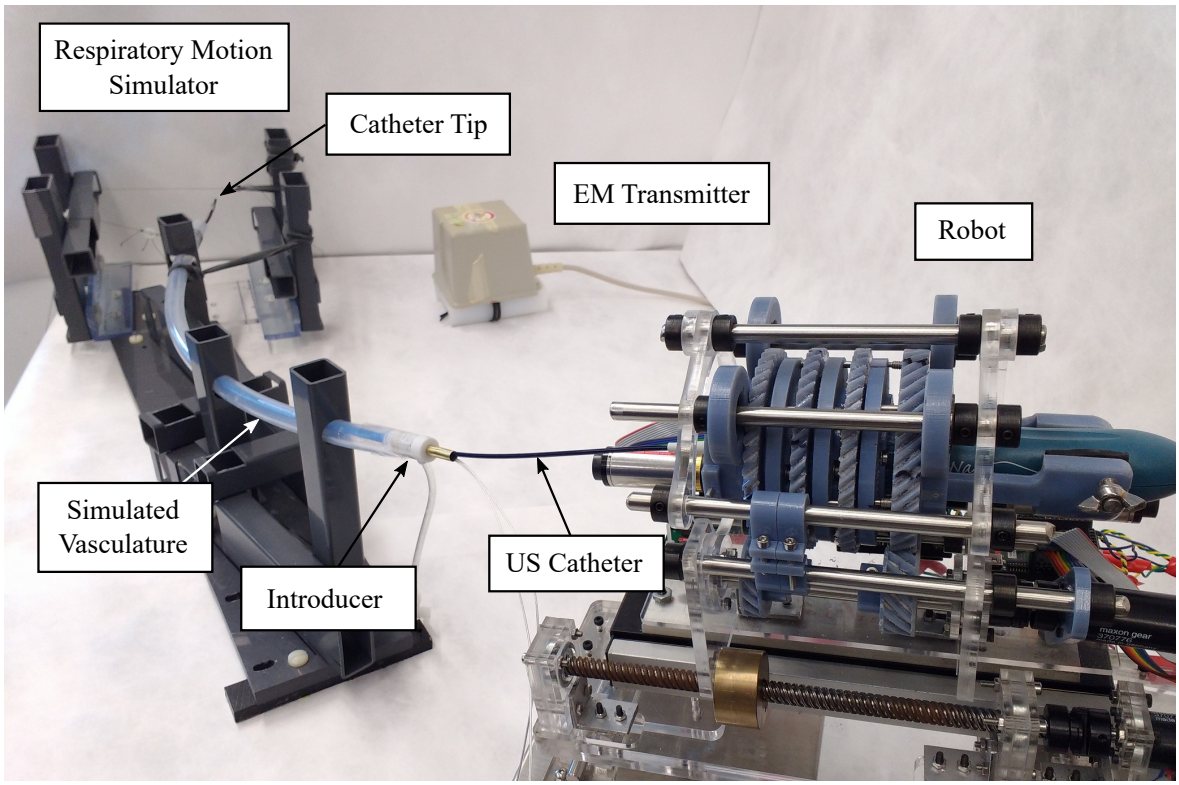

Figure 5.21: *Bench top experimental setup.*

cycle in a different direction and with a different amplitude from the IVC. Some tests were conducted while the IVC was stationary and catheter navigation was done in the world coordinate frame. In other tests the IVC was connected to the respiratory motion simulator and the robot was steered in the mobile coordinate frame.

Bench top experiments were designed to test the system's ability to position the catheter tip, rotate the US imager in specified increments, and rotate the US imager to point at a target (instrument tracking). Instrument tracking (IT) was done in Mode 2A/B (tip tracking, in which the position of the tip moved to follow the target), and Mode 3A/B (imager tracking, in which the position of the tip remained constant and the US imager was rotated to continuously point at the target). In some IT experiments the target was manually moved by a user. In other experiments the target was attached to the motion simulator and moved cyclically. In the cases with cyclical target motion we performed one set of tests with the controller reacting to target motion and then one set of tests with predictive filtering to

estimate the target location ahead of time. Some IT tests were done in a water tank. In these cases, the frame grabber was used to save images and verify that the US catheter was actually pointing at the target.

Navigation Time Tests

This section describes navigation time experiments and results to demonstrate sufficient navigation speed for respiratory motion compensation. Due to the nonlinear nature of the relationship between US imager tip space and catheter handle input joint space, it is not possible to deterministically predict navigation time. The region of cardiac anatomy, the region of the catheter workspace, the curve of the catheter through the vasculature, and many other potentially unobservable or uncontrollable factors affect the time to navigate from one pose to another. These results lend information about average time to navigate from one location to another. Actual pose navigation times vary. These results influence the design of our predictive filter.

The joint actuators used in Chapter 2 were replaced with more powerful 25 W DC motors. The controller bandwidth was increased by improving kinematic calculation and data storage efficiency. Proportional gains applied to the kinematic calculation outputs were tuned. These and other changes to the system architecture enable the system to steer the US imager quickly enough to compensate for breathing motion.

Time to Start Motion

All navigation time tests were done while the breathing motion simulator was off. Experiments measured the amount of time between initiating a position step input command and the first measurable catheter tip movement. The catheter tip was first navigated to a position in which the catheter was either straight or slightly bent. Step input commands of 5 mm in any direction were given to the robot. The controller immediately began calculating adjustments and outputting commands to the actuators. The first movement was defined as displacing 0.5 mm from the initial starting point. The time to begin motion was also measured for step input US imager angle changes of 2° in either the clockwise or

Table 5.1: *Time to start motion.*

Direction	Mean (*sec*)	Std.Dev. (*sec*)
X	0.38	0.08
Y	0.40	0.07
Z	0.35	0.05
ψ	0.52	0.10

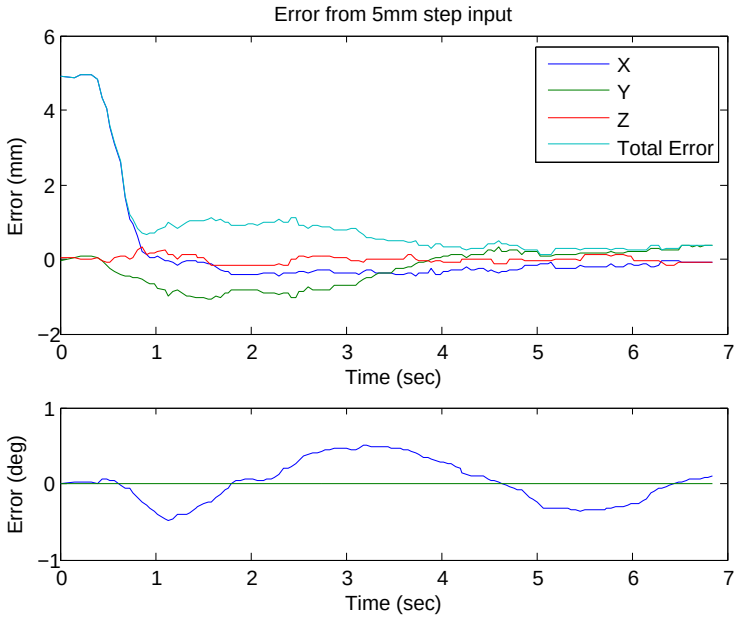

Figure 5.22: *Resulting catheter motion due to* 5 *mm step input.*

counter-clockwise directions. The test was done 90 times in total. The average time to begin movement for each direction is given in Table 5.1. Example data sets are shown in Figs. 5.22 and 5.23.

The time to start motion in the x- and y-directions was similar. Z-axis motion was faster because convergence in the z-axis is largely due to translation motion in the linear stage. Changes in ψ were slower because low torsional stiffness in the catheter body reduces handle roll efficiency. Most variation was dependent on whether or not the control knobs were engaged in the direction of motion before the initial command was given. Pull wire dead zones and backlash inside the catheter handle increased the amount of time required to initiate motion. Additional variations resulted from the catheter body configuration in

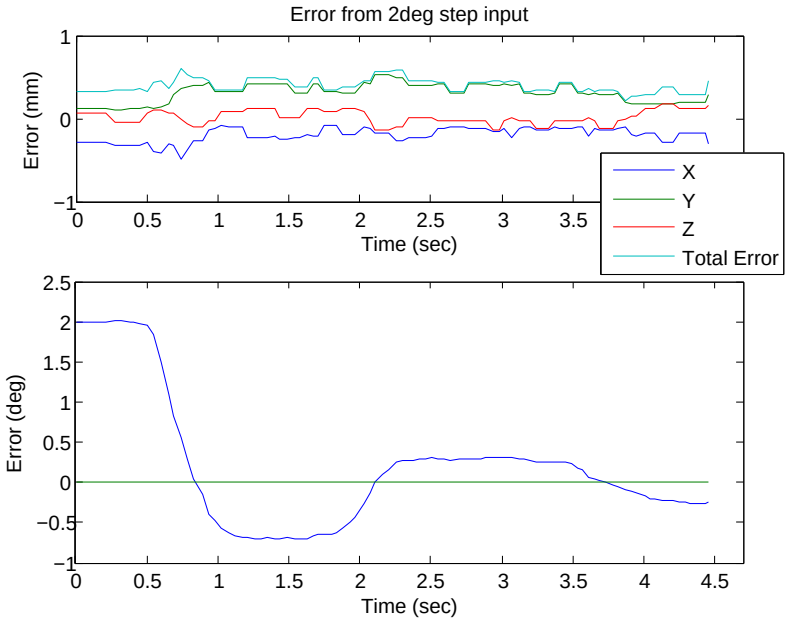

Figure 5.23: *Resulting catheter motion due to 2° step input.*

Table 5.2: *Time to settle.*

Direction	Mean (*sec*)	Std.Dev. (*sec*)
X	2.09	1.45
Y	1.52	1.05
Z	1.47	0.55
ψ	0.88	1.43

the vasculature and other unobservable effects.

Settling Time

These experiments measured the amount of time to navigate the US catheter to a commanded pose. The catheter tip was first navigated to a position in which the catheter was either straight or slightly bent. Time measurement began with a step input pose change given to the robot. The time to settle was measured as when the catheter reached within 1 *mm* (for position changes) or 1° (for imager angle changes). The test was done 90 times total and the results are summarized in Table 5.2.

As in the time to start motion results, the x- and y-directions have similar (and similarly variable) results. The z-direction motion is faster because it is largely dependent on the

Table 5.3: *Errors while maintaining a single pose.*

Direction	Mean (mm)	Std.Dev. (mm)	Mean (deg)	Std.Dev. (deg)
x	0.44	0.26	0.28	0.28
y	0.51	0.28	0.34	0.38
z	0.40	0.27	0.22	0.22
ψ	0.57	0.44	0.38	0.31
All data	0.49	0.34	0.31	0.31

linear stage motion. The time to settle ψ motion was sometimes subject to oscillation by more than 1° about the target pose. This was due to the low efficiency of handle roll, large hysteresis in direction changes, and the higher likelihood of overshoot. This resulted in a bimodal measure of settling times. In 7 out of 30 imager rotation trials the ψ step input resulted in oscillation before settling and the measured settling time was mean 3.11 *sec* ($\sigma = 1.53$ *sec*). In 23 out of 30 imager rotation trials the robot converged directly to the target pose with mean settling time 0.20 *sec* ($\sigma = 0.07$ *sec*). The overall results are reported in Table 5.2.

Without Respiration

Navigating to a Single Pose

The catheter was navigated to a region of the workspace and then the system was given a step input (5 *mm* in any direction or an imager rotation angle of 2°) as in the navigation time tests. Once reaching the target pose within 1 *mm* or 1°, the catheter was made to stay at that pose for several seconds. This test was done 90 times. The resulting errors are in Table 5.3. Example data sets are shown in Figs. 5.22 and 5.23.

Trajectory

We tested the ability of the system to navigate the catheter tip along a prescribed trajectory in space while keeping the US imager pointed in a constant direction. The robot was given 160 seconds to complete each trajectory of 160 setpoints. The trajectories were navigated a total of 15 times resulting in mean absolute error 0.97 *mm* ($\sigma = 0.60$ *mm*) and 0.48° ($\sigma = 0.55°$). Square trajectories in three different planes are demonstrated in Fig. 5.24.

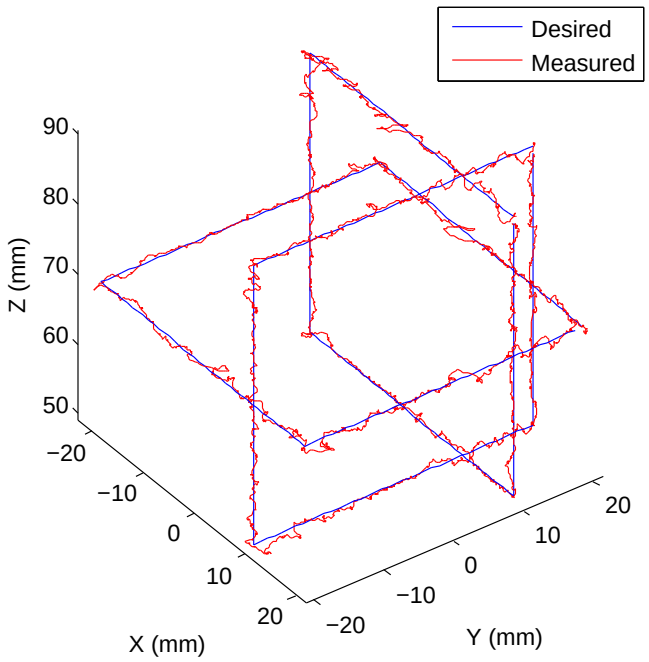

Figure 5.24: *Navigating square trajectories in various plane.*

The target and measured xyz coordinates of one square trajectory are shown in Fig. 5.25 while the resulting pose errors are shown in Fig. 5.26. Small repeated errors resulted from system nonlinearities including pull wire slack and direction changes.

The allowable time to complete the trajectory affects the accuracy. When the same square was navigated faster in 100 seconds the resulting error increased to 1.49 mm ($\sigma = 0.97$ mm) and 0.89° ($\sigma = 1.18°$). Navigating the square in 60 seconds resulted in mean absolute error 2.30 mm ($\sigma = 1.35$ mm) and 1.36° ($\sigma = 1.72°$). Example data sets are shown in Figs. 5.27 and 5.28.

This method of position control tests demonstrates the system's ability to reach a wide workspace with speeds that are sufficient to compensate for breathing motion. This claim is made by comparison with measured breathing motion in Section 5.3.2. Navigating large trajectories such as these is not directly applicable to *in vivo* studies, as the workspace within the heart is limited. This test is not repeated with the respiratory motion simulator or *in*

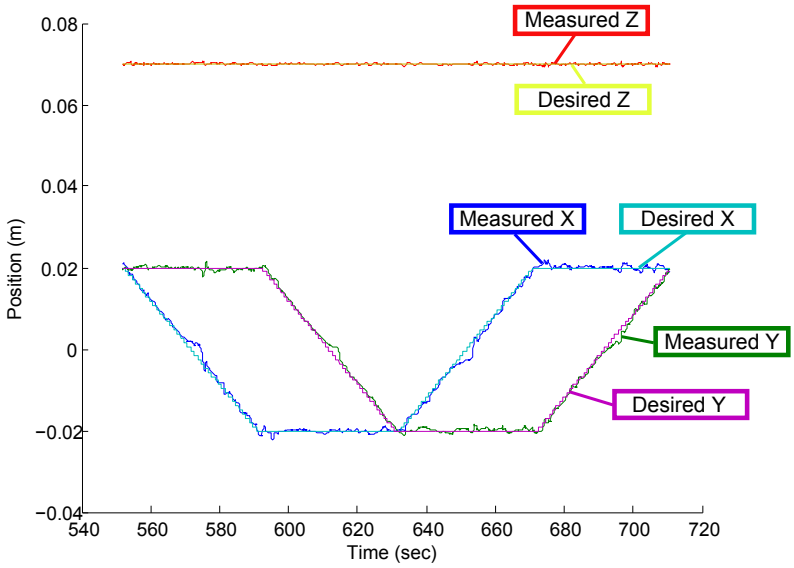

Figure 5.25: *Navigating a square trajectory in the XY-plane.*

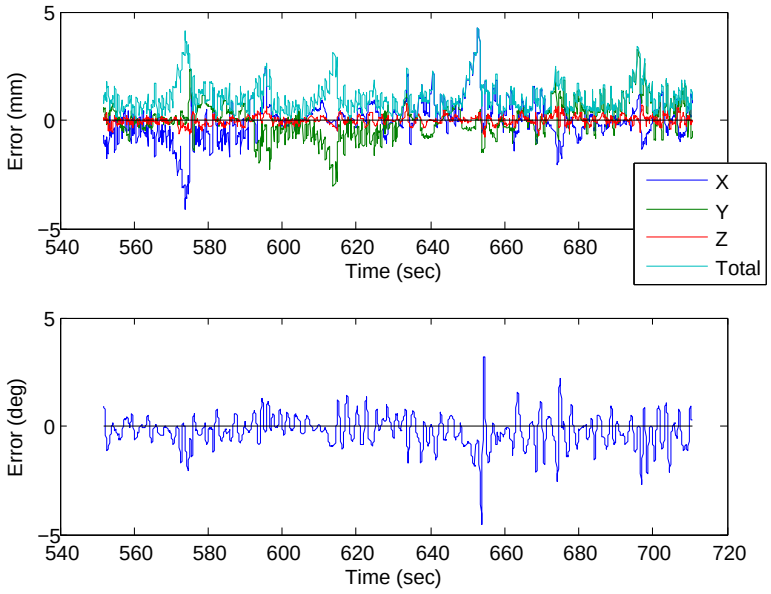

Figure 5.26: *Tip pose errors during square trajectory navigation.*

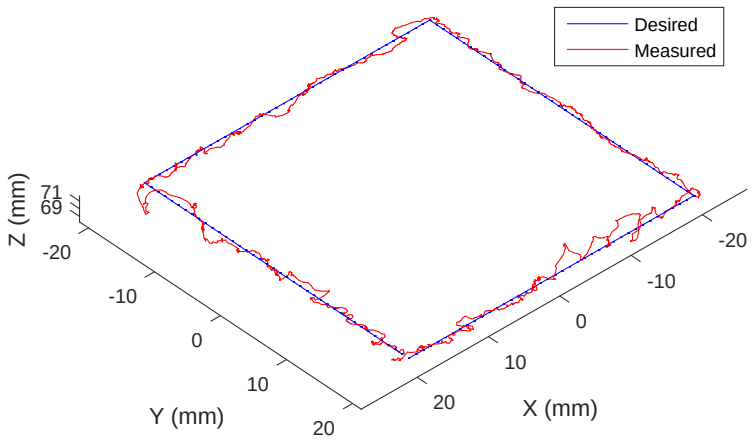

Figure 5.27: *Navigating a square trajectory in 100 seconds.*

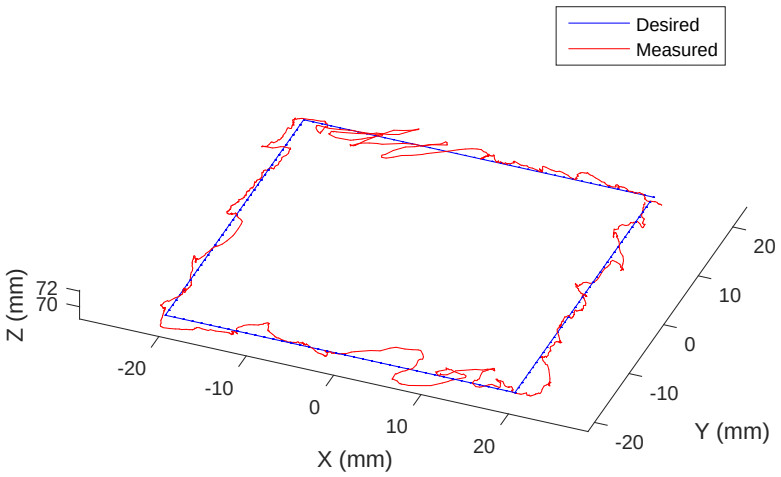

Figure 5.28: *Navigating a square trajectory in 60 seconds.*

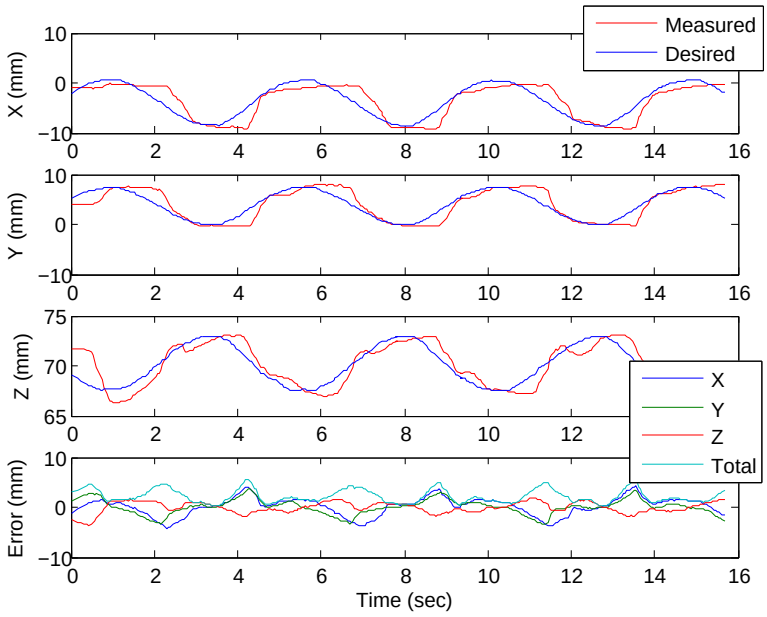

Figure 5.29: *Position tracking a cyclically moving target.*

vivo.

Instrument Tracking: Position, Cyclical

The catheter was navigated to a region of the workspace. The target was attached to the respiratory motion simulator with period 5 *sec* and amplitude 13 *mm*. IT Position mode and the respiratory motion simulator were switched on. The catheter was made to follow the target. An example data set is shown in Fig. 5.29. The desired locations in each axis are plotted in blue and the measured *CT* coordinates are plotted in red. Fig. 5.29 (*bottom*) shows the error in each axis as well as the total error.

The catheter tip continuously followed the target except for the moments when the target changed direction and the catheter lagged behind it. The position error peaked during each direction change of the target. The mean of the peak errors was 4.64 *mm* ($\sigma = 0.76$ *mm*). The average time delay before catching up to the target was 0.63 *sec* ($\sigma = 0.12$ *sec*). The mean absolute error across 268 seconds of tracking was 2.00 *mm* ($\sigma = 1.25$ *mm*). The catheter tip was within 1 *mm* of the target 22.16% of each cycle and within 2 *mm* of the target for 60.97% of each cycle.

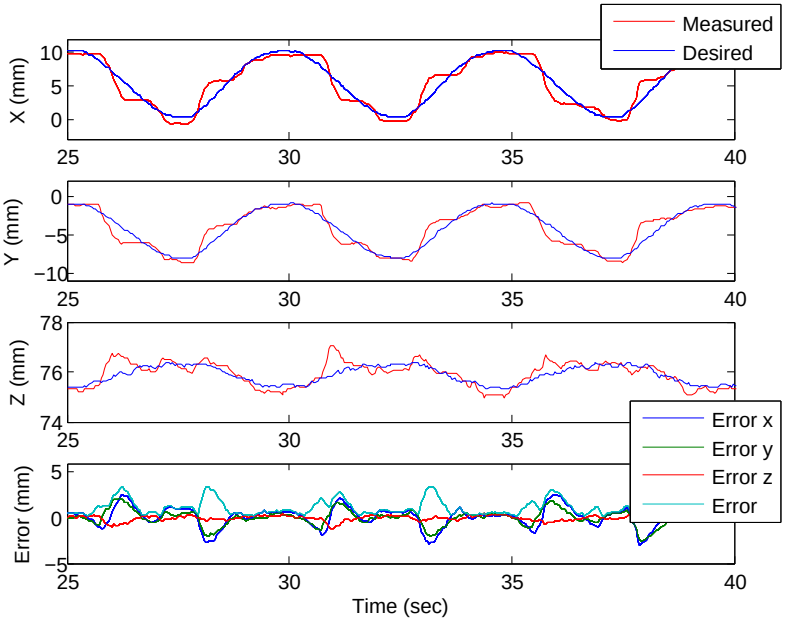

Figure 5.30: *Tracking a cyclically moving target with predictive filtering of the target position.*

Instrument Tracking: Position, Cyclical, w/EKF

The catheter was navigated to a region of the workspace. The target was attached to the respiratory motion simulator with period 5 s and amplitude 12.42 mm. The simulator was switched on. The EKF was initialized with 12 sec of target motion. IT Position mode was then switched on and the catheter began following the target. Thirteen individual tests were conducted for a combined total 742 seconds of tracking. An example data set is shown in Fig. 5.30. The desired locations in each axis are plotted in blue and the measured CT coordinates are plotted in red. Fig. 5.30 (*bottom*) shows the error in each axis as well as the total position error.

The catheter tip continuously followed the predicted location of the target. The catheter lag behind the target was reduced by the predictive filter. The mean of the peak errors was reduced to 3.68 mm ($\sigma = 0.94$ mm). The average time delay before catching up to the target was reduced to 0.29 sec ($\sigma = 0.25$ sec). The mean absolute error across 742 seconds of tracking was reduced to 1.59 mm ($\sigma = 1.10$ mm). The catheter tip was within 1 mm of the target 31.80% of each cycle and within 2 mm of the target for 75.24% of each cycle. See

Table 5.4: *Instrument tracking position results.*

Metric	Without EKF: Mean (σ)	With EKF: Mean (σ)
Position error (*mm*)	2.00 (1.25)	1.59 (1.10)
Peak error (*mm*)	4.64 (0.76)	3.68 (0.94)
Time delay (*sec*)	0.63 (0.12)	0.29 (0.25)
Time within 1 mm (%)	22.16	31.80
Time within 2 mm (%)	60.97	75.24

Table 5.4 for a summary of the results. All of these metrics of instrument tracking quality demonstrate improvement compared to tracking without predictive filtering.

Instrument Tracking: Imager, Cyclical

The target was attached to the respiratory motion simulator with period 5 *sec* and amplitude 16.7 *mm*. The catheter was navigated to a region of the workspace and rotated to point the US imager roughly towards the target. The simulator was switched on and the target began cycling back and forth. The angle between the imager and the target ranged from 0° to 3° during the cycle. In other target configurations the range was 5° or 8°. IT Imager mode was then switched on to begin tracking. The system continuously rotated the US imager to align with the target while the tip of the catheter was made to stay at the same position. Twenty individual tests were done for a combined total 510 seconds. An example data set is shown in Fig. 5.31. Fig. 5.31 (*top*) shows the position error while maintaining the same position, Fig. 5.31 (*middle*) shows the error angle between the US imager and the target, and Fig. 5.31 (*bottom*) shows the x-position of the target throughout the cycle. The target position is shown to provide context regarding when the target changes direction and when the imager angle error reaches its peak values.

The catheter continuously pointed the US imager at the target except for the moments when the target changed direction and the catheter rotation lagged behind it. The imager angle error peaked after each direction change of the target. In 510 seconds of tracking the mean absolute angle error was 1.15° ($\sigma = 1.27°$). The position was maintained with mean absolute error 0.50 *mm* ($\sigma = 0.37$ *mm*). The mean absolute value peak error was 2.39° ($\sigma = 0.74°$). The mean time delay before rotating the imager to catch up to the target

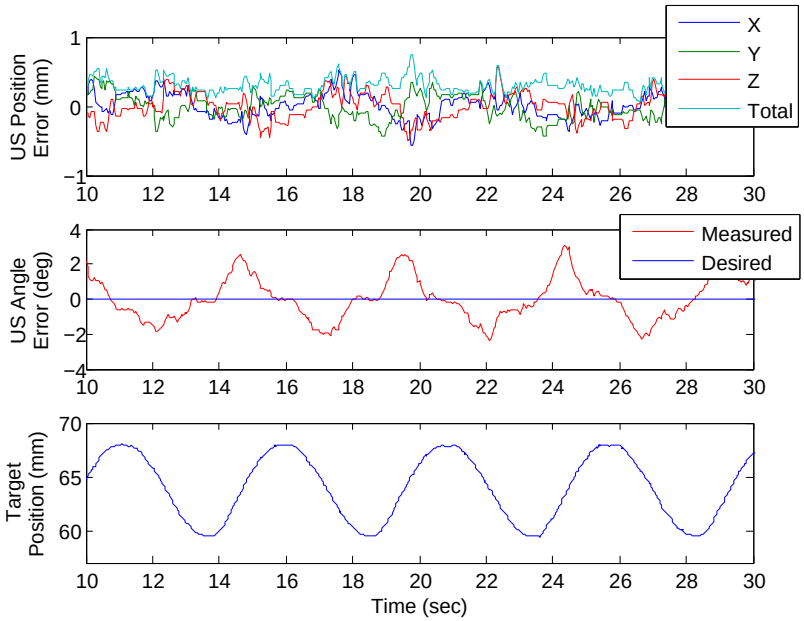

Figure 5.31: *Pointing the US imager at a cyclically moving target.*

was 0.68 *sec* ($\sigma = 0.40$ *sec*). The catheter tip was within 0.5° of the target 26.89% of each cycle, within 1° of the target 52.92% of each cycle, and within 2° of the target 85.65% of each cycle. The catheter tip was within 1 *mm* of its fixed position 90.09% of each cycle and within 2 *mm* for 99.56% of each cycle.

Instrument Tracking: Imager, Cyclical, w/EKF

The target was attached to the respiratory motion simulator with period 5 *sec* and amplitude 16.0 *mm*. The catheter was navigated to a region of the workspace and rotated to point the US imager roughly towards the target. The simulator was switched on and the EKF was initialized with 12 *sec* of target motion. The angle between the imager and the target ranged from 0° to 3° during the cycle. In other target configurations the range was 5° or 8°. IT Imager mode was then switched on to begin tracking. The system continuously rotated the US imager to align with the target while the tip of the catheter was made to stay at the same position. Twenty individual tests were done for a combined total 631 seconds. An example data set is shown in Fig. 5.32. Fig. 5.32 (*top*) shows the position error while maintaining the same position, Fig. 5.32 (*middle*) shows the error angle between the US

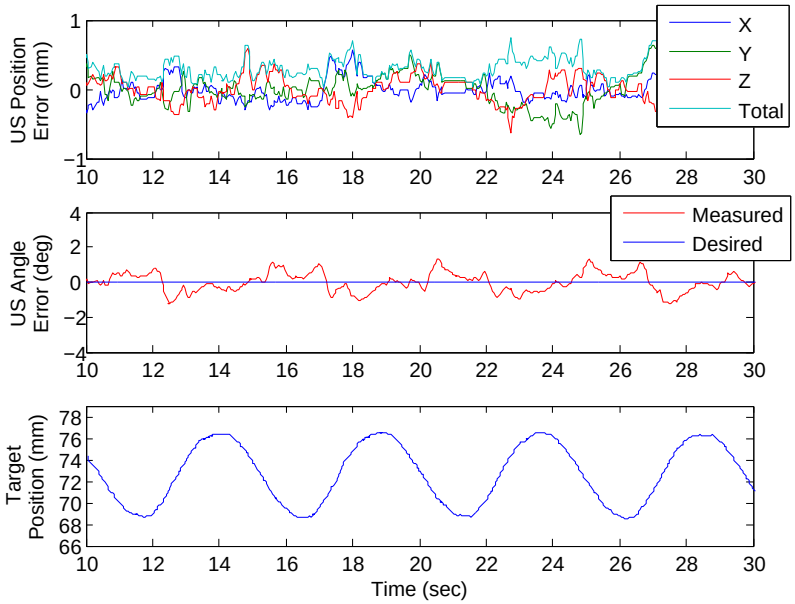

Figure 5.32: *Pointing the US imager at a cyclically moving target with predictive filtering.*

imager and the target, and Fig. 5.32 (*bottom*) shows the x-position of the target throughout the cycle. The target position is shown to provide context regarding when the target changes direction and when the imager angle error reaches its peak values.

The catheter continuously pointed the US imager at the target. The catheter rotation lag behind the target was reduced by the predictive filter. In 631 seconds of tracking the mean absolute angle error was reduced to 0.72° ($\sigma = 0.78°$). The position was maintained with mean absolute error 0.46 *mm* ($\sigma = 0.32$ *mm*). The imager angle error peaks were reduced to mean absolute error 2.01° ($\sigma = 1.04°$). The mean time delay before rotating the imager to catch up to the target was reduced to 0.34 *sec* ($\sigma = 0.24$ *sec*). The catheter tip was within 0.5° of the target 52.07% of each cycle, within 1° of the target 77.93% of each cycle, and within 2° of the target 92.86% of each cycle. The catheter tip was within 1 *mm* of its fixed position 91.34% of each cycle and within 2 *mm* for 99.91% of each cycle. See Table 5.5 for a summary of the results. All of these metrics of instrument tracking quality are better than or roughly equal to tracking without predictive filtering.

Table 5.5: *Instrument tracking imager results.*

Metric	Without EKF: Mean (σ)	With EKF: Mean (σ)
Position error (*mm*)	0.50 (0.37)	0.46 (0.32)
Angle error (°)	1.15 (1.27)	0.72 (0.78)
Peak error (°)	2.39 (0.74)	2.01 (1.04)
Time delay (*sec*)	0.68 (0.40)	0.34 (0.24)
Time within 0.5°	26.89	52.07
Time within 1°	52.92	77.93
Time within 2°	85.65	92.86
Time within 1 mm	90.09	91.34
Time within 2 mm	99.56	99.91

With Simulated Respiration

The following bench top tests were all done with the motion simulator connected to the plastic IVC. The motion simulator was always switched on. The simulator caused 12 *mm* amplitude displacement to the plastic IVC with a period of roughly 5 *sec*. The collection of each new data set required initialization of a new breathing model at each new location in space. The cycle frequency was continuously updated (by a sensor on the IVC) in order to increase the accuracy of the breathing models.

Navigating to a Single Pose

Accurate position steering with simulated respiration was demonstrated by commanding the robot to make relative position changes with respect to the breathing trajectory. The breathing model was initialized and then the robot was given relative step input commands of $0 - 2$ *mm* or 2° in various directions. This test was done 43 times for a total 1077 seconds of motion compensation. A new breathing model was initialized just before each test. The system navigated the catheter to the desired pose with respect to the moving coordinate frame while compensating for the motion applied to the plastic IVC.

Fig. 5.33 shows an example data set for a step input 2 *mm* in the x-direction. This shifts the catheter pose 2 *mm* relative to the original breathing motion, which is visible in the inset of Fig. 5.33. Within two seconds the catheter adjusts to the new desired trajectory. The catheter then continues to make slight adjustments to the pose throughout the breathing

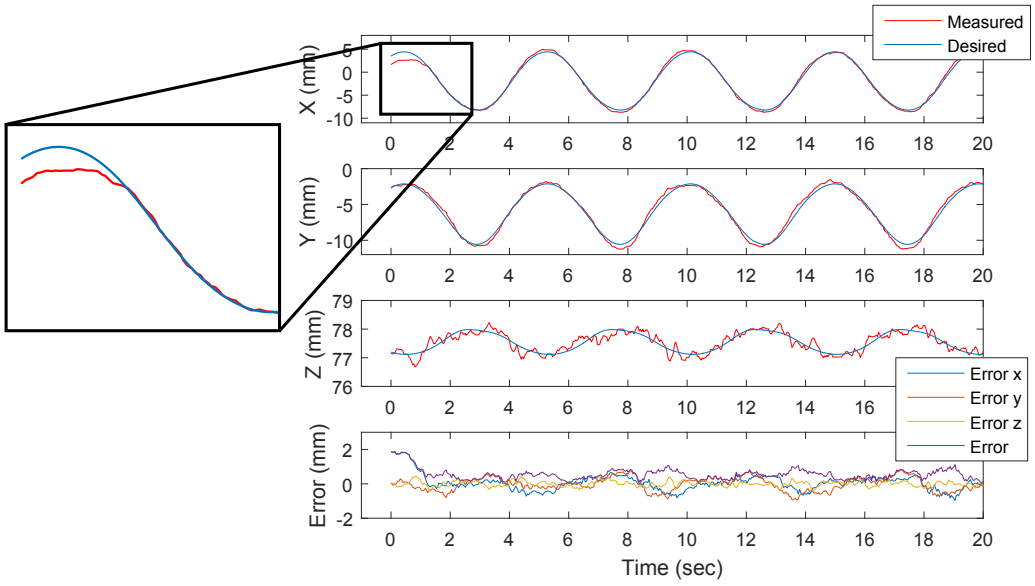

Figure 5.33: *Responding to a step input command while compensating for bench top respiratory motion.*

cycle in order to maintain the 2 *mm* offset from its original pose. The error in each axis is plotted in Fig. 5.33 (*bottom*). The mean absolute error across all trials was 0.77 *mm* ($\sigma = 0.51$ *mm*) and 0.35° ($\sigma = 0.36°$).

Instrument Tracking: Position, Cyclical

This type of navigation does not require a breathing model. The target was attached to the respiratory motion simulator with period 5 *sec* and amplitude 12 *mm*. In each breath the target and the catheter tip moved 5.4 *mm* away from each other. To begin each test, the catheter was teleoperated to be near the target. IT Position mode was switched on. The catheter tip continuously followed the target despite the cyclical disturbance to the IVC. Six tests were done with the target in its configuration. Then six additional tests were done with the target arranged in a different motion configuration moving in a different axis but with similar parameters. In total this test was done 12 times for 269 seconds of motion compensation. The mean absolute error across all 12 trials was 1.46 *mm* ($\sigma = 0.70$ *mm*). The mean peak error was 2.73 *mm* ($\sigma = 0.50$ *mm*). The catheter tip was within 1 *mm* of the target 28.33% of each cycle and within 2 *mm* of the target for 78.57% of each cycle.

Fig. 5.34 shows the desired target position and the measured catheter position for each

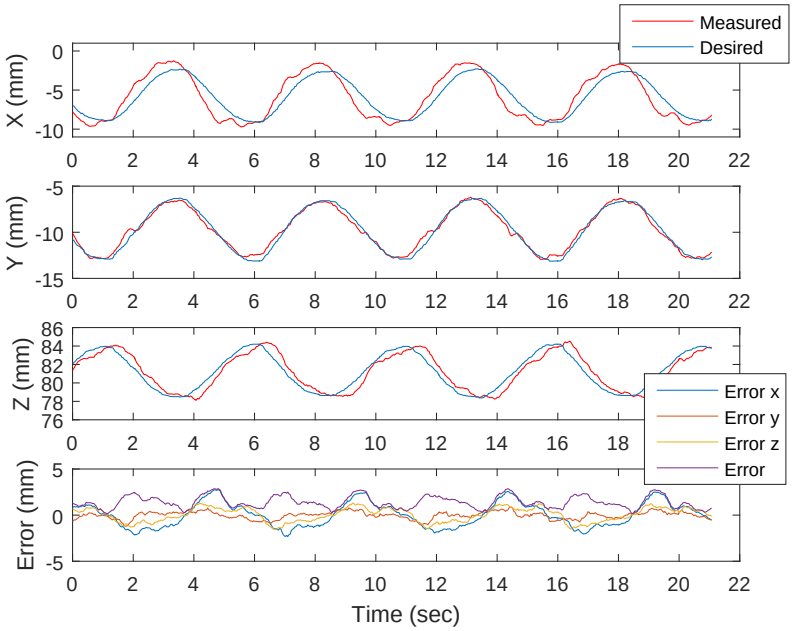

Figure 5.34: *Tracking the target position while rejecting disturbance from bench top respiratory motion.*

axis in an example data set. The error in each axis is plotted in Fig. 5.34 (*bottom*). Whereas previous instrument tracking tests showed the catheter lagging behind the target motion, in this case the catheter often leads target motion. This is due to the fact that the system takes time to calculate an adjustment, turn the motors, and bend the catheter tip. By the time a set of calculations affects the catheter tip (which was measured to be on the order of 0.40 *sec* in Section 5.4.2), the breathing motion has continued pushing the catheter body forward. The average time error was 0.15 *sec* ($\sigma = 0.11$ *sec*).

Instrument Tracking: Position, Cyclical, w/EKF

Tracking the position of a cyclically moving target with the help of predictive filtering required the use of breathing models using the process described in Section 5.3.5. The target was attached to the respiratory motion simulator in the same two configurations as in the above tests without predictive filtering. The simulator was switched on. The catheter was teleoperated to be near the target. The breathing models the EKF were both initialized. IT Position mode was then switched on. The catheter tip continuously followed the predicted location of the target.

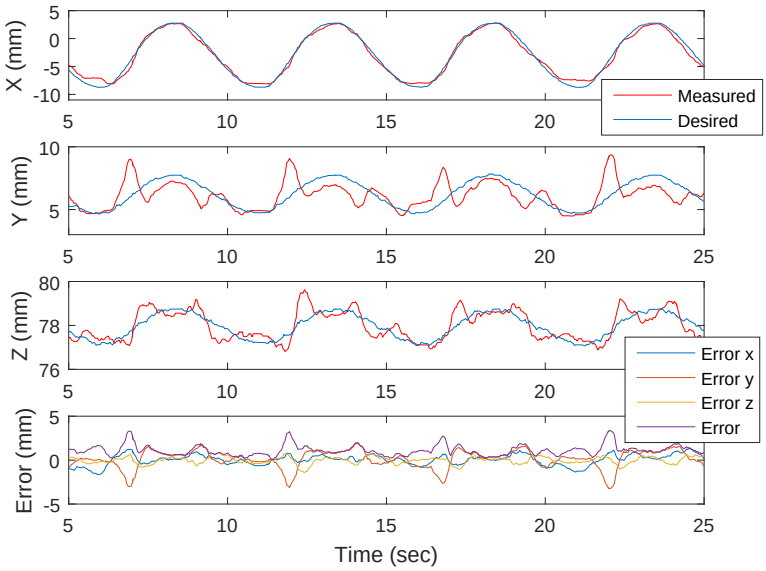

Figure 5.35: *Tracking the target position with predictive filtering while rejecting disturbance from bench top respiratory motion.*

Fig. 5.35 shows the desired target position and the measured catheter position for each axis in an example data set. The error in each axis is plotted in Fig. 5.35 (*bottom*). With the target motion in the same configuration, the catheter achieves more accurate position tracking when using the breathing models and the predictive filter. This test was done 13 times for a total 434 seconds of motion compensation. The mean absolute error was reduced to 1.11 mm ($\sigma = 0.61$ mm). The mean peak error was 2.65 mm ($\sigma = 0.45$ mm). The average time error was 0.09 sec ($\sigma = 0.12$ sec). The catheter tip was within 1 mm of the target 49.87% of each cycle and within 2 mm of the target for 90.75% of each cycle. All of these metrics of instrument tracking quality are better than or roughly equal to tracking without predictive filtering (see Table 5.6). The only parameter with inferior results was the y-axis accuracy, which frequently suffered from lack of motion in the control knob dead zone.

Instrument Tracking: Imager, Cyclical

The target was attached to the respiratory motion simulator with period 5 sec and amplitude 15 mm. The amplitude of IVC motion was 13 mm. The catheter was navigated to a region of the workspace and rotated to point the US imager roughly towards the target.

Table 5.6: *Instrument tracking position results with bench top respiration.*

Metric	Without EKF: Mean (σ)	With EKF: Mean (σ)
Position error (*mm*)	1.46 (0.70)	1.11 (0.61)
Peak error (*mm*)	2.73 (0.50)	2.65 (0.45)
Time delay (*sec*)	0.15 (0.11)	0.09 (0.12)
Time within 1 mm (%)	28.33	49.87
Time within 2 mm (%)	78.57	90.75

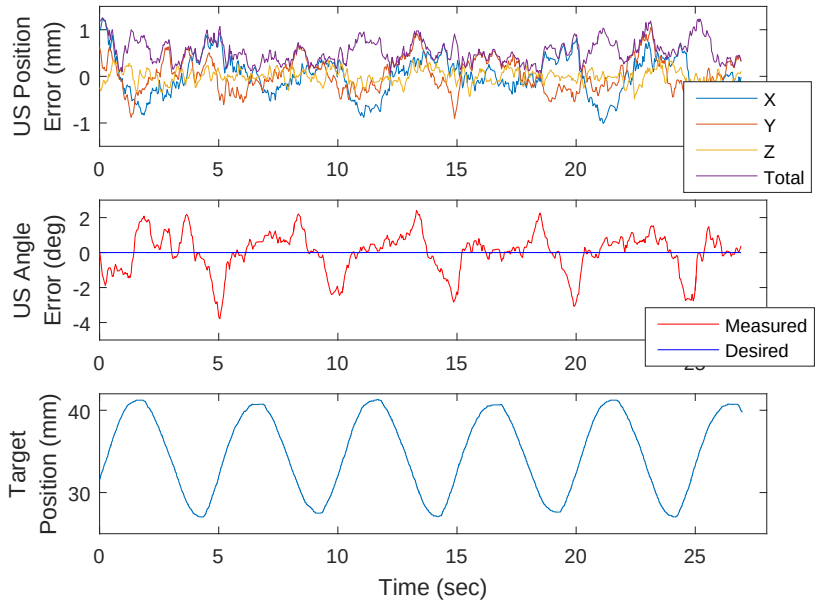

Figure 5.36: *Pointing the US imager at a cyclically moving target during bench top respiration.*

The simulator was switched on and the target and IVC began cycling back and forth. The angle between the imager and the target ranged from 0° to 5.6° during the cycle. Breathing models were initialized and then IT Imager mode was switched on to begin tracking. The system maintained the same position of the catheter tip with respect to the breathing motion and continuously rotated the US imager to align with the target.

This test was repeated 10 times for a combined total 269 seconds. An example data set is shown in Fig. 5.36. Fig. 5.36 (*top*) shows the position error while maintaining the same position, Fig. 5.36 (*middle*) shows the error angle between the US imager and the target, and Fig. 5.36 (*bottom*) shows the x-position of the target throughout the cycle. The target position

is shown to provide context regarding when the target changes direction and when the imager angle error reaches its peak values. The catheter continuously pointed the US imager at the target during the direction changes but lagged behind it when the target was moving larger distances. In 269 seconds of tracking the mean absolute angle error was 1.00° ($\sigma =$ 0.82°). The position was maintained with mean absolute error 0.72 *mm* ($\sigma = 0.38$ *mm*). The mean absolute value peak error was 2.20° ($\sigma = 0.78°$). The mean time delay before rotating the imager to catch up to the target was 0.43 *sec* ($\sigma = 0.30$ *sec*). The catheter tip was within 0.5° of the target 35.19% of each cycle, within 1° of the target 59.59% of each cycle, and within 2° of the target 86.27% of each cycle. The catheter tip was within 1 *mm* of its fixed position 80.02% of each cycle and within 2 *mm* for 99.61% of each cycle.

Instrument Tracking: Imager, Cyclical, w/EKF

The target was attached to the respiratory motion simulator in the same arrangement as the above case without predictive filtering. The catheter was navigated to a region of the workspace and rotated to point the US imager roughly towards the target. The simulator was switched on and the target and IVC began cycling back and forth. Breathing models were initialized, the EKF was initialized, and then IT Imager mode was switched on to begin tracking. The system maintained the same position of the catheter tip with respect to the breathing motion and continuously rotated the US imager to align with the predicted target location.

This test was repeated 7 times for a combined total 247 seconds. An example data set is shown in Fig. 5.37. Fig. 5.37 (*top*) shows the position error while maintaining the same position, Fig. 5.37 (*middle*) shows the error angle between the US imager and the target, and Fig. 5.37 (*bottom*) shows the x-position of the target throughout the cycle. The target position is shown to provide context regarding when the target changes direction and when the imager angle error reaches its peak values. In 247 seconds of tracking the mean absolute angle error was reduced to 0.77° ($\sigma = 0.61°$). The position was maintained with mean absolute error 0.67 *mm* ($\sigma = 0.38$ *mm*). The mean absolute value peak error was 1.72° ($\sigma = 0.61°$). The mean time delay before rotating the imager to catch up with the

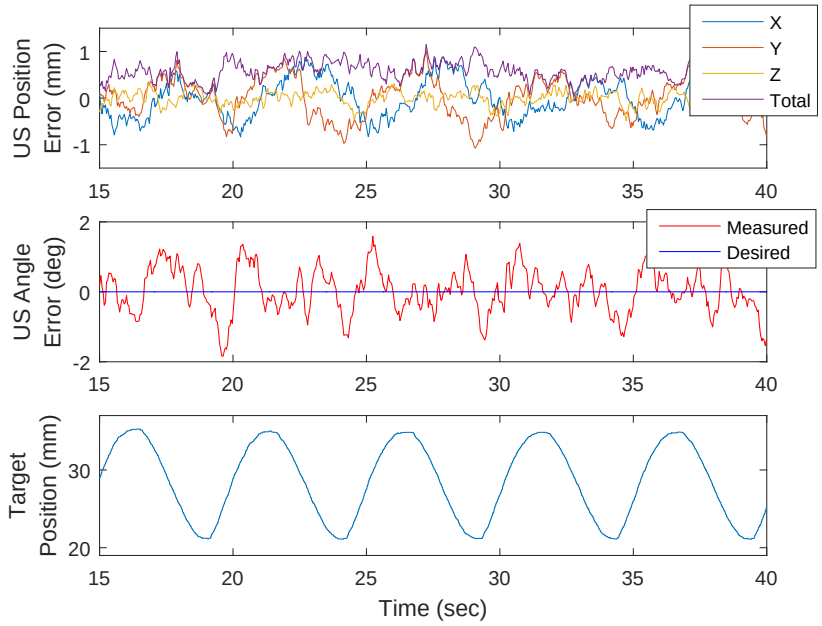

Figure 5.37: *Pointing the US imager at a cyclically moving target with predictive filtering during bench top respiration.*

target was reduced to 0.31 *sec* ($\sigma = 0.27$ *sec*). The catheter tip was within 0.5° of the target 40.58% of each cycle, within 1° of the target 71.11% of each cycle, and within 2° of the target 95.37% of each cycle. The catheter tip was within 1 *mm* of its fixed position 83.03% of each cycle and within 2 *mm* for 99.50% of each cycle. All of these metrics of instrument tracking quality are better than or roughly equal to tracking without predictive filtering.

5.4.3 In Vivo Experiments

In vivo animal testing was performed on a 64 kg live porcine model due to similarities between human and porcine cardiac anatomy. The *in vivo* protocol was approved by the Institutional Animal Care and Use Committee (IACUC). The animal received humane care in accordance with the *1996 Guide for the Care and Use of Laboratory Animals*, recommended by the US National Institutes of Health. The US catheter with two EM sensors was introduced through the stented-open 14 *Fr* introducer in the femoral vein to the right atrium (RA). A 6 *Fr* quadpolar catheter was outfitted with one EM sensor near the tip to serve as the

Table 5.7: *Instrument tracking imager results with bench top respiration.*

Metric	Without EKF: Mean (σ)	With EKF: Mean (σ)
Position error (*mm*)	0.72 (0.38)	0.67 (0.38)
Angle error (°)	1.00 (0.82)	0.77 (0.61)
Peak error (°)	2.20 (0.78)	1.72 (0.61)
Time delay (*sec*)	0.43 (0.30)	0.31 (0.27)
Time within 0.5°	35.19	40.58
Time within 1°	59.59	71.11
Time within 2°	86.27	95.37
Time within 1 mm	80.02	83.03
Time within 2 mm	99.61	99.50

imaging target. The target catheter was introduced through an 11 *Fr* introducer in the femoral artery to the left ventricle (LV). The subject's heart rate was paced at 120 *bpm*. The ventilator pumped 800 *cc* of air into the subject's lungs every 7.5 *sec*.

Navigating to a Single Pose In Vivo

The US catheter was made to stay in the same relative location inside the right atrium during breathing while pointing at anatomical structures. The breathing model was initialized and then the robot was given relative step input comments of 2° as the US imager was rotated throughout the chamber. Step input rotations were commanded a total of 18 times through a total of 133 seconds. The system navigated the catheter to the desired pose with respect to the moving coordinate frame while compensating for respiratory motion.

Fig. 5.38 shows an example data set containing 5 step input commands of 2°. The catheter remains in the same location (Fig. 5.38(*top*)) while adjusting the imager to point in the desired direction (Fig. 5.38(*bottom*)). The black dots represent moments in which the next step input command was given. The mean absolute error across 134 seconds of accurate motion compensation was 0.98° ($\sigma = 0.79°$) and 2.56 *mm* ($\sigma = 1.67$ *mm*). In other navigation tests the breathing model became outdated or the US catheter shifted to a new position for which the model was no longer representative of the breathing motion. In these instances the system remained stable but with lower accuracy. The mean absolute error across poorly-modeled trials was 6.59 *mm* ($\sigma = 4.52$ *mm*) and 2.27° ($\sigma = 2.25°$).

Instrument Tracking In Vivo: Imager, Manual

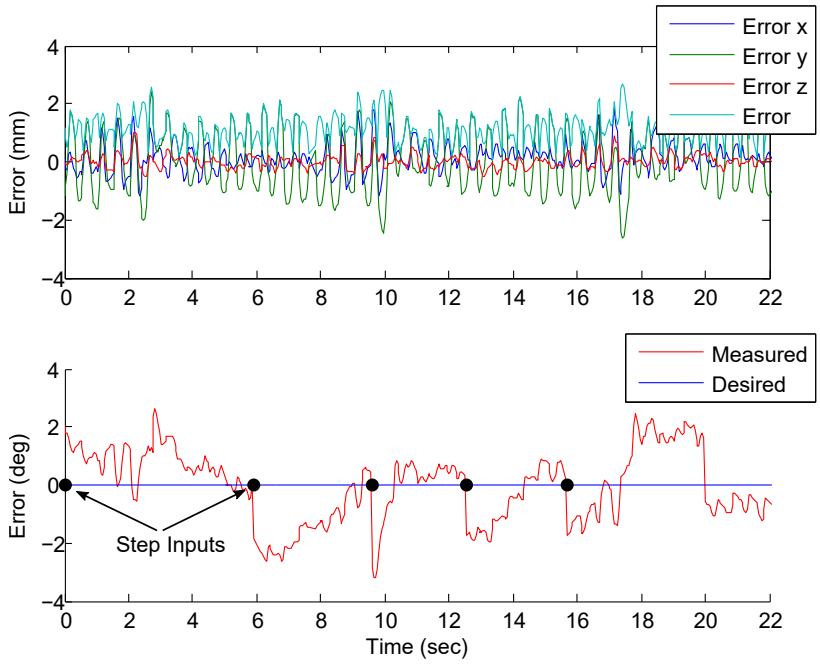

Figure 5.38: *Responding to step input commands while compensating for respiratory motion in vivo.*

The goal of this test was to demonstrate automatic US imager alignment with a target that was being manually steered. The breathing models were initialized and then the robot was activated to hold its position in the RA and point at the target. The target catheter was manually steered throughout the LV by the clinician. The clinician moved the target with varying displacements and velocities. Each time the target was moved out of view, the robot automatically reoriented the US imager to find the target tip and continue pointing at it.

This test was repeated multiple times for a combined total 431 seconds of tracking. An example data set is shown in Fig. 5.39. Fig. 5.39 (*top*) shows the position error while maintaining the same position with respect to the heart chamber, Fig. 5.39 (*middle*) shows the error angle between the US imager and the target, and Fig. 5.39 (*bottom*) shows the displacement of the target throughout the cycle. At $t = 0$ *sec* the US catheter was pointing at the target (Fig. 5.40(A)). Near $t = 12$ *sec* the clinician moved the target catheter by roughly 15 *mm*, causing the tip to go out of view (Fig. 5.40(B)). The system then successfully reoriented the US imager to continue pointing at the target catheter tip (Fig. 5.40(C)). In 431 seconds of tracking, including the moments when the clinician moved the target out

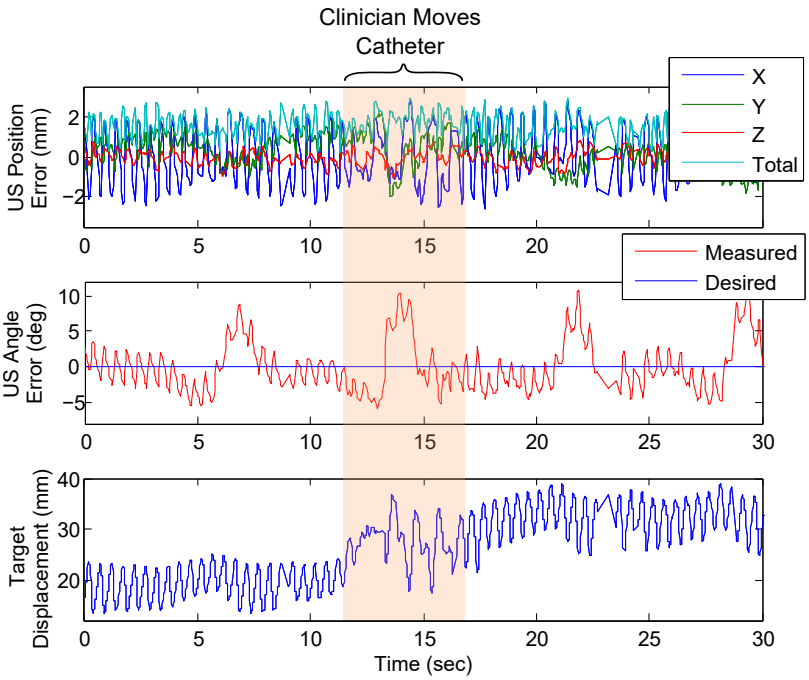

Figure 5.39: *Automatically pointing the US imager at a manually-steered target catheter in vivo.*

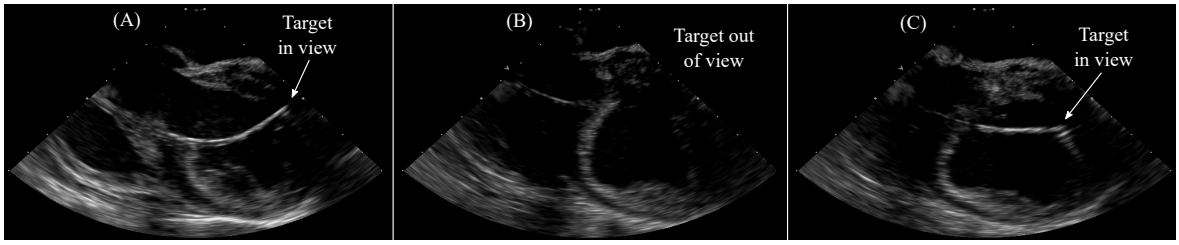

Figure 5.40: *(A) Robot points US imager at target. (B) Clinician moves target out of view. (C) Robot reorients US imager to continue pointing at target.*

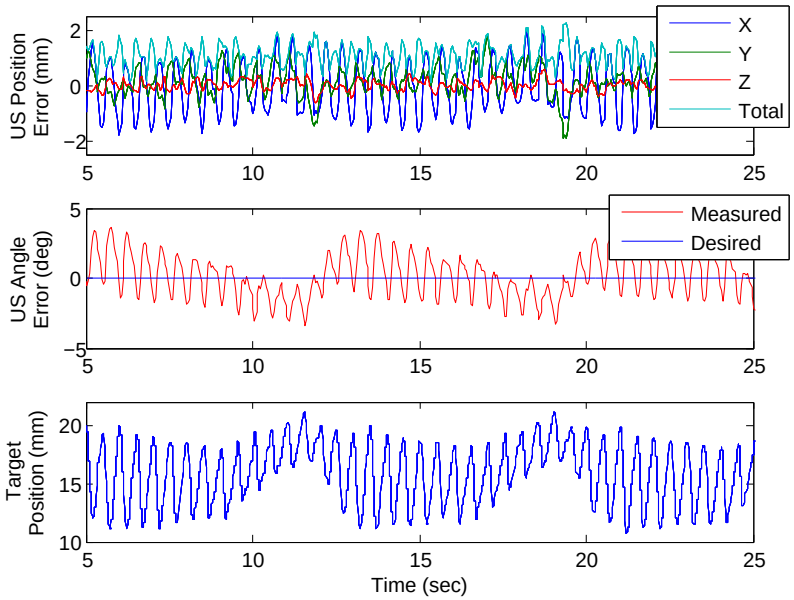

Figure 5.41: *Pointing the US imager at a target catheter in vivo.*

of view, the mean absolute angle error was 2.81° ($\sigma = 2.60°$). The US catheter maintained its position with mean absolute error 2.14 *mm* ($\sigma = 1.48$ *mm*). The catheter tip was within 1 *mm* of its desired position 16.65% of the time and within 2 *mm* for 57.33% of the time.

Instrument Tracking In Vivo: Imager, Cyclical

The target catheter tip was in the LV. At the US catheter tip the breathing motion amplitude was 7.3 *mm* and the cardiac motion amplitude was 2.8 *mm*. At the US catheter bending section base the breathing motion amplitude was 11.7 *mm* and the cardiac motion amplitude was 0.8 *mm*. At tip of the target catheter the breathing motion amplitude was 3.7 *mm* and the cardiac motion amplitude was 15.3 *mm*. These values highlight the drastic differences between respiratory and cardiac motion effects in different regions of the heart. The catheter was navigated to a region of the workspace and rotated to point the US imager roughly towards the target. Breathing models were initialized and then the robot was activated to begin tracking. The system maintained the same position of the catheter tip with respect to the breathing motion and continuously rotated the US imager to align with the target.

This test was repeated multiple times for a combined total 384 seconds of tracking. An example data set is shown in Fig. 5.41. Fig. 5.41 (*top*) shows the position error while maintaining the same position with respect to the heart chamber, Fig. 5.41 (*middle*) shows the error angle between the US imager and the target, and Fig. 5.41 (*bottom*) shows the x-position of the target throughout the cycle. The target position is shown to provide context regarding when the target changes direction and when the imager angle error reaches its peak values. In 384 seconds of tracking the mean absolute angle error was 1.48° ($\sigma = 0.94°$). The position was maintained with mean absolute error 1.10 mm ($\sigma = 0.52$ mm). The catheter tip was within 0.5° of the target 16.44% of each cycle, within 1° of the target 34.78% of each cycle, and within 2° of the target 73.26% of each cycle. The catheter tip was within 1 mm of its fixed position 44.09% of each cycle and within 2 mm for 95.34% of each cycle. Due to large cardiac motions it was not possible to accurately measure the time delays or peak errors when the system was compensating for breathing disturbances.

Instrument Tracking In Vivo: Imager, Cyclical, w/EKF

The US and target catheters were in the same arrangement as in the previous test. Breathing models were initialized, the EKF was initialized, and then the robot was activated to begin tracking. The system maintained the same position of the catheter tip with respect to the breathing motion and continuously rotated the US imager to align with the predicted target location.

This test was repeated multiple times for a combined total 329 seconds. An example data set is shown in Fig. 5.42. Fig. 5.42 (*top*) shows the position error while maintaining the same position with respect to the heart chamber, Fig. 5.42 (*middle*) shows the error angle between the US imager and the target, and Fig. 5.42 (*bottom*) shows the x-position of the target throughout the cycle. The target position is shown to provide context regarding when the target changes direction and when the imager angle error reaches its peak values. In 329 seconds of tracking the mean absolute angle error was reduced to 1.33° ($\sigma = 0.85°$). The position was maintained with mean absolute error 1.05 mm ($\sigma = 0.48$ mm). The catheter tip was within 0.5° of the target 18.40% of each cycle, within 1° of the target 38.55% of each

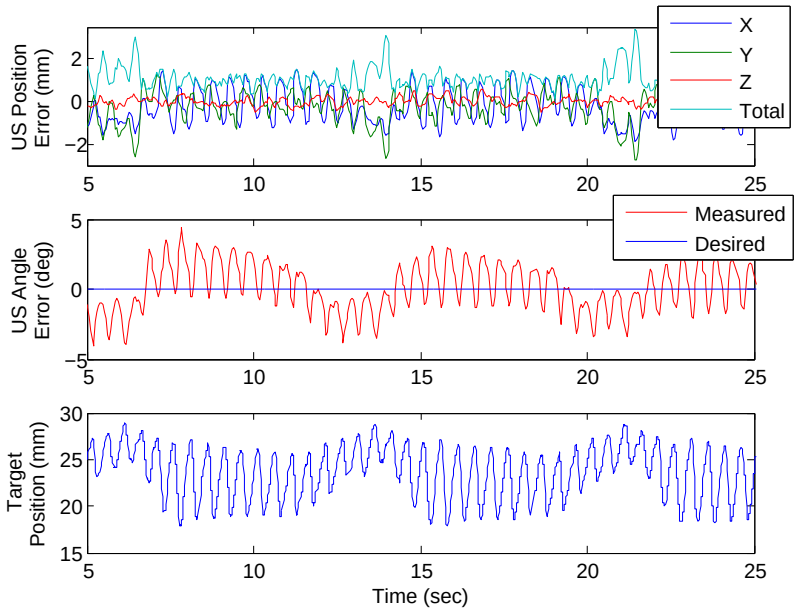

Figure 5.42: *Pointing the US imager at a target catheter with predictive filtering in vivo.*

cycle, and within 2° of the target 79.74% of each cycle. The catheter tip was within1 *mm* of its fixed position 48.87% of each cycle and within 2 *mm* for 96.34% of each cycle. All of these metrics of instrument tracking quality are slightly better than or roughly equal to tracking without predictive filtering. Table 5.8 compares the results.

Table 5.8: *In vivo instrument tracking imaging results.*

Metric	Without EKF: Mean (σ)	With EKF: Mean (σ)
Angle error (°)	1.48 (0.94)	1.33 (0.85)
Position error (*mm*)	1.10 (0.52)	1.05 (0.48)
Time within 0.5°	16.44	18.40
Time within 1°	34.78	38.55
Time within 2°	73.26	79.74
Time within 1 mm	44.09	48.87
Time within 2 mm	95.34	96.34

5.5 Discussion

In this work we have demonstrated that is it possible to automatically and accurately navigate a cardiac catheter to compensate for physiological motions. This was done by using two EM sensors on an US catheter for feedback, physiological motion modeling, and control. We chose to first measure physiological disturbance to the catheter which included breathing and cardiac motion coupled together. Low pass filtering the signal isolated respiratory motion, which was sufficiently slow for the US catheter to be steered without mechanical failure. We then examined several strategies for motion tracking and compensation and decided to fore-go external imaging sources (CT or MR) or catheter redesign in favor of using clinically accepted EM sensors. This decision was made to maximize clinical feasibility and acceptance. This also meant that the catheter lacked sufficient observers to resolve the differences between navigation and breathing measurement. As a result, during testing a breathing model had to be created before the robot could begin actuating the catheter control knobs. Repeatable respiratory motion was assumed. This sensing strategy also meant that it was not possible to directly measure the location of the cardiac tissue being imaged. The US catheter maintained the same pose with respect to the cardiac chamber it was in and used its own reference frame to feedback pose info. The strategies given above were sufficient for demonstrating successful catheter navigation and US imaging during breathing.

Large cardiac displacement on each heart beat reduced the system accuracy when compared with bench top motion simulator results. Despite the lower numbers reported, the target catheter was visible in the US images during robot actuated navigation. The system demonstrated the greatest clinical effectiveness when adjusting to point at the target immediately after the target was moved out of view. Future *in vivo* studies will investigate image-guided transseptal punctures using this technique. It may also be possible to continuously image tissue throughout an arrhythmia ablation procedure. Once focused on the target, it may be advantageous for the system to deactivate the motors until the target is relocated again.

In the beginning of each test, three breath cycles were used to create a breathing motion model for the US catheter's current position within the heart. The animal's respiratory motion was repeatable enough for the breathing model to remain accurate throughout navigation. In some cases the US catheter moved outside of the range of the model such that the breathing model was no longer accurate. In these instances the motors were deactivated and a new breathing model was created. Due to the length of time required to create a new breathing model, the system would benefit from strategies for accurately modeling respiration with the least amount of data recollection necessary. Creating an accurate model from one breath combined with prior information would save a significant amount of time. It may also be possible to model several different locations within the right atrium at the beginning of the procedure and then quickly assume breathing models by interpolation.

During US imaging tests with predictive filtering, the EKF was used to predict the location of the target catheter. The target catheter was not influenced by robot or clinician motion during those tests and therefore the target motion model could be updated continuously as new data was acquired. While this model represents different motion in a different region of the heart and therefore cannot be directly applied to the US catheter breathing models, it may be possible to apply changes in the target breathing model towards US catheter breathing models while the robot is actuating the control knobs.

The strategies for motion compensation described above were applied to respiratory motion, but they are suitable for cardiac motion as well. Mechanical improvements are necessary in order to demonstrate accurate and continuous cardiac motion compensation. Robotically compensating for cardiac motion would require the use of a catheter made of materials that can survive thousands of bending cycles. US catheters were designed for one hundred bending cycles, and therefore are not suitable. The system would also need to accurately compensate for control knob dead zones in which the pull wires are slack. Dead zone compensation for cyclical motion compensation is not examined in this work.

5.6 Conclusion

This is the first study known to the authors of automatically steering cardiac catheters with physiological motion compensation *in vivo*. By robotically actuating an off-the-shelf US catheter, we demonstrated that it is possible to automatically orient the US imager towards desired anatomical structures or working catheters. This was done by modeling and compensating for quasi-periodic physiological motions. These results have the potential to improve diagnoses and interventional treatments of cardiac diseases. The navigation strategies described above were applied to cardiac catheters but are also applicable to other flexible systems for medical or non-medical purposes. A broader application of this work may improve minimally invasive surgery with flexible manipulators.

Chapter 6

Active Stiffness Changing Catheter

6.1 Introduction

Earlier sections in this thesis (Chapters 2-5) have described methods for steering cardiac catheters. Navigating catheters (or other flexible manipulators) is useful for a range of procedures, but these techniques may fall short when a procedure necessitates both flexible navigation and the application of high force to tissue. Cardiac catheters are manufactured with a wide variety of diameters, materials, and stiffness properties for different medical applications. Different catheters might meet the needs of certain aspects of a procedure, but each catheter has a constant stiffness.

Stiffer catheters are useful for applying force to tissue, but increase the risk of injuring heart structures or perforating through the heart wall during navigation. Less-stiff catheters are safer during navigation, but unable to apply force to tissue. At present, cardiologists must switch catheters back and forth throughout a procedure in order to achieve both capabilities. Switching catheters requires time and effort, and it reduces the positioning accuracy which was achieved during navigation with the flexible catheter. This motivates a need for instruments which can actively change stiffness.

Methods for achieving variable stiffness manipulators of a larger diameter (endoscopes) have been proposed (Rex et al. (2005); Jiang et al. (2012); Zuo et al. (2011); Cheng et al. (2012)),

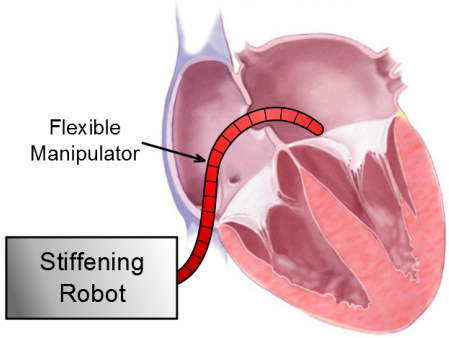

Figure 6.1: *Robotic system for automatically stiffening cardiac catheters.*

but these strategies do not succeed when scaled down to smaller diameters. Researchers have examined hybrid actuation methods and flexible manipulator stiffnesses (Stilli et al. (2014); Ataollahi et al. (2013)). A research prototype for an actively steering catheter uses the interactions between two friction-locking bead designs to assist in steering through restricted areas (Chen et al. (2010b)). Another research prototype uses wires and rotating links to affect the stiffness of the manipulator when acted upon by outside forces (Kim et al. (2014)). The patent literature also contains several examples of inventions towards variable stiffness flexible manipulators (Michelson (1996); Saadat et al. (2006); Fugoso and Tran (1996)). While many of these prototypes have demonstrated promising results, we are investigating the automation of a friction-based method which enables higher stiffnesses.

The device described in Michelson (1996) serves as the primary inspiration for our analytical contributions. This flexible surgical retractor contains cables through a central channel. Tightening the cable increases friction between vertebral segments, thereby increasing the stiffness of the instrument. It is our goal to build a catheter-sized version of this device such as in Fig. 6.1 in which it is possible to robotically tighten the cables and automatically adjust the stiffness to a desired amount.

This paper presents the design, implementation, and testing of a flexible manipulator capable of actively changing stiffness properties quickly and repeatedly. First, the system design requirements and adaptations towards steerable cardiac catheterization are described. Next, analytical models are derived for describing: (A) the design of the catheter for

achieving an appropriate workspace, (B) the stiffness properties of the catheter due to materials, (C) the amount of static friction between vertebrae as a function of cable tension, and (D) the amount of external force which causes slippage. The stiffening module is then integrated with a robotic actuation platform and experiments are conducted to test its stiffness. The work presented here has the potential to increase accuracy for minimally invasive procedures, improve clinical workflow, and reduce procedure times. The work presented in this chapter is an extension of preliminary studies conducted by Emiko Zumbro, Stephen F. Burke, and Alexandra R. Forelli while working under my supervision.

6.2 Methods

6.2.1 Design Approach

The robotic catheter system presented here must be able to navigate the catheter tip to a desired position and then withstand external force. The system must therefore shift between two modes: steering mode (low stiffness) and force application mode (high stiffness). In steering mode the catheter tip must have low stiffness to enable navigation. In force application mode the stiffness should reach a minimum of 500 N/m, so that a force of 1.5 N against cardiac tissue will deflect the catheter tip by less than 3 mm (Wagner et al. (2006)). The catheter tip position must remain stationary while switching between states. This is a safety precaution to prevent the obstruction of cardiac motion or damage to structures while switching modes.

Actively increasing the stiffness of a long, thin, flexible plastic tool poses a significant design challenge. Several methods inspired by prior art for stiffening thin flexible manipulators were explored: shape memory alloys, interlocking tooth mechanisms, granular jamming, and hydraulics (Rex et al. (2005); Jiang et al. (2012); Zuo et al. (2011); Cheng et al. (2012)). The chosen design strategy for varying catheter stiffness, based on Michelson (1996), used a series of plastic vertebrae with four channels for pull wires spaced 90° apart (Fig. 6.2). Channels were shaped conically to increase the pull wire range of motion. Tensioning all

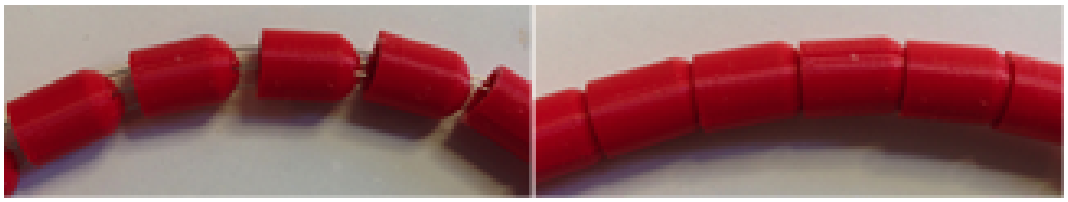

Figure 6.2: *(left) Vertebrae are connected in series by pull wires. (right) Pull wires are tensioned to lock vertebrae in place.*

pull wires causes the vertebrae to press against each other. Friction forces prevent sliding at interfaces between vertebrae, thereby increasing the overall stiffness of the catheter.

6.2.2 Initial Testing - Catheter

The first iteration of the active stiffness changing manipulator was built to prove that this technique is possible within the range of forces and stiffnesses required. Vertebrae were fabricated on a high-resolution 3D printer and connected with para-aramid synthetic fiber (Kevlar) pull wires for tensioning. Fifteen vertebrae were connected by pull wires ($0.3\ mm$ diameter) and installed into a test fixture (Fig. 6.3). The four pull wires were connected to a force gauge to measure the amount of total tension applied. A whiffle tree was used to ensure that each pull wire was tensioned equally. A force of $1\ N$ was applied to the catheter tip while the pull wires were tensioned incrementally from $0 - 90\ N$. The resulting vertical deflections were measured by post-processing images from a webcam. As the total tension on the wires increased, the deflection decreased towards $1\ mm$ (Fig. 6.4). A linear fit ($\Delta x = -0.0205T + 2.99$) represents the trend with $R^2 = 0.68$. Detailed analysis on the properties of the manipulator is discussed in the following sections. These results are the first proof of concept that it is possible to actively change the stiffness of a catheter using 3D printed materials in this force range.

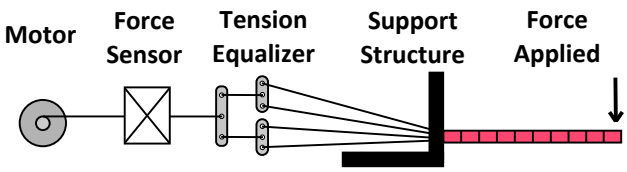

Figure 6.3: *Test fixture for initial testing of vertebrae prototype.*

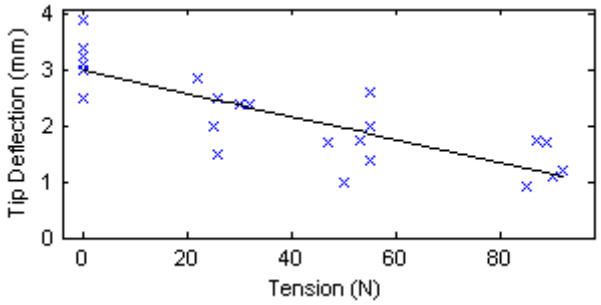

Figure 6.4: *Catheter tip deflection as a function of total tension applied to the pull wires. Black line represents a linear fit.*

6.3 Modeling

6.3.1 Workspace Calculations

Each vertebra features a tip radius that is slightly larger than the radius of the actual bead. This allows the vertebrae to slide and rotate within some allowable range. Fig. 6.5 (*left*) shows the mating geometry between two vertebrae. Each vertebra is capable of sliding by the maximum angle ϕ before colliding with the cylindrical side of the vertebra. The maximum angle is solved by

$$\phi = 2cos^{-1}\left(\frac{D}{2R}\right), \tag{6.1}$$

where D is the vertebra diameter and R is the tip radius. Fig. 6.5 (*right*) shows a black dot at the center of each tip circle. These dots are used to calculate the location of the vertebrae in terms of z (height) and x (distance from the initial centerline). For N vertebrae, the final

position of the most distal point on the catheter is given by

$$z_N = -Rsin\frac{\phi}{2} + L\left[\sum_{0}^{N-1} cos\left(N\phi\right)\right] + Rcos\left(\left(N-1\right)\phi\right), \tag{6.2}$$

$$x_N = L\left[\sum_{1}^{N-1} sin\left(N\phi\right)\right] + Rsin\left(\left(N-1\right)\phi\right). \tag{6.3}$$

This workspace model provides insight into the design of the catheter. A longer vertebral length is advantageous for a larger workspace at the cost of increasing the turning radius. The dimensions of the diameter of the vertebrae relative to the tip radius must be tuned to reach an adequate bending angle. Fig. 6.6 plots the maximum deflection as a function of D/R. The max diameter is limited to $D \leq 2R$. The geometric parameters used for the preliminary tests in this work are shown in Fig. 6.7.

6.3.2 Vertebral Contact Model

Lateral force applied to the tip of the catheter causes vertebrae to rotate with respect to each other. To understand this relationship, we analyze the contact between two vertebrae and develop appropriate models. Examination of stiffness data shows two types of motion during stiffening tests (Fig. 6.8): (A,C) elastic structural displacement and (B) sliding displacement. As forces are applied to the catheter tip a small amount of elastic displacement occurs in the mechanical structure of the system due to pull wire stretch, pull wires shifting inside channels, vertebral compression, plastic effects, defects in vertebrae, fasteners, etc. (schematic line A in Fig. 6.8). As higher forces are applied to the distal vertebra, a moment about the proximal vertebra overcomes the static Coulomb frictional moment between surfaces and causes the spherical surfaces on each vertebra to begin sliding (schematic line B in Fig. 6.8). The stiffness is significantly reduced during sliding, but the slope of the stiffness curve remains positive due to additional structural deformation. Removal of the tip force then causes the elastic deformations to relax (schematic line C in Fig. 6.8). These motions are shown in Fig. 6.9.

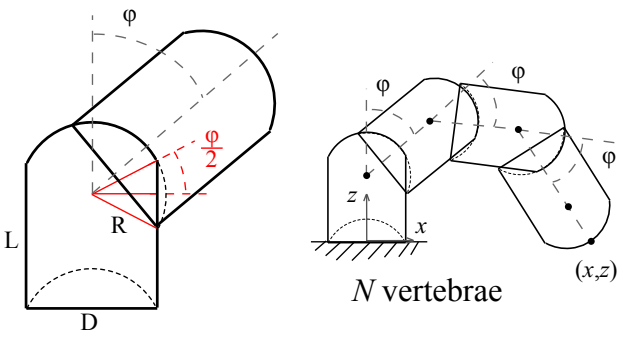

Figure 6.5: *Diagram of geometric parameters and maximum catheter workspace.*

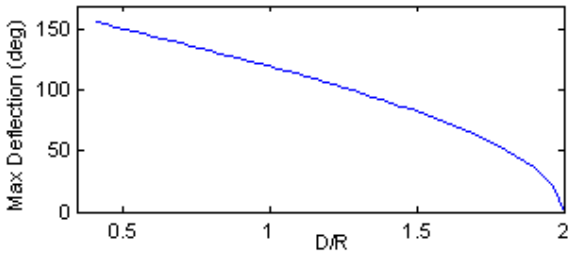

Figure 6.6: *Max vertebrae rotation allowable (deg) as a function of the ratio between vertebrae diameter and tip radius.*

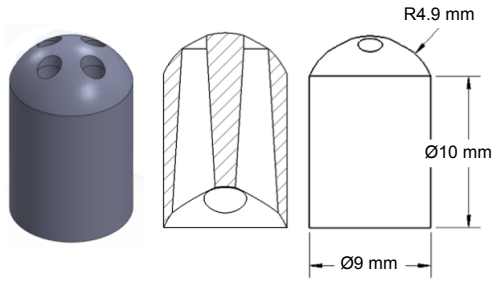

Figure 6.7: *Vertebrae bead design and cross sectional view with dimensions.*

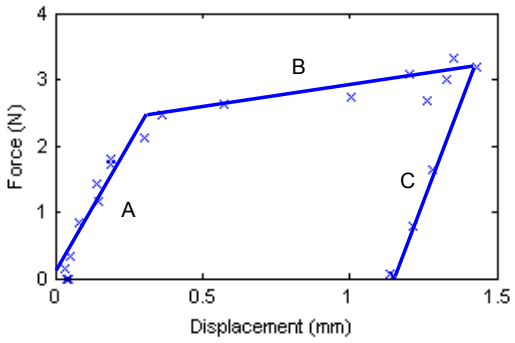

Figure 6.8: *Typical force vs. displacement during catheter tip contact. Schematic line A results from elastic structural deformation. Schematic line B results from sliding friction. Schematic line C results from relaxation of elastic deformation.*

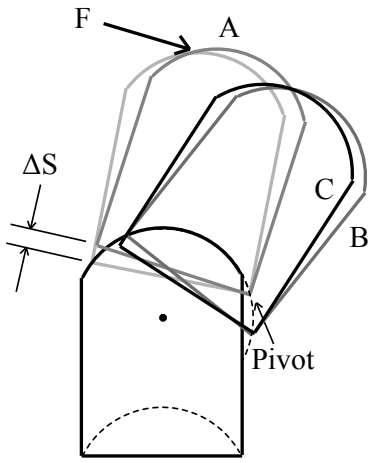

Figure 6.9: *(A) Elastic structural deformation. (B) Sliding friction. (C) Relaxation of elastic deformation.*

6.3.3 Elastic Structural Displacement

Catheter motion due to elastic structural displacement can be modeled through the principles of virtual work. For the simplest case of a catheter with two vertebrae, a lateral force F can be applied to the distal vertebra in order to create a small lateral displacement Δx. These quantities are related by stiffness K_{tip}. The resulting angular displacement, $\Delta\theta$, occurs as the vertebrae are made to pivot about the corner of contact (Fig. 6.10). The structural elements of the system comply elastically as the pull wire is slightly elongated, and the sum of these effects is modeled by a spring with stiffness k_{ES}. The work applied to the catheter tip, W_{app}, is calculated by multiplying the applied tip force, F, with the catheter tip displacement along the arc created by the pivot point. This is equated with the work done by the elastic structural spring with stiffness k_{ES} by

$$W_{app} = F\Delta x = \frac{1}{2}k_{ES}\Delta s^2 \tag{6.4}$$

where Δs is the elastic structural deformation of the system. By using small angle approximations it is possible to calculate K_{tip} as a function of L, R, and k_{ES} as in

$$\Delta x \approx (L+R)\,\Delta\theta, \Delta s \approx L\Delta\theta$$

$$K_{tip} = \frac{F}{\Delta x} = \frac{F}{(L+R)\,\Delta\theta} = \frac{k_{ES}L^2}{2(L+R)^2}. \tag{6.5}$$

The slope of the stiffness curve in elastic structural deformation, K_{tip}, is a constant which is dependent on vertebral geometry and k_{ES}.

6.3.4 Sliding Displacement

If the applied force increases to create a rotational moment about the vertebra which exceeds the threshold of the friction moment, then the vertebra will begin sliding. This threshold of maximum static friction can be estimated by forming a model to relate the vertebral parameters with the friction moment. Once sliding has occurred, sliding friction is not modeled analytically. Dynamic effects are neglected because the catheter is designed to remain stationary during stiffness changes. The convex spherical protrusion on the tip

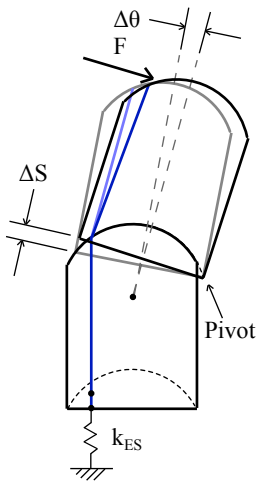

Figure 6.10: *Elastic structural deformation kinematics.*

of each vertebra mates with the concave spherical intrusion at the tail of the next distal vertebra. High tension forces from the pull wires compress these vertebral surfaces together and create static friction. This interaction can be approximated as a ball in socket problem, in which a Coulomb frictional moment resists rotation of the vertebrae. An estimate of the frictional moment will be calculated by assuming that the two spherical surfaces contact each other as a point force. A more accurate calculation of the friction moment could be obtained by using the techniques described in Faraz and Payandeh (2001) to represent the interaction as a surface with Hertzian contact. However, the point force assumption is sufficient in this case.

Fig. 6.11 shows a schematic of the two vertebrae with point forces applied and resulting forces. Fig. 6.12 shows the same forces applied to a convex spherical surface which is inverted from the concave vertebral interaction surface. A 3D force F applied to one vertebra. The force is applied at the location (l_x, l_y, l_z) with angle a rotation from the y-axis and angle b rotation from the x-axis. The spherical surface of the vertebra presses against the adjoining vertebra at the location (n_x, n_y, n_z). The adjoining vertebra is not shown in Fig. 6.12. The total tension in the pull wires, T, acts at the location of the point force. The normal force, N, points towards the center of the sphere. The directionality of N is known to be angle

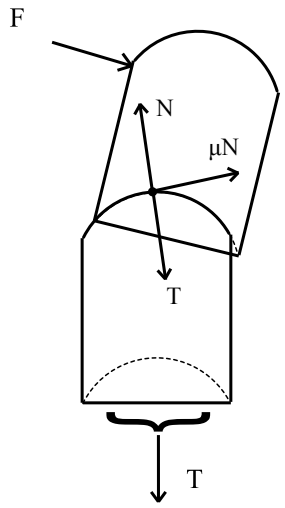

Figure 6.11: *Diagram of forces acting between two vertebrae just before sliding displacement.*

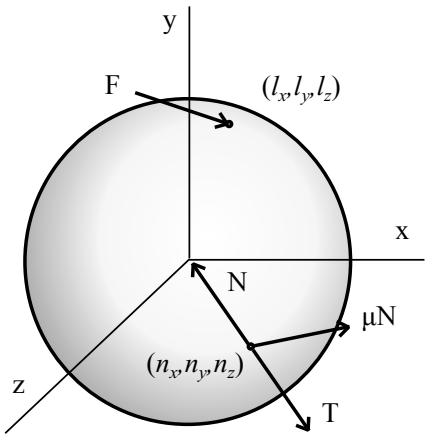

Figure 6.12: *Diagram of forces acting just before sliding displacement, inverted to convex spherical surface.*

c rotation from the y-axis and angle d rotation from the x-axis. The third force acting on the system is the friction force, μN, which occurs at the same location as N and has directionality angle e from the z-axis and angle f from the x-axis. The constant μ represents the static coefficient of friction for the vertebra material. The angles c and d are equal to θ and ϕ as in Faraz and Payandeh (2001), and these quantities are known by the sensor reporting the current location of the vertebrae. The location of N can be related to θ and ϕ by

$$c = \theta,\ d = \phi,\ n_x = R\sin\theta\cos\phi$$

$$n_y = -R\cos\theta,\ n_z = R\sin\theta\sin\phi.$$

Angles a, b, and force F are known quantities during experiments. The remaining unknown quantities are angles e, f, and normal force N, which must be solved in order to calculate the friction moment. The first step is to calculate the sum of the forces and moments in (6.6)-(6.9), where $s_a = \sin a$ and $c_a = \cos a$.

$$\sum F_x : Fs_ac_b - Ns_cc_d + \mu Ns_ec_f + Ts_cc_d = 0 \tag{6.6}$$

$$\sum F_y : -Fc_a + Nc_c + \mu Nc_e - Tc_c = 0 \tag{6.7}$$

$$\sum M_x : Fc_al_z + Fs_as_bl_y - Nc_cn_z + Ns_cs_dn_y + \mu Ns_es_fn_y$$
$$- \mu Nc_en_z + Tc_cn_z - Ts_cs_dn_y = 0 \tag{6.8}$$

$$\sum M_z : -Fc_bs_al_y - Fc_al_x - Ns_cc_dn_y + Nc_cn_x + \mu Nc_en_x$$
$$+ \mu Ns_ec_fn_y + Ts_cc_dn_y - Tc_cn_x = 0 \tag{6.9}$$

The sum equations are then combined in order to solve for e and f in terms of N, resulting in (6.10) and (6.11).

$$e = cos^{-1}\left[\frac{Tc_c + Fc_a - Nc_c}{\mu N}\right] \tag{6.10}$$

$$f = tan^{-1}\left[\frac{Fc_al_z + Fs_as_bl_y + Ns_cs_dn_y - Fc_an_z - Ts_cs_dn_y}{-Fc_bs_al_y - Fc_al_x - Ns_cc_dn_y + Fc_an_x + Ts_cc_dn_y}\right] \tag{6.11}$$

Next, (6.10)-(6.11) can be substituted into (6.6) to obtain (6.12), from which N can be solved.

$$Fc_b s_a - Nc_d s_c + Tc_d s_c + \frac{N\mu\sqrt{1-\left(\frac{Fc_a - Nc_c + Tc_c}{N\mu}\right)^2}}{\sqrt{\left(\frac{Fc_a l_z + Fs_a s_b l_y - FRc_a s_d s_c - NRc_c s_d s_c + RTc_c s_d s_c}{Fc_a l_x + Fc_b s_a l_y - FRc_a c_d s_c - NRc_d c_c s_c + RTc_d c_c s_c}\right)^2 + 1}} = 0 \tag{6.12}$$

The last step relates the friction moment, the threshold above which the vertebrae will slide, as

$$M_{friction} = R \times F_{friction} = R\mu N. \tag{6.13}$$

6.4 Experiments

6.4.1 Robot Measurement System

A robotic system was designed to manipulate the variable stiffness catheter (Fig. 6.13). In steering mode the catheter is navigated to desired positions automatically. The steering process has been demonstrated in prior work (Loschak et al. (2013b, 2014)) and earlier chapters and will not be examined here. Once the catheter tip has reached the desired position, all pull wires are tensioned to stiffen the catheter at its current location. When desired, the pull wires are relaxed and the catheter is navigated to a new position. The test system consists of the catheter (3D-printed vertebrae), actuators, tension sensors, connection electronics, and an optical tracking system. Four high-torque stepper motors (Changzhou Songyang Machinery & Electronics, China) steer the four pull wires. The motors are connected to an Arduino microcontroller via two motor shields (Adafruit, USA). S-type 100 kg load cell tension sensors (Phidgets, Canada) are integrated into the robotic system for measuring cable tensions. The entire system is interfaced through Matlab (MathWorks, USA). A closed-loop controller actuates the steppers to reach desired tensions in each of the four pull wires.

A short catheter consisting of two vertebrae (Fig. 6.14) was connected to the robot system in order to isolate the effects of pull wire tension on one friction surface between two vertebrae. The robotic cardiac catheter stiffening system was used to increase the tension

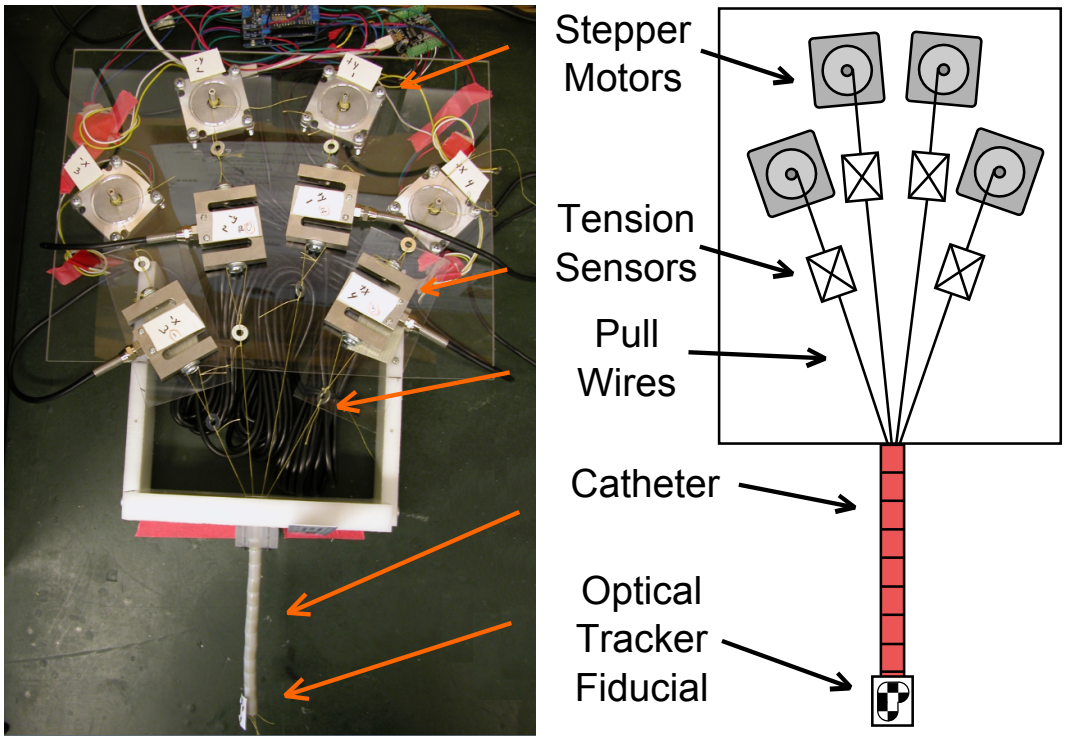

Figure 6.13: *(left) Photo and (right) diagram of catheter stiffening robot system (view from top).*

in the pull wires throughout a series of stiffness testing trials. A single axis load cell rated for $0 - 25$ *kg* (Futek, USA) was used to apply force to the tip of the catheter and measure the amount of force applied. Position measurements of the catheter tip were recorded by a high-resolution optical tracking system with resolution 0.25 *mm* RMS (Claron Technology Inc., Canada). Position measurements were recorded at roughly 30 *Hz*. A tracking fiducial measuring 1 by 2 *cm* was attached to the tip of the catheter. The force and displacement measurements were used to calculate the overall catheter stiffness.

6.4.2 Results - Elastic Structural

A set of data was collected by applying force to the tip of the catheter to create elastic deformation followed by sliding friction. All trials were conducted with the catheter in the straightened position. This section focuses on the stiffness properties of the elastic region in which static friction between vertebral surfaces prevents sliding, but structural deformations

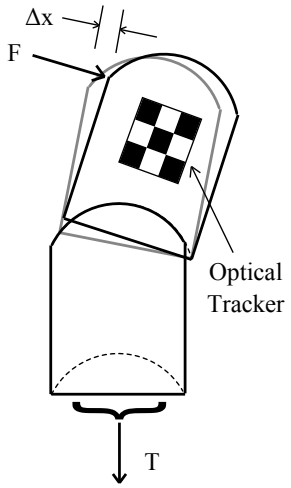

Figure 6.14: *(left) Photo and (right) diagram of catheter stiffening robot system (view from top).*

cause linearly elastic deformations to occur. The measurements of force and displacement were used to calculate the overall stiffness of this region by using (6.5) for a range of different pull wire tensions. The mean K_{tip} value was 9181.5 N/m ($\sigma = 3869.8$ N/m). The mean k_{ES} value was 2067.8 N/m ($\sigma = 871.5$ N/m).

The stiffness of the elastic structural deformation is related to compliance in the construction of the robot, the vertebrae, and elongation of the pull wires. A linear stress-strain relationship,

$$\sigma = \frac{T}{A} = E\varepsilon = \frac{E\Delta s}{L_1}, \tag{6.14}$$

is used to draw a comparison between the measured tip deflection and the measured pull wire tension forces, T, where σ is stress in the pull wires, A is pull wire cross sectional area, L_1 is pull wire length, and E is pull wire modulus of elasticity (Kevlar $E = 70 - 110$ GPa). All four pull wires are tensioned differently when a lateral force is applied to the catheter tip. The calculated forces on each pull wire are summed to result in T ranging from $0 - 40$ N. This is on the same order of magnitude as the measured pull wire tension forces, therefore demonstrating that elastic structural deformation largely results from uniaxial pull wire strains.

6.4.3 Results - Sliding Friction

This section focuses on sliding contact between spherical vertebral surfaces. The applied forces were used to calculate the applied moment on the distal vertebra. Force vs. displacement curves are shown for three pull wire tension forces in Fig. 6.15. Applied moments as a function of the total pull wire tension for 46 trials are shown as "X" marks in Fig. 6.16. As the pull wire tension force increases, the moment required to create sliding displacement trends upwards. This trend validates the model summarized in (6.13), represented by the line in Fig. 6.16, which was used to calculate the moment required to overcome static friction. The two-vertebrae catheter was then replaced with a full length catheter of ten vertebrae. The overall stiffness of the catheter before sliding is shown in Fig. 6.17. A linear fit (Stiffness $= 8.80T + 197.5$) represents the trend with $R^2 = 0.84$.

6.5 Conclusion

The work presented here is an initial prototype of a robotic system which actively changes the stiffness of a flexible manipulator to resist deformations due to external forces. A force applied to the tip of the manipulator causes elastic deformation and potentially sliding between vertebrae. Therefore, an analytical model was derived to calculate the stiffness of the manipulator as a function of vertebral geometry and pull wire tension. The stiffness in the initial elastic deformation region, K_{tip}, is a constant value related to the geometry of the vertebrae and the physical properties of the pull wires. The stiffness then decreases when the force applied to the tip of the catheter exceeds the static Coulomb friction between vertebral surfaces, thereby causing sliding to occur (Fig. 6.18). The spherical contact friction moment model relates the pull wire tension to the max force before sliding occurs (Fig. 6.19). The robotic system was constructed in order to measure the stiffness of the manipulator and validate the analytical model. The analytical model describing the interactions between two vertebrae was validated on a robot system with a catheter of two vertebrae. The analytical model must then be expanded to accurately predict stiffness properties for a long catheter

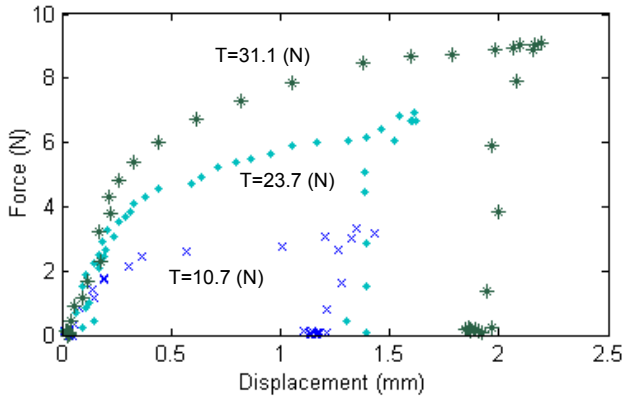

Figure 6.15: *Moment applied to catheter tip creates sliding displacement for three different pull wire tensions.*

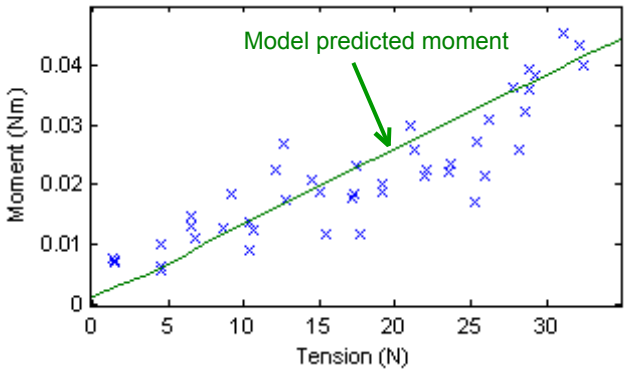

Figure 6.16: *Moment applied to catheter tip creates sliding displacement as a function of the total pull wire tension. Line represents the model estimated moment to cause sliding.*

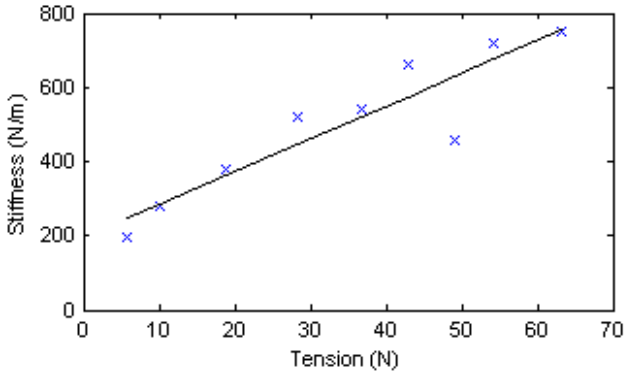

Figure 6.17: *Overall catheter stiffness before sliding as a function of the total pull wire tension (10 vertebrae). Black line represents linear fit.*

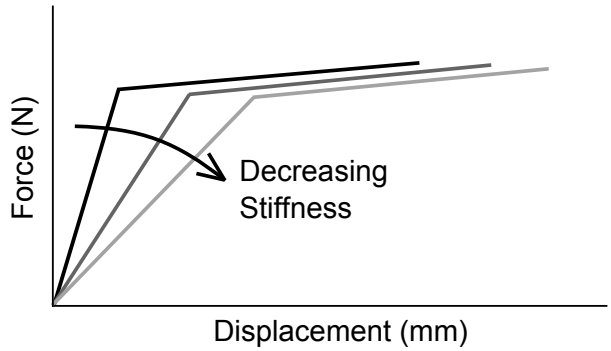

Figure 6.18: *The linear elastic stiffness, K_{tip}, determines how much displacement occurs before vertebral slip.*

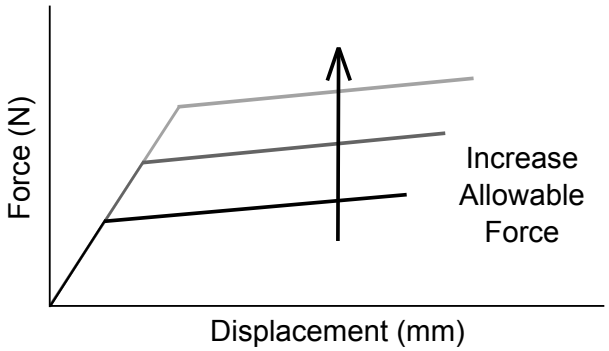

Figure 6.19: *Increased pull wire tension increases the force required to cause vertebral slip.*

and validated accordingly.

While this system successfully demonstrated controlled stiffening of a flexible manipulator, there are several additional improvements to address through future work. A biocompatible rubber or plastic sleeve must be placed around the catheter in order to make this instrument clinically feasible and it will be necessary to examine its effects on the manipulator. The workspace model accuracy can be improved by accounting for the conic holes in each vertebra. Elastic deformation in the manipulator could be reduced by replacing the pull wires and the vertebrae with a material of higher E. Future vertebrae will be fabricated using materials of greater friction coefficients in order to increase the stiffening capability of the catheter while reducing the burden on pull wire tension, which is advantageous for patient safety. A working channel will enable instruments, fluids, or

wires to pass through the center of the manipulator. Lastly, the non-uniform forces between different vertebrae along the length of the catheter will cause differences in the friction properties. These effects must be analyzed.

The analytical model describing the stiffness of the flexible manipulator was successfully validated on the prototype robot system with a two-vertebrae catheter. The resulting system expanded to a full length catheter would allow a user to navigate the manipulator to a target destination while compliant. The user would then increase tension on the pull wires with the magnitude of the tension set to prevent vertebrae sliding below the maximum anticipated tip load. The tip stiffness up to the sliding limit is then determined by the structural stiffness of the wires and the robot, which can be designed to provide desired tip stiffness. It is expected that the clinician will use the catheter in the structural elastic deformation region, and if the maximum force is exceeded then the catheter will simply slide. This would essentially act as a mechanical fuse to avoid exerting dangerously high forces on tissue. A system for actively stiffening flexible manipulators may be useful for many minimally invasive procedures in which a clinician must exert varying forces against tissue.

Chapter 7

Cardiac Catheter Brace

7.1 Introduction

Another motivation for structural support with cardiac catheters relates to crossing the atrial septum. Many procedures in the left atrium (LA) gain access by navigating catheters through the venous system into the RA and then puncturing through the atrial septum. A primary target procedure is an experimental mitral valve repair which may benefit from being done via catheterization rather than existing techniques. Unfortunately, catheters are currently not well-suited to performing dexterous tasks such as valve repair. While certain instances of valve replacement can be done via catheter (Lifesciences (2016)), and simple cardiac defects are repaired with catheter-based occluders (Medical (2016); Vascular (2016)), complex valve repairs require a combination of stability and dexterity which is not currently available with existing tools. Therefore, most valve repair (and other similarly complex tasks) can currently only be performed while stopping the heart and using heart-lung bypass.

We propose a bracing solution to address the issue of providing stability and therefore improving dexterity during catheter-based valve repair. The research prototype presented in this work is able to be navigated through tortuous blood vessels and can be deployed to provide stability. While several commercially available devices have demonstrated success

with navigating through tortuous vessels and deployment, there are no commercially available or research prototype cardiac catheter bracing solutions known to the authors.

This chapter provides the development and implementation of a device for bracing and stabilizing cardiac catheters. The following sections discuss anatomical constraints and bracing strategies, the primary difficulties in creating an effective cardiac bracing structure, and the prototyping methods used to fabricate the brace. The prototype brace is then tested bench top experiments. The results validate the feasibility of using the brace to stabilize against forces that are analogous to those required for valve regurgitation repair. The success of the cardiac catheter brace may lead to greater stability and dexterity during catheter-based interventional procedures, therefore enabling a range of complex cardiac procedures (such as valve repair) to be done via catheterization while the heart is beating. The work presented in this chapter was performed in collaboration with Leah P. Gaffney while working under my supervision.

7.2 Design Specifications

The experimental target procedure was chosen to be a catheter-based mitral valve annuloplasty, which is a valve repair typically done through surgery in the LA with rigid tools. To perform this procedure through catheterization requires accessing the top of the mitral valve and installing engineered features around the annulus of the valve. This procedure was chosen due to its demanding requirements for stability, dexterity, and force application to tissue. The difficulty of achieving this through catheterization poses many constraints on the design bracing device.

The LA is reached by introducing a catheter through the venous system (typically in the femoral vein), into the RA, and then performing a transseptal puncture through the atrial septum (Fig. 7.1). From this position, the catheter can be flexed and navigated anteriorly towards the top of the mitral valve. The catheter must be flexible as it bends through tortuous vasculature in order to reach the left atrium. Therefore, the bracing device must also be flexible as it is navigated towards the heart and then switched into a bracing mode

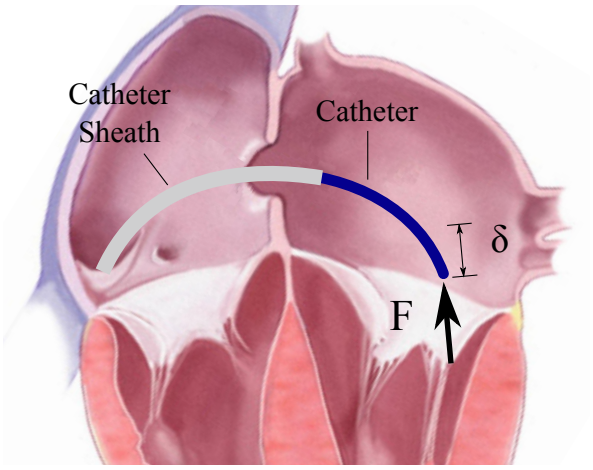

Figure 7.1: *The transseptal catheter applies force to the mitral valve annulus.*

after reaching the destination.

The bracing device must also maintain a low profile through the vasculature. The clinician must be able to easily deploy the device at the proper site (by applying under 10 N force), perform the procedure, and then remove the device. If the device is mounted to a catheter, then the device must include a clear inner lumen for working instruments to pass through to the surgical site. Any device attached to a catheter must be limited to a total maximum diameter of 24 Fr or 8 mm (which is the size of the largest transcatheter heart valve (Lifesciences (2016))).

Installing the annuloplasty devices around the valve annulus requires application of 1.5 N of force against tissue (Wagner et al. (2006)). The catheter instrument applying the force must be rigidly braced to avoid displacement; or it must reduce displacement as much as possible. This brace will be designed to restrict displacement below 5 mm due to 2 N forces, corresponding to a moment which will be calculated and discussed in the following sections.

A summary of technical requirements is listed below. The bracing device must be:

- Flexible enough to bend through tortuous vasculature
- Easily deployable (actuation force < 10 N) and removable

- Rigid enough to restrict deflection < 5 mm in response to 2 N force
- Of maximum diameter < 24 Fr (8 mm)
- Designed to have an open inner channel which is compatible with existing catheter tools
- Safe, biocompatible, covered to prevent blood coagulation on its surface, and include no sharp components

7.3 Design Methodology

We design a bracing device for stabilizing cardiac catheters when accessing the LA to enable dexterous application of force to cardiac tissue. The solution presented in the following sections will be generally applicable to all cardiac procedures of the LA, but will reference mitral valve repair as a specific case study.

7.3.1 Anatomy

The cardiac catheter bracing device must mechanically couple the catheter to the cardiac anatomy in order to provide mechanical grounding support. Stability is improved by bracing the catheter against the structures that are as close to the catheter tip as possible. Through research on the structural support of various cardiac structures, initial prototypes, and discussions with clinicians and cardiac researchers, it was determined that a device fixed to the atrial septum is most likely to provide adequate bracing for a catheter. The atrial septum is close to the mitral valve, there is a low likelihood of interfering with electrical signals, the device has the potential advantage of clasping onto both sides of the structure, and it achieves additional stability from the set of fibrous rings connecting the atrial walls to the valves.

7.3.2 Strategy

Numerous material solutions for bracing against the atrial septum were explored including balloons, shape memory alloys (SMA), and rigid devices with flexible joints. SMA materials are useful for assuming a pre-formed shape, but they must be compliant enough to navigate through tortuous blood vessels. This compliance would compromise the ability of the device to effectively act as a brace.

Balloons were explored as a potential bracing solution because many balloon-related devices are already in clinical use. A range of balloon prototypes were created using thermoplastics and thermoforming techniques. Initial testing was done by applying normal forces to and torques about the balloon surface. The balloon provided sufficient bracing against normal forces, but bracing against torque was inadequate. Further balloon prototyping investigated more rigid materials and the addition of plastic struts and Kevlar string networks. Consistently through all torque trials, the fluid was redistributed inside the balloon which resulted in a large unwanted rotation. Balloons met the requirements for size and insertion, but were not suitable for stiff bracing.

A bracing device with rigid segments connected by flexible joints is capable of providing the required stiffness for bracing support. The brace clamps the atrial septum while the inner lumen supports the catheter protruding into the LA (schematic in Fig. 7.2, prototype CAD in Fig. 7.3). While an effective structural design with rigid components can maintain stability in the braced configuration, the joint design must allow the catheter to bend in all directions during navigation through the vasculature. The following sections present the design and fabrication of a device which is flexible, deployable, and rigid.

7.3.3 Insertion

The joints between rigid segments of the brace were designed for easy navigation through the vasculature by bending freely in all directions. The most tortuous region along the path of the catheter occurs at the junction of the IVC and the RA. Ultrasound images of patient vasculature were consulted to determine average values of IVC curvature (Goldflam

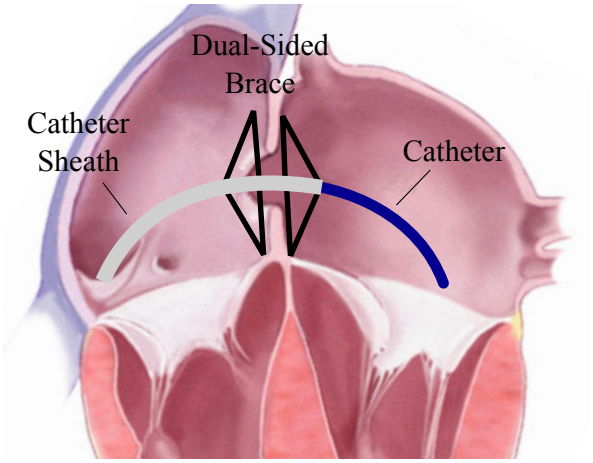

Figure 7.2: *Schematic of rigid foldable brace.*

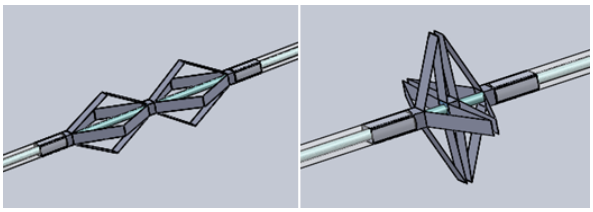

Figure 7.3: *CAD model of rigid foldable brace (left) partially deployed, (right) fully deployed.*

et al. (2011)). The arc of the IVC was estimated to curve 90 ° with radius of curvature 2 *cm* (measured from US). The analytical design for geometry and flexibility of the device is discussed in Section 7.4.

7.3.4 Deployment

This device was designed to be easily manually deployed with limited localization guidance (X-ray fluoroscopy should not be used unless necessary). The distal and proximal sections are independently deployable. First, the clinician uses standard practice for a transseptal puncture. Next, the bracing catheter is advanced over the guidewire through the atrial septum. The distal tip is advanced into the LA and then deployed by a pull wire secured to the distal end of the brace catheter. The brace catheter is retracted until the deployed distal section contacts the atrial septum on the left side. Finally, the proximal brace half is deployed by advancing the outer lumen. This process is repeatable such that the clinician can undo the brace deployment and re-seat the device if necessary.

7.3.5 Bracing

The brace was designed with each linkage lying flat against the outer wall of the catheter during navigation and then folding into a triangular shape during bracing (Fig. 7.3). The set of triangles in this arrangement enables the edges of the linkages to reach the edges of the septum where the cardiac tissue exhibits greater rigidity. Force applied to the catheter tip causes a moment to occur about the brace. The tips of the brace linkages exert force against the septum. The geometry of the linkages is important because this affects which part of the septum it is braced against, how far the support extends into the LA, and the minimum turning radius during navigation. The required anatomical patient data, exact geometry of the linkage, and resulting sizing options are discussed in Section 7.6 on sizing analysis. A minimum of three linkages ensures proper bracing in all directions. Four linkages were used in this design due to manufacturing symmetry.

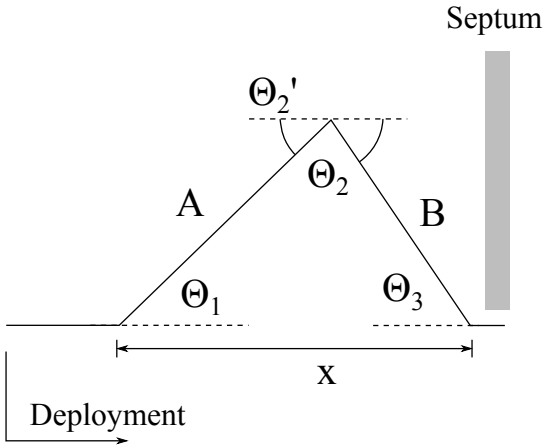

Figure 7.4: *Brace linkage geometry.*

7.4 Analysis and Design

This investigation focuses on the two main components in the rigid foldable design: rigid links and flexible joints. The other design features (biasing ring and deployment mechanism) are presented as important conceptual elements of the proposed solution.

7.4.1 Linkage Geometry

One side of the bracing linkage is the triangle shown in Fig. 7.4. The joint farthest from the septum will be referred to as Joint 1, and the joint nearest the septum is Joint 3. Joint 2 is the middle joint where Θ_2 refers to the angle of the triangle and Θ_2', the supplementary angle to Θ_2, refers to the total angle that the joint rotates through.

For joint design it is important to know the range of angular rotation of each joint. Without a bias ring or any locking joint, the displacement can translate through $(A + B) - (A - B)$, which is 24 mm in the present case. The variable x thus has possible dimensions from 26 mm to 2 mm. The geometry of the triangle is given by the equations

$$\Theta_1 = cos^{-1}\left(\frac{A^2 + x^2 - B^2}{2Ax}\right) \tag{7.1}$$

$$\Theta_2 = cos^{-1}\left(\frac{A^2 + B^2 - x^2}{2AB}\right) \tag{7.2}$$

$$\Theta_3 = cos^{-1}\left(\frac{B^2 + x^2 - A^2}{2Bx}\right) \tag{7.3}$$

$$\Theta_2' = \pi - \Theta_2. \tag{7.4}$$

The bias ring restricts overextension of either brace half so that the central piece between the two brace halves is aligned with the septum. For the present brace, that extension is limited to 20 mm.

The proof of concept device developed here was designed for a patient with a relatively small atrial diameter and septum (30 mm atrial diameter (University (2016)), 2 mm septum thickness (Rosenquist et al. (1979))) to ensure that the smallest adult-sized device could be built. The link lengths were $A = 14$ mm and $B = 12$ mm for all testing and design. This geometry would result in the distal tip of the brace to be located 7.2 mm away from the septum in the 30 mm wide left atrium, which enables sufficient access for the clinician to work inside the atrium.

7.4.2 Rigid Link and Catheter Design

The most common rigid metals used for biological implants are stainless steel and titanium. Titanium is the most biocompatible metal (Mihov and Katerska (2010)), however it is more expensive then stainless steel per volume and more difficult to machine. Those factors make stainless steel a better prototyping material. To improve patient safety the stainless steel links will be covered in a polymer sheet and the whole brace will be deployed for maximum three hours.

The lengths of the metal links were designed to be 12 mm and 14 mm. The thickness was designed from critical force calculations to ensure that the links do not buckle as compressed columns. The critical force required to buckle a column is

$$P_{cr} = \frac{\pi^2 EI}{(KL)^2}. \tag{7.5}$$

The maximum compressive force a cardiologist may be expected to apply is 20 N. Modeling a link as a sideways column that is fixed at both ends, the effective length $K = 0.5$. For the

case of two fixed ends it is typically recommended to design with $K = 0.65$. The Young's Modulus of stainless steel is $E = 200\ GPa$. The smallest second moment of area of the link rectangular cross section is $I = \frac{wt^3}{12}$. The width dimension, w, is determined by the diameter of the catheter and the thickness dimension, t, is determined by the strength required to avoid buckling.

The catheter tubing was made of nylon inner tubing (ID: 2.2 mm, OD: 3.2 mm) and PTFE outer tubing (ID: 3.2 mm, OD: 4.8 mm). The outer diameter was 5 mm (15 Fr) and thus on the same order of magnitude as a typical cardiac catheter. The rigid links attached to the outside of the catheter increased the final diameter.

Four linkages per brace half of 3.2 mm width were chosen as the starting point for design. More linkages use the available space of the round cross section of catheter tubing more efficiently. Also, more linkages provide more points of contact on the septum, which increases structural stability. Three linkages would provide the minimum acceptable bracing configuration. Four linkages were used for ease of manual prototyping.

Using $w = 3.2\ mm$ and $L = 14\ mm$ with Equation 7.5:

$$20N = \frac{\pi^2 E \frac{wh^3}{12}}{(KL)^2} \rightarrow h = 0.196mm. \tag{7.6}$$

With a 2X factor of safety to prevent buckling, the device must have stainless steel links of minimum 0.41 mm thickness.

7.4.3 Joint Design - Strategy

In this section we examine strategies for designing the joints of the bracing device. The joints must bend through large angles with a small radius of curvature without failure. Additionally, the whole bracing structure must be flexible enough to bend through tortuous vasculature. This means that at least one of the joints must be flexible out of the plane of the bending triangle.

Miniature pin joints were first considered for designing the small scale bending joints of the bracing device. Pin joints are used in some articulating cardiac catheter devices

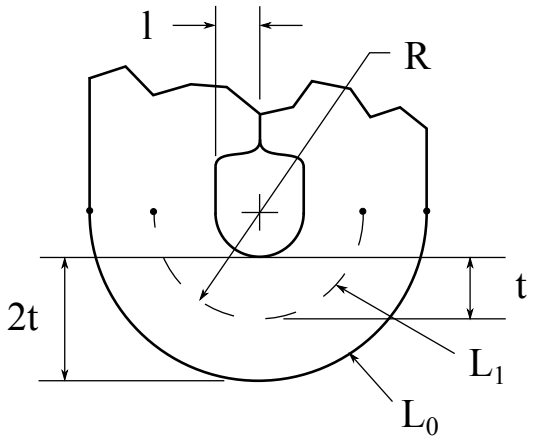

Figure 7.5: *Bending dimensions of a living hinge (MatWeb (2016)).*

such as biopsy forceps. However, the inner lumen of the device needs to be clear for the catheter to pass through and this reduces the feasibility of using a pin joint. The joints must also collectively be compliant enough for easy deployment and insertion, yet create a rigid triangular truss during bracing without designing the brace to lock at any one particular location. For these reasons pin joints were not used.

Plastic living hinges are commonly used in thin extrusions for bends about sharp angles. Plastics have very high tensile strengths and can be bent through much sharper bending radii than spring steel or other elastic metals (like nitinol). Plastics could provide enough rigidity to constrain the linkages while also bending through the large angular deflections with a small radius of curvature. Bending strains were considered in designing the plastic hinge joints. The allowable strain of a material dictates how sharply it can bend and at what thicknesses. Referring to Fig. 7.5,

$$\epsilon = \frac{L_0 - L_1}{L_1} \tag{7.7}$$

where $L_1 = \theta R$ and $L_0 = \theta\left(R + t\right)$. Therefore,

$$\epsilon = \frac{\theta t}{L_1}. \tag{7.8}$$

Joint thicknesses and lengths must be designed to withstand the bending strains from large angular deflections. Some plastic deformation is acceptable, as the joints must

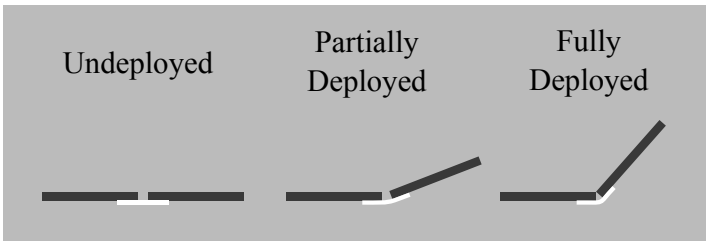

Figure 7.6: *Joint 1 shown deploying and then braced.*

withstand only a few deployments. Exact joint angle deflections will vary depending on the brace size chosen for each patient.

Before deployment, insertion through tortuous vasculature requires at least one joint to be flexible to bending out of the plane. Increasing out of plane flexibility reduces the bracing ability of the joint when the device is deployed. Therefore the best brace will have the minimum number of joints for bending out of plane. Joint 2 is the best candidate for being built with out of plane flexibility because it allows the brace to be designed with three segments that are rigid to out of plane bending. The first segment is between the proximal Joints 1 and 2. The second segment is between the proximal Joint 2 and the distal Joint 2. The third segment is between the distal Joints 2 and 1. Joints 1 and 3 can then be designed for zero out of plane bending and therefore can have higher bracing stiffness.

7.4.4 Joint Design - Materials

Each of the three joints has different requirements for bending during insertion, bending during deployment, and bracing once deployed. Numerous joint materials and geometries were examined to determine which material would satisfy the requirements of each different joint.

Joint 1

For the current brace size, the angular deflection of Joint 1 reaches 59°. This means that there can be a mechanical stop beyond 59 ° to allow this joint to rotate freely but have little room for deflection in the bracing state (Fig. 7.6). Polyethylene terephthalate (PET) of thickness 3*mil* was selected as a stiff yet extensible option. This thickness was chosen to

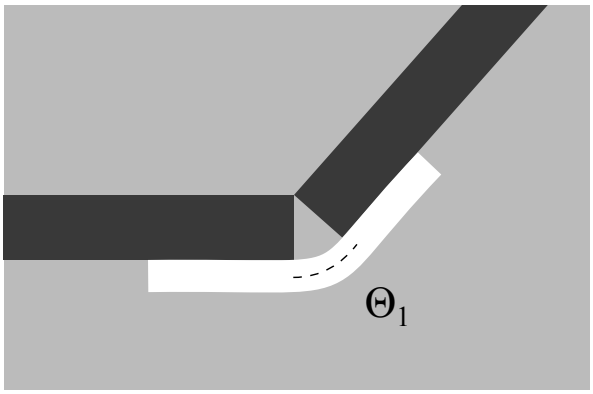

Figure 7.7: *Braced position of Joint 1.*

maintain stiffness of the joint while minimizing the thickness added to the overall outer diameter. The required length to achieve the locking design was calculated as the arc length of the neutral axis (dotted line in Fig. 7.7) of the bending joint,

$$l = R\theta = 0.46\ mm. \tag{7.9}$$

The final joint length was tuned to account for laser beam width. Laser beam imprecision produced joints ranging from 0.46 *mm* to 0.48 *mm*. This would cause a strain of $\approx 9\%$, significantly lower than the strain limit of PET.

Joint 2

The design of Joint 2 must accomplish two contradicting goals: Joint 2 must be flexible enough allow bending during insertion but also strong enough to brace the catheter when deployed. A material that is too soft would allow the joint to compress or translate during bracing, compromising the stiffness of the entire structure. To solve this problem, dual layers of thermoplastic polyurethane (TPU) were arranged with different amounts of slack on the top and bottom layers (Fig. 7.8). During Joint 2 bending the top layer of TPU is stretched. The excess TPU in the bottom layer kinks and becomes compressed by the two links. The kinked TPU resists deflections from forces along the length of the link during bracing. Several different plastics of various thicknesses were tested with this design and 12 *mil* thick 85A polyurethane at 0.8 *mm* thickness was chosen. In bracing it provided high

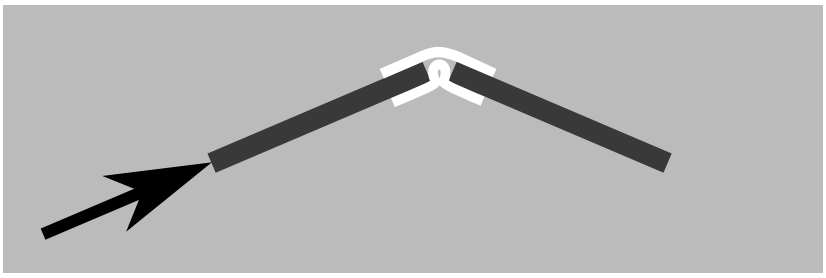

Figure 7.8: *Joint 2 dual layer design.*

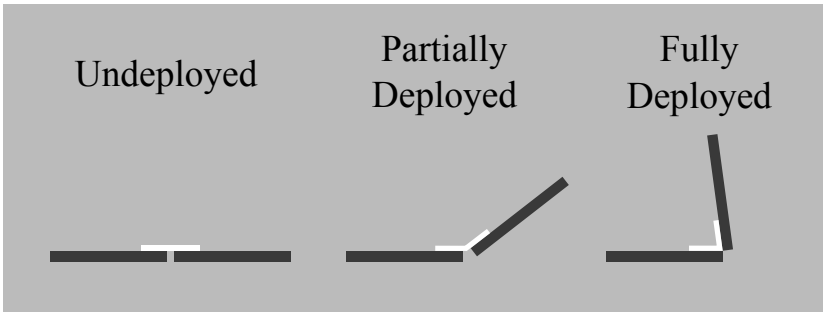

Figure 7.9: *Joint 3 shown deploying and then braced.*

stiffness, and when flat it easily bent in multiple planes to enable insertion. TPU is also useful for its favorable blood contact properties and a thinner layer can be used to cover the entire external surface of the device.

Joint 3

Joint 3 must bend up to 100° and thus cannot be designed to lock in the same manner as Joint 1. The joint length was decreased to the minimum size possible by manufacturing limitations; 0.13 *mm*. 2 *mil* nylon was selected during prototyping because of its smaller bend radius and for its strong adhesion to the stainless steel links. Strong adhesion is important especially at this joint because its design causes it to be the most prone to delaminating under shear stresses. Maximum strains $\approx$ 35% are below the maximum elongation of nylon (90%).

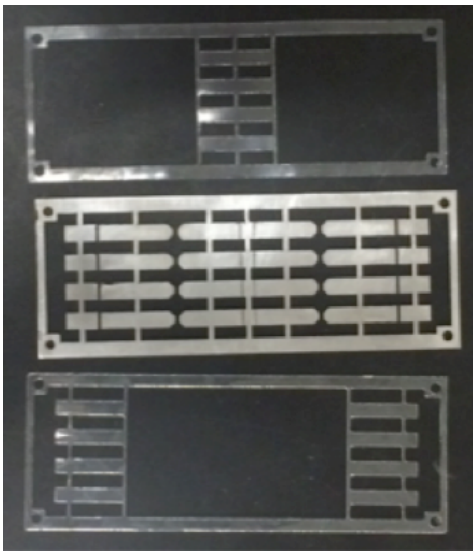

Figure 7.10: *Steel and plastic alignment frames.*

7.4.5 Assembly

Metal frames of 0.41 *mm* thickness were cut using a Kern 150 *W* laser. The laser cutting resolution was 0.13 *mm*. An example assembly frame (30 *mm* by 80 *mm*) is shown in Fig. 7.10. The frames were designed with thin bridges between individual metal links to precisely hold links apart before attaching the joints.

For the fabrication of the final proof of concept design, the plastic joints (Joints 1 and 3) and metal links were laser cut in alignment frames (Fig. 7.10). 0.5 *mil* Pyralux B-stage adhesive was used for a strong bond between the metal links and plastics joints. The materials were prepared for adhesion with ultrasonic cleaning and plasma etching. The adhesive was also cut in alignment frames. These 5 layers (Fig. 7.11) were pressed with 55 *kg* of force at 200°*C* for two hours to securely bond the joints to the metal frame.

The elastomeric Joint 2 was subsequently secured by hand with medical device cyanoacrylate (Loctite 4011). Finally, the four linkages were removed from the frame by shearing the thin metallic bridges or by a release laser cut. The linkages were secured to the catheter tubing with Loctite 4011. The final prototype is pictured in Fig. 7.12.

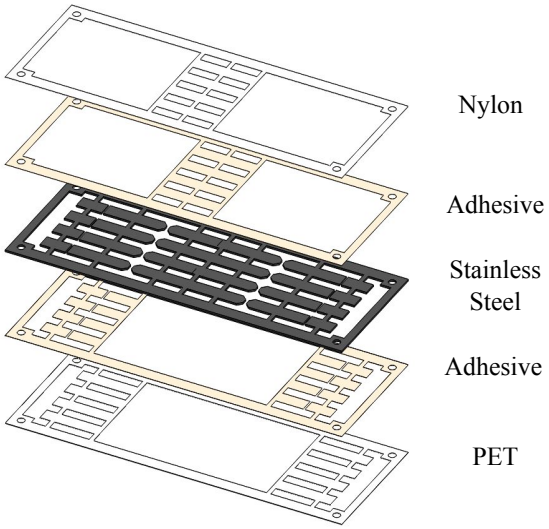

Figure 7.11: *Layers are aligned and then compressed under heat.*

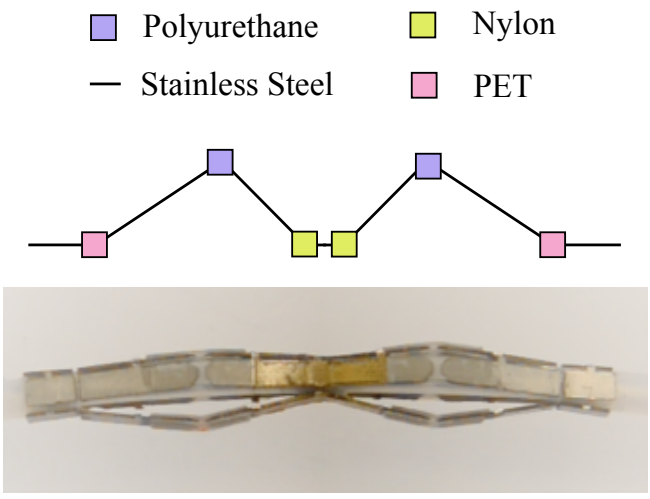

Figure 7.12: *Final prototype.*

Figure 7.13: *IVC analog for insertion testing.*

7.5 Experiments and Results

7.5.1 Insertion

A simulated IVC was built to demonstrate catheter insertion with the undeployed brace (Fig. 7.13). The diameter of the curve is 2.2 *cm* (the normal adult range for IVC diameter is 1.5 *cm* to 2.5 *cm*). The radius of curvature is 4.47 *cm* and the curve angle is 90°.

During a cardiac catheterization procedure a guide wire would first be delivered to the target destination, and then the bracing catheter would be guided along the wire. In this insertion feasibility test the undeployed brace catheter was manually navigated through the simulated IVC without a guide wire (Fig. 7.14). This demonstrated that the brace was sufficiently flexible in its undeployed configuration. Section 7.6 presents a derivation of brace sizing based on patient geometry to ensure that the brace can turn through the required radius. To ease the insertion as much as possible, the clinician may benefit from respiration-induced IVC contraction by temporarily holding the patient's breath when the IVC is in its largest state.

Figure 7.14: *Braced catheter turning through the IVC analog.*

7.5.2 Deployment

A force-testing frame (Instron) was used for all deployment testing (Fig. 7.15). First the brace was manually deployed by 0.5 *mm* to begin at a 10° bias angle. One half of the brace was deployed as shown in Fig. 7.15. This was achieved by translating the outer tube downward over the inner tube. Inner and outer tubes were secured at the central location between the two halves of the brace. Thus, holding both inner and outer tubes fixed for the second brace half allowed for controlled deployment of one side of the brace. Fig. 7.16 shows deployment force test results, demonstrating that the brace can be deployed with less than 1.2 N of input force. The system was lubricated but not entirely frictionless. The friction between tubes was measured separately (Fig. 7.17) and may account for about 10% of the recorded deployment force. This low input force result indicates that manual deployment is feasible and unlikely to damage the brace.

The required deployment is well below the 10 N upper allowable limit and should be easily deployable. After the Instron comes into full contact with the device for deployment (at bias angle 10°), 1.2 N additional force begins deployment. Then the force reduces to between 0.6 N and 0.8 N.

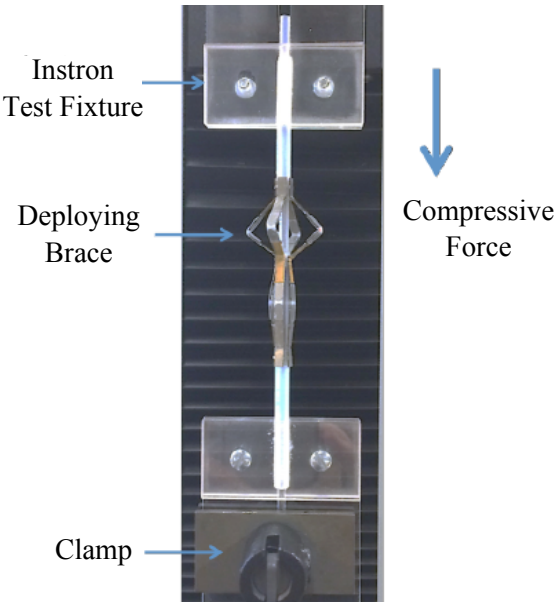

Figure 7.15: *Deployment testing setup.*

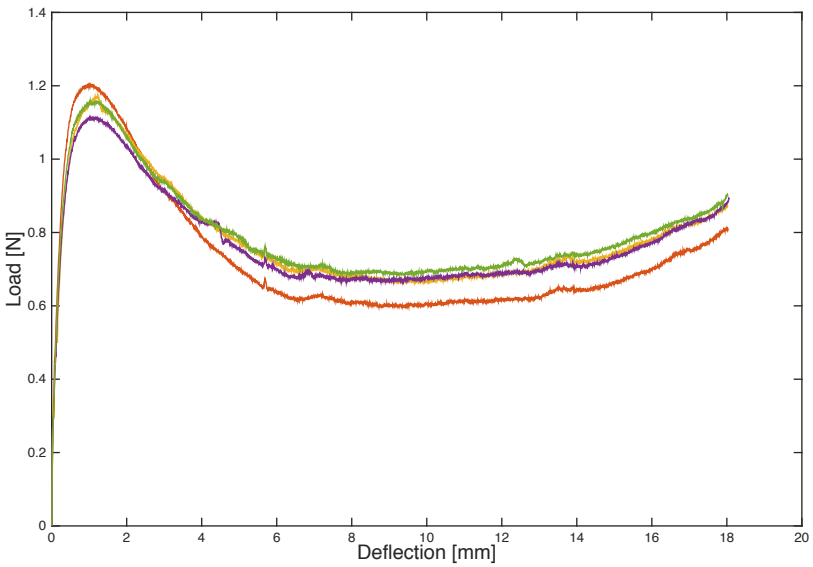

Figure 7.16: *Experimental deployment force.*

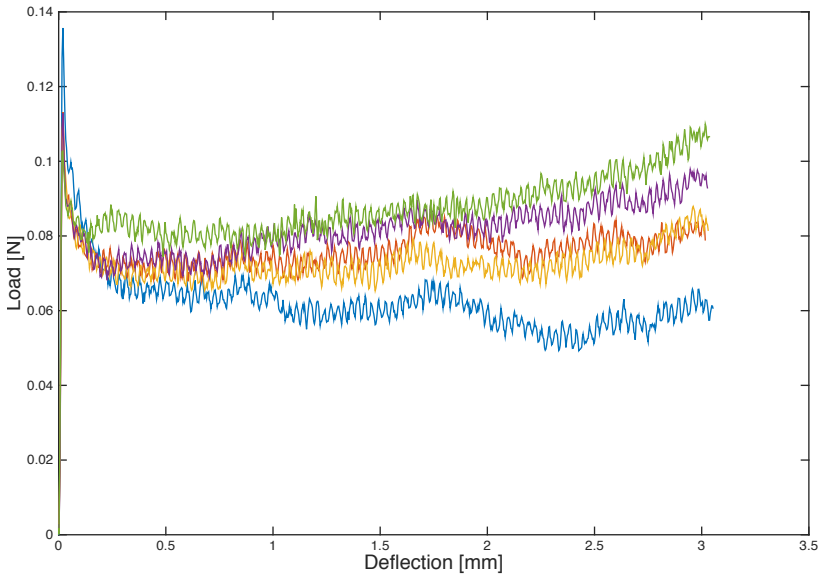

Figure 7.17: *Friction between catheter tubes.*

7.5.3 Bracing

Test Setup

The same Instron frame was used for bracing tests. The bracing test setup is shown in Fig. 7.18. A rigid 0.64 *cm* acrylic sheet provided vertical stability and was clamped into the Instron with the help of two flanges to ensure strong clamping and orthogonality. Interchangeable septum analogs were attached to the blue 0.64 *cm* acrylic base. The brace/catheter system was threaded through an oversized (7 *mm* diameter) hole in the septum. The septum hole was oversized to avoid supporting the catheter. This is consistent with cardiac anatomy because the atrial septum does not provide structural support to transseptal catheters.

The braced catheter was manually deployed and clamped in the braced position with collar clamps. The test method was set to compressive extension with an end of test stoppage point at maximum load 2 N. For each test the plunger was positioned above the catheter brace centered 3 *mm* away from the end of the brace. The force at the plunger can be summarized by a resultant force acting 3 *mm* beyond Joint 1 (which is 7.2 *mm* away from

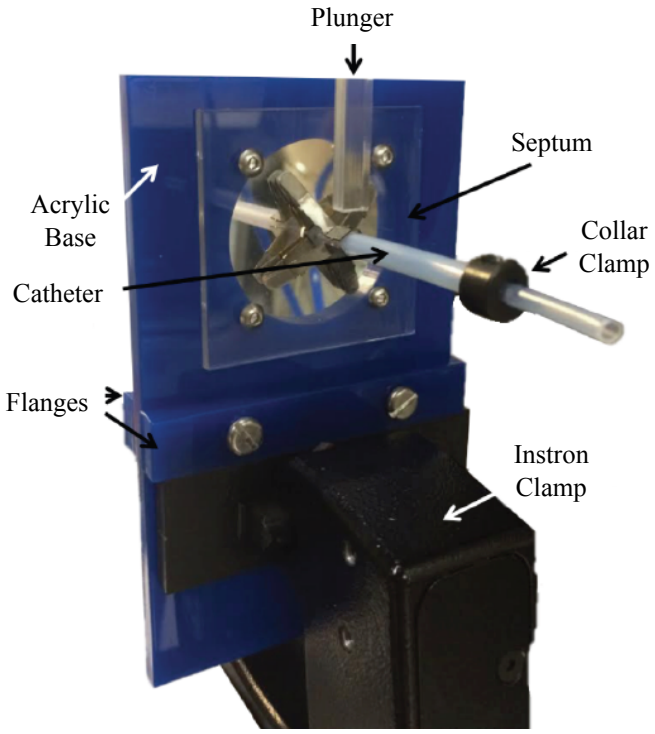

Figure 7.18: *Bracing testing setup.*

the septum). Thus, the moment arm was 10.2 mm.

Prior to each trial, the plunger arm was positioned above the catheter sheath so that the load cell of the Instron machine was initially unloaded. The plunger displaced downwards a small distance before making contact with the catheter and applying force. To calculate brace stiffness, the actual vertical displacement of the catheter in response to 2 N must be extracted. This is equivalent to the deflection of the plunger arm after making contact with the catheter until the 2 N end of test is reached. Fig. 7.19 shows five example bracing tests.

The overall catheter deflection was the difference between the maximum and minimum extension values. The leftmost (first) trial represented a settling point and was considered a calibration of the system that effectively seated the catheter before applying further forces. The first trial of each data set will now be deemed a calibration and only subsequent data trials 2-5 will be considered. The measurement resolution from the Instron was < 0.003 mm.

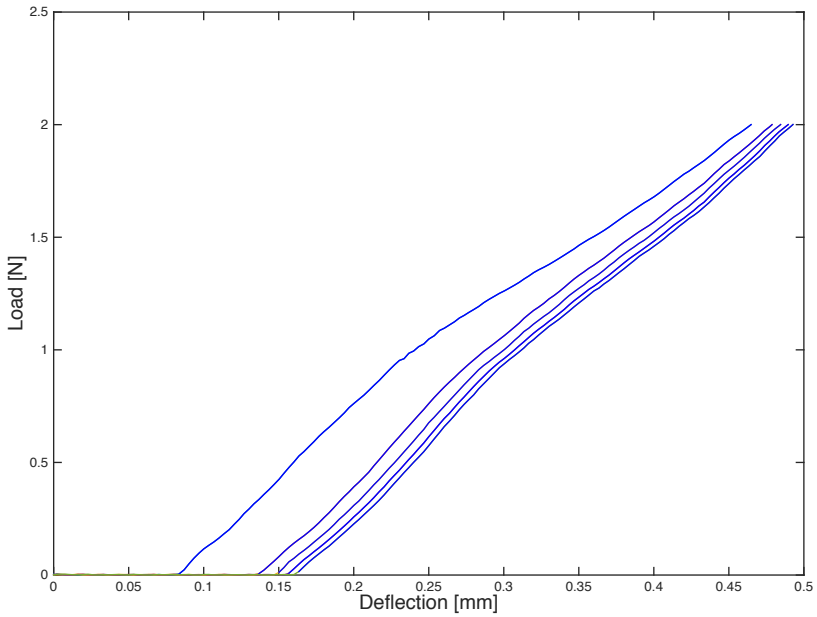

Figure 7.19: *Example bracing data.*

Test Results

A 2 N force was applied to the catheter 40 times (Fig. 7.20). The central catheter and the septum analog were rigid. Half of the tests were done such that two of the brace arms were deployed vertically in the same plane as the plunger's applied force (Fig. 7.21(*left*)). In the remaining deployments the brace was rotated about its axis by 45° to assess the effect of forces applied between arms of the brace (Fig. 7.21(*right*)). This distinction is made because it is important to know whether the angle between the catheter applied force and the brace rotation affects the bracing stiffness. Due to the imaging methods currently available in interventional cardiology catheter labs and the amount of torsional windup which occurs along the length of a catheter, it would be challenging to control the rotational orientation of the brace. No statistically significant difference was found between these two cases ($p = 0.3804$). Both cases are shown together in Fig. 7.20.

This result shows a very high stiffness at the tip of the brace (nearly 6 N/mm). Fig. 7.22 shows how the stiffness at the end of the brace corresponds to the stiffness of the brace/catheter system at the catheter tip. We assume that the catheter itself is a rigid

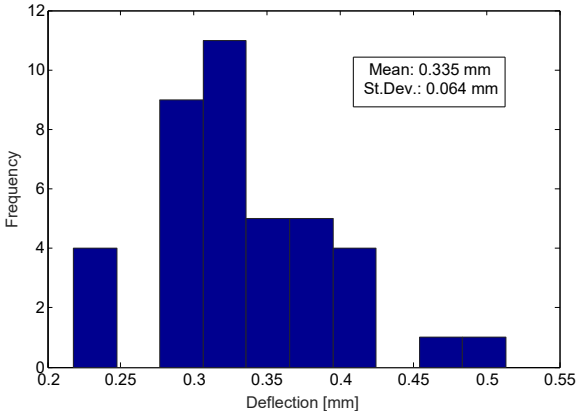

Figure 7.20: *Bracing results histogram from 40 loadings.*

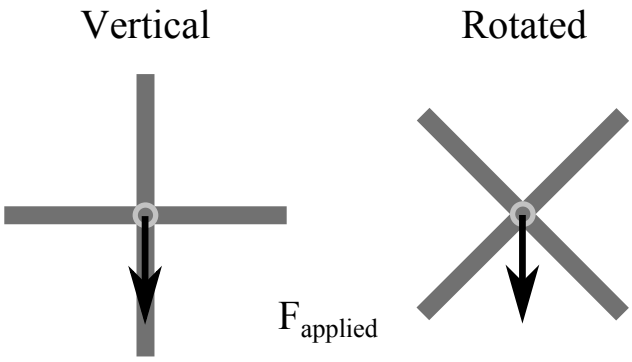

Figure 7.21: *Rotational orientation of the brace.*

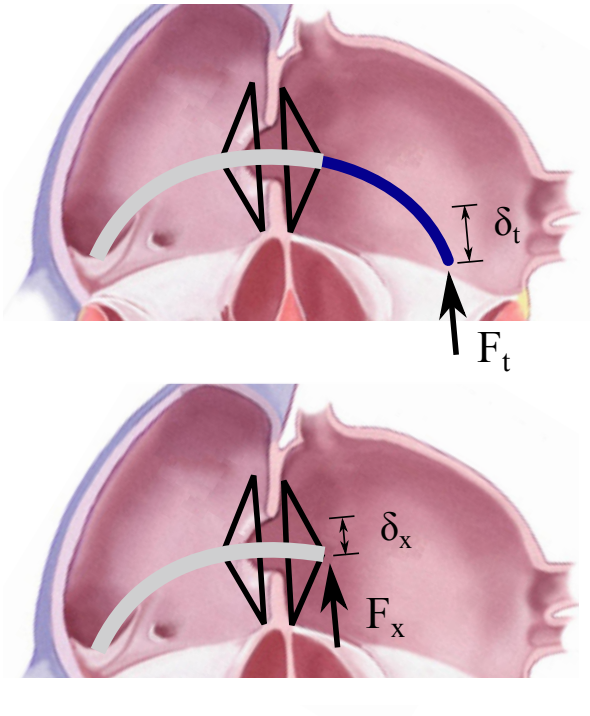

Figure 7.22: *Catheter tip stiffness derivation.*

body, which could be possible with the continued development of catheters that can stiffen in place. We use this assumption to calculate the stiffness of the brace/catheter system at the catheter tip by first calculating

$$\delta_x = \frac{x}{t}\delta_t \tag{7.10}$$

where x is the distance from the septum to the tip of the brace and t is the moment arm distance from the septum to the tip of the catheter. Similarly, the location of force application affects the moment arm and applied moment. An equivalent moment is applied about the septum with vertical forces at position x or t,

$$F_t = F_x \frac{x}{t}. \tag{7.11}$$

Therefore,

$$k_t = \frac{F_t}{\delta_t} = \frac{F_x \frac{x}{t}}{\delta_x \frac{t}{x}} = \frac{F_x}{\delta_x}\left(\frac{x}{t}\right)^2. \tag{7.12}$$

An estimated stiffness of a catheter tip at any location in the atrium can be extrapolated

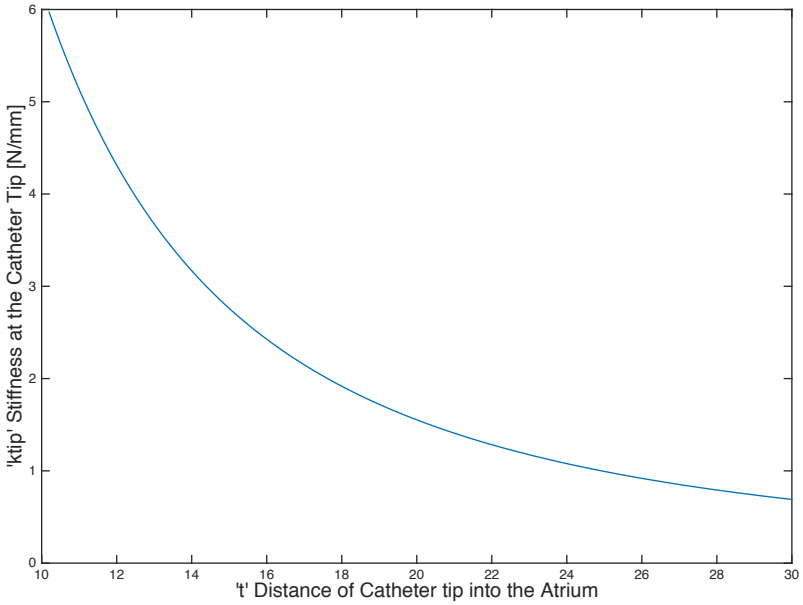

Figure 7.23: *Calculated range of catheter tip stiffness.*

from the measured stiffness of the brace at $x = 10.2\ mm$ (Figure 7.23). With an overall desired target stiffness of $k = \frac{2N}{5mm} = 0.4\frac{N}{mm}$, this brace will meet the target for any length of catheter protruding beyond the brace and into the LA. This suggests that even with a very stiff brace, the bracing location must be at the septum or closer. The stiffness of the septum becomes the limiting factor for catheter bracing.

Since stiffness of the inner catheter is a contributing factor to the overall stiffness of the system, bracing data was also collected to determine this effect. A set of tests was conducted while the inner lumen had no inner catheter for support. The deflection at the brace tip increased from 0.335 mm to 0.381 mm ($p = 0.0179$). This increase in deflection is the result of a hollow catheter (with no inner support) bending in response to an applied moment. Because it is expected that this brace will always be used with a working catheter inside, this hollow stiffness measurement demonstrates the lower bound of bracing stiffness.

The stiffness of the septum used during bench top testing also contributes to the overall stiffness of the system. The brace must also succeed in supporting the catheter when the septum is compliant (rather than rigid acrylic used in our initial tests). Clinical data of the

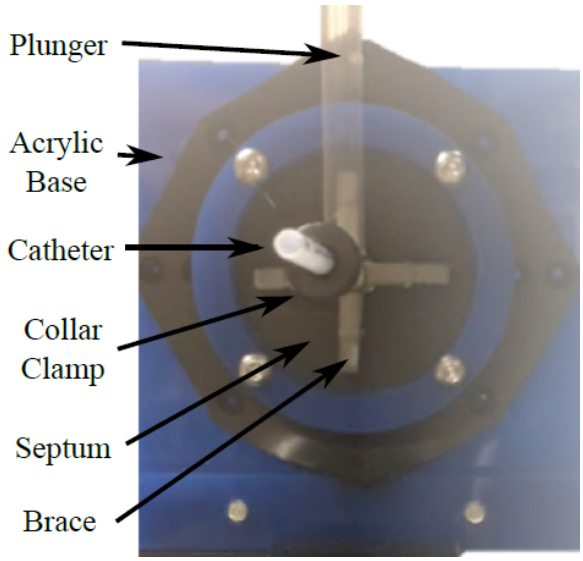

Figure 7.24: *Bracing test setup with rubber septum analog.*

mechanical properties of the human interatrial septum have not been found in the literature. Without access to septal material properties, we conduct an additional set of bracing tests while bracing onto a 60A durometer rubber septum. The same test rig was used with rubber sheets replacing the acrylic septum in different loading conditions (Figure 7.24).

The rubber was orthogonal to the Instron plunger and the Instron was used to measure the rubber stiffness, k_s, assuming a point load force was applied. The force applied orthogonally to the rubber was analogous to reaction forces between the loaded brace and the septum. A 2 N force was applied, and the deflection of the overall catheter and brace system is plotted with respect to the deflection of the septum. This motivates the idea that the physical environment is the limiting factor due to the success of the brace.

The deflection of the braced catheter system is linearly correlated $\left(R^2 = 0.9095\right)$ with the deflection of the clamped rubber septum analogs due to 2 N of applied force and thus the compliance of the rubber (Fig. 7.25). Therefore the compliance of the *in vivo* environment can be assumed to be the limiting factor in terms of overall brace stiffness. Because human septum properties are unknown and not adjustable, the best way to ensure stiffest possible bracing is to reach the areas of the septum that will provide the strongest brace grounding.

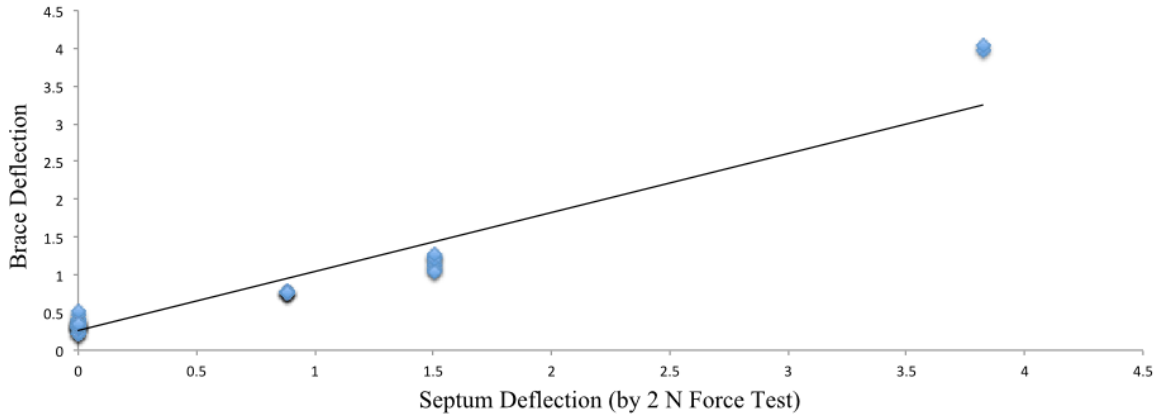

Figure 7.25: *Brace deflections for various septum analogs.*

This can be achieved by informed sizing of the brace, to be discussed in Section 7.6.

7.6 Clinical Sizing Analysis

This section presents an algorithm for determining the correctly sized brace for a given patient. The determination of discrete sizing based on this model is then possible upon completion of a comprehensive population analysis that would determine the range of patient anatomical variables. First, the IVC curve must be considered. The vascular pathway from the femoral vein to the RA is relatively straight in patients with normal vasculature. The IVC joining the RA is the most tortuous section and thus the limiting factor (Fig. 7.26).

Pre-operative US imaging can be used to determine the curvature of the pathway from the IVC into the atria towards the fossa ovalis of the atrial septum. Standard image processing can fit an arc to this curved pathway. Perhaps the two easiest dimensions to define the curve from this type of arc fit are the radius of curvature of the arc, R, and the linear distance between the ends of the arc, d. The diameter of the IVC, D_{ivc}, can also be determined through standard ultrasound imaging protocol. Recording this dimension is already standard protocol. With these three pre-operative measurements (R, d, and D_{ivc}) the geometry of the curved pathway is completely defined.

The following equations define the other variables in Figure 7.26 in terms of R, d, and

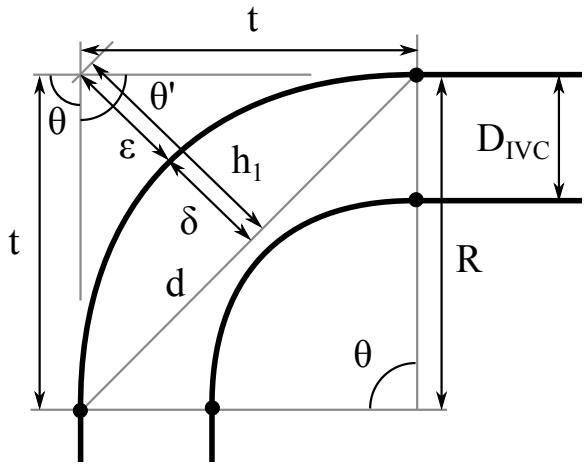

Figure 7.26: *Defining IVC geometry.*

D_{ivc}. From the triangle defined by d, R, and θ,

$$\theta = 2sin^{-1}\left(\frac{d}{2R}\right). \tag{7.13}$$

The supplementary angle to θ defines another triangle that shares chord length d,

$$\theta' = \pi - \theta \tag{7.14}$$

$$t = \frac{d}{2sin\left(\frac{\theta'}{2}\right)}. \tag{7.15}$$

The height of this triangle is now defined as

$$h_1 = \sqrt{t^2 - \left(\frac{d}{2}\right)^2}. \tag{7.16}$$

Finally, this height can be decomposed into the portion that is inside the curve,

$$\delta = R\left(1 - cos\left(\frac{\theta}{2}\right)\right), \tag{7.17}$$

and the portion external to the curve ($\epsilon = h_1 - \delta$). The equation for δ comes from simple geometry of a chord (Fig. 7.27). $R = x + \delta$ and $x = Rcos\left(\frac{\theta}{2}\right)$.

Now that the geometry of the catheter pathway is defined, the catheter can be placed inside the pathway to determine the constraints on sizing imposed by the curvature and

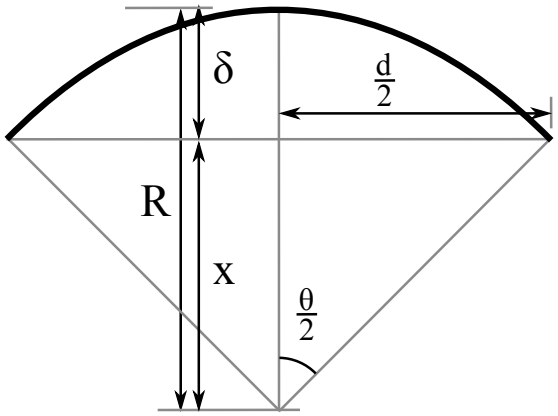

Figure 7.27: *Chord geometry.*

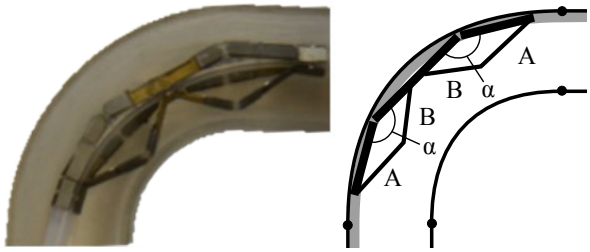

Figure 7.28: *Catheter brace turning through IVC and corresponding geometric model.*

diameter of the IVC. Fig. 7.28 shows the catheter curving through a representative IVC with sufficient space to make the turn. The radial positioning of the catheter as it makes this curve is very challenging to control. Thus, the worst case scenario will be considered throughout this analysis. That scenario is when the plane of curvature (cross section shown in Fig. 7.28) is exactly coincident with the midline of a link as it bends through the inner section of the curve (requiring the largest opening of the brace during curving). All other radial configurations will require less opening of the brace and thus less overall volumetric space. It is important to note that this is a completely general solution for any number of linkages. The schematic in Fig. 7.28 places the brace at the outer curve to determine the maximum possible brace sizing for given IVC dimensions.

The angle α is the critical dimension to establish the amount of radial expansion of the brace imposed by the curvature of the IVC. Because θ must anatomically be roughly 90

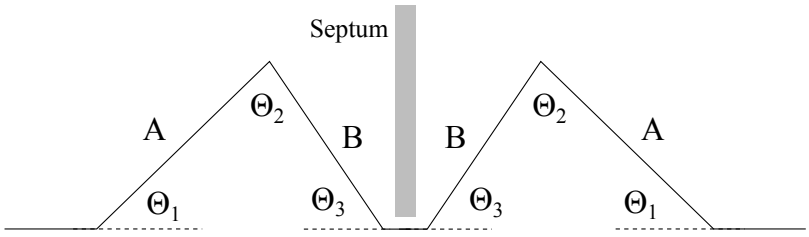

Figure 7.29: *Brace geometry.*

degrees, it is highly unlikely that a solution exists where any rigid length is longer than the chord length d. For this reason, the following analysis will focus on solutions where the longest rigid length is less than d.

Fig. 7.29 defines the sizes of the two main components of the brace to be referred to in future steps of the analysis. A and B are the respective lengths of the triangle that is the crux of the bracing. Joint 2 between lengths A and B is the elastomeric joint that has non-negligible length and can bend and twist in planes other than the bending plane required for deployment. The other joints are designed to only rotate in the plane of the cross section shown below. In this insertion analysis, therefore, Joint 2 defines a break between rigid links and Joints 1 and 3 do not. Lengths A and B, as defined for the purposes of the analysis, include the lengths of the individual stainless steel pieces and roughly half the length of the elastomeric joint as it contributes to the lengths of the triangle. Finally, length D is defined as the central rigid length composed of both B links and the piece through the septum, s, as in

$$D = 2B + s. \tag{7.18}$$

The maximum expansion of the brace occurs for the largest possible value of α' (the supplementary angle to α) or conversely the smallest value of α. Considering the catheter proceeding through the curve, touching the outer curve, the angle between any two links increases as the first link enters the arc region. The angle between the links increases and continues to increase as the second link enters the arc. α' reaches a maximum when both links are inside the confines of the arc. α' will remain constant as the connected links proceed around the curve and will begin to decrease when the first length begins to exit

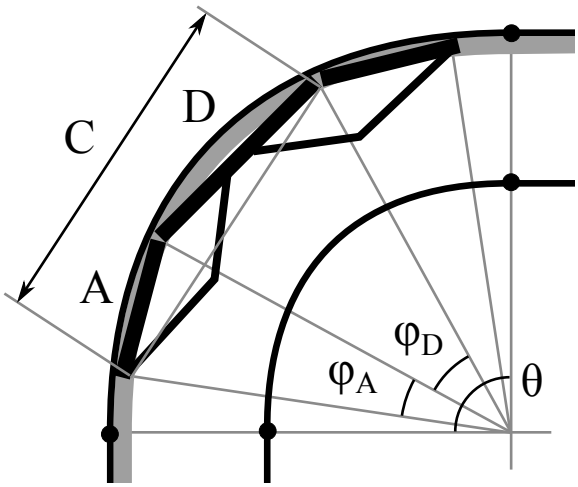

Figure 7.30: *Defining the bend angle between joints during insertion.*

the arc to a straight trajectory. Thus, maximum α' can be determined for a given joint (and this is a symmetric problem so the analysis only needs to be done once) when the two connecting links are anywhere inside the curved portion of the path. One such position is shown in Fig. 7.30. α can be defined using Fig. 7.30 to derive the following equations:

$$\phi_D = 2sin^{-1}\left(\frac{D}{2R}\right) \tag{7.19}$$

$$\phi_A = 2sin^{-1}\left(\frac{A}{2R}\right) \tag{7.20}$$

$$C = 2Rsin\left(\frac{\phi_A + \phi_D}{2}\right). \tag{7.21}$$

Now, triangle ADC is defined and angle α can be determined using the law of cosines,

$$\alpha = cos^{-1}\left(\frac{A^2 + D^2 - C^2}{2AD}\right). \tag{7.22}$$

Consider the central part of the curve to determine what brace sizing can fit a given curve. The three consecutive schematics of Fig. 7.31 show A and B getting larger. α increases as a result and the brace gets closer to filling the entire IVC. Next the model will embrace two conservative estimates to build in a factor of safety. First, the septum length is considered to be negligibly small such that triangle Bh_bX exists. This assumes the B arm is always slightly

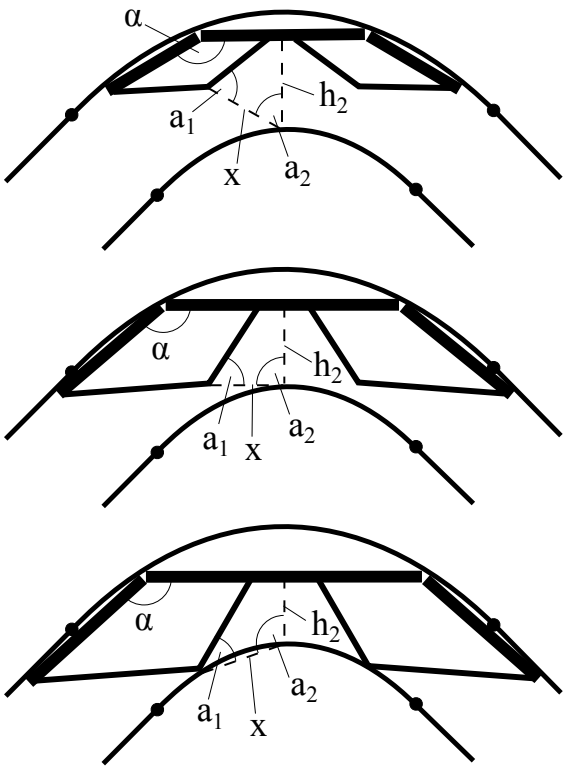

Figure 7.31: *Defining the largest possible brace.*

closer in to the center than is physically possible (there must be some septum length s).

The second conservative consideration comes in determining the final cutoff for angle a_2. Angle a_2 defines where the tip of link B is in relation to the apex of the curve. To ensure that link B never interferes with the wall of the IVC and the brace can make it around the entire curve, a conservative mandate that $a_2 \leq 90^\circ$ is enforced. This imposes a small area of safety (hashed area in Fig. 7.31(b)). Thus, the braces in Fig. 7.31(a) and Fig. 7.31(b) would pass whereas the brace in Fig. 7.31(c) would fail. The final calculations to determine a_2 are below.

First we define h_b in Fig. 7.32. Using the same chord geometry as in Fig. 7.27,

$$h_a = R - \sqrt{R^2 - \left(\frac{D}{2}\right)^2}. \tag{7.23}$$

Thus, $h_b = D_{ivc} - h_a - w$. The law of cosines is applied to calculate a_2 as in

$$X^2 = B^2 + h_b^2 - 2h_b B cos\left(\alpha - 90^\circ\right) \tag{7.24}$$

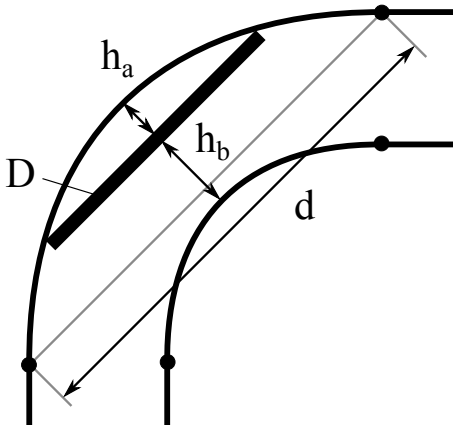

Figure 7.32: *Defining IVC geometry with respect to the long rigid brace segment.*

$$\alpha_1 = sin^{-1}\left(\frac{h_b sin\,(\alpha - 90^\circ)}{X}\right) \tag{7.25}$$

$$a_2 = 180^\circ - (\alpha - 90^\circ) - a_1 = 270^\circ - \alpha - a_1 \leq 90^\circ. \tag{7.26}$$

Finally, this algorithm can be employed to inform clinicians' decisions about sizing based solely on three pre-operative measurements. For IVC curvature, the final constraint is $\alpha_2 \leq 90^\circ$. Solving the algorithm numerically yields possible combinations of lengths A and B that satisfy this requirement. These possible combinations vary across different patient profiles. Since θ will likely be about 90°, it is most interesting to consider variation in D_{ivc} and R (the radius of curvature of the IVC). Fig. 7.33 and Fig. 7.34 show possible brace sizes for a range of D_{ivc}. The diameter of an adult IVC ranges from 1.5 cm to 2.5 cm. Here, a $1-2$ cm range is presented to address the smaller, more restrictive end of the spectrum and include children in the analysis (Krause et al. (2001)).

For discrete possible values of A, the maximum possible value of B is plotted as a function of IVC diameter. Thus, all B lengths below each A curve represent possible combinations of B and A where vertical segments of these possibilities represent all possibilities for a given D_{IVC}. Fig. 7.33 is generated for a defined $\theta = 90^\circ$ and $R = 44.75$ mm. Notice that the curve allows for larger B options, for any given A, with larger D_{IVC}. Also notice that smaller A values are above larger A values. This makes intuitive sense as a smaller A would decrease α and allow for slightly larger lengths of B to fit through the same curve. Shown here is

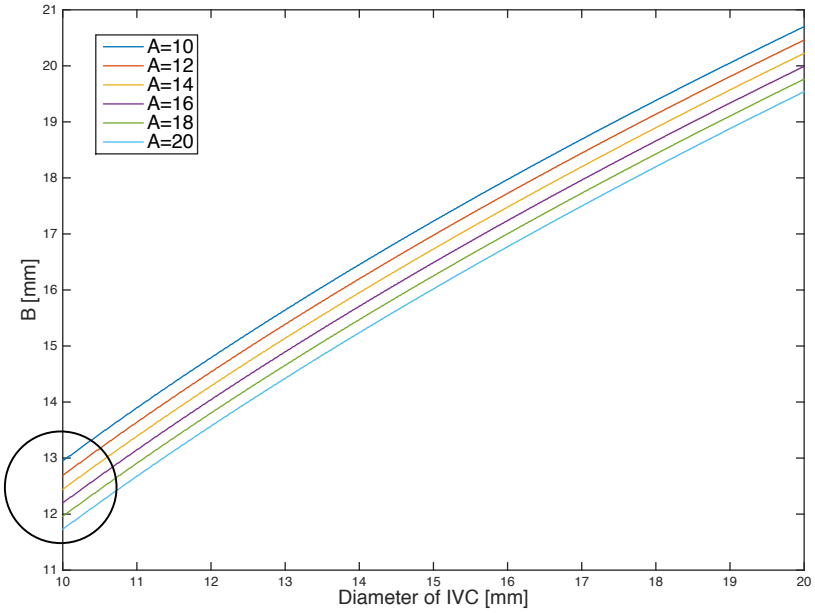

Figure 7.33: *Brace dimension options ($R = 44.75$ mm).*

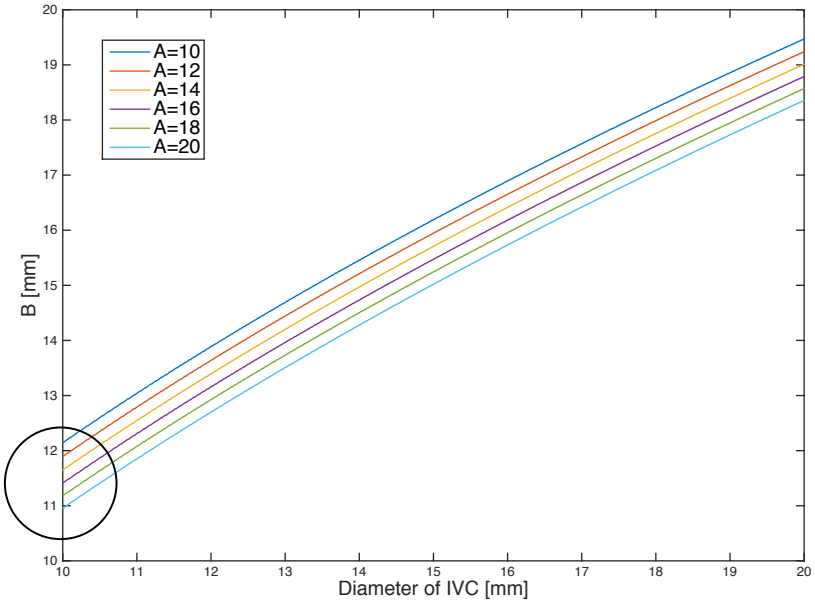

Figure 7.34: *Brace dimension options, adjusting R ($R = 40$ mm).*

the range from $A = 10\ mm$ to $A = 20\ mm$. Outside this range would follow the same trend, however this is the likely range for anatomically relevant braces.

Now consider the juxtaposition with Fig. 7.34. Here, the same concept is plotted with an adjustment to the constant patient variable R. Reducing the radius of the IVC curve shifts the plot downward accordingly. This shows that if the curve is tighter, the maximum possible size for a brace decreases.

There are in fact two additional sizing constraints beyond the curvature of the IVC. Firstly, the triangular brace design only functions as a triangular brace that reaches the septum for $A > B$. Secondly, the distal half of the brace must be able to fit inside the left atrium in a flat configuration before deployment. The diameter of the left atrium is thus an important limiting factor where $A + B < D_{atria}$. There will necessarily be a clinically relevant safety factor here that is left for determination in future work.

These constraints are added to the preceding plots with new plots (Figs. 7.35-7.36). Firstly, the constraint $A > B$ caps B_{max} values at $B_{max} = A$. Notice that for $A = 12$ and 10 and consequently all smaller A values, for the entire range of D_{IVC} shown all B values below $B = A$ are possible. Therefore, the curve of the IVC is not the limiting constraint below $A = 12$. Fig. 7.36 additionally considers the atrial diameter constraint (with the case $D_{atria} = 30\ mm$). Notice now that the ultimate maximum value for B is 15 mm (half of 30 mm). For brace hypotenuse $A > 15\ mm$, the other length of the brace (B) is now further limited to $D_{atria} - A$, which in this case is $30\ mm - A$. This means that the size of the atrium is limiting the highest B value, which determines how high on the atrial septum the brace can reach. Fig. 7.36 then tells the entire story for patients of $D_{atria} = 30\ mm$, $R = 44.75\ mm$, and D_{IVC} from $1 - 2\ cm$.

It is now critical to consider what the clinicians' goals are when sizing a brace and how to best present them with options for any patient. The normal range for the diameter of the left atrium is $28 - 40\ mm$ (Mihov and Katerska (2010)). This analysis will extend beyond the lower normal limit, showing D_{atria} beginning at 20 mm to represent the most restrictive case. The anatomy of the actual patient population will need to be surveyed for final sizing

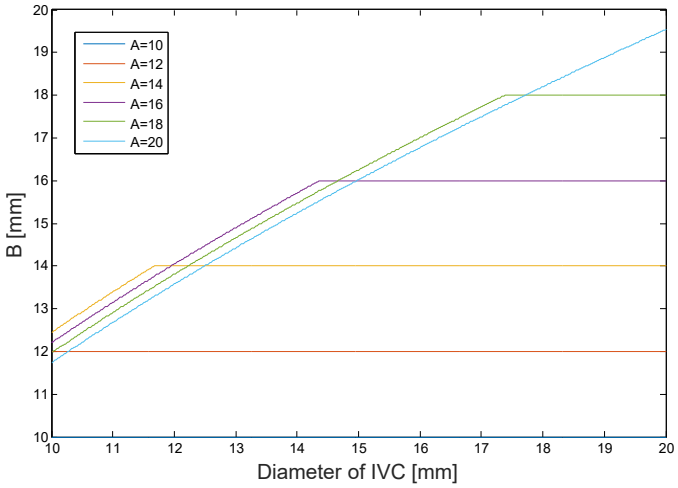

Figure 7.35: *Bracing dimension options, adding the triangular brace constraint.*

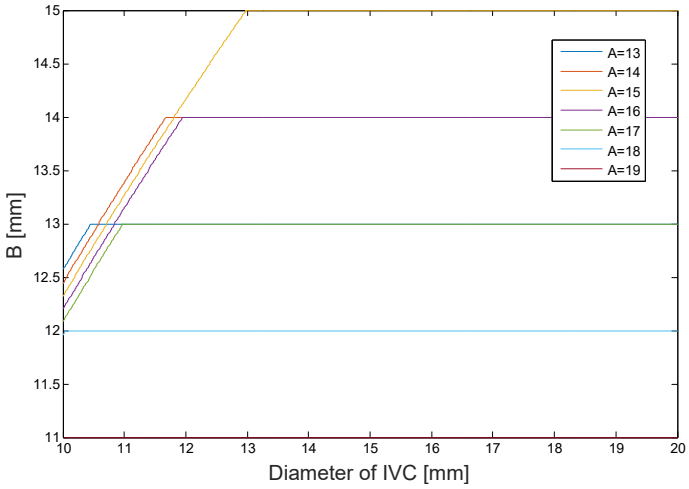

Figure 7.36: *Bracing dimension options, adding the triangular brace constraint and the atrial diameter constraint.*

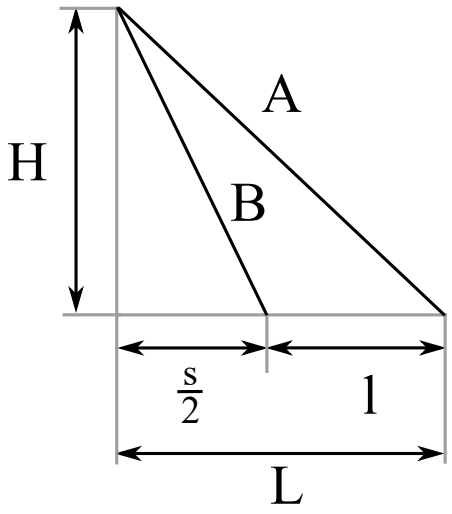

Figure 7.37: *Defining lengths L and H.*

recommendation.

The previous plots (all representing B versus D_{IVC}) are useful to show what brace dimensions (A and B) will fit through a given curve. With many combinations of A and B possible, we then turn to optimizing the size choice. The clinician cares most about dimensions H (the height of the brace about the septum) and L (the distance of the brace into the atrium when deployed) (Fig. 7.37). For any given A and B, H and L are defined quantities with small variability due to septum thickness variability. For any brace, the brace dimension s will be chosen such that it is thicker than the septum at likely points of brace tip contact. A septum thickness profile can be estimated with pre-operative imaging to motivate this size selection. Take the smallest case, for example. 2 mm is chosen here as a reasonable small size to accommodate septums thinner than 2 mm. The clinician ultimately wants to choose a brace size (determined by s, A, and B) for a desired H and L. Even for a given brace size, H and L will vary slightly depending on the true thickness of the septum where the brace is finally seated. To accommodate this range, the minimal H value (if the septum is infinitely thin), and its corresponding L, will be considered (Fig. 7.37).

L defines the possible working space inside the atrium,

$$L = \frac{s}{2} + l = \sqrt{A^2 - B^2 + \left(\frac{s}{2}\right)^2}. \tag{7.27}$$

L also determines what fractional length of the catheter is supported by the brace. Therefore, longer L increases k_{tip} (the stiffness at the tip of the catheter) because more of the catheter body is supported by the rigid brace. However, L must be chosen to leave sufficient room for access to the necessary areas of the atrium.

H is given by

$$H = \sqrt{B^2 - \left(\frac{s}{2}\right)^2}. \tag{7.28}$$

For bracing purposes, it is also desirable to maximize H to reach the upper and lower edges of the patient's septum. Recall that the septum meets the atrial wall near the base of the valves where the fibrous skeleton of the heart may provide a rigid bracing seat. The height of the atrium can also be determined by pre-operative US.

The anatomical constraints defined previously should then be presented with these motivations for selecting L and H in mind. Consider the plots of B and D_{IVC}. Those are shown below for $D_{atria} = 20$, 30, and 40 mm. Notice that the possible brace length values are very different due to the anatomical variation. At the final level of clinician decision-making, all pre-operative measurements will have been taken, and the clinician is making decisions for a particular patient with a known profile. The analysis will thus continue for a patient with IVC diameter of $1.5cm$. Figs. 7.38-7.40 compare three patients: $D_{atria} = 20\ mm$, $D_{IVC} = 15\ mm$; $D_{atria} = 30\ mm$, $D_{IVC} = 15\ mm$; and $D_{atria} = 40\ mm$, $D_{IVC} = 15\ mm$.

Recall that, in B versus D_{IVC} plots, discrete values of A were plotted for the maximum corresponding B that comprised a brace that met all the aforementioned constraints. Any curve represents a value of A for which all values of B below the curve are viable. Therefore, at any ordinate, that value of B falls within the scope of possible B's for all A's that exist vertically above it. This can be solved numerically for a range of B values, where each possible A value is converted to the corresponding L, the value of interest. H is easily calculated from Equation 7.27. Since septum thickness s is small compared to link lengths

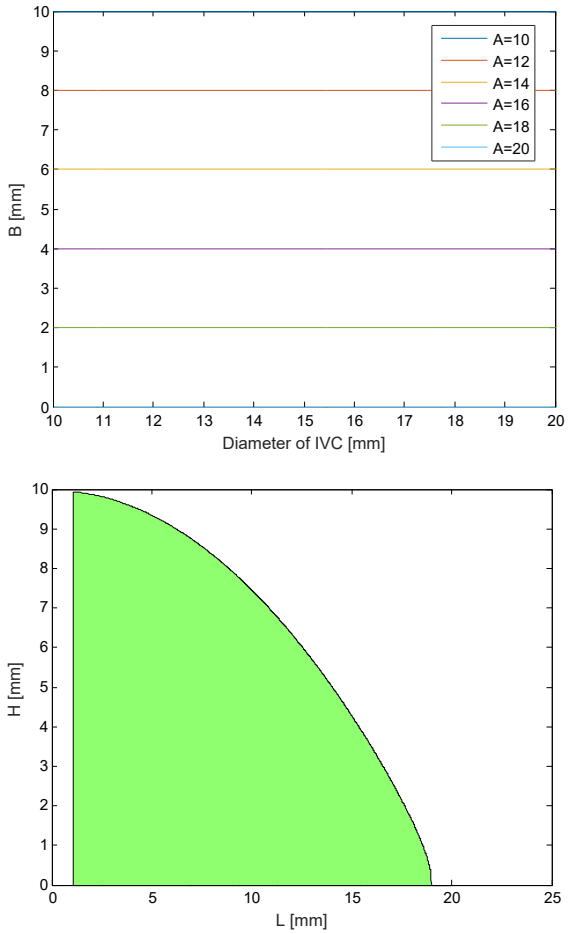

Figure 7.38: *Understanding the final clinician tradeoff plot ($D_{atria} = 20\ mm$, $D_{IVC} = 15\ mm$).*

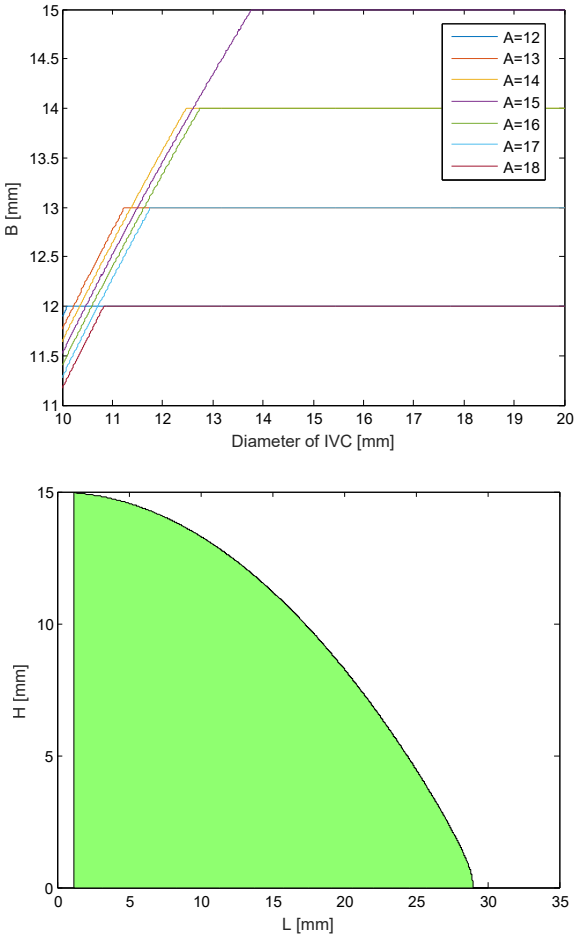

Figure 7.39: *Understanding the final clinician tradeoff plot ($D_{atria} = 30\ mm$, $D_{IVC} = 15\ mm$).*

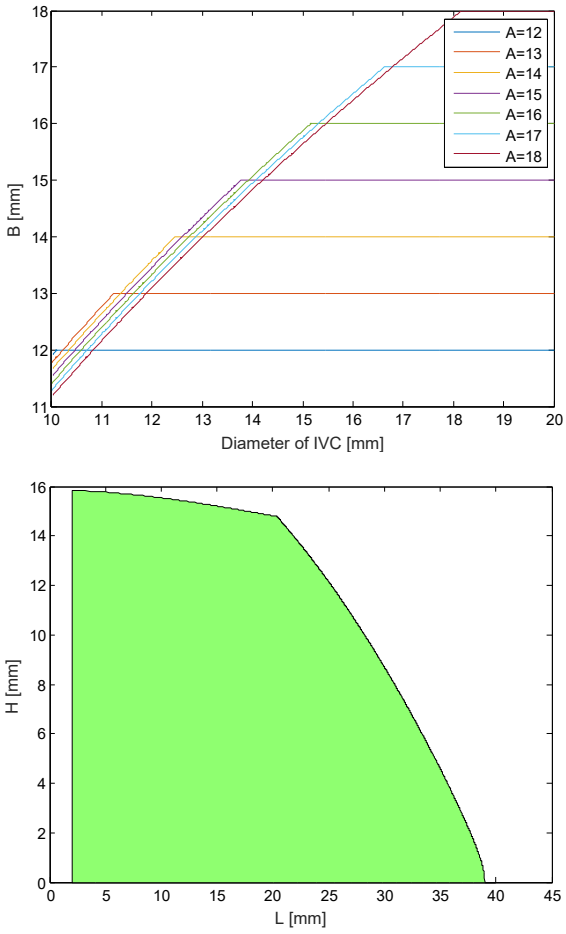

Figure 7.40: *Understanding the final clinician tradeoff plot ($D_{atria} = 40\ mm$, $D_{IVC} = 15\ mm$).*

A and B, $H \approx B$. Thus, the main utility of this step is the numerical solution which derives possible corresponding values of L for possible B (and consequently H) values. This numerical solution summarizing the clinician's decision matrix is plotted below each B versus D_{IVC} plot.

The shaded blue area represents possible selections for H and L on an individual patient basis. A population study to determine the full range of potential anatomies would allow optimization of discrete sizing choices. These could be represented as dots within these shaded areas. The clinician would then have the knowledge of which existing sized braces could fit their patient. With multiple size options, they could then choose the best size for their needs (which may require a tradeoff between optimal H height and optimal L length).

Notice the inflection point in the third graph. This point marks a change in the constraining regime that is most restrictive. For the $D_{atria} = 20\ mm$ and $D_{atria} = \ 30mm$ cases, the diameter of the atrium is the most restrictive constraint for all possible B lengths. Note also that the B versus D_{IVC} plots only show a few values for A for ease of viewing. In solving for the H versus L plot, a higher resolution of at least 100 values for A ranging from $0 - D_{atria}$ was implemented. For the $D_{atria} = 40\ mm$ case, the inflection point marks the change from D_{atria} being the more restrictive constraint (for low B) to the curvature of the IVC being the most restrictive constraint (for high B). The inflection point exists near $H \approx B = 14.8\ mm$, which is where (with all A's from $0 - 40\ mm$ plotted) the vertical line $D_{IVC} = 15\ mm$ first intersects the curved lines above the horizontal constraints. Further along the line $D_{IVC} = 15\ mm$, the final A value representing the highest possible B value is reached at $15.8\ mm$. Thus, the curvature of the IVC restricts brace sizing options in this region ($B \approx H$, between $14.8 - 15.8\ mm$) and the brace height cannot reach up to half of D_{atria} (20 mm in this case) as in the other cases where D_{atria} is the entirely limiting factor. You can expect a similar inflection point for patients with $D_{atria} = 30\ mm$ and $D_{IVC} < 13\ mm$, for example.

With this understanding of the different constraints on brace sizing, a patient specific chart can provide clinicians with the necessary knowledge to make informed brace sizing

Table 7.1: *Cardiac catheter brace specifications. *Stiffness depends on inner catheter and septum rigidity. In vivo testing required for best evaluation.*

Requirement	Current Status
$\geq 0.4\ N/mm$ stiffness at tip	*Stiffness range: $0.7\ N/mm$ to $6.0\ N/mm$ ✓
$\leq 24\ Fr$	$18\ Fr$ ✓
Open inner lumen	✓
Insertable through vasculature	✓
Deployable $\leq 10\ N$	$1.2\ N$ ✓
Designed with medical device constraints	✓

decisions.

7.7 Discussion

The cardiac catheter bracing prototype was built through a series of prototype iterations. The joints were designed to be flexible enough to steer through tortuous blood vessels and structurally sound enough to provide bracing support when deployed. Bench top test results demonstrated that the brace successfully could be inserted through tortuous vasculature and deployed with very low forces. Bracing tests were conducted by applying force to the catheter inside the brace and measuring the resulting displacement. These tests were repeated in a rigid environment and a nonrigid environment. In both cases, the brace provided additional stiffness to the catheter. Table 7.1 is a summary of these technical requirements and the corresponding current specifications of the brace. All of the technical requirements were met. Finally, an analytical patient-specific sizing algorithm was derived. A calculator could be created such that the clinician enters key anatomical information and the best brace size is automatically selected.

Additional work aims towards testing the brace in *ex vivo* and then *in vivo* porcine models. A protective outer coating is necessary to encapsulate the entire device. There is a wide range of biocompatible polymers with many different properties that could serve as a

soft outer bag. Stretchable elastomers, like TPU, could expand over the device as it deploys. Alternatively, less elastic plastics like PTFE could be loose and folded up prior to deployment and then wrapped tightly over the device when deployed. The sizing algorithm must be experimentally verified and population tested to determine the best sizes for manufacturing. The development of a bracing mechanism or strategy is critical to the overall success of improving surgical dexterity through cardiac catheters, with the aim of enabling more cardiac procedures to be feasible through catheter.

7.8 Conclusion

This chapter develops a novel device to improve cardiac surgery by mechanically supporting flexible catheter tools inside the beating heart. The cardiac catheter brace maintains a low profile as part of a flexible catheter during navigation. Upon deployment it provides high stiffness to ground catheters to cardiac anatomy. This will allow for enhanced surgical dexterity through catheters, allowing precise manipulation of left atrial tissue during procedures like mitral valve repair. The innovation could greatly benefit patients by permitting less invasive surgical strategies.

Chapter 8

Conclusions

This thesis investigates navigation and control of off-the-shelf flexible manipulators as well as support techniques and structures for stabilization. In Chapter 2 the first prototype system for steering a 4-DOF US imaging catheter in a constrained bench top setting was developed. In Chapter 3 the robot was redesigned to improve accuracy and clinical usability for *in vivo* experiments. Chapter 4 addressed disturbances to the catheter body from unconstrained catheter bending and physiological motion. The robust disturbance rejection controller was demonstrated through *in vivo* experiments. In Chapter 5 a respiratory breathing model was applied to the disturbance rejection controller. The system demonstrated the use of respiratory motion compensation as well as target predictive filtering through *in vivo* experiments. Chapters 6 and 7 focused on structural support for cardiac catheters. Chapter 6 presented a model for actively changing the stiffness of a custom-built flexible manipulator. Chapter 7 demonstrated an inter-atrial septum stabilizing brace for cardiac catheters.

This work examines several key topics towards improving minimally invasive surgery with flexible manipulators. Specific contributions include:

- A kinematics and control strategy for positioning and orienting 4-DOF flexible manipulators
- Rejecting disturbances to the body of a flexible manipulator
- Catheter steering with model-based respiratory motion compensation

- Applying predictive filtering towards steering flexible manipulators
- Accurate automatic cardiac catheter steering in *in vivo* porcine experiments
- Modeling friction interactions to control stiffness in segmented flexible manipulators
- Patient-specific catheter brace design which is flexible, deployable, and structurally supportive

8.1 Insights and Future Work

8.1.1 Kinematics and Control

Many kinematic strategies have been presented in the literature on flexible manipulators, and this work focuses on Denavit-Hartenberg and geometry derived kinematic solutions. We assume bending occurs in one plane only, curvature is circular, and control knob efficiency is ideal. This strategy succeeds due to control gains (< 1) and the iterative nature of the controller. Specifically, the inverse kinematic calculations solve for joint knob adjustments which steer the catheter pose in the correct direction. Motion is smoothed by using dynamically changing control gains to scale down the magnitudes of the control knob adjustments. Iterative control calculations cause the catheter tip to converge to the desired pose.

There are several strategies which can be employed to increase motion smoothness and speed to converge on the target pose. Modeling non-circular curvature would increase the accuracy of the inverse kinematic solutions. It may also be possible to optimize the dynamic gain adjustments. Currently, a linear model is used to decrease the gains as the catheter tip gets closer to the desired pose. An optimized linear or non-linear model would provide faster convergence. Motion can also be improved by examining catheter mechanics nonlinearities such as pull wire dead zones, backlash, and plastic compression. Additionally, software changes to the system can reduce time for calculations and communications. This would increase the system bandwidth and increase speed.

The controller is also robust to poor control knob efficiency because the catheter features

two sensors measuring the tip and the base of the bending section. The base sensor enables the system to measure how much roll, pitch, yaw, and translation have been transmitted to the bending section and then calculate 4-DOF kinematics accordingly. Without sensors at these locations, a different sensing strategy such as fiber-optics or x-ray would be needed in order to observe catheter body motion.

8.1.2 Motion Compensation

The model-based motion compensation techniques implemented in Chapter 5 were demonstrated in one *in vivo* animal experiment thus far, with plans for additional experiments. The success of the first *in vivo* experiment demonstrates the first instance of robotic cardiac catheter steering with motion compensation known to the author. Further work is needed to understand the limitations of this model-based technique. The model is based on catheter motion data collected in a specific region of the heart throughout multiple respiratory cycles. Relocating the catheter to a different region of the heart reduces the accuracy of the model, and a new model must be created. The robot motors must then be deactivated for at least three respiratory cycles while the new model is calculated.

It would be advantageous for the system to be able to adjust respiratory motion models while the robot is running. It may be possible to create respiratory motion maps across a whole heart chamber, such as the RA. This would require measuring respiratory motion in several different locations throughout the RA and then interpolating between those models to calculate the catheter's respiratory model at any current location. This strategy would be beneficial because the catheter could move freely about the RA and the updated respiratory motion model would always reflect the effects of breathing on the catheter at that location within the heart. A different strategy could use the target model (which is continuously updated by the EKF) to adjust catheter breathing models while the catheter is in motion. This would provide respiration-specific changes measured in the target pose to be reflected in the catheter tip and base poses, but it would not increase the region represented by the current model.

8.1.3 Predictive Filtering

The US catheter steering system uses a predictive filter to compensate for delays by estimating the future location of the target catheter and beginning to point towards the correct direction ahead of time. An EKF continuously predicts and updates a model of target motion due to respiration only. The EKF was chosen for its ability to accurately estimate motion with uncertainty, and for its demonstrated success in previous robotic motion compensation work. The EKF was effective during the first US catheter steering *in vivo* experiment, but the method of filtering only respiratory motion resulted in tracking that was less accurate than it could be. This is because the target catheter was located in the LV which has large cardiac displacement on each heartbeat. The EKF was meant to model respiratory motion only, but the updated values were highly influenced by cardiac motion. In future *in vivo* experiments it may be necessary to filter the raw cardiac + respiratory motion signal rather than filtering the isolated respiratory motion. This would also affect the current strategy of compensating for low pass filter delays. It would also be beneficial to examine other predictive filtering methods (such as the WFLC) which are commonly demonstrated in the literature for physiological motion tracking.

8.1.4 Catheter Handle

Chapter 3 develops a robot for quickly and easily interfacing with the US catheter handle. We chose to interface with the catheter handle so that clinicians can switch back and forth between manual and automated steering motions as desired. Numerous downsides to this strategy include pull wire related nonlinearities due to excessive pull wire slack. The alternative strategy would be to interface directly with the pull wires. This would be beneficial because then the system could monitor the amount of slack in each line (with direct tension measurements or with indirect motor current sensing) and quickly compensate for many mechanical nonlinearities, but then the clinician would not be able to steer the catheter by hand. Interfacing with the US catheter handle results in lower bandwidth motion, which has now been proven suitable for lower speed respiratory compensation.

It is expected that interfacing directly with the pull wires would be necessary in order to achieve the high speeds required for cardiac motion compensation. A higher bandwidth system would need to be implemented in order to verify this. Ultimately, how to manage the trade off between clinical feasibility and improved control is still an open discussion and this work does not seek to find the conclusion. This work demonstrates some possibilities of what can be done while interfacing with the catheter handle.

8.1.5 Catheter Navigation Sensing

To continue on the topic of clinical feasibility and acceptance, this work on US catheter steering used an EM-based sensing strategy. EM sensing was chosen over full-body catheter sensors (fiber optics) and 3D medical imaging modalities (CT, MRI) because it is low cost and already clinically accepted. Cardiac electrophysiology suites are already built to reduce EM field disturbance and the catheters already have EM sensors embedded inside. Our US catheter steering system measures two points on the US catheter bending section, the tip of the target catheter, and the patient chest wall. Observability during instrument tracking tests is sufficient because the target instrument is sensed and the US catheter is steered to point at it. Accurate catheter steering is achieved by a robust kinematics and control strategy for rejecting disturbances (Section 8.1.1). However, a key issue remains: the system is currently unable to directly measure the location of cardiac tissue. It is not possible to attach an EM sensor to every tissue target. During image reconstruction tests the system can move the US imager by a user-defined amount, but it is not yet possible to use US images for feedback to the controller. The system can maintain the US catheter in a fixed pose with respect to the cardiac chamber throughout the respiratory cycle, but there is no guarantee that the same US imager pose is measuring the same tissue point on each breath. This limits the accuracy of tissue imaging tests. Future work will aim to use the 2D US images in controller feedback. Contextual information will be required in order to track tissue when features move out of the 2D US imaging plane.

8.1.6 Structural Support

Two methods for structural support were developed in Chapters 6 and 7. The active stiffness changing catheter system in Chapter 6 requires further work integrating a working channel through the center of the manipulator and an outer covering with minimal effects on stiffness calculations. It is also necessary to expand the model from the two-vertebrae solution to a multi-vertebrae solution. Then the active stiffness changing system and the cardiac catheter brace can be tested with *ex vivo* animal tissues in a realistic bench top setting, and later during *in vivo* experiments as well.

8.1.7 Applications

The US catheter steering system in its current state is already able to assist with tracking working instruments and visualizing tissue. Instrument tracking with the US imager may be useful for existing procedures such as monitoring tissue during catheter-based cardiac ablation and verifying safety during transeptal punctures. Instrument tracking can also be applied to US monitoring stem cell injections and localizing biopsy collection. Image mosaic reconstruction may be useful for visualizing anatomical regions and diagnosing cardiac disease. The control strategy can also be applied to a catheter steering system in which tip positioning (rather than imager orientation) is the primary goal. These techniques can be applied to steering ablation or other working catheters while compensating for cardiac and respiratory motion. Catheter steering with accurate motion compensation and structural support devices has the potential to enable less-invasive cardiac surgery procedures.

References

H.-C. Kung, D. L. Hoyert, J. Xu, S. L. Murphy *et al.*, "Deaths: final data for 2005," *Natl Vital Stat Rep*, vol. 56, no. 10, pp. 1–120, 2008.

M. Moscucci, *Grossman & Baim's Cardiac Catheterization, Angiography, and Intervention*. Lippincott Williams & Wilkins, 2013.

J. M. Murkin, W. D. Boyd, S. Ganapathy, S. J. Adams, and R. C. Peterson, "Beating heart surgery: why expect less central nervous system morbidity?" *The Annals of thoracic surgery*, vol. 68, no. 4, pp. 1498–1501, 1999.

G. W. Roach, M. Kanchuger, C. M. Mangano, M. Newman, N. Nussmeier, R. Wolman, A. Aggarwal, K. Marschall, S. H. Graham, C. Ley *et al.*, "Adverse cerebral outcomes after coronary bypass surgery," *New England Journal of Medicine*, vol. 335, no. 25, pp. 1857–1864, 1996.

A. Ali, D. H. Plettenburg, and P. Breedveld, "Steerable catheters in cardiology: Classifying steerability and assessing future challenges," *IEEE Transactions on Biomedical Engineering*, vol. 63, no. 4, pp. 679–693, 2016.

I. Catheter Robotics. (2016) Catheter Robotics, Inc. *Amigo Remote Catheter System*. [Online]. Available: http://www.catheterrobotics.com/

I. Corindus. (2016) Corindus, Inc. *CorPath Robotic PCI*. [Online]. Available: http://www.corindus.com/

Stereotaxis. (2016) Stereotaxis *V-Drive Robotic Navigation System*. [Online]. Available: http://www.stereotaxis.com/products/vdrive/

I. Stereotaxis. (2016) Stereotaxis *Niobe ES*. [Online]. Available: http://www.stereotaxis.com/products/niobe/

I. Hansen Medical. (2016) Hansen Medical, Inc. *Sensei X Robotic Catheter System*. [Online]. Available: http://hansenmedical.com

I. Intuitive Surgical. (2016) da Vinci Xi Surgical System. [Online]. Available: http://www.intuitivesurgical.com/products/da-vinci-xi/

F. M. Creighton IV, R. C. Ritter, R. R. Viswanathan, N. Kastelein, J. M. Garibaldi, and W. Flickinger, "Operation of a remote medical navigation system using ultrasound image," Sep. 5 2008, uS Patent App. 12/205,137.

Y. Thakur, J. S. Bax, D. W. Holdsworth, and M. Drangova, "Design and performance evaluation of a remote catheter navigation system," *Biomedical Engineering, IEEE Transactions on*, vol. 56, no. 7, pp. 1901–1908, 2009.

J. W. Park, J. Choi, H.-N. Pak, S. J. Song, J. C. Lee, Y. Park, S. M. Shin, and K. Sun, "Development of a force-reflecting robotic platform for cardiac catheter navigation," *Artificial organs*, vol. 34, no. 11, pp. 1034–1039, 2010.

F. Arai, R. Fujimura, T. Fukuda, and M. Negoro, "New catheter driving method using linear stepping mechanism for intravascular neurosurgery," in *Robotics and Automation, 2002. Proceedings. ICRA'02. IEEE International Conference on*, vol. 3. IEEE, 2002, pp. 2944–2949.

L. Cercenelli, E. Marcelli, and G. Plicchi, "Initial experience with a telerobotic system to remotely navigate and automatically reposition standard steerable ep catheters," *ASAIO Journal*, vol. 53, no. 5, pp. 523–529, 2007.

T. Wang, D. Zhang, and L. Da, "Remote-controlled vascular interventional surgery robot," *The International Journal of Medical Robotics and Computer Assisted Surgery*, vol. 6, no. 2, pp. 194–201, 2010.

R. J. Webster and B. A. Jones, "Design and kinematic modeling of constant curvature continuum robots: A review," *The International Journal of Robotics Research*, 2010.

D. B. Camarillo, C. R. Carlson, and J. K. Salisbury, "Task-space control of continuum manipulators with coupled tendon drive," in *Experimental Robotics*. Springer, 2009, pp. 271–280.

Y. Ganji and F. Janabi-Sharifi, "Catheter kinematics for intracardiac navigation," *Biomedical Engineering, IEEE Transactions on*, vol. 56, no. 3, pp. 621–632, 2009.

R. S. Penning, J. Jung, J. A. Borgstadt, N. J. Ferrier, and M. R. Zinn, "Towards closed loop control of a continuum robotic manipulator for medical applications," in *Robotics and Automation (ICRA), 2011 IEEE International Conference on*. IEEE, 2011, pp. 4822–4827.

J. Jagadeesan, R. V. Patel, and S. Nikumb, "Robot-assisted active catheter insertion: algorithms and experiments," *The International Journal of Robotics Research*, vol. 28, no. 9, pp. 1101–1117, 2009.

J. Jagadeesan, M. Azizian, and R. V. Patel, "Bilateral telemanipulation of a flexible catheter in a constrained environment," in *Robotics and Automation, 2008. ICRA 2008. IEEE International Conference on*. IEEE, 2008, pp. 649–654.

J. Jung, R. S. Penning, N. J. Ferrier, and M. R. Zinn, "Model validation and simulation studies: Effects of nonlinear internal device friction on continuum robotic manipulators," in *IEEE Int. Conf. Robotics and Automation*, 2012.

M. Khoshnam, A. C. Skanes, and R. V. Patel, "Modeling and estimation of tip contact force for steerable ablation catheters," *IEEE Transactions on Biomedical Engineering*, vol. 62, no. 5, pp. 1404–1415, 2015.

M. C. Yip and D. B. Camarillo, "Model-less hybrid position/force control: a minimalist approach for continuum manipulators in unknown, constrained environments," *IEEE Robotics and Automation Letters*, vol. 1, no. 2, pp. 844–851, 2016.

Y. Ganji, F. Janabi-Sharifi, and A. N. Cheema, "Robot-assisted catheter manipulation for intracardiac navigation," *International journal of computer assisted radiology and surgery*, vol. 4, no. 4, pp. 307–315, 2009.

R. J. Webster III, A. M. Okamura, and N. J. Cowan, "Toward active cannulas: Miniature snake-like surgical robots," in *Intelligent Robots and Systems, 2006 IEEE/RSJ International Conference on*. IEEE, 2006, pp. 2857–2863.

P. Sears and P. Dupont, "A steerable needle technology using curved concentric tubes," in *Intelligent Robots and Systems, 2006 IEEE/RSJ International Conference on*. IEEE, 2006, pp. 2850–2856.

R. J. Webster, J. S. Kim, N. J. Cowan, G. S. Chirikjian, and A. M. Okamura, "Nonholonomic modeling of needle steering," *The International Journal of Robotics Research*, vol. 25, no. 5-6, pp. 509–525, 2006.

S. P. DiMaio and S. Salcudean, "Needle steering and motion planning in soft tissues," *Biomedical Engineering, IEEE Transactions on*, vol. 52, no. 6, pp. 965–974, 2005.

N. V. Vasilyev, A. H. Gosline, E. Butler, N. Lang, P. J. Codd, H. Yamauchi, E. N. Feins, C. R. Folk, A. L. Cohen, R. Chen *et al.*, "Percutaneous steerable robotic tool delivery platform and metal mems device for tissue manipulation and approximation: Closure of patent foramen ovale in an animal model," *Circulation. Cardiovascular interventions*, vol. 6, no. 4, 2013.

R. J. Hendrick, C. R. Mitchell, S. D. Herrell, and R. J. Webster, "Hand-held transendoscopic robotic manipulators: A transurethral laser prostate surgery case study," *The International Journal of Robotics Research*, p. 0278364915585397, 2015.

G. J. Vrooijink, T. Ellenbroek, P. Breedveld, J. G. Grandjean, and S. Misra, "A preliminary study on using a robotically-actuated delivery sheath (rads) for transapical aortic valve implantation," in *Robotics and Automation (ICRA), 2014 IEEE International Conference on*. IEEE, 2014, pp. 4380–4386.

S. Seung, P. Liu, S. Park, J.-O. Park, and S. Y. Ko, "Single-port robotic manipulator system for brain tumor removal surgery: Siromans," *Mechatronics*, vol. 26, pp. 16–28, 2015.

R. E. Goldman, A. Bajo, L. S. MacLachlan, R. Pickens, S. D. Herrell, and N. Simaan, "Design and performance evaluation of a minimally invasive telerobotic platform for transurethral surveillance and intervention," *Biomedical Engineering, IEEE Transactions on*, vol. 60, no. 4, pp. 918–925, 2013.

G. Chen, M. T. Pham, T. Maalej, H. Fourati, R. Moreau, and S. Sesmat, "A biomimetic steering robot for minimally invasive surgery application," *Advances in Robot Manipulators*, pp. pp–1, 2010.

B. Bardou, P. Zanne, F. Nageotte, and M. De Mathelin, "Control of a multiple sections flexible endoscopic system," in *Intelligent Robots and Systems (IROS), 2010 IEEE/RSJ International Conference on*. IEEE, 2010, pp. 2345–2350.

T. Ota, A. Degani, D. Schwartzman, B. Zubiate, J. McGarvey, H. Choset, and M. A. Zenati, "A highly articulated robotic surgical system for minimally invasive surgery,"*The Annals of thoracic surgery*, vol. 87, no. 4, pp. 1253–1256, 2009.

L. Ott, F. Nageotte, P. Zanne, and M. De Mathelin, "Robotic assistance to flexible endoscopy by physiological-motion tracking," *IEEE Transactions on Robotics*, vol. 27, no. 2, pp. 346–359, 2011.

B. A. Jones and I. D. Walker, "Kinematics for multisection continuum robots," *Robotics, IEEE Transactions on*, vol. 22, no. 1, pp. 43–55, 2006.

G. S. Chirikjian and J. W. Burdick, "Kinematically optimal hyper-redundant manipulator configurations," *Robotics and Automation, IEEE Transactions on*, vol. 11, no. 6, pp. 794–806, 1995.

H. Mochiyama and T. Suzuki, "Dynamical modelling of a hyper-flexible manipulator," in *SICE 2002. Proceedings of the 41st SICE Annual Conference*, vol. 3. IEEE, 2002, pp. 1505–1510.

D. C. Rucker and R. J. Webster III, "Mechanics of continuum robots with external loading and general tendon routing," in *Experimental Robotics*. Springer, 2014, pp. 645–654.

I. A. Gravagne, C. D. Rahn, and I. D. Walker, "Large deflection dynamics and control for planar continuum robots," *Mechatronics, IEEE/ASME Transactions on*, vol. 8, no. 2, pp. 299–307, 2003.

H. Calkins, P. Jais, and J. S. Steinberg, *A practical approach to catheter ablation of atrial fibrillation*. Lippincott Williams & Wilkins, 2008.

J.-F. Ren and F. E. Marchlinski, "Utility of intracardiac echocardiography in left heart ablation for tachyarrhythmias," *Echocardiography*, vol. 24, no. 5, pp. 533–540, 2007.

L. M. Epstein, M. A. Mitchell, T. W. Smith, and D. E. Haines, "Comparative study of fluoroscopy and intracardiac echocardiographic guidance for the creation of linear atrial lesions," *Circulation*, vol. 98, no. 17, pp. 1796–1801, 1998.

N. F. Marrouche, D. O. Martin, O. Wazni, A. M. Gillinov, A. Klein, M. Bhargava, E. Saad, D. Bash, H. Yamada, W. Jaber *et al.*, "Phased-array intracardiac echocardiography monitoring during pulmonary vein isolation in patients with atrial fibrillation impact on outcome and complications," *Circulation*, vol. 107, no. 21, pp. 2710–2716, 2003.

J. M. Cooper and L. M. Epstein, "Use of intracardiac echocardiography to guide ablation of atrial fibrillation," *Circulation*, vol. 104, no. 25, pp. 3010–3013, 2001.

S. G. Dravid, B. Hope, and J. J. McKinnie, "Intracardiac echocardiography in electrophysiology: a review of current applications in practice," *Echocardiography*, vol. 25, no. 10, pp. 1172–1175, 2008.

M. Jongbloed, J. Bax, N. de Groot, M. Dirksen, H. Lamb, A. de Roos, E. van der Wall, and M. Schalij, "Radiofrequency catheter ablation of paroxysmal atrial fibrillation; guidance by intracardiac echocardiography and integration with other imaging techniques,"*European Journal of Echocardiography*, vol. 4, no. 1, pp. 54–58, 2003.

P. Loschak, L. Brattain, and R. Howe, "Automated pointing of cardiac imaging catheters," in *Robotics and Automation (ICRA), 2013 IEEE Int'l Conf. on*, May 2013, pp. 5794–5799.

D. B. Camarillo, C. R. Carlson, and J. K. Salisbury, "Configuration tracking for continuum manipulators with coupled tendon drive," *Robotics, IEEE Trans. on*, vol. 25, no. 4, pp. 798–808, 2009.

D. C. Rucker and R. J. Webster, "Statics and dynamics of continuum robots with general tendon routing and external loading," *Robotics, IEEE Transactions on*, vol. 27, no. 6, pp. 1033–1044, 2011.

R. J. Schilling, "Fundamentals of robotics: Analysis and control," *PHI, New Delhi*, pp. 38–40, 1992.

R. O. Bude and R. S. Adler, "An easily made, low-cost, tissue-like ultrasound phantom material," *Journal of clinical ultrasound*, vol. 23, no. 4, pp. 271–273, 1995.

L. J. Brattain, P. M. Loschak, C. M. Tschabrunn, E. Anter, and R. D. Howe, "Instrument tracking and visualization for ultrasound catheter guided procedures," in *Augmented Environments for Computer-Assisted Interventions*. Springer, 2014, pp. 41–50.

L. Brattain, "Enhanced ultrasound visualization for procedure guidance," Ph.D. dissertation, Harvard University, 2014.

S. B. Kesner and R. D. Howe, "Design and control of motion compensation cardiac catheters," in *Robotics and Automation (ICRA), 2010 IEEE International Conference on*. IEEE, 2010, pp. 1059–1065.

M. Khoshnam, M. Azizian, and R. V. Patel, "Modeling of a steerable catheter based on beam theory," in *Robotics and Automation (ICRA), 2012 IEEE International Conference on*. IEEE, 2012, pp. 4681–4686.

P. M. Loschak, Y. Tenzer, A. Degirmenci, and R. D. Howe, "A 4-dof robot for positioning ultrasound imaging catheters," in *ASME 2015 International Design Engineering Technical Conferences and Computers and Information in Engineering Conference*. American Society of Mechanical Engineers, 2015, pp. V05AT08A046–V05AT08A046.

P. M. Loschak, A. Degirmenci, Y. Tenzer, C. M. Tschabrunn, E. Anter, and R. D. Howe, "A four degree of freedom robot for positioning ultrasound imaging catheters," in *ASME J. Mechanisms Robotics*. American Society of Mechanical Engineers, 2016, pp. 051 016–051 016–9.

P. A. Noseworthy, Z. J. Malchano, J. Ahmed, G. Holmvang, J. N. Ruskin, and V. Y. Reddy, "The impact of respiration on left atrial and pulmonary venous anatomy: implications for image-guided intervention," *Heart Rhythm*, vol. 2, no. 11, pp. 1173–1178, 2005.

S. Roujol, E. Anter, M. E. Josephson, and R. Nezafat, "Characterization of respiratory and cardiac motion from electro-anatomical mapping data for improved fusion of mri to left ventricular electrograms," *PloS one*, vol. 8, no. 11, p. e78852, 2013.

D. Peressutti, G. P. Penney, R. J. Housden, C. Kolbitsch, A. Gomez, E.-J. Rijkhorst, D. C. Barratt, K. S. Rhode, and A. P. King, "A novel bayesian respiratory motion model to estimate and resolve uncertainty in image-guided cardiac interventions," *Medical image analysis*, vol. 17, no. 4, pp. 488–502, 2013.

T. Ortmaier, M. Groger, D. H. Boehm, V. Falk, and G. Hirzinger, "Motion estimation in beating heart surgery," *IEEE Transactions on Biomedical Engineering*, vol. 52, no. 10, pp. 1729–1740, 2005.

I. Accuray. (2016) Accuray, Inc. *CyberKnife System*. [Online]. Available: http://www.accuray.com/solutions

A. Schweikard, G. Glosser, M. Bodduluri, M. J. Murphy, and J. R. Adler, "Robotic motion compensation for respiratory movement during radiosurgery," *Computer Aided Surgery*, vol. 5, no. 4, pp. 263–277, 2000.

R. Richa, A. P. Bó, and P. Poignet, "Towards robust 3d visual tracking for motion compensation in beating heart surgery," *Medical Image Analysis*, vol. 15, no. 3, pp. 302–315, 2011.

C. Riviere, A. Thakral, I. Iordachita, G. Mitroi, and D. Stoianovici, "Predicting respiratory motion for active canceling during percutaneous needle insertion," in *Engineering in Medicine and Biology Society, 2001. Proceedings of the 23rd Annual International Conference of the IEEE*, vol. 4. IEEE, 2001, pp. 3477–3480.

A. Thakral, J. Wallace, D. Tomlin, N. Seth, and N. V. Thakor, "Surgical motion adaptive robotic technology (smart): Taking the motion out of physiological motion," in *International Conference on Medical Image Computing and Computer-Assisted Intervention*. Springer, 2001, pp. 317–325.

L. Cuvillon, J. Gangloff, M. de Mathelin, and A. Forgione, "Toward robotized beating heart tecabg: Assessment of the heart dynamics using high-speed vision," in *International Conference on Medical Image Computing and Computer-Assisted Intervention*. Springer, 2005, pp. 551–558.

L. Cuvillon, J. Gangloff, M. De Mathelin, and A. Forgione, "Towards robotized beating heart tecabg: assessment of the heart dynamics using high-speed vision," *Computer aided surgery*, vol. 11, no. 5, pp. 267–277, 2006.

W. Bachta, P. Renaud, L. Cuvillon, E. Laroche, A. Forgione, and J. Gangloff, "Motion prediction for computer-assisted beating heart surgery," *IEEE Transactions on Biomedical Engineering*, vol. 56, no. 11, pp. 2551–2563, 2009.

I. Biosense Webster. (2016) Biosense Webster, Inc. *CARTO System*. [Online]. Available: https://www.biosensewebster.com/products/carto-3.aspx

Y. Nakamura, K. Kishi, and H. Kawakami, "Heartbeat synchronization for robotic cardiac surgery," in *Robotics and Automation, 2001. Proceedings 2001 ICRA. IEEE International Conference on*, vol. 2. IEEE, 2001, pp. 2014–2019.

Ö. Bebek and M. C. Çavusoglu, "Intelligent control algorithms for robotic-assisted beating heart surgery," *Robotics, IEEE Transactions on*, vol. 23, no. 3, pp. 468–480, 2007.

R. Ginhoux, J. Gangloff, M. de Mathelin, L. Soler, M. M. A. Sanchez, and J. Marescaux, "Active filtering of physiological motion in robotized surgery using predictive control," *IEEE Transactions on Robotics*, vol. 21, no. 1, pp. 67–79, 2005.

M. Bowthorpe, A. A. Garcia, and M. Tavakoli, "Gpc-based teleoperation for delay compensation and disturbance rejection in image-guided beating-heart surgery," in *2014 IEEE International Conference on Robotics and Automation (ICRA)*. IEEE, 2014, pp. 4875–4880.

M. Bowthorpe, M. Tavakoli, H. Becher, and R. Howe, "Smith predictor-based robot control for ultrasound-guided teleoperated beating-heart surgery," *IEEE Journal of biomedical and Health Informatics*, vol. 18, no. 1, pp. 157–166, 2014.

B. Cagneau, N. Zemiti, D. Bellot, and G. Morel, "Physiological motion compensation in robotized surgery using force feedback control," in *Proceedings 2007 IEEE International Conference on Robotics and Automation*. IEEE, 2007, pp. 1881–1886.

C. N. Riviere, R. S. Rader, and N. V. Thakor, "Adaptive cancelling of physiological tremor for improved precision in microsurgery," *IEEE Transactions on Biomedical Engineering*, vol. 45, no. 7, pp. 839–846, 1998.

S. G. Yuen, D. T. Kettler, P. M. Novotny, R. D. Plowes, and R. D. Howe, "Robotic motion compensation for beating heart intracardiac surgery," *The International Journal of Robotics Research*, vol. 28, no. 10, pp. 1355–1372, 2009.

P. J. Parker and B. D. Anderson, "Frequency tracking of nonsinusoidal periodic signals in noise," *Signal Processing*, vol. 20, no. 2, pp. 127–152, 1990.

P. M. Novotny, "Real-time processing of three dimensional ultrasound for intracardiac surgery," Ph.D. dissertation, Harvard University, 2007.

S. B. Kesner and R. D. Howe, "Robotic catheter cardiac ablation combining ultrasound guidance and force control," *The International Journal of Robotics Research*, vol. 33, no. 4, pp. 631–644, 2014.

D. K. Rex, M. Khashab, G. S. Raju, J. Pasricha, and R. Kozarek, "Insertability and safety of a shape-locking device for colonoscopy," *The American journal of gastroenterology*, vol. 100, no. 4, pp. 817–820, 2005.

A. Jiang, G. Xynogalas, P. Dasgupta, K. Althoefer, and T. Nanayakkara, "Design of a variable stiffness flexible manipulator with composite granular jamming and membrane coupling," in *Intelligent Robots and Systems (IROS), 2012 IEEE/RSJ International Conference on* . IEEE, 2012, pp. 2922–2927.

S. Zuo, K. Masamune, K. Kuwana, M. Tomikawa, S. Ieiri, T. Ohdaira, M. Hashizume, and T. Dohi, "Nonmetallic rigid–flexible outer sheath with pneumatic shapelocking mechanism and double curvature structure," in *Medical Image Computing and Computer-Assisted Intervention–MICCAI 2011*. Springer, 2011, pp. 169–177.

N. G. Cheng, M. B. Lobovsky, S. J. Keating, A. M. Setapen, K. Gero, A. E. Hosoi, K. D. Iagnemma *et al.*, "Design and analysis of a robust, low-cost, highly articulated manipulator enabled by jamming of granular media," in *Robotics and Automation (ICRA), 2012 IEEE International Conference on*. IEEE, 2012, pp. 4328–4333.

A. Stilli, H. Wurdemann, and K. Althoefer, "Shrinkable, stiffness-controllable soft manipulator based on a bio-inspired antagonistic actuation principle," in *Intelligent Robots and Systems (IROS 2014), 2014 IEEE/RSJ International Conference on*. IEEE, 2014, pp. 2476–2481.

A. Ataollahi, R. Karim, A. Soleiman Fallah, K. Rhode, R. Razavi, L. Seneviratne, T. Schaeffter, and K. Althoefer, "3-dof mr-compatible multi-segment cardiac catheter steering mechanism," *IEEE Transactions on Robotics*, vol. PP, no. 99, 2013.

Y. Chen, J. H. Chang, A. S. Greenlee, K. C. Cheung, A. H. Slocum, and R. Gupta, "Multi-turn, tension-stiffening catheter navigation system," in *2010 IEEE International Conference on Robotics and Automation (ICRA)*. IEEE, 2010, pp. 5570–5575.

Y.-J. Kim, S. Cheng, S. Kim, and K. Iagnemma, "A stiffness-adjustable hyperredundant manipulator using a variable neutral-line mechanism for minimally invasive surgery," *IEEE Transactions on Robotics*, vol. 30, no. 2, pp. 382–395, 2014.

G. K. Michelson, "Gooseneck surgical instrument holder," May 7 1996, uS Patent 5,513,827.

V. Saadat, R. C. Ewers, and E. G. Chen, "Shape lockable apparatus and method for advancing an instrument through unsupported anatomy," May 9 2006, uS Patent 7,041,052.

M. L. Fugoso and D. H. Tran, "Adjustable stiffness dilatation catheter," Aug. 13 1996, uS Patent 5,545,138.

C. R. Wagner, D. P. Perrin, R. D. Howe, N. Vasilyev, and P. J. Del Nido, "Force feedback in a three-dimensional ultrasound-guided surgical task," in *14th Symposium on Haptic Interfaces for Virtual Environment and Teleoperator Systems*. IEEE, 2006, pp. 43–48.

A. Faraz and S. Payandeh, "Towards approximate models of coulomb frictional moments in:(i) revolute pin joints and (ii) spherical-socket ball joints," *Journal of engineering mathematics*, vol. 40, no. 3, pp. 283–296, 2001.

P. M. Loschak, L. J. Brattain, and R. D. Howe, "Automated pointing of cardiac imaging catheters," in *IEEE International Conference on Robotics and Automation (ICRA)*, 2013, pp. 5794–5799.

——, "Algorithms for automated pointing of cardiac imaging catheters," in *Computer-Assisted and Robotic Endoscopy*. Springer, 2014, pp. 99–109.

E. Lifesciences. (2016) Edwards Lifesciences *SAPIEN 3 Transcatheter Heart Valve*. [Online]. Available: http://www.edwards.com/eu/Products/TranscatheterValves/Pages/sapien3.aspx?WT.ac=S3campaignprod

S. J. Medical. (2016) St. Jude Medical *AMPLATZER*. [Online]. Available: https://professional-intl.sjm.com/products/vas/peripheral-vascular-embolization/embolization-devices/amplatzer-family-of-vascular-plugs

A. Vascular. (2016) Abbott Vascular *MitraClip Percutaneous Mitral Valve Repair System*. [Online]. Available: http://www.abbottvascular.com/int/products/structural-heart/mitraclip.html?sq4uek6bo5dx3uvrt3xr

K. Goldflam, T. Saul, and R. Lewiss, "Focus on: inferior vena cava ultrasound," *ACEP News*, vol. 6, pp. 24–25, 2011.

S. University. (2016) *Echocardiography in ICU*. [Online]. Available: https://web.stanford.edu/group/ccm_echocardio/cgi-bin/mediawiki/index.php/Left_atrium_dimensions

G. C. Rosenquist, L. J. Sweeney, R. N. Ruckman, and H. A. McAllister, "Atrial septal thickness and area in normal heart specimens and in those with ostium secundum atrial septal defects," *Journal of Clinical Ultrasound*, vol. 7, no. 5, pp. 345–348, 1979.

D. Mihov and B. Katerska, "Some biocompatible materials used in medical practice," *Trakia Journal of Sciences*, vol. 8, no. 2, pp. 119–125, 2010.

MatWeb. (2016) *Tensile Property Testing of Plastics*. [Online]. Available: http://www.matweb.com/reference/tensilestrength.aspx

I. Krause, E. Birk, M. Davidovits, R. Cleper, L. Blieden, L. Pinhas, Z. Gamzo, and B. Eisenstein, "Inferior vena cava diameter: a useful method for estimation of fluid status in children on haemodialysis," *Nephrology Dialysis Transplantation*, vol. 16, no. 6, pp. 1203–1206, 2001.

Appendix A

Respiratory Motion Data

This section examines respiratory motion data from two live animal subjects. These were data used in the development of the breathing motion compensation algorithms.

Pig 1: Data were collected in different regions in and around the right side of the heart. The *Instr* tracker was on the sternum throughout all measurements. Pig 2: The trackers mounted in the correct locations on the ICE catheter, but not calibrated. The x-axes of the trackers were aligned with the catheter z-axis. The EM sensor y- and z-axes were not aligned with the catheter coordinate frame. The displacement data are plotted below. The rotation matrix data are not used. The *Instr* tracker was not reliable during these measurements.

Motion studies were done by placing the sensorized ICE catheter tip in different sections of the right side of the heart: middle of right atrium, in the tricuspid valve between right atrium/ventricle, fully in the right ventricle, at the top of the right atrium near the superior vena cava, and at the bottom of the right atrium near the inferior vena cava. The clinician aimed to place the catheter in the same locations in both animal subjects, but some variation is expected.

In all trials the catheter was measured for at least 30 seconds. The ICE catheter was not actuated (manually or robotically) during this time.

A.1 Right Atrium

US catheter in middle of RA near tricuspid. Data available for Pig 1 (P1) only.

Measured and low pass filtered sensor displacement

(*left col.*) data_P1_009_20150630_151542, (*right col.*) data_P1_009_20150630_151643

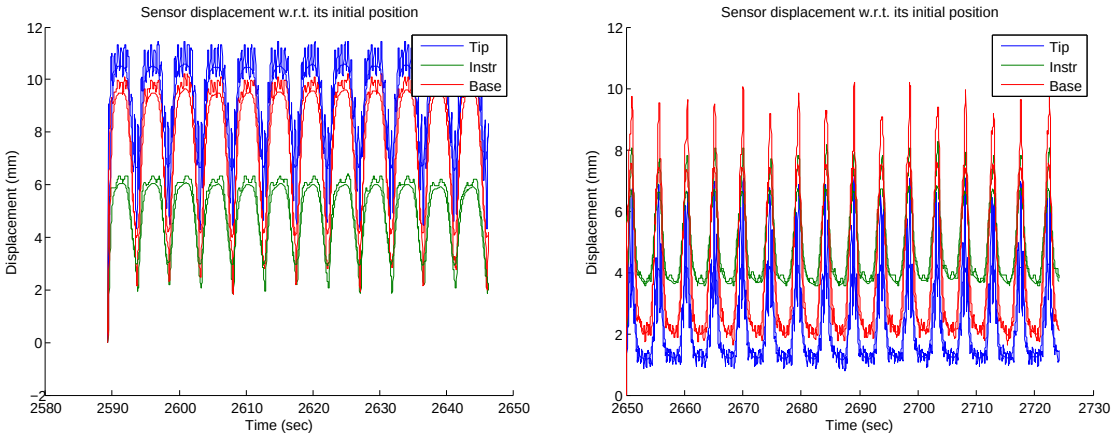

(*left col.*) data_P1_009_20150630_151542, (*right col.*) data_P1_009_20150630_151643

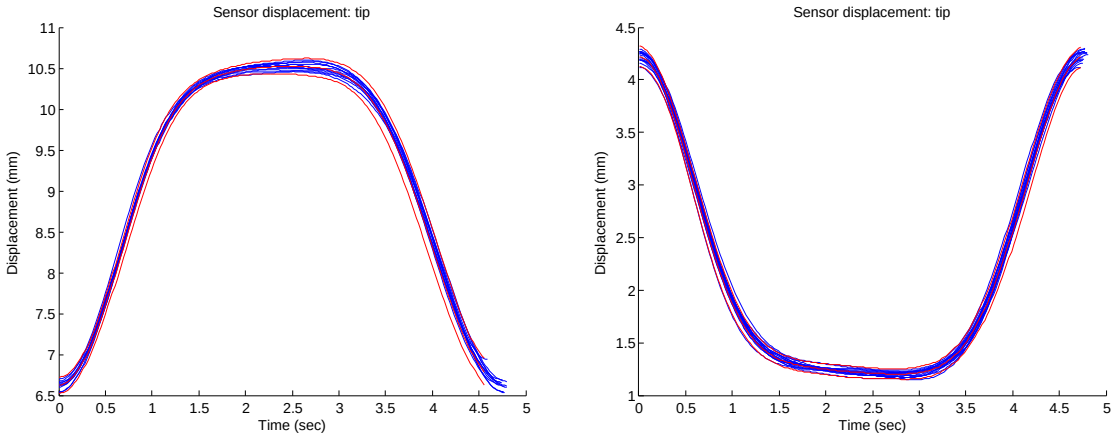

(*left col.*) data_P1_009_20150630_151542, (*right col.*) data_P1_009_20150630_151643

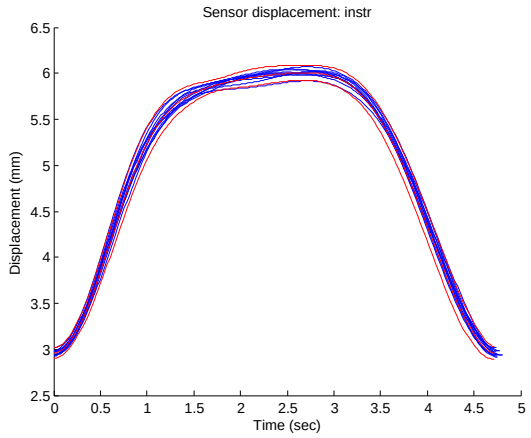

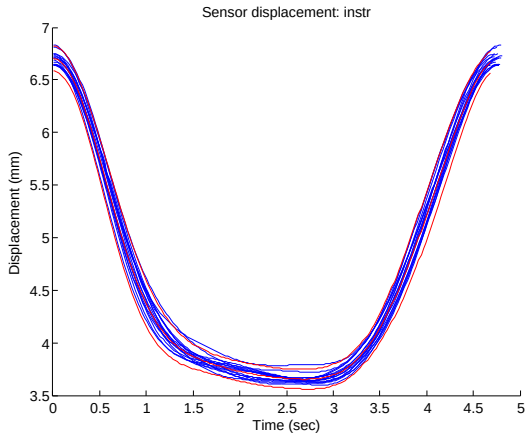

(*left col.*) data_P1_009_20150630_151542, (*right col.*) data_P1_009_20150630_151643

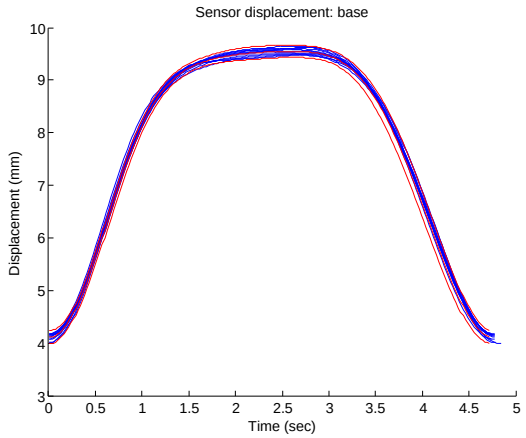

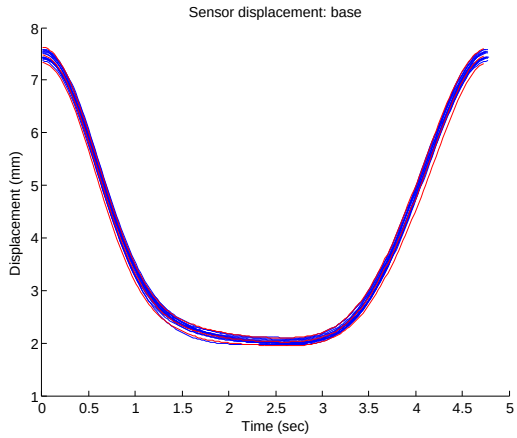

Measured and low pass filtered BB rotation change with respect to fixed BB (base motion induced by breathing)

(*left col.*) data_P1_009_20150630_151542, (*right col.*) data_P1_009_20150630_151643

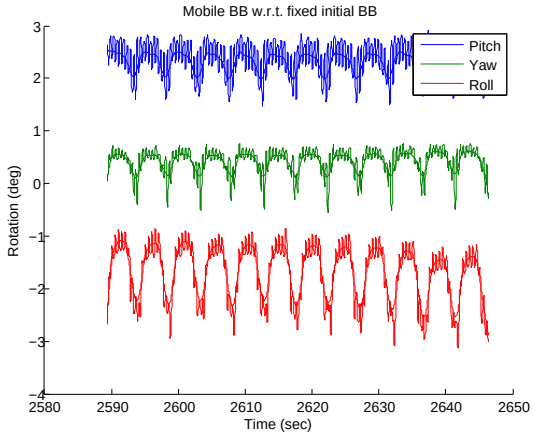

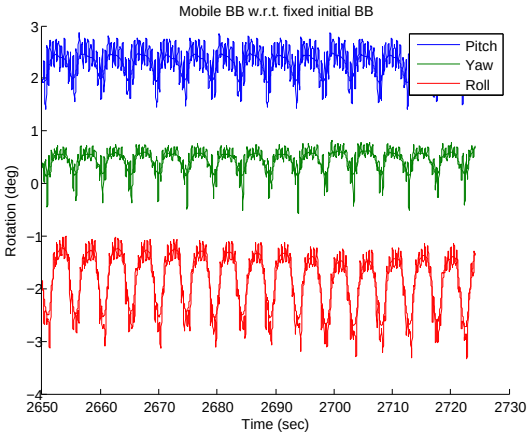

(*left col.*) data_P1_009_20150630_151542, (*right col.*) data_P1_009_20150630_151643

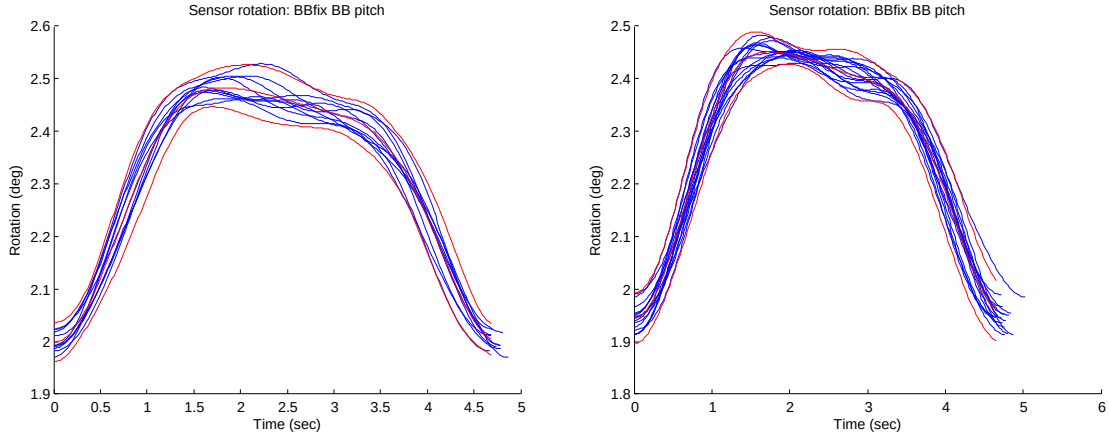

(*left col.*) data_P1_009_20150630_151542, (*right col.*) data_P1_009_20150630_151643

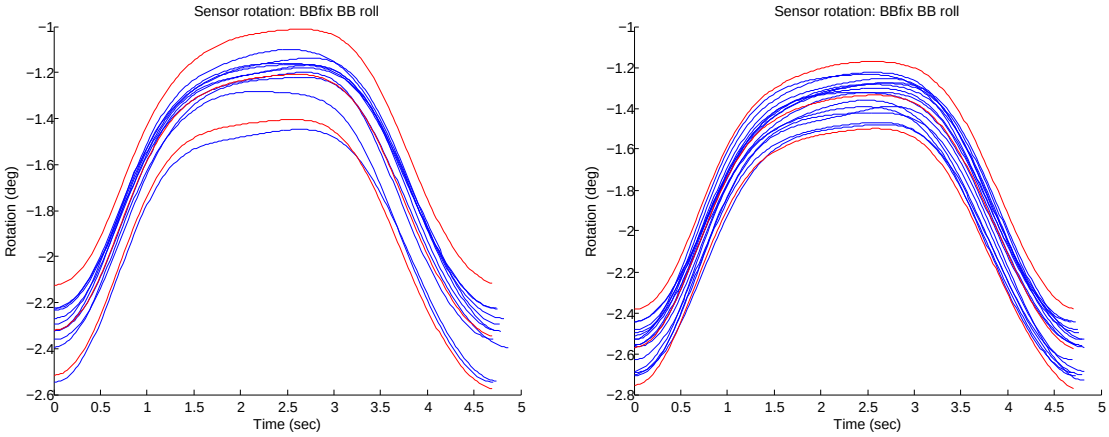

(*left col.*) data_P1_009_20150630_151542, (*right col.*) data_P1_009_20150630_151643

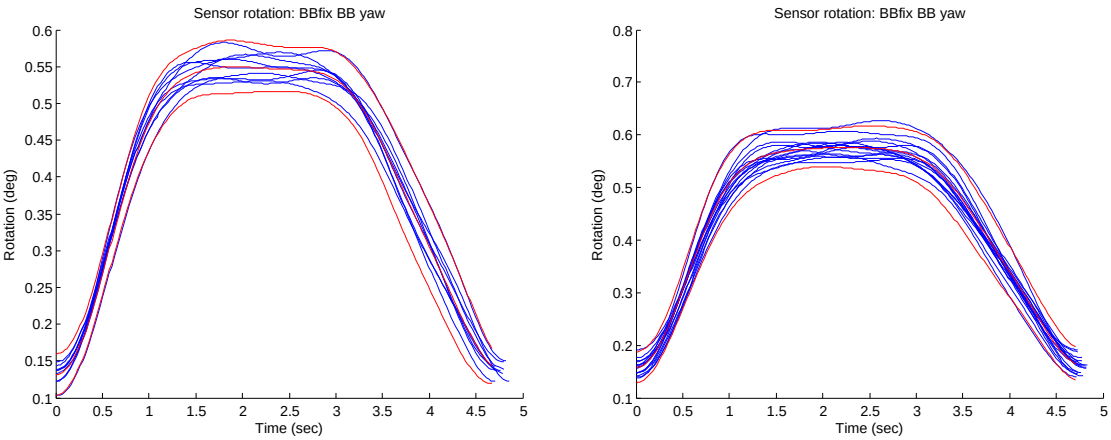

Measured and low pass filtered CT rotation change with respect to mobile BB (tip

rotation induced by breathing)

(*left col.*) data_P1_009_20150630_151542, (*right col.*) data_P1_009_20150630_151643

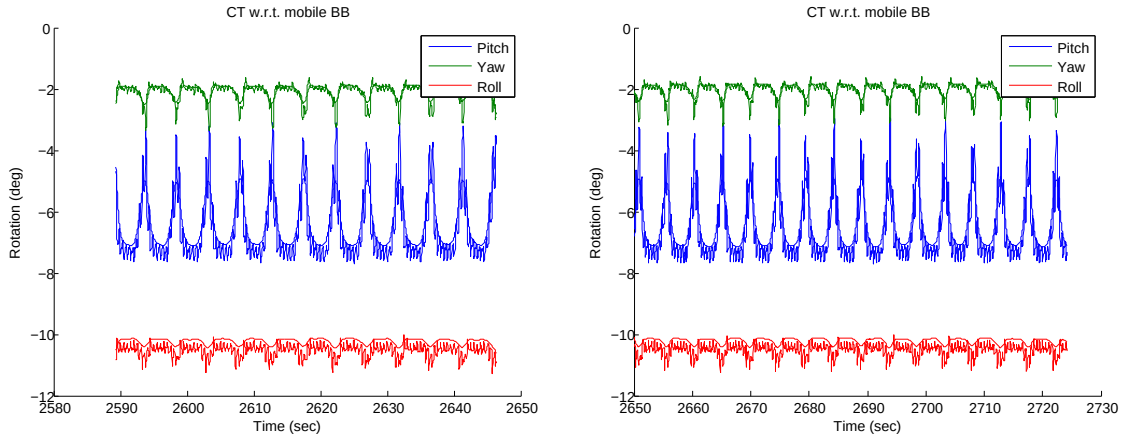

(*left col.*) data_P1_009_20150630_151542, (*right col.*) data_P1_009_20150630_151643

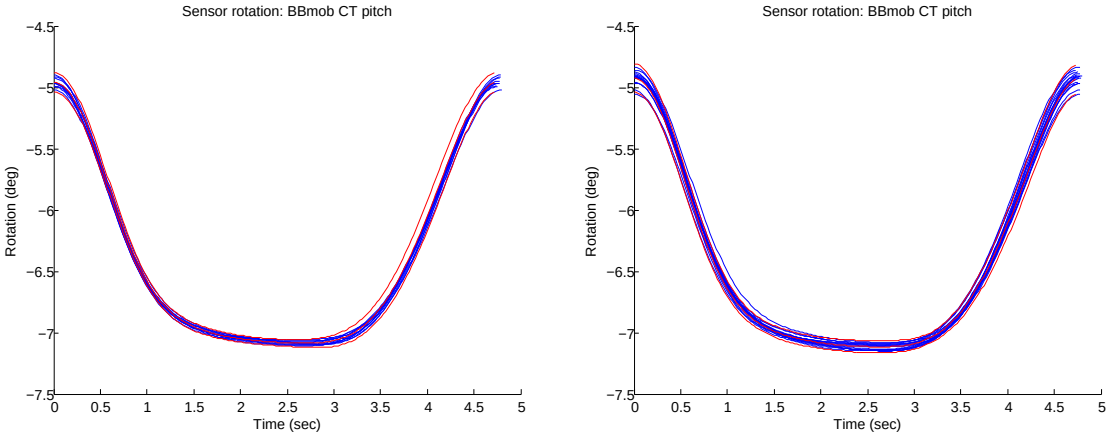

(*left col.*) data_P1_009_20150630_151542, (*right col.*) data_P1_009_20150630_151643

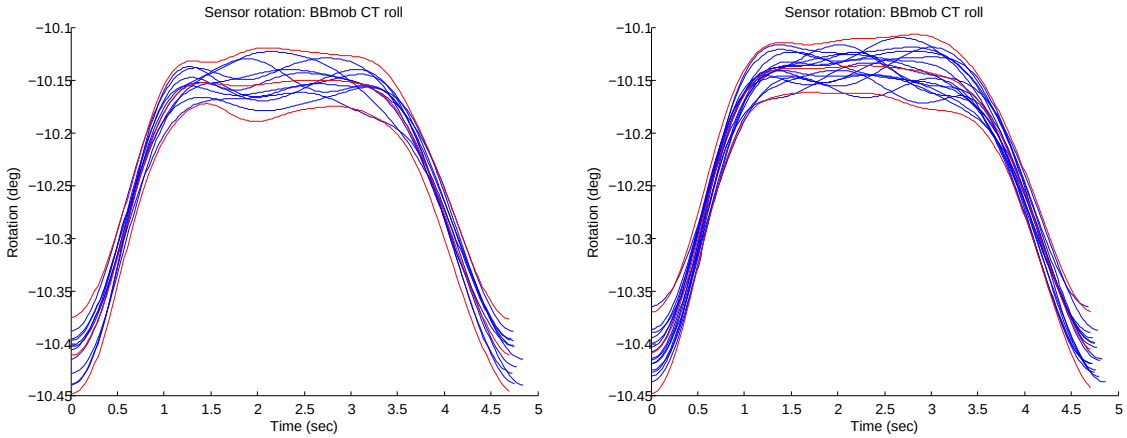

(*left col.*) data_P1_009_20150630_151542, (*right col.*) data_P1_009_20150630_151643

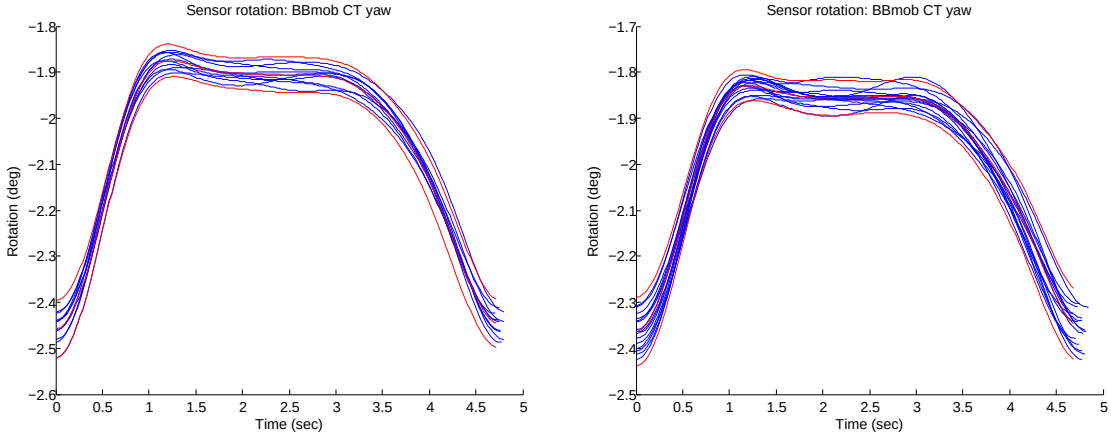

A.2 Right Ventricle

US catheter in right ventricle. Pig 1 (P1) data includes displacement and orientation info. Pig 2 (P2) data includes displacement only. Pig 2 *Instr* sensor disconnected.

Measured and low pass filtered sensor displacement

(*left*) data_P1_010_20150630_152919, (*right*) data_P1_010_20150630_153013

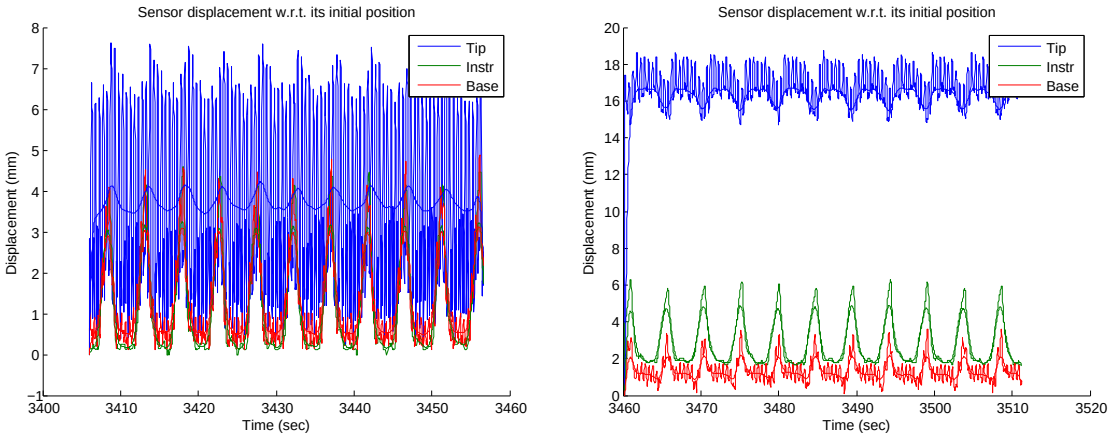

(*left*) data_P1_010_20150630_153106, (*right*) data_P2_213_20150903_173601

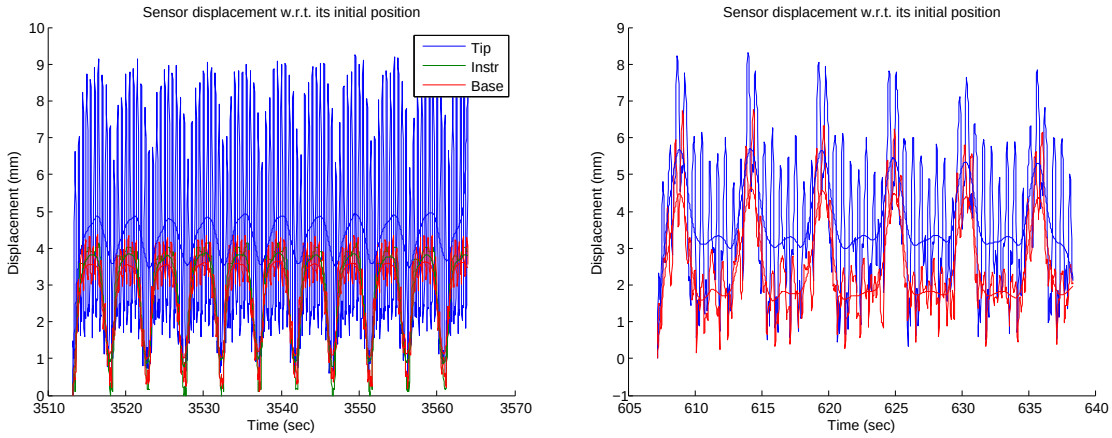

(*left*) data_P1_010_20150630_152919, (*right*) data_P1_010_20150630_153013

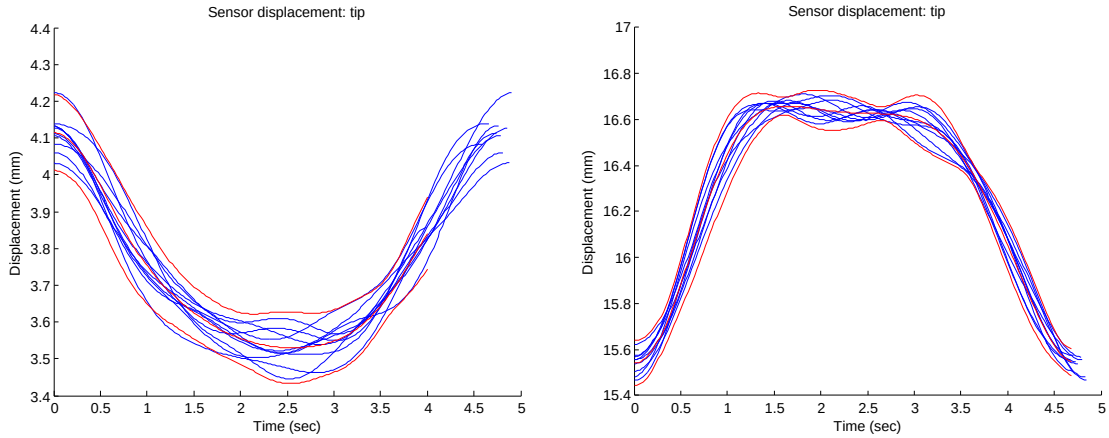

(*left*) data_P1_010_20150630_153106, (*right*) data_P2_213_20150903_173601

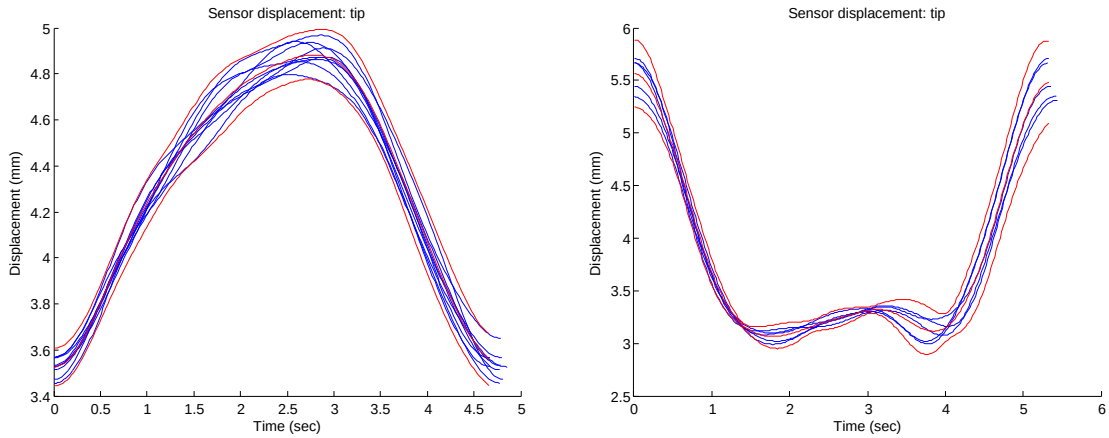

(*left*) data_P1_010_20150630_152919, (*right*) data_P1_010_20150630_153013

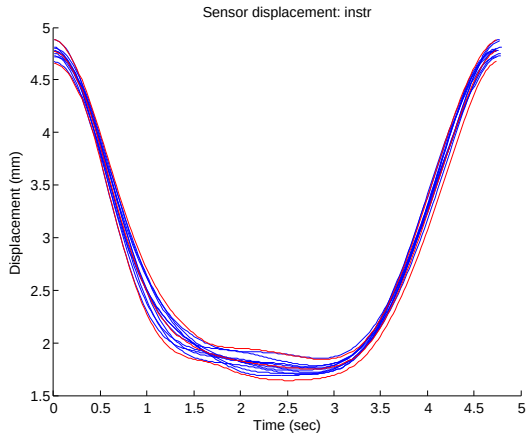

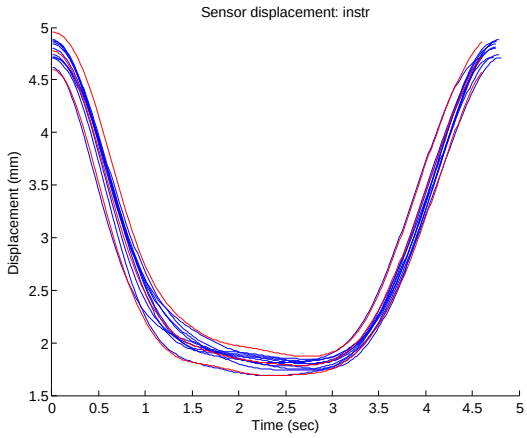

(*left*) data_P1_010_20150630_153106

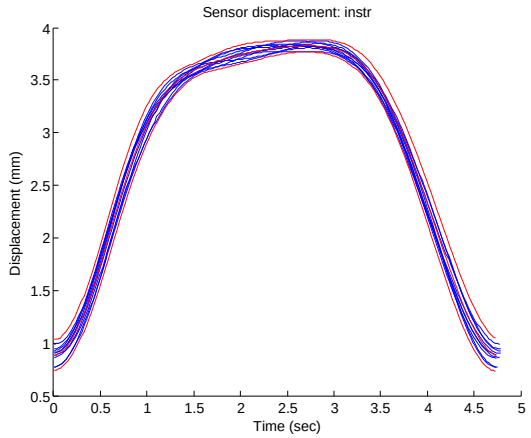

(*left*) data_P1_010_20150630_152919, (*right*) data_P1_010_20150630_153013

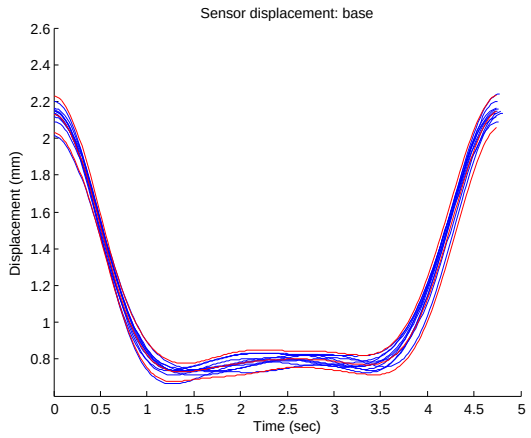

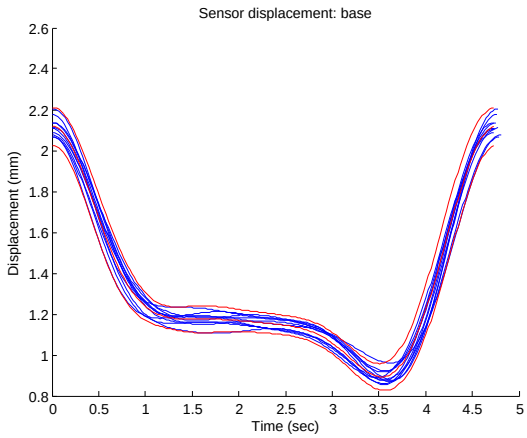

(*left*) data_P1_010_20150630_153106, (*right*) data_P2_213_20150903_173601

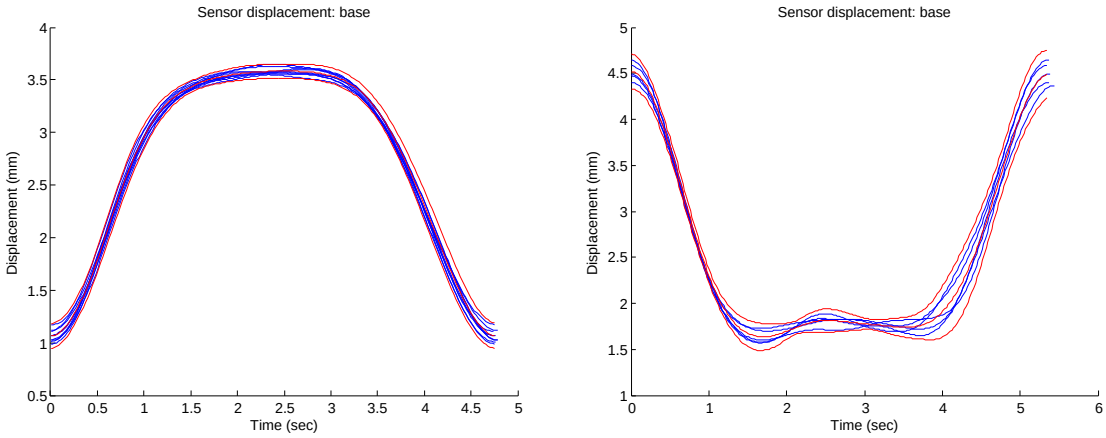

Measured and low pass filtered BB rotation change with respect to fixed BB (base motion induced by breathing)

(*left*) data_P1_010_20150630_152919, (*right*) data_P1_010_20150630_153013

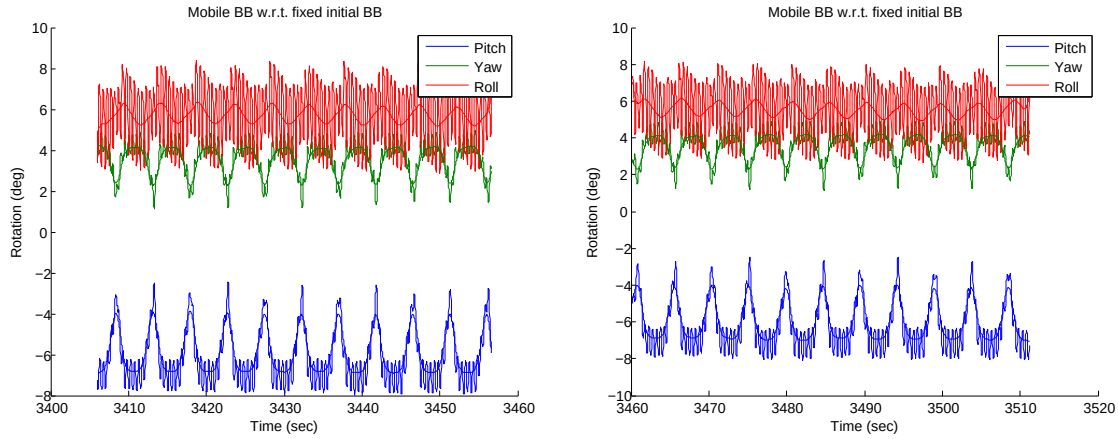

(*left*) data_P1_010_20150630_153106

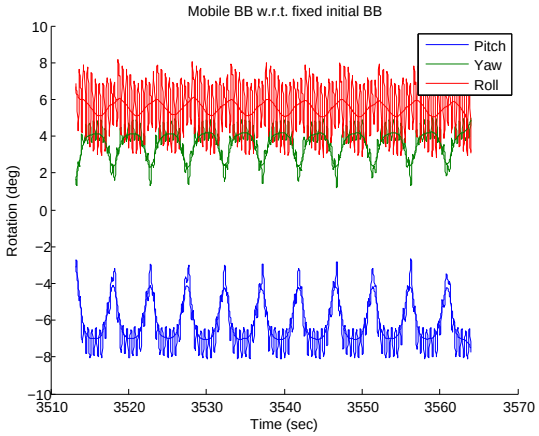

(*left*) data_P1_010_20150630_152919, (*right*) data_P1_010_20150630_153013

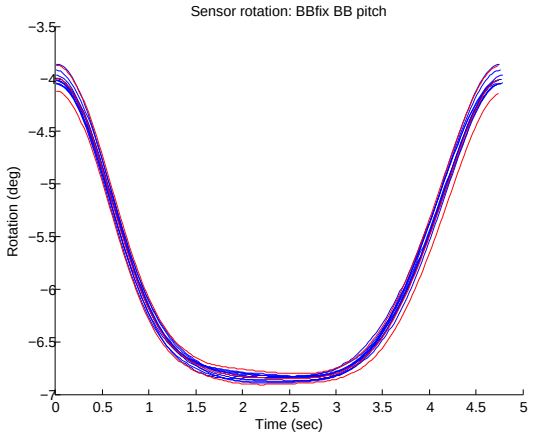

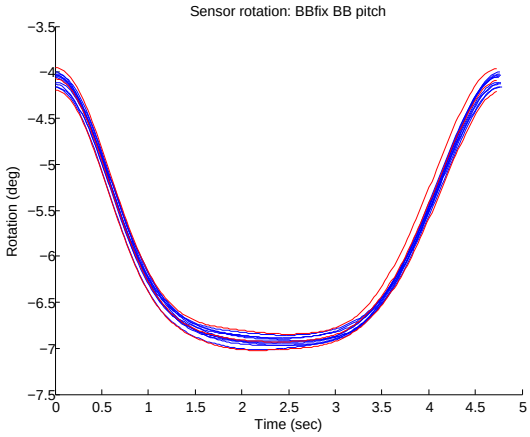

(*left*) data_P1_010_20150630_153106

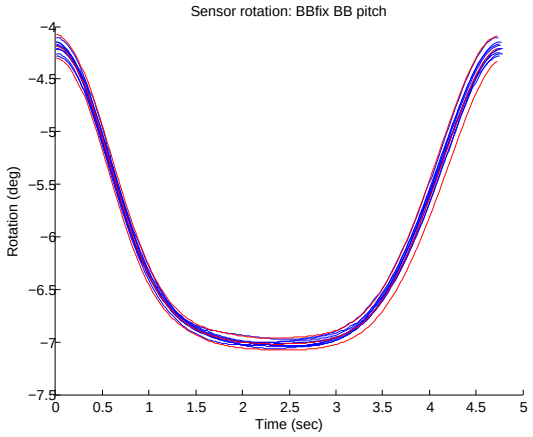

(*left*) data_P1_010_20150630_152919, (*right*) data_P1_010_20150630_153013

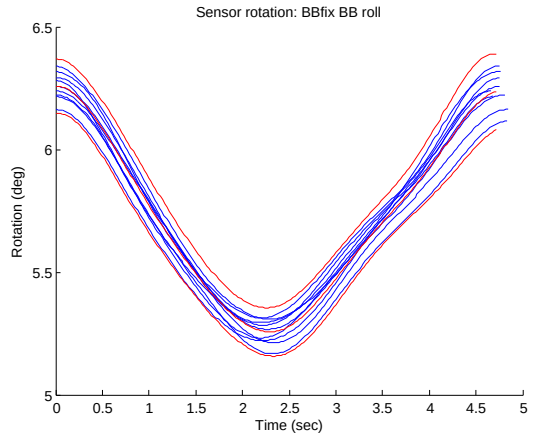

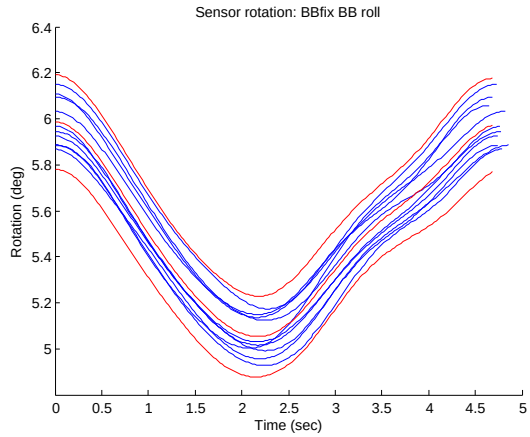

(*left*) data_P1_010_20150630_153106

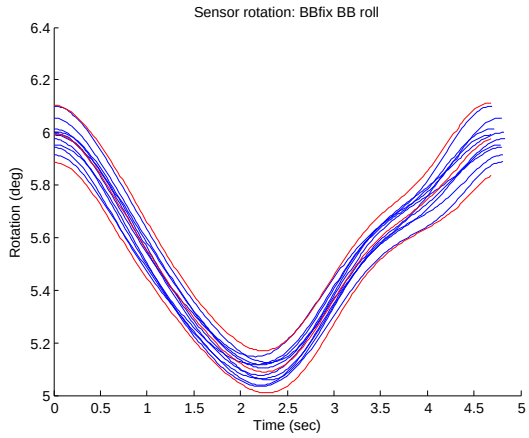

(*left*) data_P1_010_20150630_152919, (*right*) data_P1_010_20150630_153013

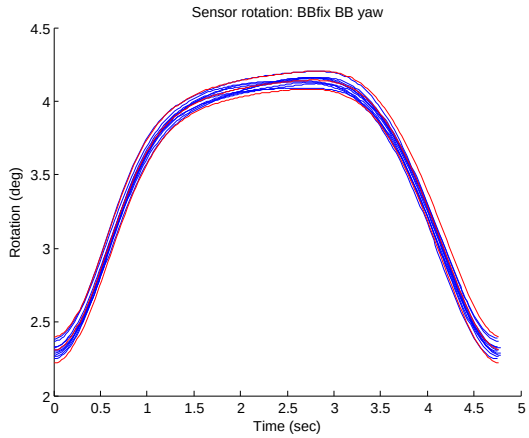

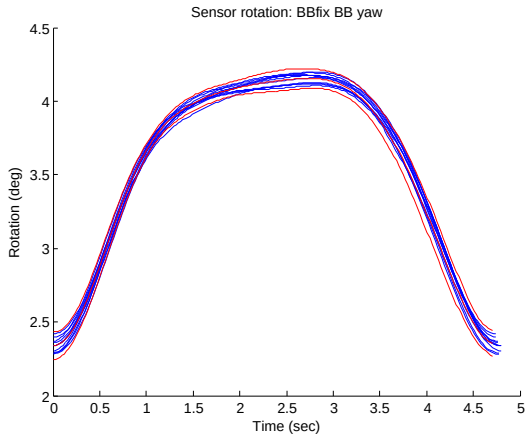

(*left*) data_P1_010_20150630_153106

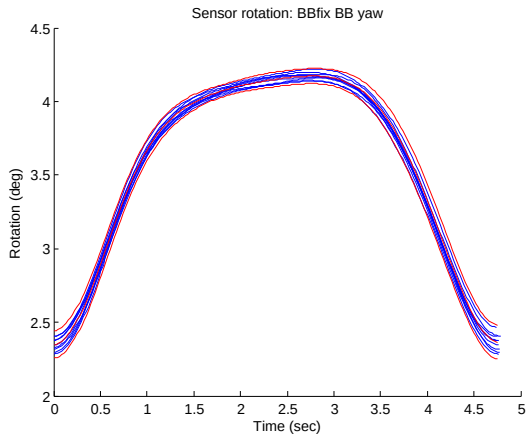

Measured and low pass filtered CT rotation change with respect to mobile BB (tip rotation induced by breathing)

(*left*) data_P1_010_20150630_152919, (*right*) data_P1_010_20150630_153013

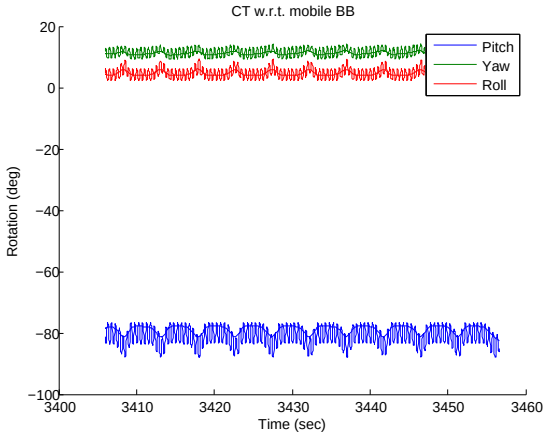

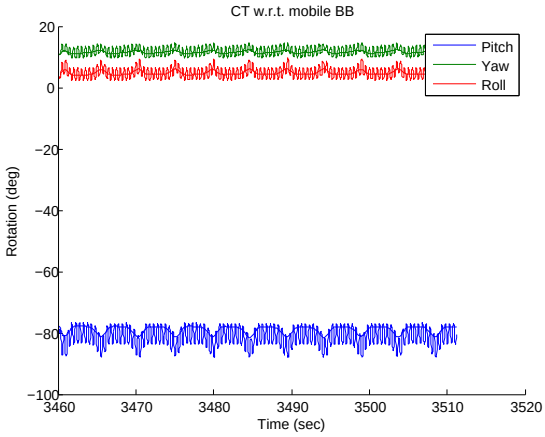

(*left*) data_P1_010_20150630_153106

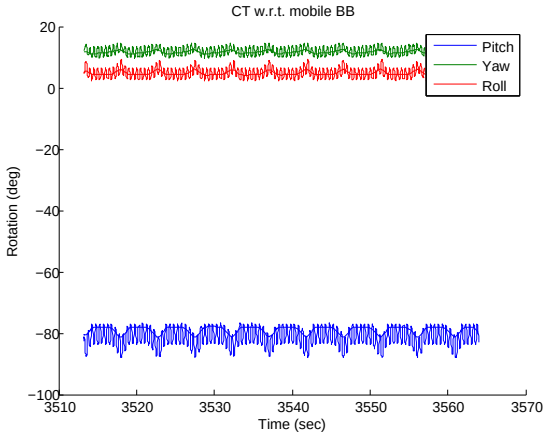

(*left*) data_P1_010_20150630_152919, (*right*) data_P1_010_20150630_153013

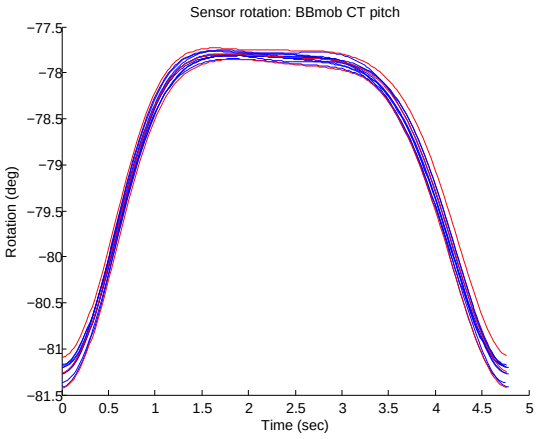

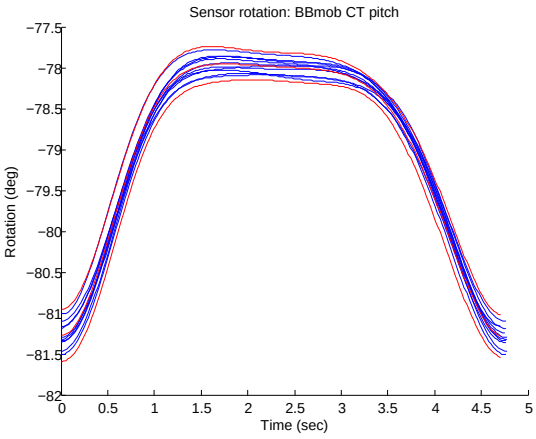

(*left*) data_P1_010_20150630_153106

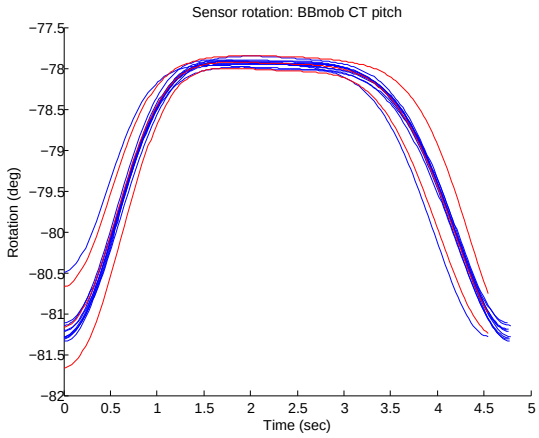

(*left*) data_P1_010_20150630_152919, (*right*) data_P1_010_20150630_153013

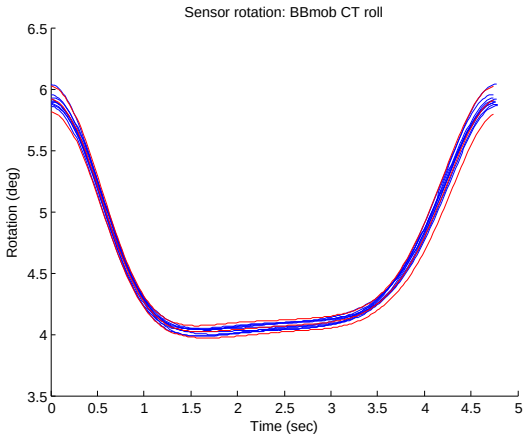

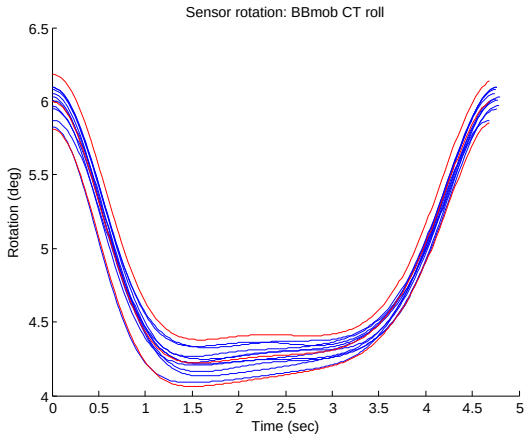

(*left*) data_P1_010_20150630_153106

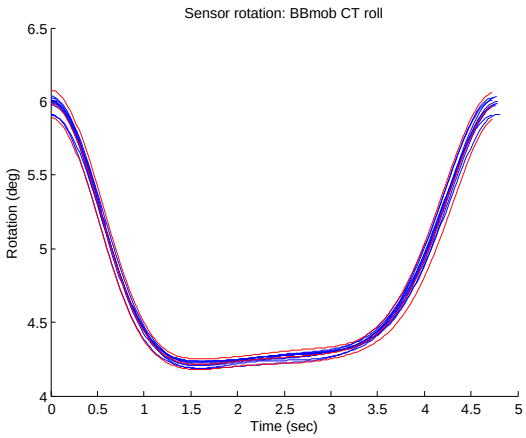

(*left*) data_P1_010_20150630_152919, (*right*) data_P1_010_20150630_153013

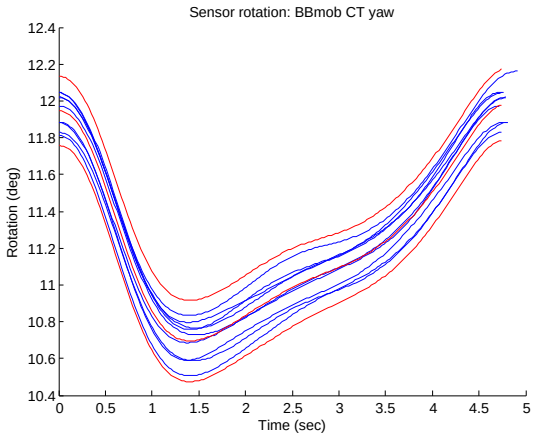

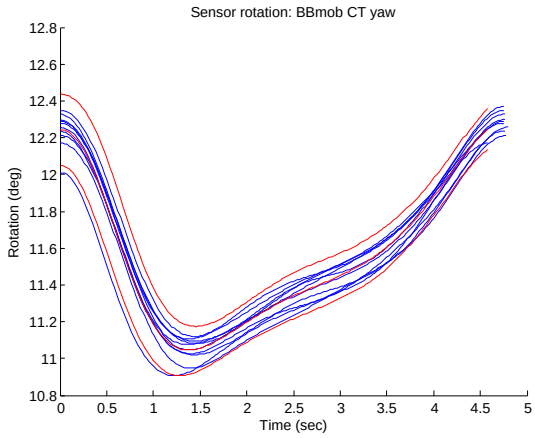

(*left*) data_P1_010_20150630_153106

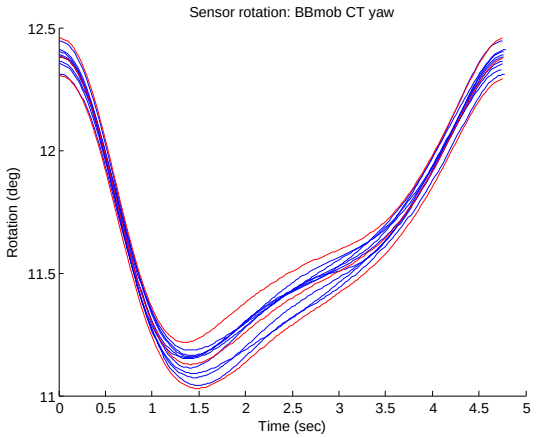

A.3 Tricuspid Valve

US catheter underneath tricuspid or inside tricuspid valve. Pig 1 (P1) data includes displacement and orientation info. Pig 2 (P2) data includes displacement only. Pig 2 *Instr* sensor disconnected. It is likely that the US catheter tip and base locations were different between Pigs 1 and 2.

Measured and low pass filtered sensor displacement

(*left*) data_P1_011_20150630_153617, (*right*) data_P1_011_20150630_153709

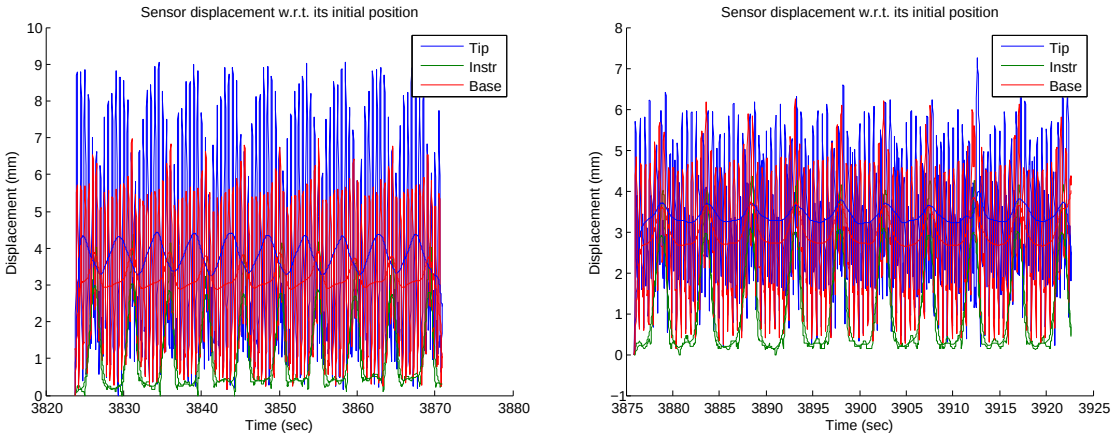

(*left*) data_P1_011_20150630_153758, (*right*) data_P2_214_20150903_174003

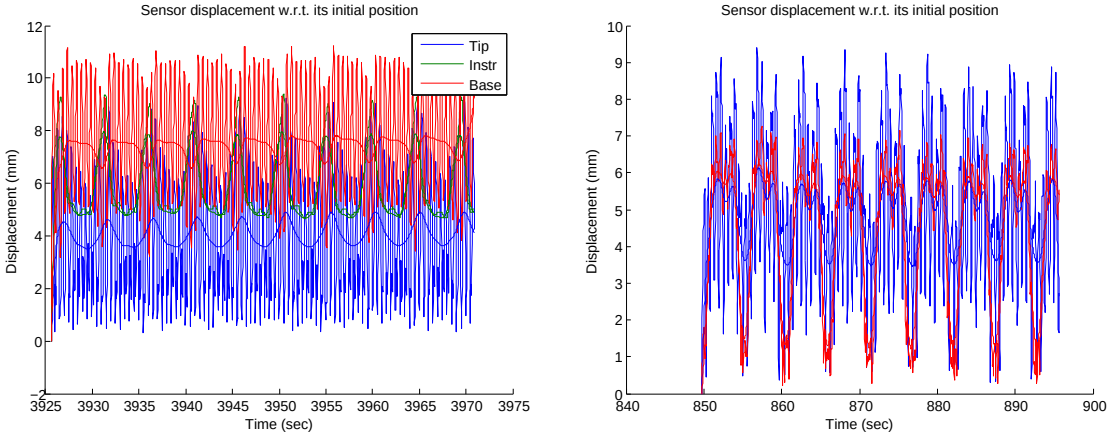

(*left*) data_P1_011_20150630_153617, (*right*) data_P1_011_20150630_153709

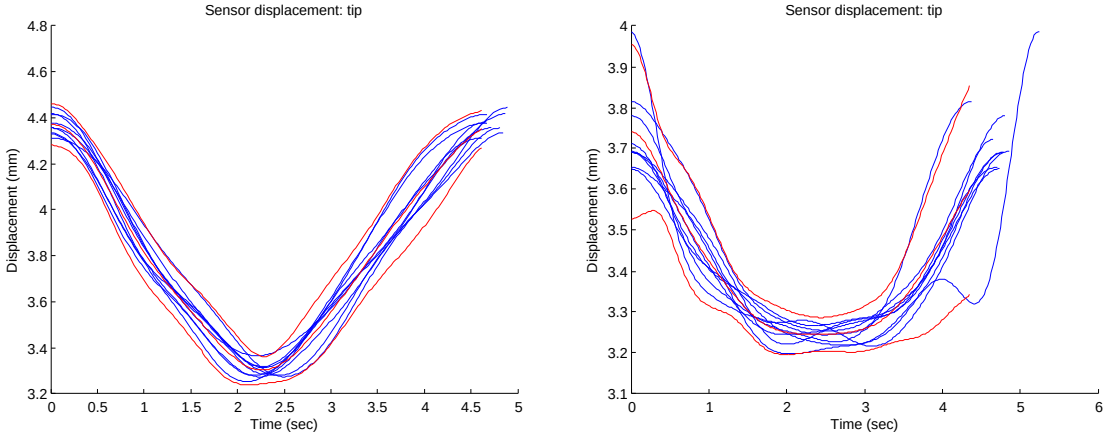

(*left*) data_P1_011_20150630_153758, (*right*) data_P2_214_20150903_174003

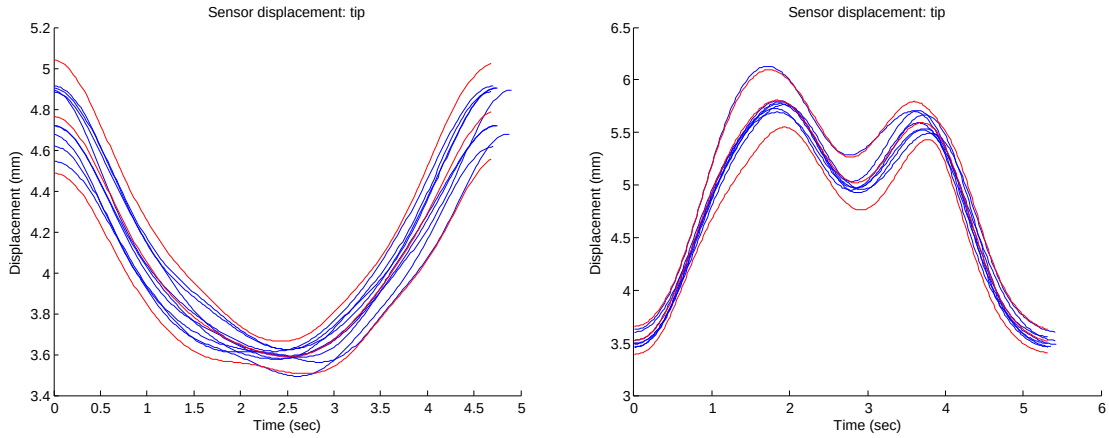

(*left*) data_P1_011_20150630_153617, (*right*) data_P1_011_20150630_153709

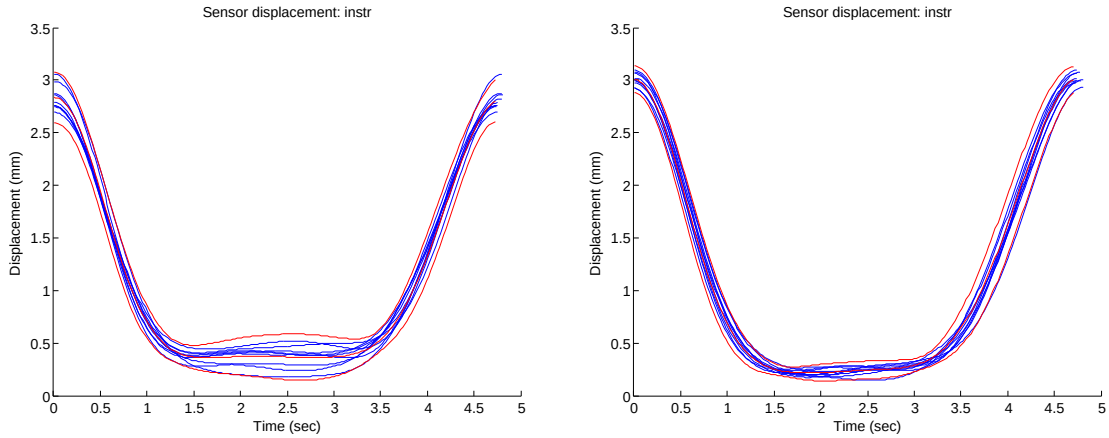

(*left*) data_P1_011_20150630_153758

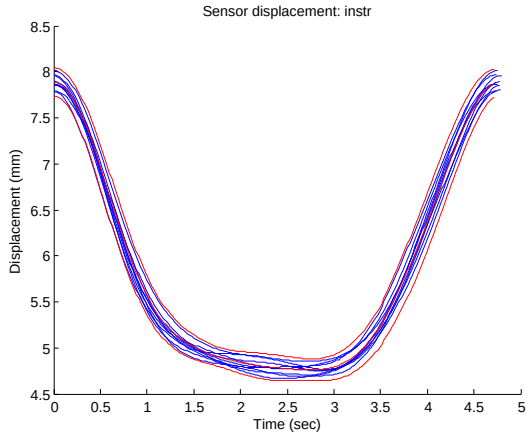

(*left*) data_P1_011_20150630_153617, (*right*) data_P1_011_20150630_153709

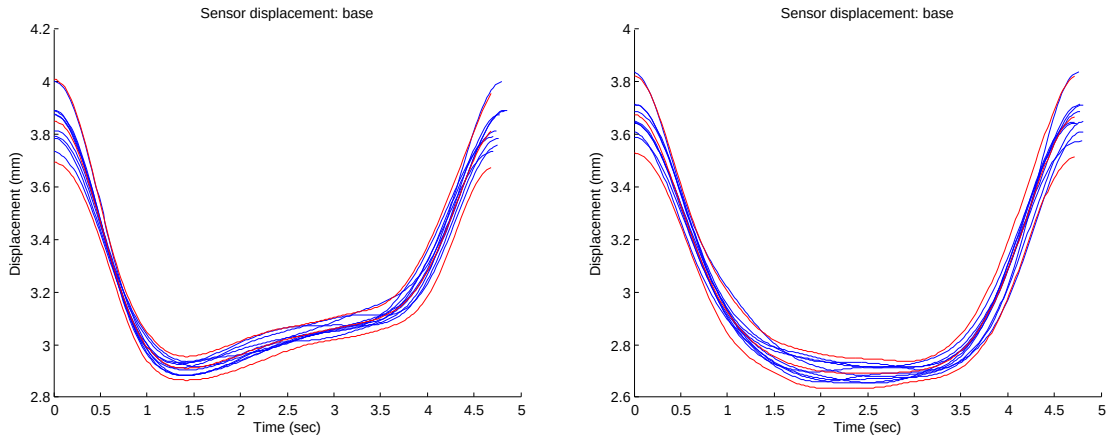

(*left*) data_P1_011_20150630_153758, (*right*) data_P2_214_20150903_174003

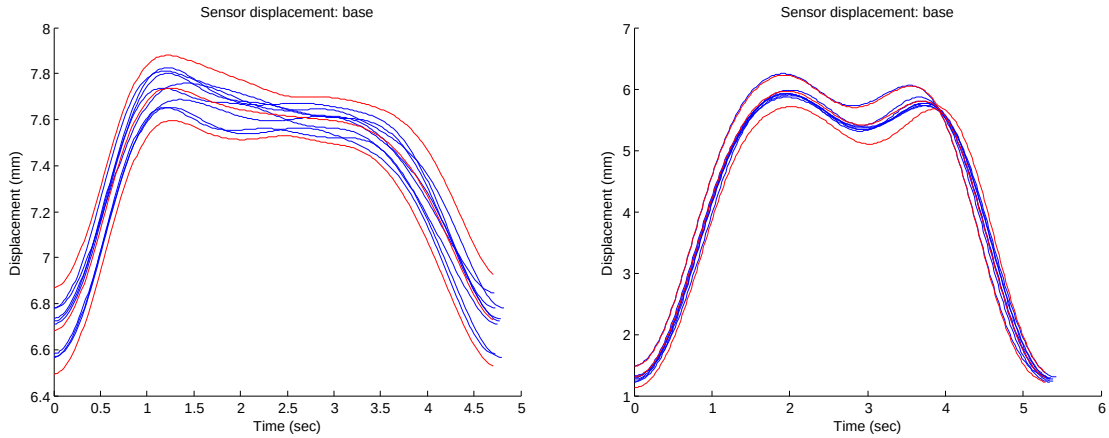

Measured and low pass filtered BB rotation change with respect to fixed BB (base motion induced by breathing)

(*left*) data_P1_011_20150630_153617, (*right*) data_P1_011_20150630_153709

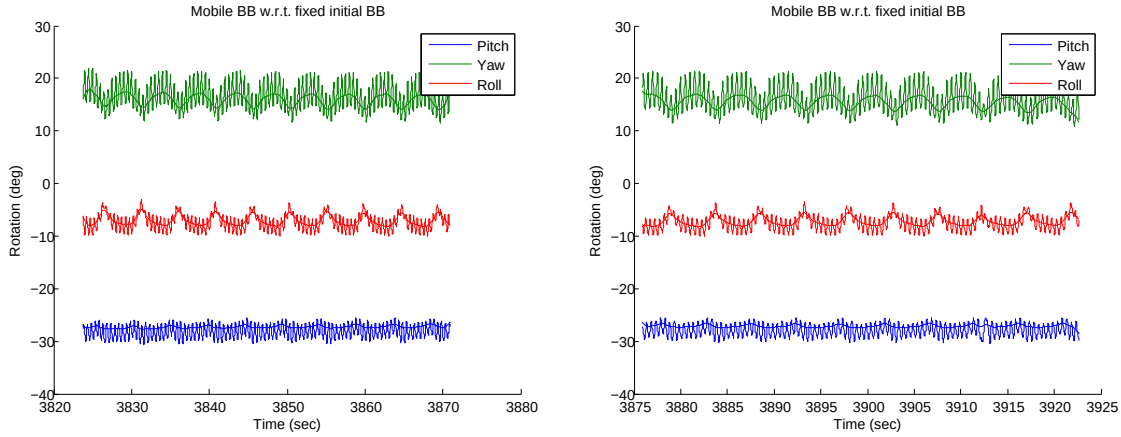

(*left*) data_P1_011_20150630_153758

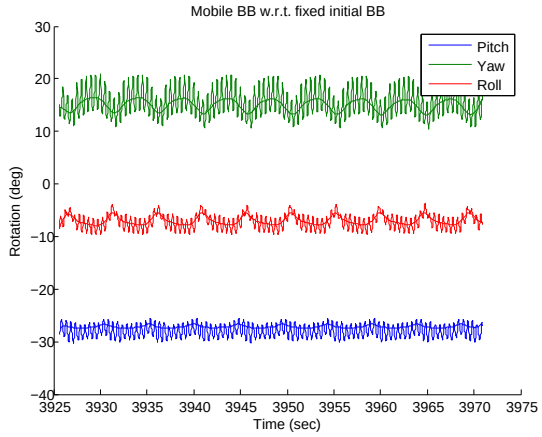

(*left*) data_P1_011_20150630_153617, (*right*) data_P1_011_20150630_153709

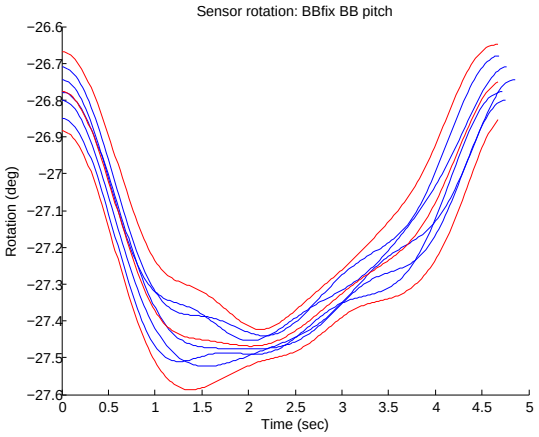

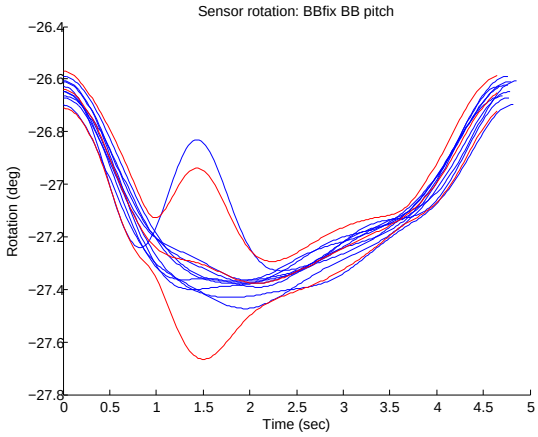

(*left*) data_P1_011_20150630_153758

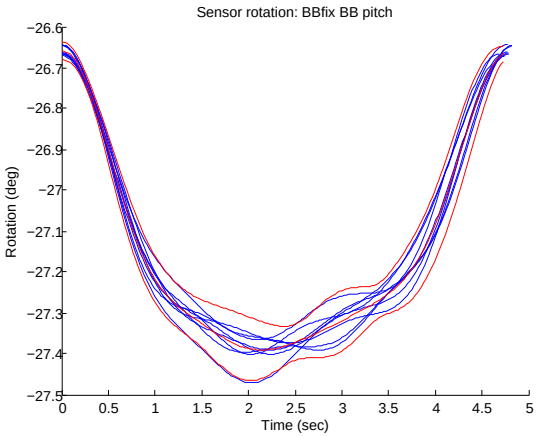

(*left*) data_P1_011_20150630_153617, (*right*) data_P1_011_20150630_153709

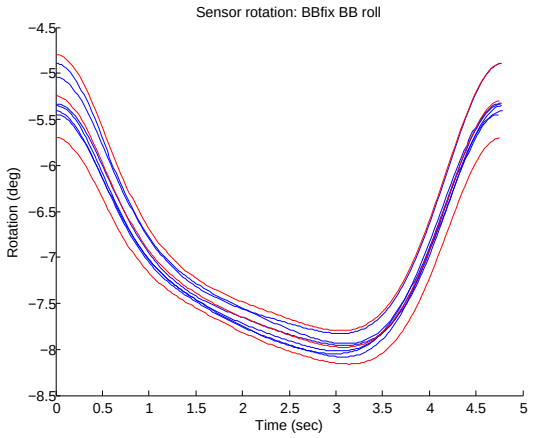

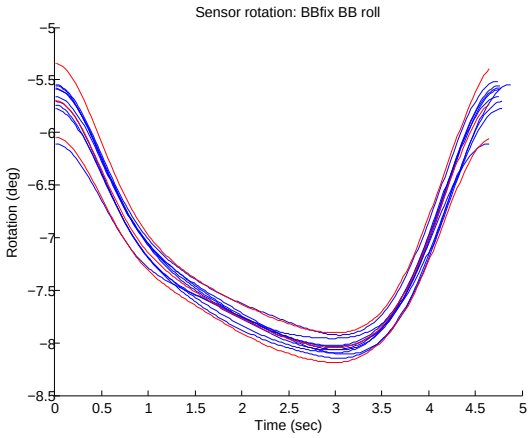

(*left*) data_P1_011_20150630_153758

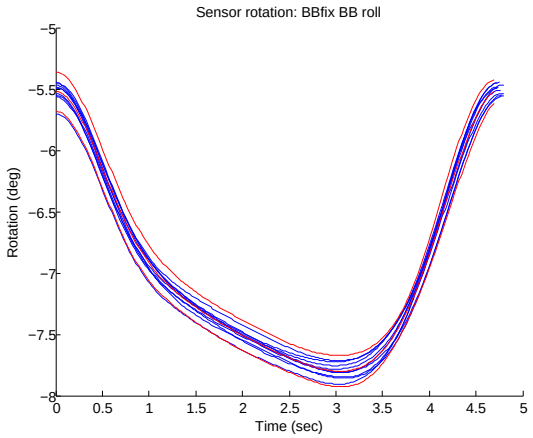

(*left*) data_P1_011_20150630_153617, (*right*) data_P1_011_20150630_153709

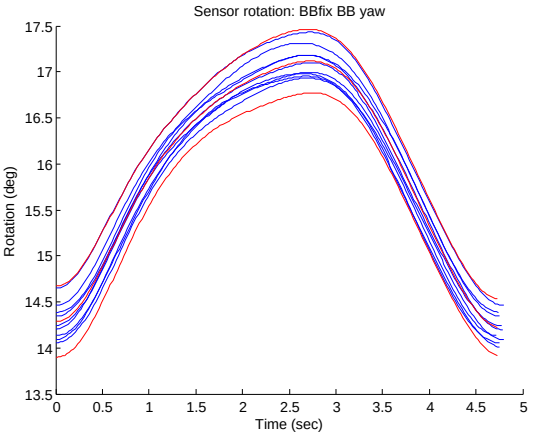

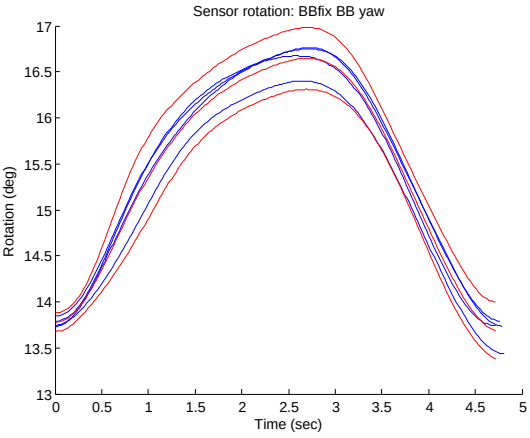

(*left*) data_P1_011_20150630_153758

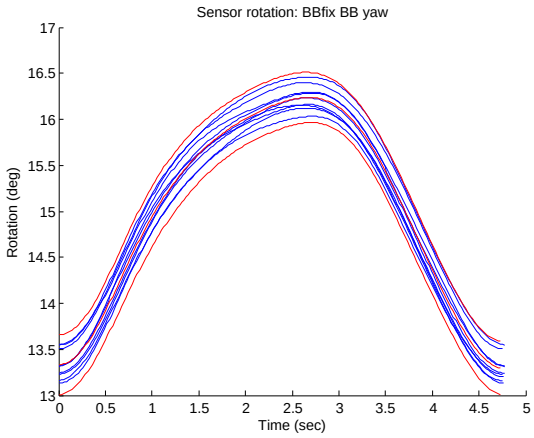

Measured and low pass filtered CT rotation change with respect to mobile BB (tip rotation induced by breathing)

(*left*) data_P1_011_20150630_153617, (*right*) data_P1_011_20150630_153709

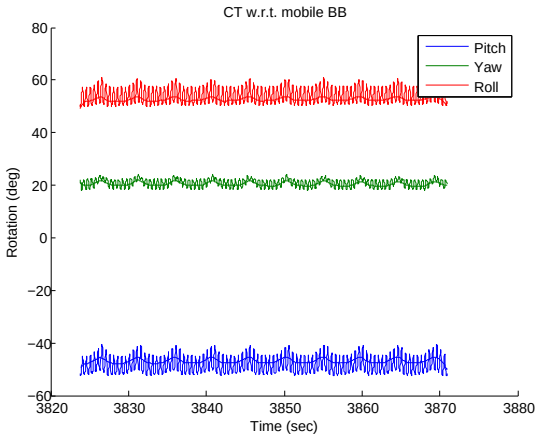

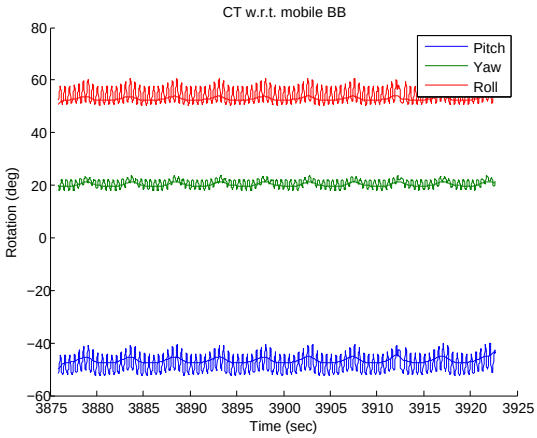

(*left*) data_P1_011_20150630_153758

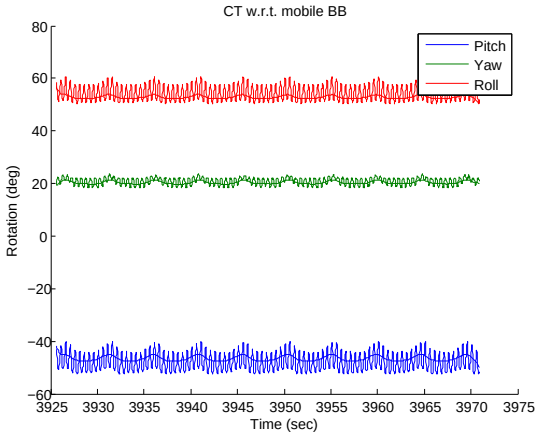

(*left*) data_P1_011_20150630_153617, (*right*) data_P1_011_20150630_153709

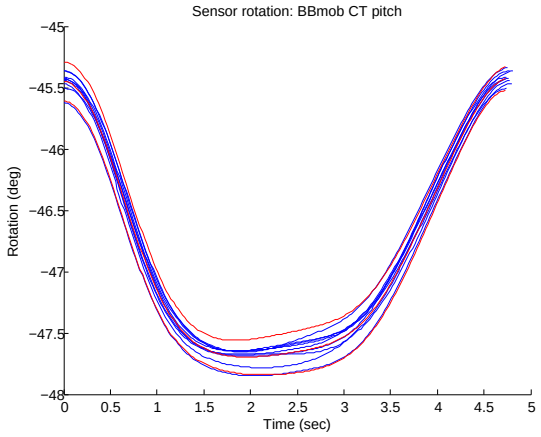

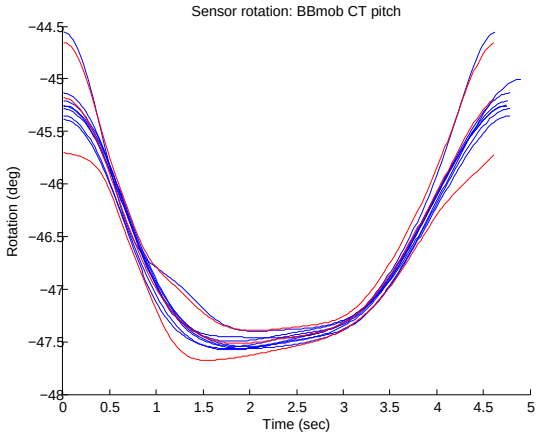

(*left*) data_P1_011_20150630_153758

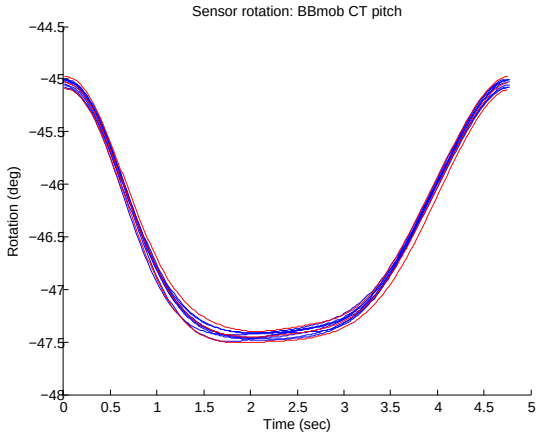

(*left*) data_P1_011_20150630_153617, (*right*) data_P1_011_20150630_153709

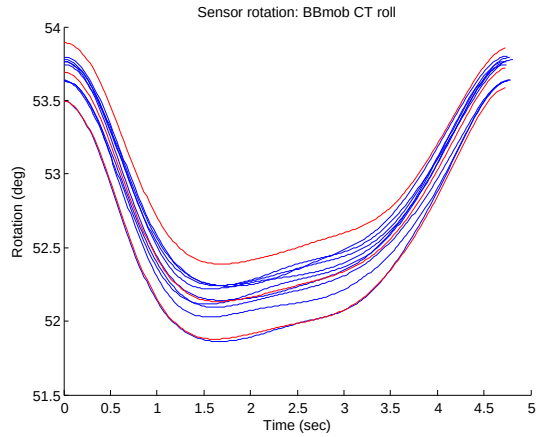

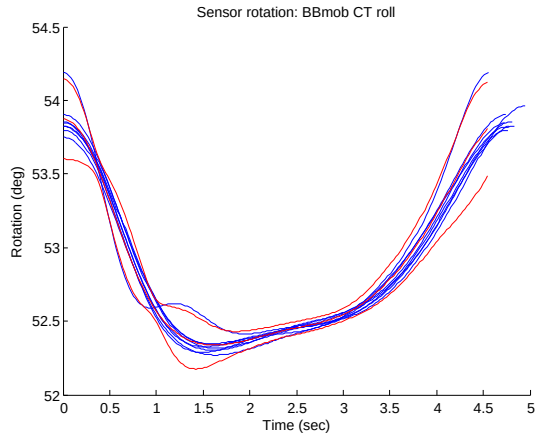

(*left*) data_P1_011_20150630_153758

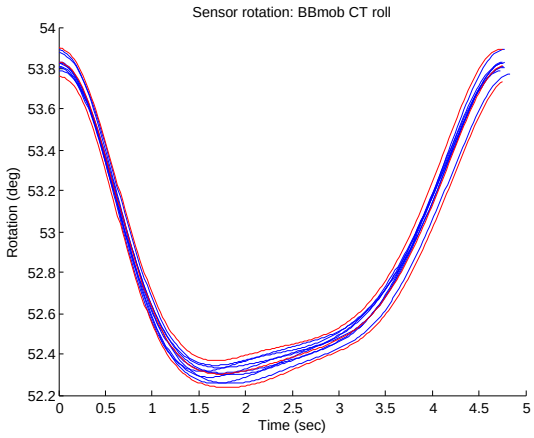

(*left*) data_P1_011_20150630_153617, (*right*) data_P1_011_20150630_153709

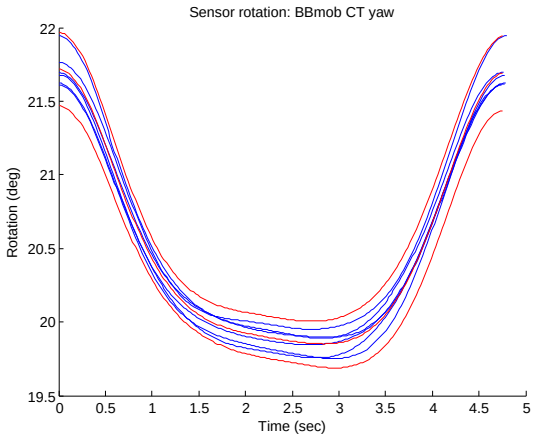

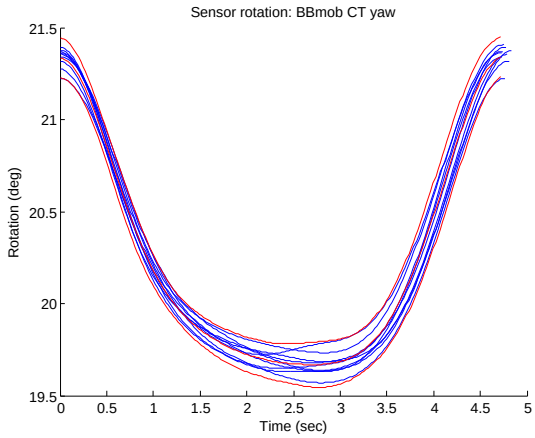

(*left*) data_P1_011_20150630_153758

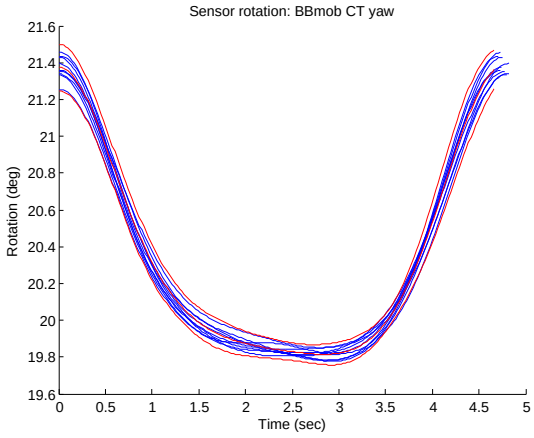

A.4 Upper Right Atrium

US catheter at the top of the RA near the junction of the SVC. Pig 1 (P1) data includes displacement and orientation info. Pig 2 (P2) data not available.

Measured and low pass filtered sensor displacement

(*left*) data_P1_012_20150630_154538, (*right*) data_P1_012_20150630_154644

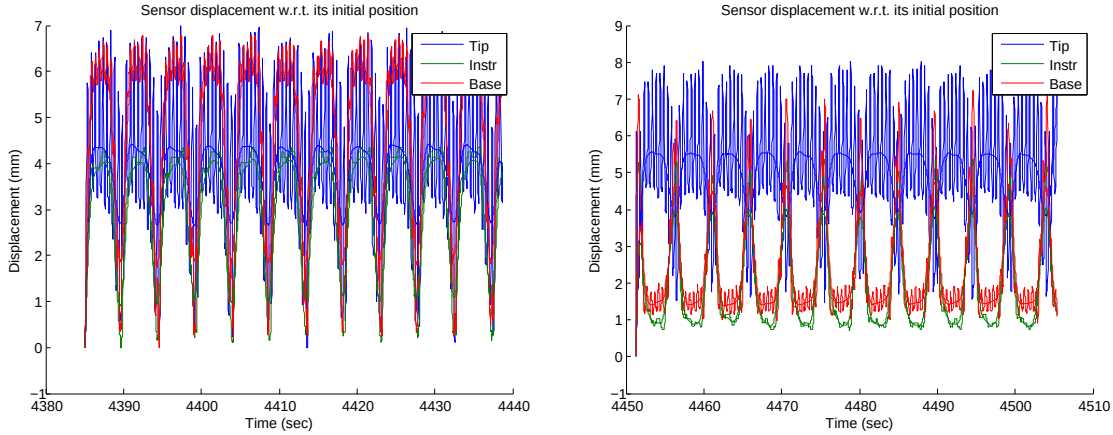

(*left*) data_P1_012_20150630_154538, (*right*) data_P1_012_20150630_154644

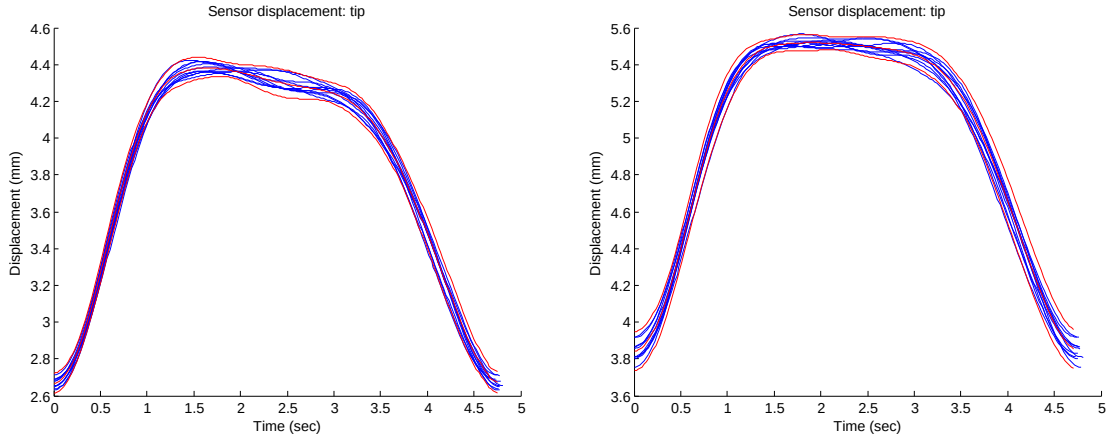

(*left*) data_P1_012_20150630_154538, (*right*) data_P1_012_20150630_154644

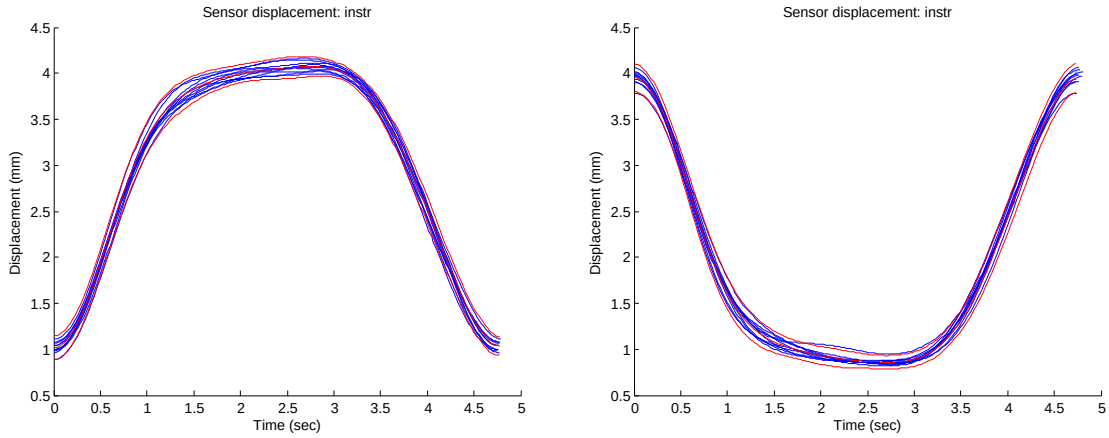

(*left*) data_P1_012_20150630_154538, (*right*) data_P1_012_20150630_154644

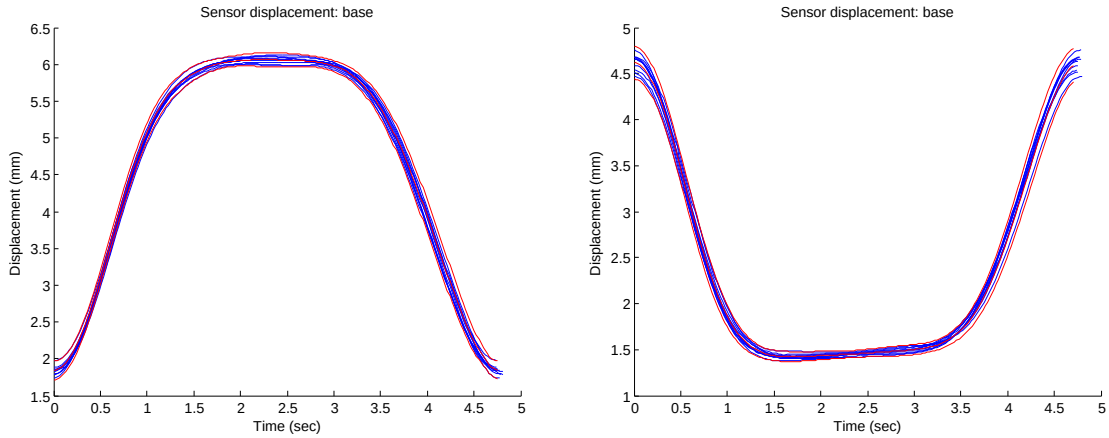

Measured and low pass filtered BB rotation change with respect to fixed BB (base motion induced by breathing)

(*left*) data_P1_012_20150630_154538, (*right*) data_P1_012_20150630_154644

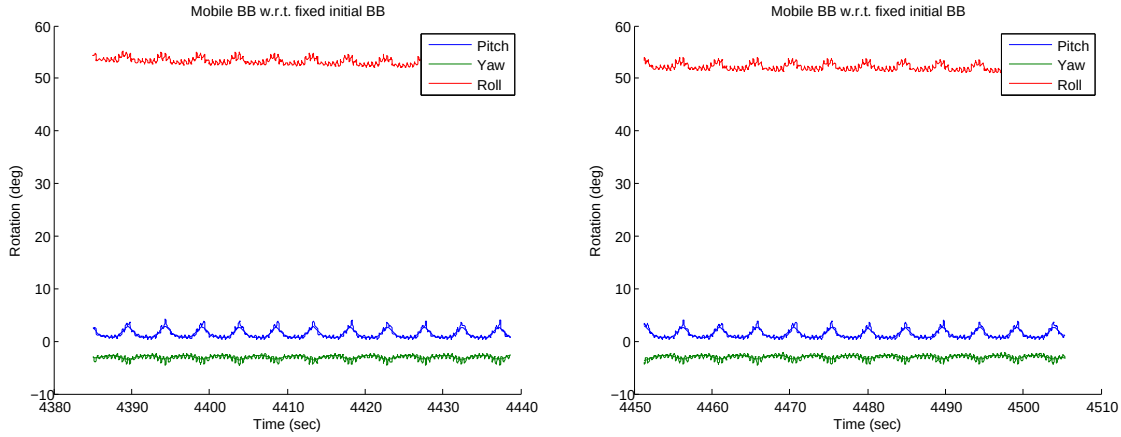

(*left*) data_P1_012_20150630_154538, (*right*) data_P1_012_20150630_154644

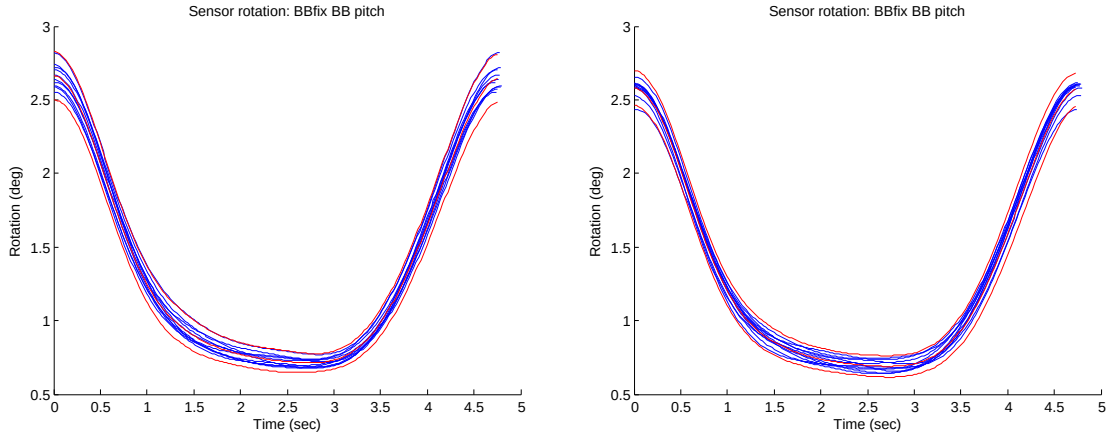

(*left*) data_P1_012_20150630_154538, (*right*) data_P1_012_20150630_154644

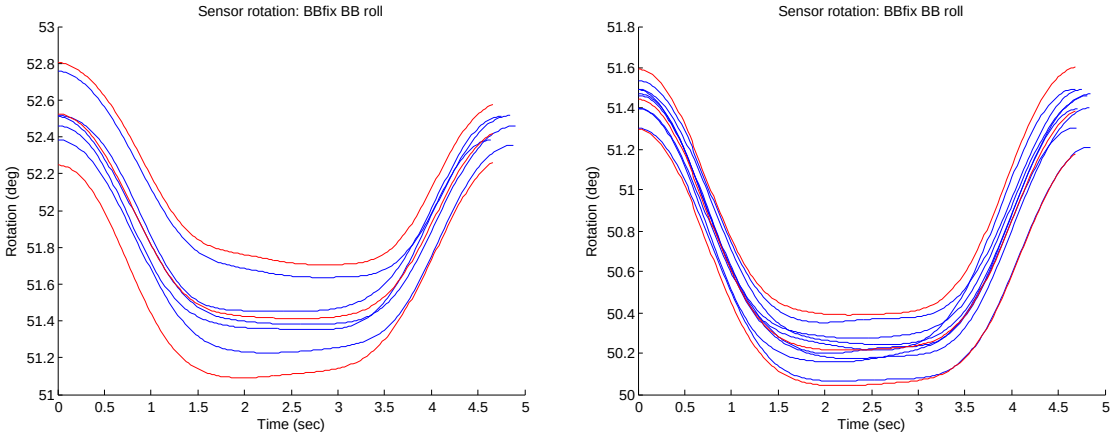

(*left*) data_P1_012_20150630_154538, (*right*) data_P1_012_20150630_154644

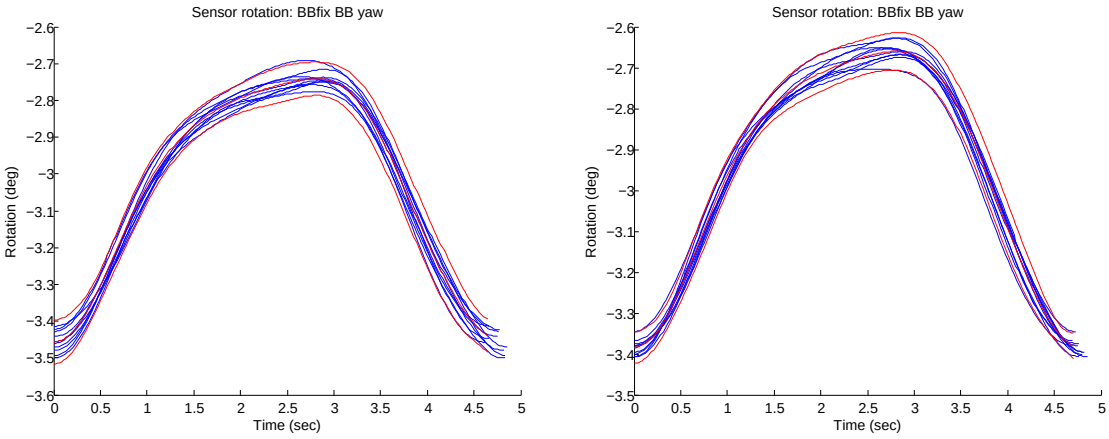

Measured and low pass filtered CT rotation change with respect to mobile BB (tip

rotation induced by breathing)

(*left*) data_P1_012_20150630_154538, (*right*) data_P1_012_20150630_154644

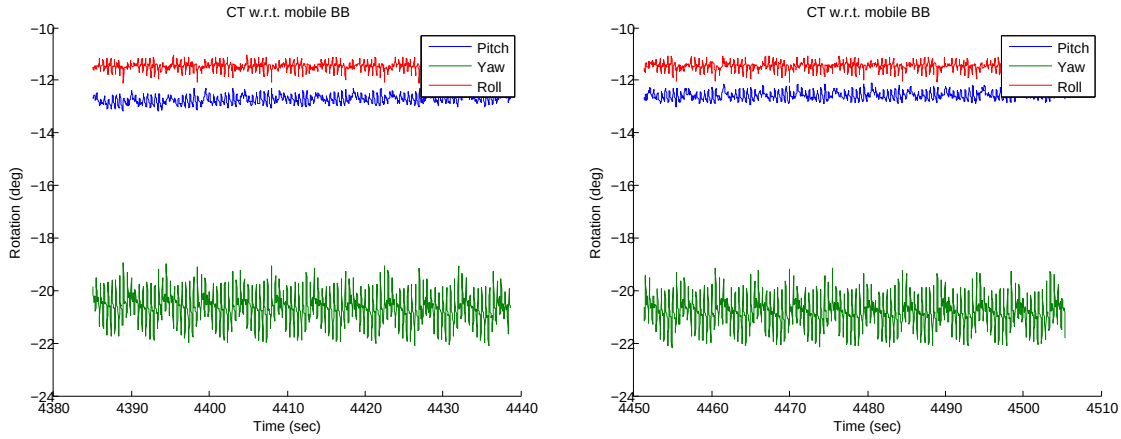

(*left*) data_P1_012_20150630_154538, (*right*) data_P1_012_20150630_154644

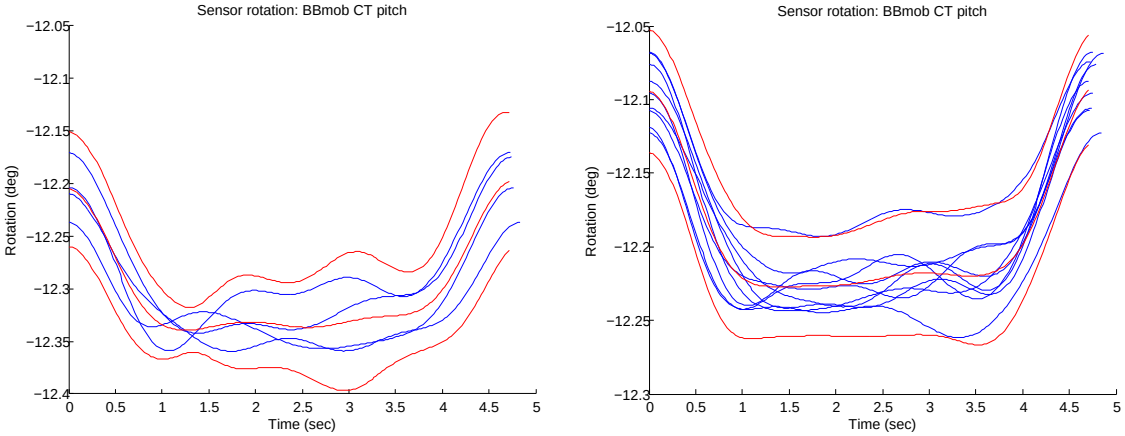

(*left*) data_P1_012_20150630_154538, (*right*) data_P1_012_20150630_154644 (peak detection failed due to low roll)

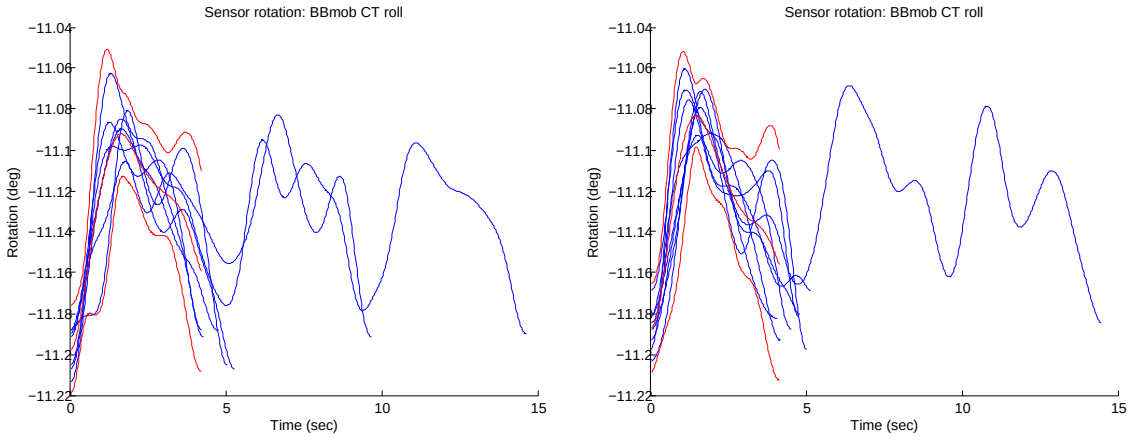

(*left*) data_P1_012_20150630_154538, (*right*) data_P1_012_20150630_154644

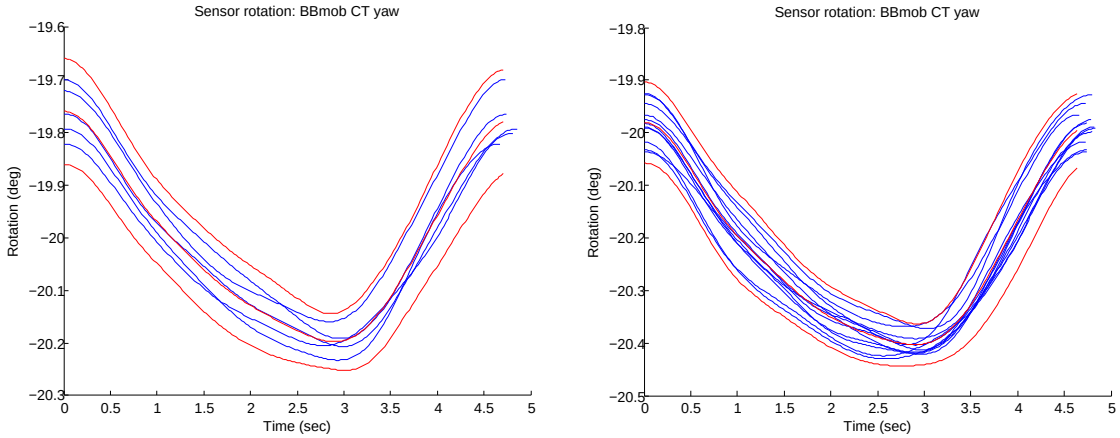

A.5 Inferior Vena Cava

US catheter located in the IVC. Pig 1 (P1) data includes displacement and orientation info. Pig 2 (P2) data includes displacement only. Pig 2 *Instr* sensor disconnected.

Measured and low pass filtered sensor displacement

(*left*) data_P1_013_20150630_155518, (*right*) data_P1_013_20150630_155607

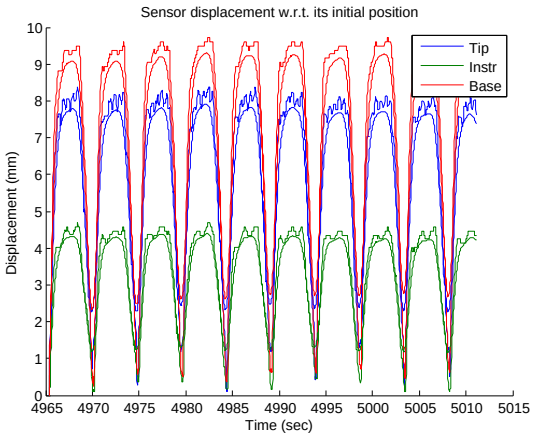

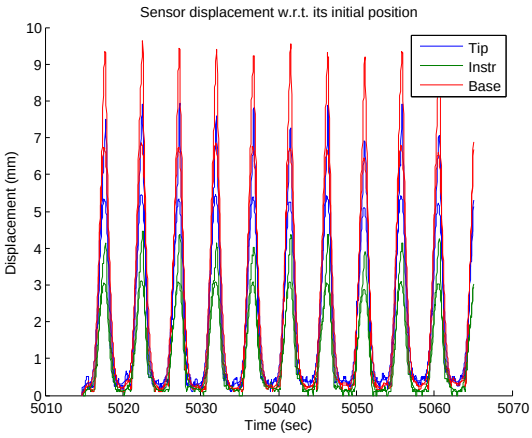

(*left*) data_P1_013_20150630_155700, (*right*) data_P2_215_20150903_174341

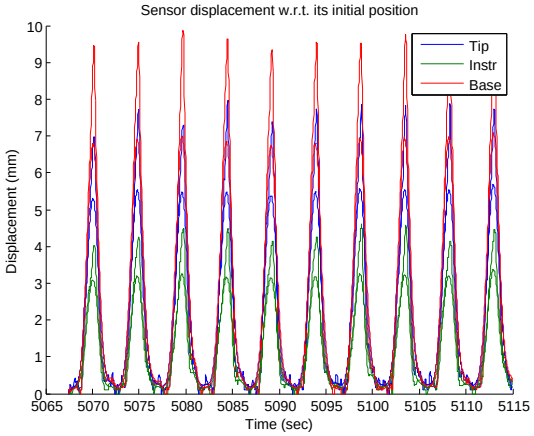

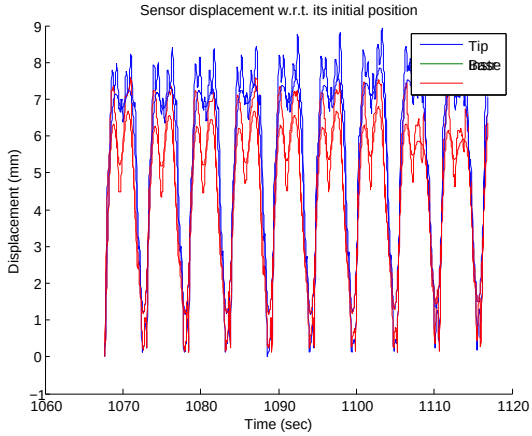

(*left*) data_P1_013_20150630_155518, (*right*) data_P1_013_20150630_155607

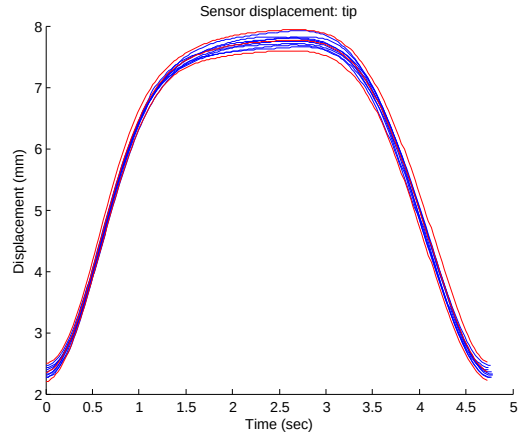

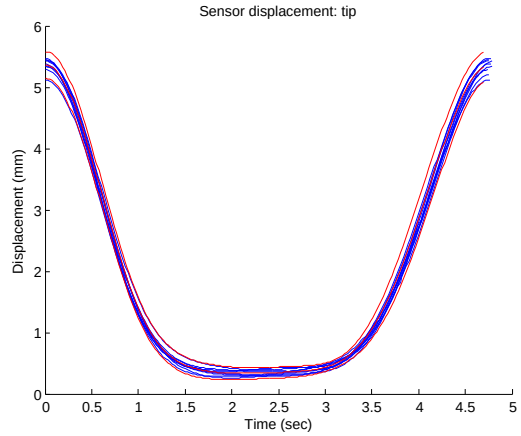

(*left*) data_P1_013_20150630_155700, (*right*) data_P2_215_20150903_174341

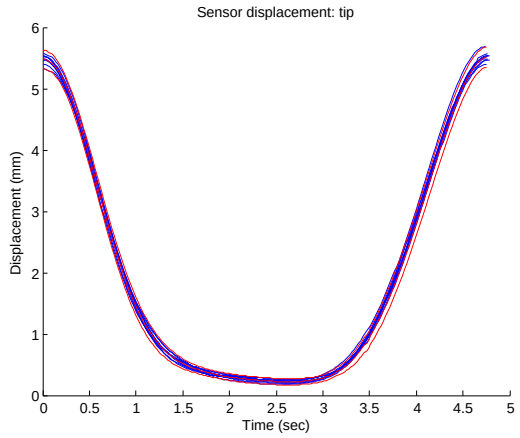

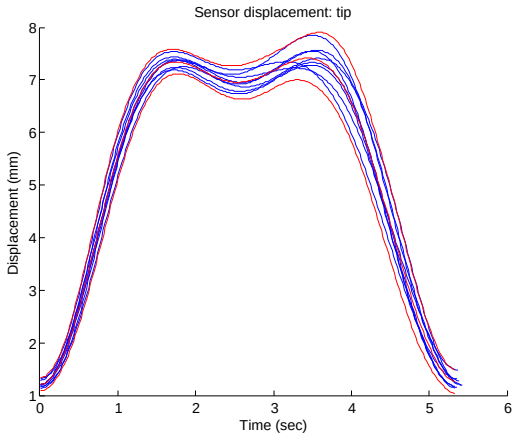

(*left*) data_P1_013_20150630_155518, (*right*) data_P1_013_20150630_155607

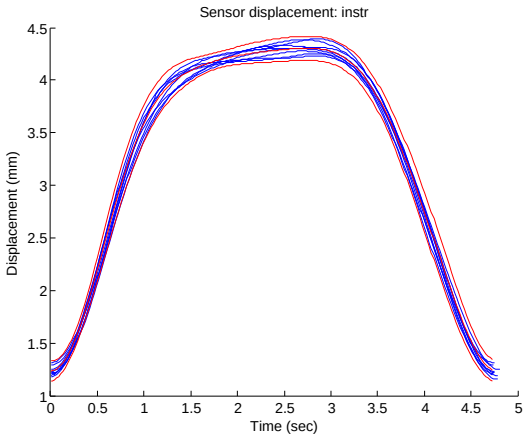

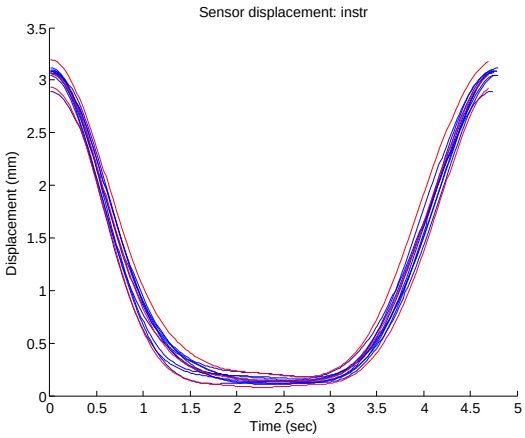

(*left*) data_P1_013_20150630_155700

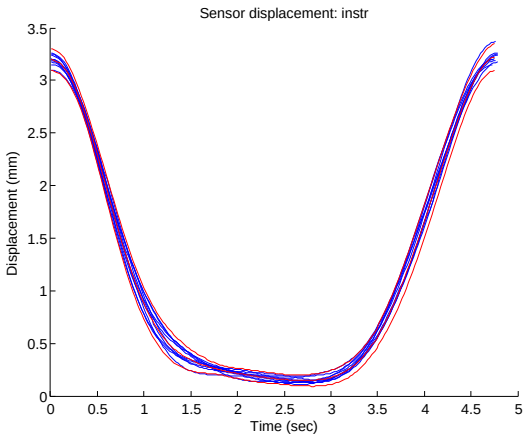

(*left*) data_P1_013_20150630_155518, (*right*) data_P1_013_20150630_155607

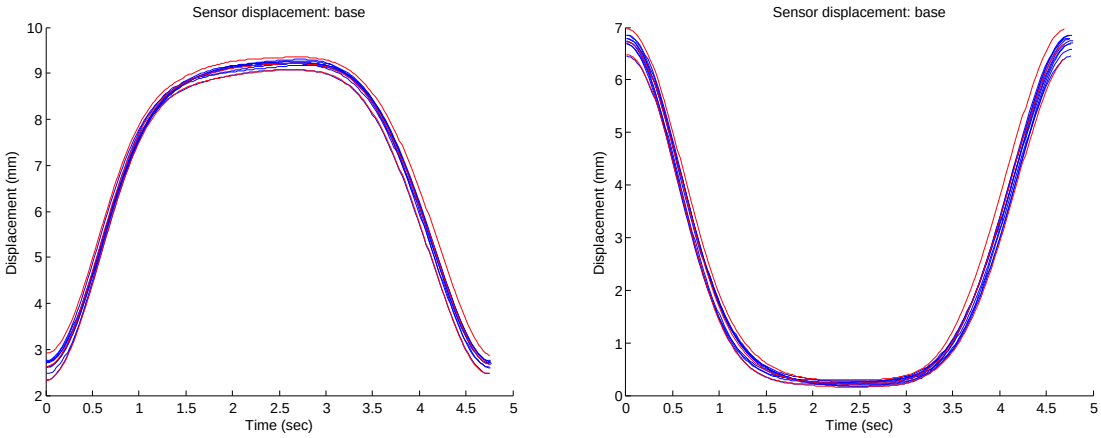

(*left*) data_P1_013_20150630_155700, (*right*) data_P2_215_20150903_174341

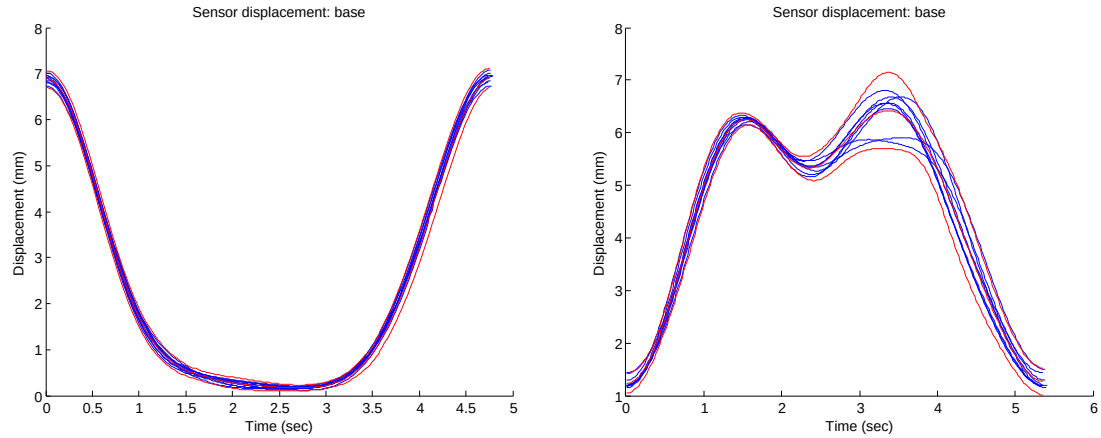

Measured and low pass filtered BB rotation change with respect to fixed BB (base motion induced by breathing). Peak detection on roll angle failed.

(*left*) data_P1_013_20150630_155518, (*right*) data_P1_013_20150630_155607

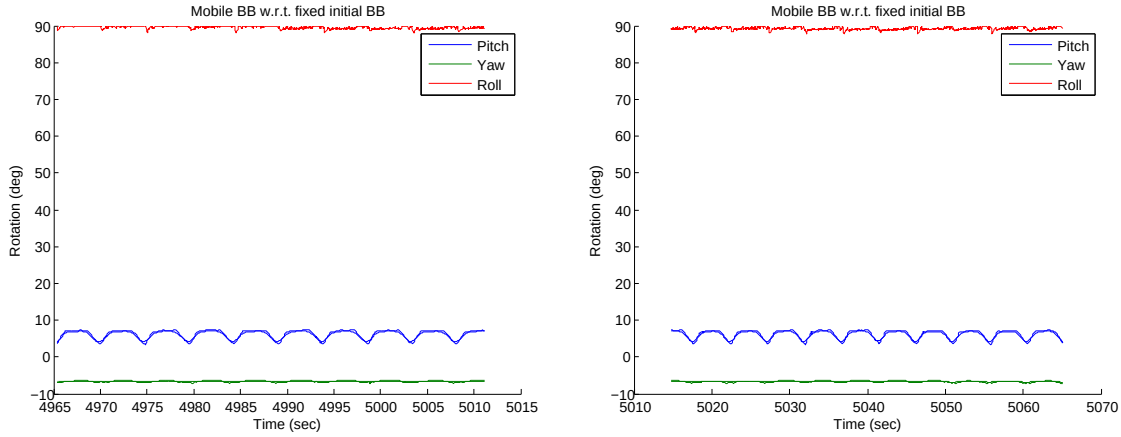

(*left*) data_P1_013_20150630_155700

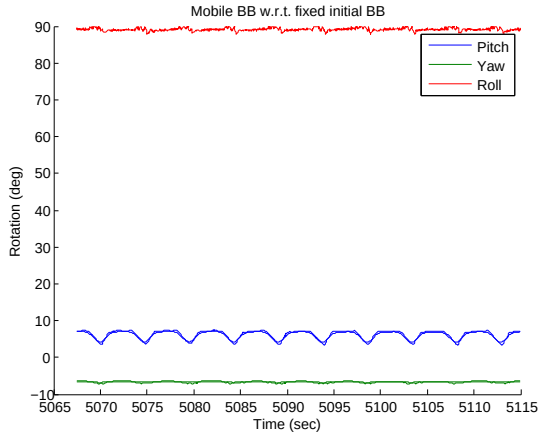

(*left*) data_P1_013_20150630_155518, (*right*) data_P1_013_20150630_155607

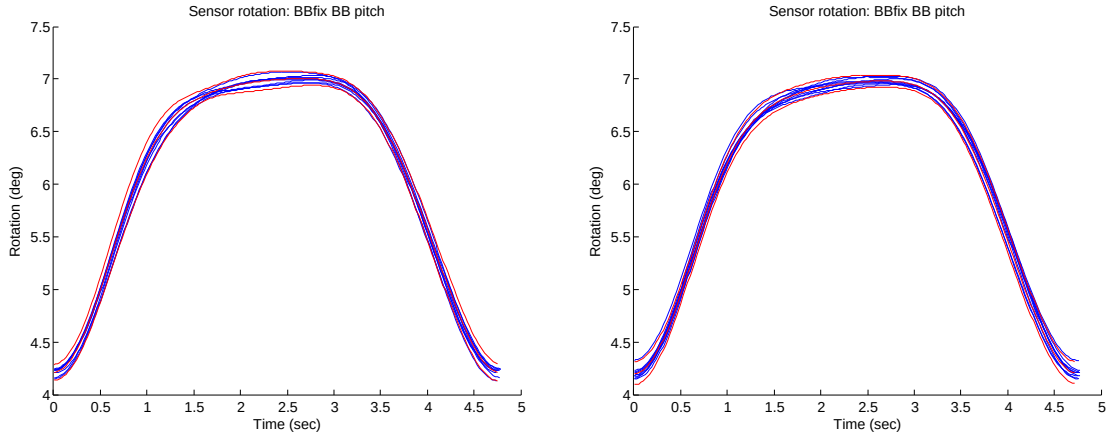

(*left*) data_P1_013_20150630_155700

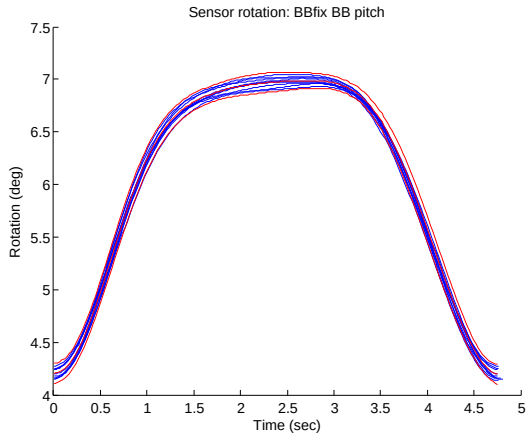

(*left*) data_P1_013_20150630_155518, (*right*) data_P1_013_20150630_155607

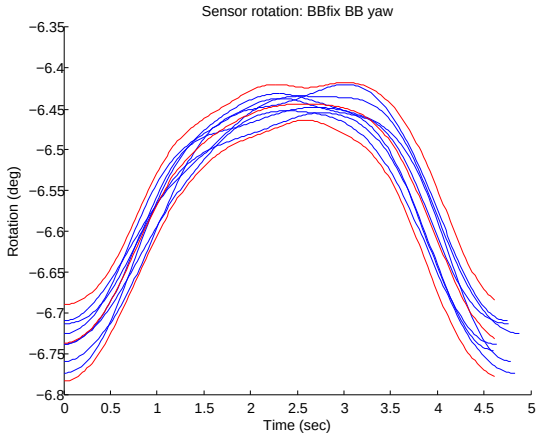

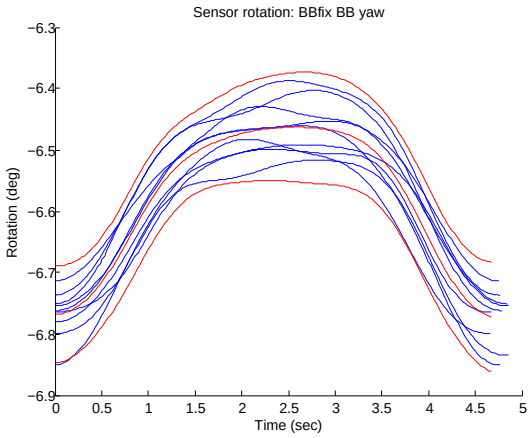

(*left*) data_P1_013_20150630_155700

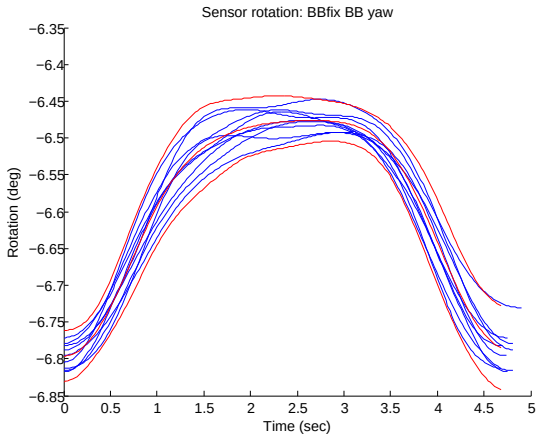

Measured and low pass filtered *CT* rotation change with respect to mobile *BB* (tip rotation induced by breathing)

(*left*) data_P1_013_20150630_155518, (*right*) data_P1_013_20150630_155607

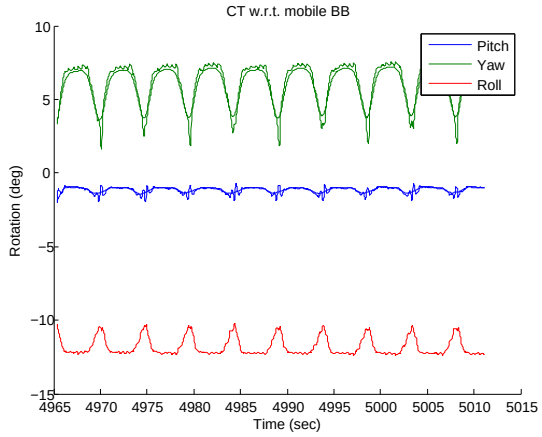

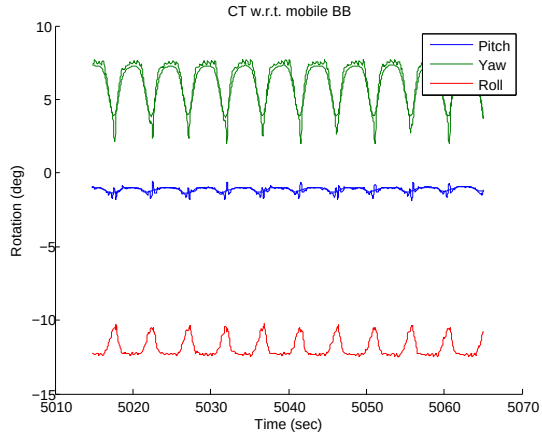

(*left*) data_P1_013_20150630_155700

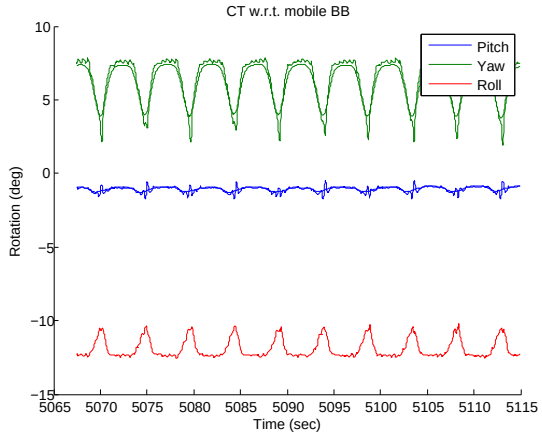

(*left*) data_P1_013_20150630_155518, (*right*) data_P1_013_20150630_155607

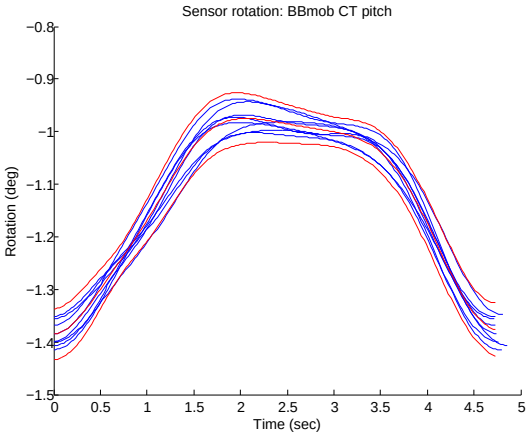

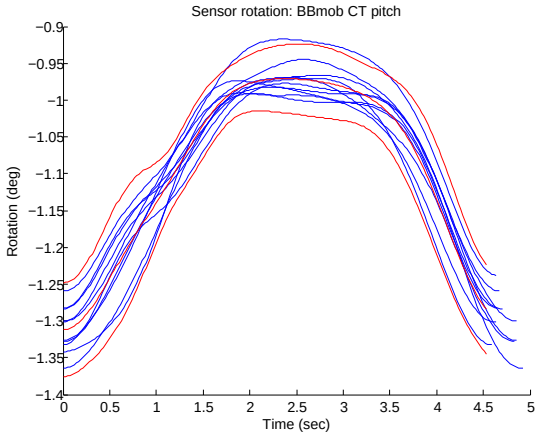

(*left*) data_P1_013_20150630_155700

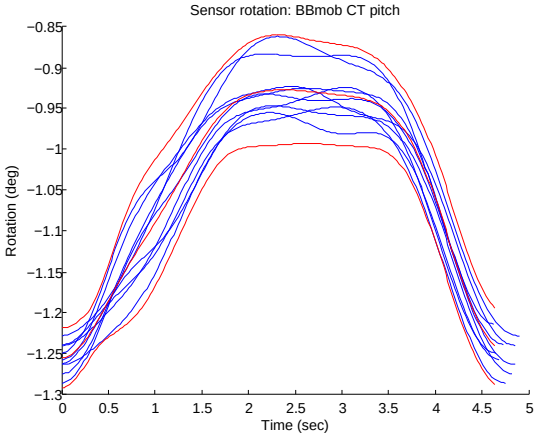

(*left*) data_P1_013_20150630_155518, (*right*) data_P1_013_20150630_155607

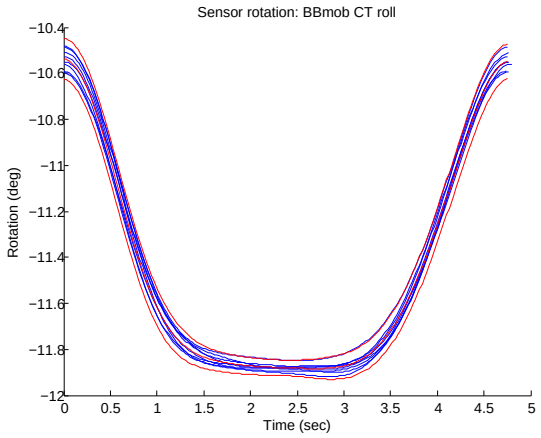

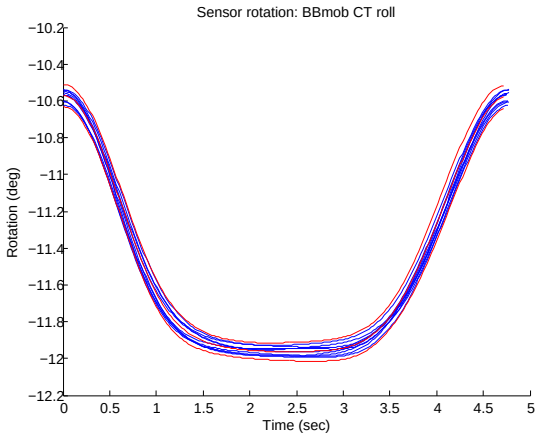

(*left*) data_P1_013_20150630_155700

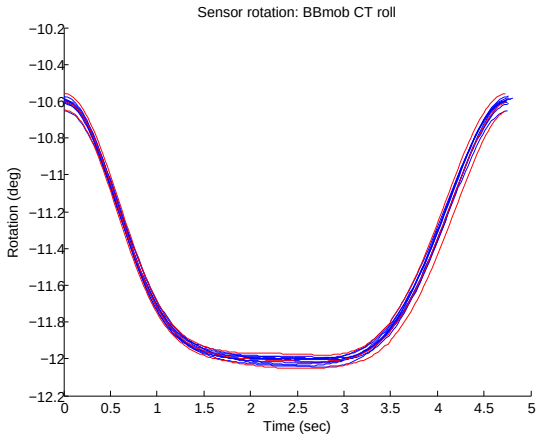

(*left*) data_P1_013_20150630_155518, (*right*) data_P1_013_20150630_155607

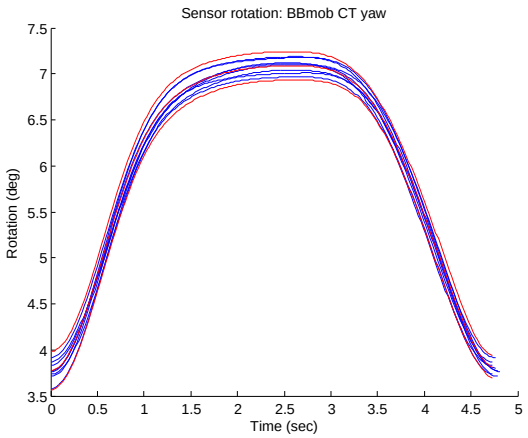

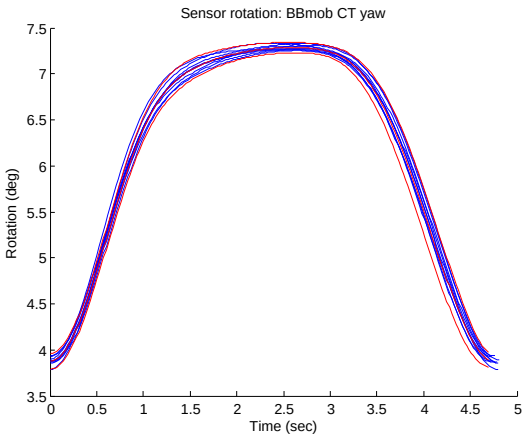

(*left*) data_P1_013_20150630_155700

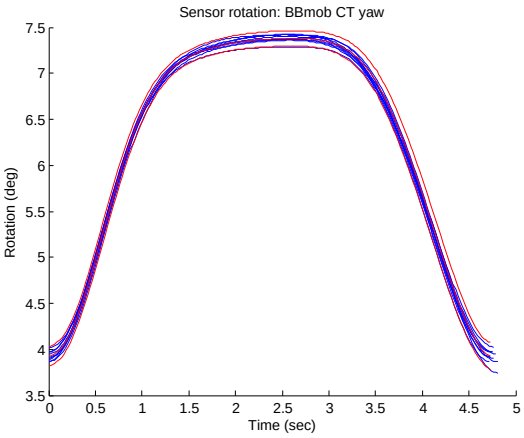
Sensor rotation: BBmob CT yaw
Rotation (deg)
Time (sec)
7.5
7
6.5
6
5.5
5
4.5
4
3.5
0
0.5
1
1.5
2
2.5
3
3.5
4
4.5
5